



Obsah:

36	MATERIALS AND TECHNOLOGIES FOR THE CONSOLIDATION OF HISTORIC PLASTERS BY THE WETTING AND SURFACE PENETRATION METHOD <i>Klára Kroftová, Tomáš Čejka</i>
37	CIRCULAR FOUNDATION PARAMETERS OPTIMIZATION BY METHOD OF BOUNDARY ELEMENTS <i>Alla Morgun, Ivan Met, Roksolana Malachkovska</i>
38	GROUTED SLEEVE CONNECTION FOR PRECAST CONCRETE MEMBERS <i>Kulondwa Kahama Espoir, Xie Fuzhe, Geng Haojie</i>
39	PRINCIPLES AND INSTRUCTIONS FOR COMPLEX PROTECTION OF HISTORIC BUILDINGS WITH VAULTED STRUCTURES FROM THE EFFECTS OF DYNAMIC LOADS <i>Jiří Witzany</i>
40	PREDICTION OF TBM PENETRATION RATE OF WATER CONVEYANCE TUNNELS IN IRAN USING MODERN METHODS <i>Alireza Afradi, Arash Ebrahimabadi, Tahereh Hallajian</i>
41	SEISMIC DAMAGE FIELD OBSERVATION AND VULNERABILITY ANALYSIS OF MULTILAYER REINFORCED CONCRETE FRAME STRUCTURE <i>Siqi Li, Tianlai Yu, Jianqiang Yu</i>
42	DEVELOPMENT OF RURAL ARCHITECTURE – DESIGN AND CREATION OF A WEB DATABASE <i>Petr Soukup, Kryštof Sýkora</i>
43	MEASUREMENT OF TRAFFIC CONGESTION FOR INDORE <i>H.S. Goliya, Kundan Meshram, Suchetan Mahapatra</i>
44	STUDY ON THE INFLUENCE OF CABLE/SLING DAMAGE ON THE NATURAL VIBRATION CHARACTERISTICS OF SPECIAL-SHAPED CABLE-STAYED ARCH BRIDGE WITHOUT BACK CABLE <i>Kexin Zhang, Tianyu Qi, XingWei Xue, Zhimin Zhu, Quansheng Sun</i>

45	<p>APPLICATION OF GEOMATICS METHODS IN THE RESEARCH OF STRUCTURES OF HISTORICAL KITCHENS <i>Miroslava Cejpová, Zdeněk Poloprutský, Štěpánka Poučová, Adam Bujok, Michael Rykl</i></p>
46	<p>EFFECTS OF LARGE-SCALE UNLOADING ON EXISTING SHIELD TUNNELS IN SANDY GRAVEL STRATA <i>WU Hao, MIAO Miao, ZHOU Hui, FENG Zhi-hua</i></p>
47	<p>MODELING AND SIMULATION OF MECHANICAL PROPERTIES OF PULVERIZED COW BONE AND LATERITIC PAVING TILES <i>Peter O. Omoniyi, Jacob O. Aweda, Idehai O. Ohijeagbon, Ridwan A. Busari and Mustapha Ndagi</i></p>
48	<p>STUDY ON EARTHQUAKE DAMAGE MECHANISM OF AQUEDUCT STRUCTURE BASED ON DIFFERENT BOUNDARY <i>Xinyong Xu, Xuhui Liu, Cheng Zhang, Xinyun Xu, Jianwei Zhang</i></p>
49	<p>IMPACT OF ECO FRIENDLY BLAST FURNACE SLAG ON PRODUCTION OF BUILDING BLOCKS <i>Ashish Nim and Kundan Meshram</i></p>
50	<p>TEMPERATURE MODELLING IN ASPHALTIC CONCRETE FACINGS, THE REFLECTIVE SURFACE EFFECT SIMULATION CASE STUDY: GHRIB DAM (AIN DEFLA, ALGERIA) <i>Chebbah Lynda, Djemili Lakhdar, Chiblak Mohamed, Bouziane Mohammed Tawfik</i></p>
51	<p>MATERIALS AND TECHNOLOGIES FOR THE STRENGTHENING OF HISTORIC MASONRY BY THE DEEP GROUT INJECTION AND SURFACE PENETRATION METHOD <i>Jiří Witzany, Radek Zigler, Klára Kroftová, Tomáš Čejka, Jan Kubát</i></p>

MATERIALS AND TECHNOLOGIES FOR THE CONSOLIDATION OF HISTORIC PLASTERS BY THE WETTING AND SURFACE PENETRATION METHOD

Klára Kroftová and Tomáš Čejka

Czech Technical University in Prague, Faculty of Civil Engineering, Department of Architecture, Prague, Thákurova 7, Czech Republic; klara.kroftova@fsv.cvut.cz, tomas.cejka@fsv.cvut.cz

ABSTRACT

The term of a historic plaster or surface coating, respectively, denotes a layer or a multilayer of materials firmly bonded to the substrate, whose structural and technical condition significantly affects not only the aesthetic effect, but mainly the service life of this surfacing. Due to the permanent exposure of plaster surfaces to the external environment (in the exterior as well as the interior), they belong to the group of the most exposed parts of historic and heritage buildings, often exhibiting a high degree of degradation and disintegration. The consolidation and rehabilitation of plasters with, among other things, a degraded binder component, damaged structure and insufficient adhesion of individual layers to each other and to the masonry substrate is a challenging task in the restoration of historic buildings. The paper presents the alternative of strengthening degraded surface layers by means of nanomaterials based on calcium hydroxide applied by the surface penetration method.

KEYWORDS

Plaster, Calcium hydroxide, Consolidation, Nanosuspension, Penetration

INTRODUCTION

The most common defects and failures of plasters are characterized mainly by changes in their structure, by overall disintegration, reduced cohesion of surface layers and their spalling from the substrate, the formation of bumps, occurrence of cracks and a change, or a loss of the colour of surface coatings. In the final phase of degradation, the plaster no longer fulfils its function and falls off. Depending on the manifestations of degradation, a suitable rehabilitation method can be chosen to observe the heritage conservation requirements, particularly in terms of preserving the value of the heritage building and its surface coating. The basic objective of the consolidation of surface coatings is the improvement of the mechanical properties of materials, strengthening of subsurface and surface layers and their return to a state close to the original properties of the treated material. Achieving this goal is one of the most challenging tasks in the restoration of historical heritage [1]. The principle of plaster renewal is based on adding the weathered and degraded binder to the structure of the treated material, or attaching the separated parts to the substrate (or to each other) and filling in the missing parts (cracks, cavities, etc.). The essential part of this process is, in particular, structural reinforcement, which is achieved with the help of appropriately selected consolidating agents based on the analysis of the treated material and the

causes of its poor structural and technical condition. The role of the consolidating agent is to stabilize the damaged plaster system or replace the “leached” original binder material, ideally with a material of identical properties [2].

The improvement of adhesion between the surface coating and masonry, the strengthening of surface and subsurface layers, i.e. surface grouting, is currently most often performed by repeated impregnation (spraying, painting), by methods based on the capillary activity (wetting, sprinkling, capillary elevation) or microinjection of damaged parts [3]. In most cases, it is advisable to combine individual consolidation methods with each other to achieve the best results possible (e.g. microinjection and spraying, etc.). Among the commonly used consolidating agents, there are, above all, inorganic materials (silicic acid esters, aqueous SiO₂ dispersions). Their use is limited by the moisture content in the plaster (in the case of organosilicon esters), or salts (in the case of a colloidal silica solution) [4]. In the last decades, the number of lime water applications, in particular, has increased, which, however, is associated with a series of problems [5]. In the case of using lime water, which has only a low lime component content in the injected agent (CaCO₃ solubility in water is ca 1.6 g/l at a water temperature of 20°C), the application must be repeated in tens of cycles (120 to 180 cycles), which results in a significant long-term wetting of the structure and the activation of salts in the reinforced substrate.

In the last 20 years, the possibilities of using disperse and colloidal systems of not only organic consolidants, but also mineral systems with particle sizes in the nanoscale have been verified in the cultural heritage conservation. The use of nanomaterials with particle sizes of up to 1µm, whose properties are somewhere at the intersection between the properties at the level of molecules and matter [10, 11], is the subject of extensive scientific research due to their positive physical and mechanical properties such as high chemical performance, excellent plastic, consolidation and diffusion properties, cleaning capabilities and more. The tested nanomaterials mainly include nanodispersions based on hydroxides, carbonates, or sulphates [12, 13, 14].

In the case of hydroxide-based nanodispersions, there are products commercially available of mostly German and Italian origin (e.g. CaLoSiL®, or NanoRestore®) or SiO₂-based colloids (e.g. Syton X30, Tosil).

The lime nanosuspension is composed of calcium hydroxide nanoparticles dispersed in an alcoholic medium, where individual sorts differ from each other in concentrations and the type of alcohol. The curing of this material results, in a simplified way, in carbonation where calcium hydroxide reacts with atmospheric carbon dioxide to produce calcium carbonate, like in fresh plaster [15]. Due to the deposition of calcium carbonate in the degraded material, the bonds are re-strengthened and the material reinforced.

Nanosuspensions can be diluted to a concentration of 5 to 50 g/litre, where the alcohol will evaporate completely after the application. The degree of penetration is significantly affected by the particle size, where in the case of lime nanodispersions we can achieve penetration rates to such depths where common lime suspensions (prepared from slaked lime) do not penetrate, thanks to the low particle size with a large specific surface area [16, 17]. The penetration depth can be affected either by adding a small amount of other solvents such as acetone or pentane, or by choosing a suitable application technique. The positive properties of these materials include excellent water vapour permeability, the absence of chemical changes or shiny effects and the absence of the formation of surface hydrophilic films.

MATERIALS AND METHODS

The strengthening and stabilization method of historic plasters by overall surface pressure grouting (penetration) and wetting is based on an additional mechanical supply of Ca²⁺-based nanomaterials to the structure of materials and the activation of unreacted Ca²⁺-based substances contained in the structure of grouted materials, which increases their strength, cohesion or adhesion to the substrate.

Before performing the overall surface pressure grouting (penetration) and wetting of historic plasters, the edges of cracks or cavity walls must be cleaned of dirt, dust, oils, grease and other particles that reduce adhesion, and then they must be filled with adequate lime mortar and levelled on the surface.

In overall surface pressure grouting, the grouting solution is “pushed” into the pore (injectable) plaster system (surface coating) so that the required gradual saturation of the pores of the respective layers occurs. The main advantage of this method is its high efficiency and uniformity in terms of strengthening the plaster and increasing its adhesion to the substrate.

During wetting (mechanical application), the grouting solution penetrates through the capillary phenomena into the pore system and thus into the plaster structure. The grout propagation speed and the penetration depth depend on the grout properties, the number of wetting repetitions, the type of pore system [18, 19], but also on the moisture and salt content in the grouted material.

Grouting mixtures and agents for the wetting and surface penetration method

The choice of consolidating agents must fully respect the requirements for application to historic or heritage masonry and its surface coating. For overall surface pressure grouting (penetration) and wetting, calcium hydroxide-based grouting agents were prepared, which have a high penetration and distribution (uniform) ability, material and chemical compatibility and adequate consolidation ability (to avoid local over-reinforcement of the treated substrate compared to untreated material - the strength of the treated material should not increase by more than 10 - 20%).

The grouting agents based on calcium hydroxide nanoparticles were developed within the NAKI II DG16P02M055 research project in the researchers' workplace cooperation with the Centre of Polymer Systems (Tomas Bata University in Zlin):

- **Ca4O (V5)** The test portion of calcium oxide CaO was dispersed in ethanol and distilled water was added. The reaction was complete after 4 hours. The suspension was successively made up to a volume of 2 litres. The Ca(OH)₂ concentration was ca 7 g/l. The prepared nanosuspension contains a lot of sliced hexagonal Ca(OH)₂ crystals with a different size distribution. According to DLS, 2 peaks are visible – one with a maximum of 4813 nm, which is probably caused by large agglomerates of Ca(OH)₂ particles, and then the peak with a maximum of 1667 nm, which, in our case, corresponds to the size of (separated) Ca(OH)₂ particles in the solution. Consolidation, sealing of concrete and brick, stone and mixed masonry (Figure 1a);
- **CaMg1 (V7)** Test portions of Ca(OAc)₂·H₂O and Mg(OAc)₂·4H₂O were mixed and dispersed in isopropyl alcohol. Water was added to the suspension and precursors were dissolved. The NaOH (28.0 g in 700 ml H₂O) solution was added to the solution of Ca and Mg precursors and a white suspension was formed. The reaction was left in the mg mixer for 24 hours and then the white hydroxide precipitate was separated by centrifugation and washed with a mixture of water and isopropyl alcohol. After washing, the product was centrifuged and dispersed in 2 l of isopropyl alcohol. The resulting Ca(OH)₂+Mg(OH)₂ concentration is ca 7 g/l. Elemental (EDX) analysis confirmed the content of magnesium (8.5 wt%), calcium (37.8 wt%) and oxygen (48.4 wt%). Consolidation, sealing of concrete and brick, stone and mixed masonry (Figure 1b);
- **CaMg2 (V8)** Test portions of Ca and Mg were dispersed in iPrOH and water was added. The reaction was complete after 6 hours. The suspension was made up to a volume of 2 litres (by adding 0.5 l of iPrOH). The Ca(OH)₂+Mg(OH)₂ concentration is 6 g/l. Elemental (EDX) analysis

confirmed the content of magnesium (7.3 wt%), calcium (43.4 wt%) and oxygen (44.5 wt%) (Figure 1c);

- Ca4O-Si (V9)** The test portion of CaO was dispersed in EtOH and water was added. Then, APTES (aminopropyltriethoxy silane) was added. The suspension thickened and EtOH was added. The total volume of the suspension is thus 2.8 litres, and the Ca(OH)₂ concentration is approximately 5 g/l. According to DLS, 2 peaks are visible - the first, more intense peak with a maximum of 792 nm can be assigned to Ca(OH)₂ particles. The peak with a maximum of 184 nm corresponds to alkoxy silane or silica structures formed after the addition of APTES to the reaction mixture. Elemental (EDX) analysis confirmed the content of silicon (11.5 wt%), calcium (39.3 wt%) and oxygen (33.7 wt%) (Figure 1d).



Fig. 1 - Ca(OH)₂ particle size in nanolime suspensions was measured by the dynamic light scattering (DLS) method. The Malvern Zetasizer ZS device was used for the measurement: a) CaMg1; b) CaMg1; c) CaMg2; d) Ca4O-Si.

Verification of consolidation of historic plasters

The verification of injectability and selection of a suitable grouting mixture are based on experimental studies performed during the project research in 2018 and 2019, which included the verification of grouting technologies of historic masonry and its surface coating, masonry elements and binders with similar or different pore systems for selected materials (Figure 2).

Verification of consolidation of historic plasters by the wetting and surface penetration method

The technological principle was verified by consolidation tests of historic plasters reinforced by overall surface pressure grouting - penetration and wetting, performed in-situ on historic lime, partially degraded plasters [20]. Prior to grouting, degraded plaster specimens were sampled and laboratory moisture and porosimetry measurements performed.

The grouts were (a) repeatedly uniformly pushed into historic plasters using a highly absorbent and compressible material applied with a gradually increasing compressive force induced by the front plate; (b) repeatedly applied with a brush (wetting method), (Figure 3).

In the case of both methods, the consolidating agent was applied in 3 to 5 cycles with a comparable resulting volume during the experimental verification. In both cases, the grout was applied in such a way to avoid its surface run-off (or minimize the run-off). Each subsequent application cycle was performed before the previously applied grout was completely dry.

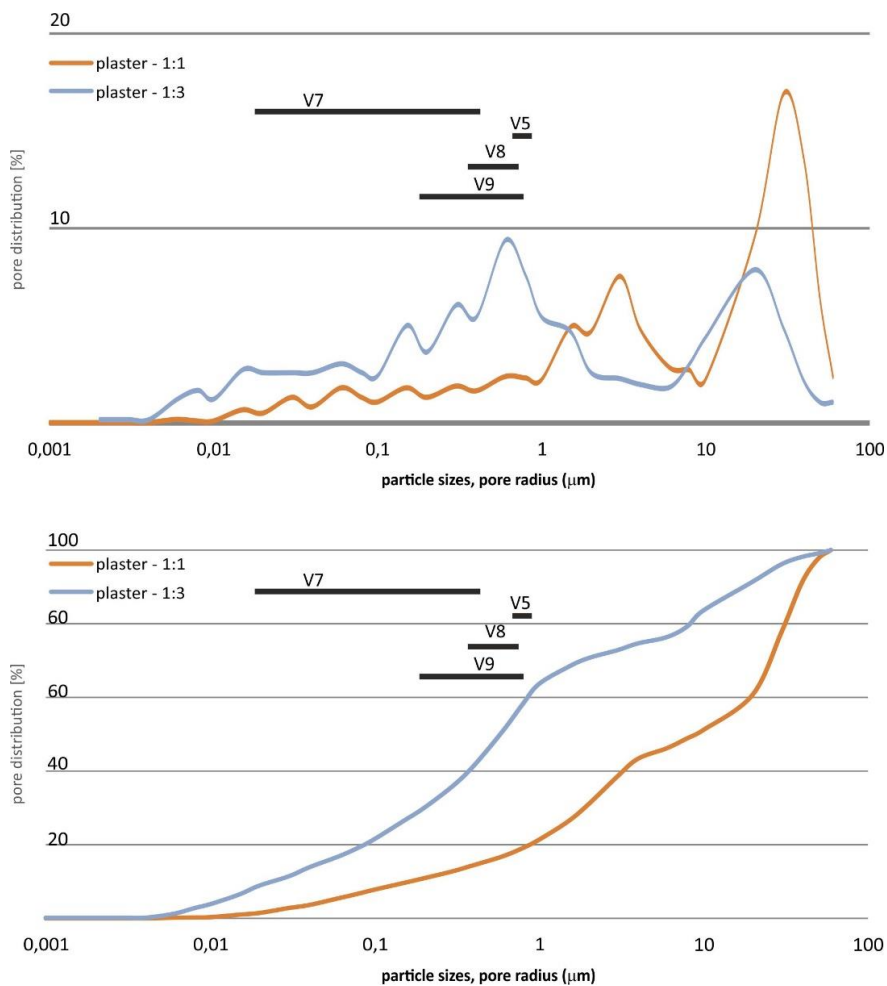


Fig. 2 - Comparison of pore radii in plaster (distribution and integral curves) and particle sizes of grouting agents based on nanolime (legend: plaster 1:1 and 1:3 – slaked lime-sand mixing ratio)

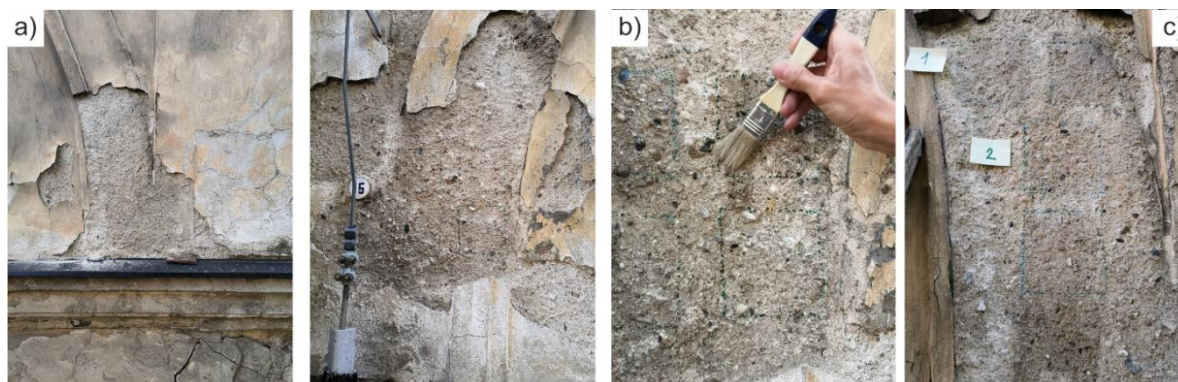


Fig. - 3 Documentation of a degraded historic plaster used for the verification of the degree of consolidation by means of prepared nanomaterials: a) selected points for consolidation and sampling; b) consolidation of plasters by wetting, c) structure with consolidated surfaces

Scotch Tape tear-off test

To verify the effectiveness of the consolidating agent or the consolidation method used, in-situ "Scotch Tape tests" were conducted [21, 22]. The tear-off test was performed on the surface of plasters (i.e. individual tested fields) before and after grouting. As part of the laboratory verification, the total porosity, distribution and integral curves describing the pore system were identified after the consolidation of plasters.

The in-situ measurement of the cohesion of surface and shallow subsurface layers (lime plaster on mixed masonry) was performed after 28 days of maturing. The sampling procedure for the Scotch Tape tear-off test was as follows: a marked adhesive tape 20 mm wide with a high adhesion capacity and softness was pressed against the tested surface and after approximately 60 seconds it was peeled off perpendicular to the surface and successively put in the transport case (Figure 4). The sampling from each spot was repeated 10 times to reduce the degree of bias in the results due to uneven material moisture contents, weathering, surface roughness and the application method used (degree of pushing and peel-off speed and angle). Each strip with torn-off material was weighed and the weighted average was calculated after weighing.

The sampling was performed at a temperature of 20.5 ° C and a relative humidity of 49%.

The amount of separated material is indicative and only serves to compare the values before and after consolidation. The measurement results show some variance in the measured values and thus also the resulting characteristics, which is probably caused by some deviations in plaster properties at individual sampling points, by local moisture contents of the material, inhomogeneity of the plaster, roughness or the degree of surface degradation and the execution method, in particular the pushing and tear-off speed and angle.

The results of Scotch Tape tear-off tests are presented in Table 1.

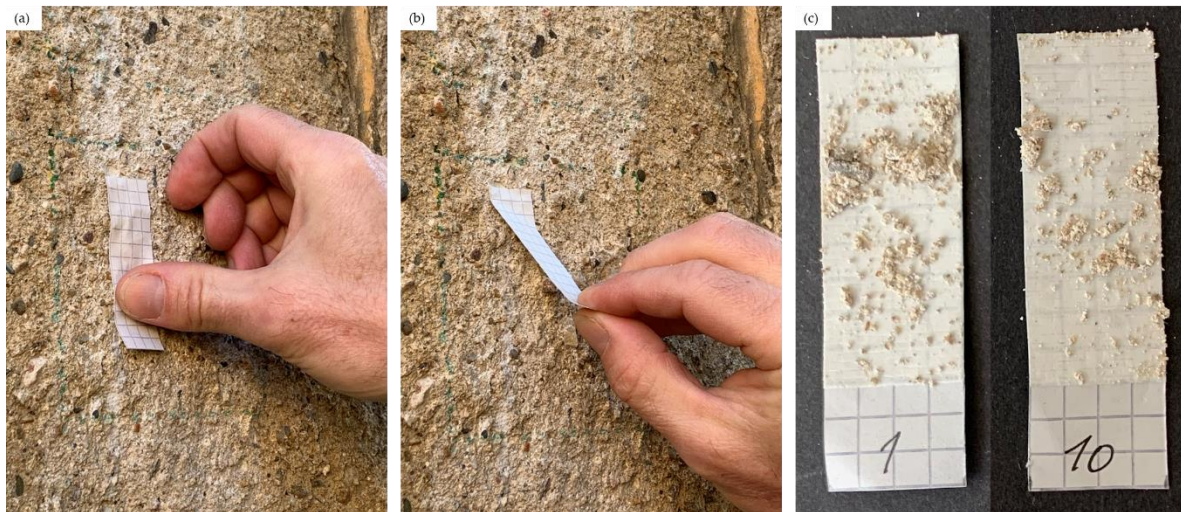


Fig. 4 - Scotch Tape test performed 28 days after the application of grouts: a) adhesive tape pressing against the tested surface; b) test tape peel-off by smooth movement; c) comparison of the first and the last tear-off tape of a specimen consolidated by pressure penetration of Ca4O-Si nanosuspension

Tab. 1 - Results of the Scotch Tape test in relation to the grouting technology used

specimen marking	grouting agent	grouting technology	Scotch Tape test mean (g)	Scotch Tape test 1 st , 5 th , 10 th peel-off (g)
No. 1	Ca4O-Si	wetting	0. 4354	0. 4648
				0. 4005
				0. 3366
No. 2	Ca4O	wetting	0. 3164	0. 6467
				0. 3840
				0. 2724
No. 3	CaMg1	wetting	0. 4442	0. 3268
				0. 2780
				0. 3239
No. 4	CaMg2	wetting	0. 4358	0. 3368
				0. 2870
				0. 3241
No. 5	Ca4O-Si	pressure penetration	0. 3534	0. 4902
				0. 3188
				0. 4428
No. 6	Ca4O	pressure penetration	0. 3159	0. 4477
				0. 4872
				0. 6152
No. 7	CaMg1	pressure penetration	0. 4435	0. 5059
				0. 3886
				0. 4043
No. 8	CaMg2	pressure penetration	0. 5685	0. 9696
				0. 5299
				0. 4858
No. 9 REF	-	-	0. 4653	0. 6025
				0. 6182
				0. 3003

Determining changes in porosity

The pore distribution was determined by high-pressure mercury porosimetry on sampled plaster specimens. The measurements were performed on plaster specimens with a size of cca 5 mm (cca 1 cm³), and two independent measurements were always made on each specimen in a set of Pascal 140 + 240 porosimeters manufactured by Thermo Electron - Porotec. The Pascal 140 porosimeter serves as a filling device and low-pressure measurements up to a pressure of 100 kPa are performed in it. The 240 porosimeter operates in a pressure range of 0.1 to 200 MPa. Before the analysis, the specimens were evacuated at a temperature of 90 °C and then they were evacuated to a constant pressure of less than 0.01 kPa in the device. The evaluation was performed in instrument software vers.1.05, using the surface stress value $\sigma = 480 \cdot 10^{-3} \text{ N}\cdot\text{m}^{-1}$ and the contact angle value $\varphi = 140^\circ$.

When a pressure interval of 0.1 kPa to 200 MPa is used, pores with radii from 3.7 nm to 58 μm can be indicated, which represents the identification of meso, macro and coarse pores due to the standard pore distribution according to their radius into micropores ($r < 1 \text{ nm}$), mesopores ($r = 1 - 25 \text{ nm}$), macropores ($r = 25 - 7500 \text{ nm}$) and coarse pores ($r > 7500 \text{ nm}$).

In terms of a change in total porosity, no significant changes in the total porosity of the samples were found in the majority of tested specimens. In specimens No. 2, 4 and 7, the total porosity identified was by ca 10% higher compared to the total porosity of the reference specimen. In specimen No. 6, there was a decrease in total porosity by ca 20% compared to the total porosity of the reference specimen. The results of changes in total porosity are presented in Tables 2 and 3 and in Figure 5.

Tab. 2 - Change in total porosity in relation to the grouting technology used

specimen marking	grouting agent	grouting technology	total porosity (%)
No. 1	Ca4O-Si	wetting	29.415
No. 2	Ca4O	wetting	31.91
No. 3	CaMg1	wetting	29.55
No. 4	CaMg2	wetting	32.785
No. 5	Ca4O-Si	pressure penetration	29.945
No. 6	Ca4O	pressure penetration	23.875
No. 7	CaMg1	pressure penetration	32.85
No. 8	CaMg2	pressure penetration	29.385
No. 9 REF	-	-	29.875

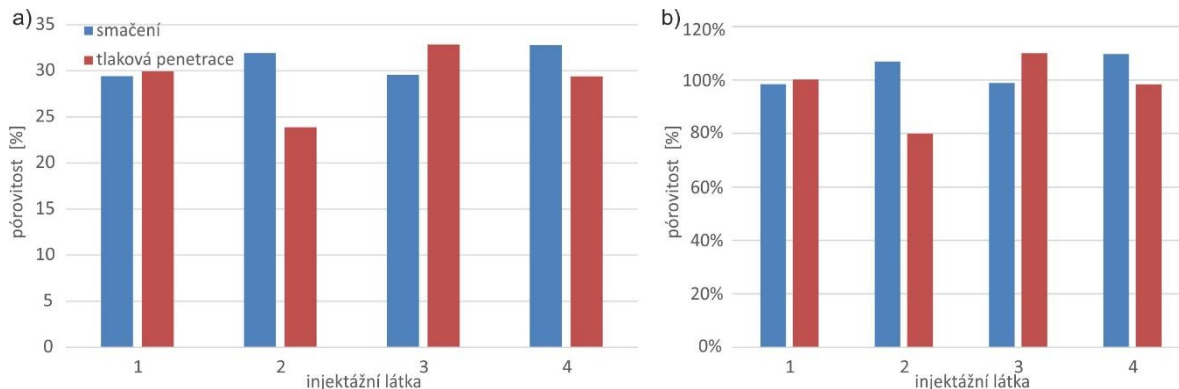


Fig. 5 - Total porosity of plaster (a) related to the reference specimen (b) in relation to grouting agents and grouting technology

In terms of changes in the pore distribution, the effect of grouting was manifested mainly in the domain of macropores and coarse pores compared to the pore distribution in the reference specimen. With the exception of specimen No. 7, the proportion of pores with a radius of 5000 to 100000 nm decreased by ca 6 to 32% compared to the reference specimen. The change in the proportion of pores with a radius of 700 to 5000 nm was more significant in the case of pressure penetration where there was a decrease in the proportion of these pores by up to 15% compared to the reference specimen. In the case of the wetting technology, the decrease in these pores was by ca 5% compared to the reference specimen. When both grouting technologies were used, the proportion of pores with a radius of 10 to 700 nm increased (by ca 5 to 15%) or decreased by ca 5% compared to the reference sample. The changes in the pore system distribution are shown in Figures 6, 7 and in Table 3.

Tab. 3 - Change in the pore distribution and total porosity

specimen marking	grouting agent	total porosity [%]	pore radius [%]			pore radius [%]		
			10-700 nm	700-5000 nm	5000-100000 nm	10-700 nm	700-5000 nm	5000-100000 nm
No. 1	Ca4O-Si	98.5	51.4	51.3	15.5	109.0	94.6	94.4
No. 2	Ca4O	106.8	46.8	51.2	15.5	99.3	94.5	94.4
No. 3	CaMg1	98.9	52.6	54.4	10.9	111.5	100.4	66.7
No. 4	CaMg2	109.7	43.9	57.9	11.9	93.1	106.7	72.5
No. 5	Ca4O-Si	100.2	46.2	56.1	13.5	97.9	103.6	82.2
No. 6	Ca4O	79.9	49.6	54.4	12.1	105.3	100.4	73.7
No. 7	CaMg1	110.0	45.2	46.0	21.9	95.8	84.9	133.9
No. 8	CaMg2	98.4	54.3	49.5	12.8	115.2	91.3	78.4
No. 9 REF	-	100.0	47.2	54.2	16.4	100.0	100.0	100.0

Note: The total sum of the proportion of pore radii can be greater than 100 % due to overlapping intervals of pore radii.

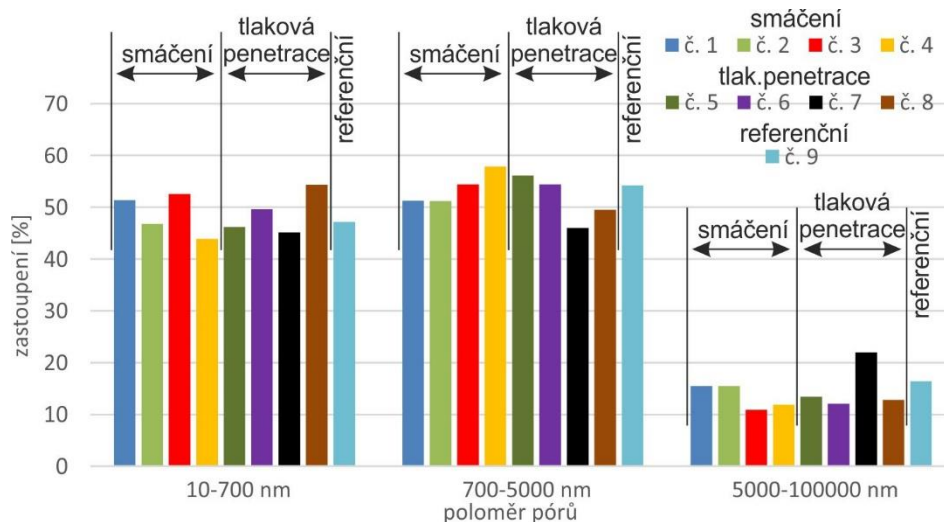


Fig. 6 - Changes in the pore distribution in selected intervals of pore radii

While comparing the effect of the particle size of grouting agents on changes in the pore distribution of historic plaster specimens, based on the analysis of the results of mercury porosimetry, we can conclude that there was a change – drop by 5 to 33% – in the proportion of pores with a radius of 5000 to 100000 nm in the majority of grouts. The changes in the proportion of pores with smaller radii were mostly manifested in the CaMg1 grouting agent applied by the pressure penetration technology. In all cases of a drop in the proportion of pores with a radius of 5000 to 100000 nm, there was an increase in the proportion of pores with radii of 10 to 700 nm and 700 to 5000 nm.

CONCLUSION

The visual evaluation of the colour of test surfaces after the application of nanosuspensions indicates the deposition of lime particles and the undesirable formation of a whitish shade of the plaster. A significant deposition occurred mainly in the case of the Ca4O-Si and Ca4O nanosuspensions when applied by wetting. When applied by pressure penetration, the whitish surface deposits are minimal.

The possibility of removing the colour shade by the application of H₂O (distilled water) was not part of the in-situ performed test in order not to affect the penetration depth and the degree of consolidation by the nanosuspension.

The highest degree of strengthening was achieved by the pressure penetration application in the case of CaMg2 nanosuspensions (by ca 50%), then Ca4O-Si (by ca 35%) and CaMg1 (by ca 20%). When applied by wetting (by painting) there was a partial strengthening of the shallow surface layer, but the overall degree of consolidation is insufficient.

Based on the analysis of changes in total porosity and pore distribution, it can be stated that the grout did not fully penetrate into the deeper pore structure of the plaster, and remained only in the surface layers. In the applied grouting technologies (wetting and surface penetration), the grouts mostly fill in the pores with a radius greater than 700nm. When pressure penetration was used, there was a more significant reduction in the proportion of pores with a radius of 5000 - 100000 nm compared to the wetting technology. Due to the changes in total porosity and pore distribution, the pressure penetration technology is more effective. Among the grouting agents

used, the most effective is Ca4O injected by pressure penetration due to changes in total porosity and pore distribution.

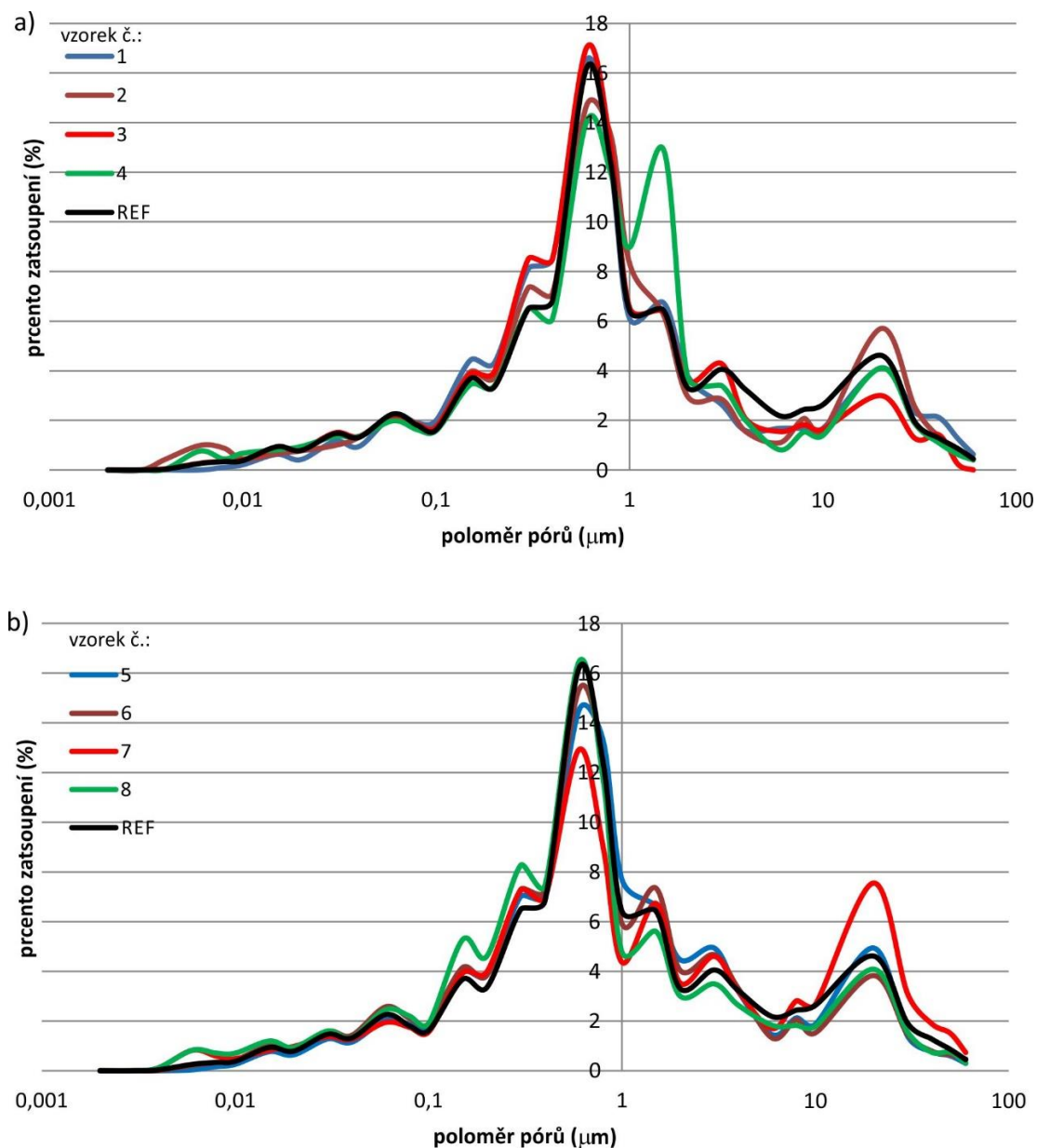


Fig. 7 - Distribution curves of plaster specimens grouted by wetting (a) and pressure penetration technology (b)

ACKNOWLEDGEMENTS

The article was written with support from the NAKI DG16P02M055 project "Development and Research into Materials, Procedures and Technologies for Restoration, Conservation and Strengthening of Historic Masonry Structures and Surfaces and Systems of Preventive Care of Historic and Heritage Buildings Threatened by Anthropogenic and Natural Risks".

REFERENCES

- [1] Solař: K otázce restaurování v památkové péči. *Obnova památek 2008 – Restaurování*. Sborník příspěvků k 8. ročníku konference. Studio Axis, ISBN 978-80-904081-0-4, pp. 12- 22
- [2] V. Girsá, D. Michoinová: *Historické omítky-záchrana, konzervace, obnova*. Metodika přístupu k historickým omítkám a k jejich záchran. České vysoké učení technické v Praze. ISBN 978-80-01-05229-7.
- [3] Tišlová, R., 2016, Metodika pro určení mezí a intervalů významných materiálových charakteristik opravných materiálů a technologií pro kompatibilní zásah, online: <http://www.nusl.cz/ntk/nusl-261491>
- [4] Bárta, J., 2004, *Obnova historických omítek – praktické zkušenosti*, Konference „Obnova památek – Omítky historických budov“, online: <https://www.studioaxis.cz/index.asp?menu=633&record=4015>
- [5] Heidingsfeld, V., 2004, *Technologické aspekty zpevňování omítek*. In: Křivoklát 2004: Zpevňování historických omítek. Odborný seminář STOP. Praha, pp. 8.
- [6] Baglioni, P. et al., 2012, Soft condensed matter for the conservation of cultural heritage, *C.R.Chimie*, Vol.12, pp.61-69
- [7] Chelazzi, D. et al., 2012, Hydroxide nanoparticles for cultural heritage: Consolidation and protection of wall paintings and carbonate materials. *Journal of Colloid Interface Science*, <http://dx.doi.org/10.1016/j.jcis.2012.09.069>
- [8] Rathouský, J., 2012, Nanovápno pro konsolidaci porézních materiálů – principy, mechanismy, In: Sborník semináře Nanomateriály v památkové péči, STOP, pp. 28 – 31
- [9] Škrdlantová, M. et al., 2012, Laboratorní použití micelárních roztoků a mikroemulzí při čištění historických materiálů. In: Sborník semináře Nanomateriály v památkové péči, STOP, pp. 18 – 22
- [10] Kotlík, P., 2012, Možnosti využití nanomateriálů v památkové praxi, Sborník semináře Nanomateriály v památkové péči, STOP, pp. 4 – 9
- [11] Baglioni, P. et al., 2015, Nanomaterials in art conservation, *Nature Nanotechnology*, pp. 287 – 290, online: <https://www.researchgate.net/publication/274726417>
- [12] Baglioni, P., et al., 2005, Microemulsions and micellar solution for the cleaning of wall paintings, *Studies in Conservation*, pp. 128-136, <http://dx.doi.org/10.1179/sic.2005.50.2.128>
- [13] Giorgi, R., et. al., 2008, Nanoparticles for Cultural Heritage Conservation: Calcium and Barium Hydroxide Nanoparticles for Wall Painting Consolidation, *Chemistry and European Journal* 16, pp. 9374-9382, <http://dx.doi.org/10.1016/j.culher.2008.06.012>
- [14] Grassi, S., et. al., 2007, The conservation of the Vecchieta's wall paintings in the Old Sacristy of Santa Maria della Scala in Siena: The use of nanotechnological cleaning agents, *Journal of Cultural Heritage*, vol. 8, no. 2, pp. 119-125
- [15] Machačko, L. et al., 2012, Testování „nanosuspenzí“ na bázi hydroxidu vápenatého v rámci projektu Stonecore, In: Sborník semináře Nanomateriály v památkové péči, STOP, pp. 32 – 36
- [16] Vavřík, D., Jandajsek, I., Slížková, Z., 2013, Observation of lime nanoparticles distribution during evaporation of transportation media. *Tomography of materials and structures*. Ghent : University press,, pp. 285-287 ISBN 978-9-4619713-0-2. International Conference on Tomography of Materials and Structures /1./. Ghent (BE).
- [17] Slížková, Z., et al., 2016, Metodika pro určení rozhodných materiálových charakteristik historických materiálů pro plánování restaurátorského zásahu. Metodika vypracovaná v rámci projektu MK ČR NAKI DF12P01OVV018.
- [18] Klisińska, A., Tislova, R., Adamski, G., Kozłowski, R., 2010, Pore structure of historic and repair Roman cement mortars to establish their compatibility, *Journal of Cultural Heritage* 11, pp. 404-410.
- [19] Witzany, J., et al., 2018, The Effect of Pore Distribution in Historic Masonry on the Grouting Method and Grouting Mix Selection, *The Civil Engineering Journal*, 3(10), pp. 307-329. ISSN 1805-2576.
- [20] Tabasso, L. M., Simon, S., 2006, Testing methods and criteria for the selection/evaluation of products for the conservation of porous building materials. *Reviews in Conservation* (7).

- [21] Drdáký, M., et al., 2012, Standardization of peeling tests for assessing the cohesion and consolidation characteristics of historic stone surfaces. *Materials and Structures*, 45, Vol. 4, pp. 505-520. ISSN 1359-5997.
- [22] Drdáký, M., Slížková, Z., 2013, Enhanced affordable methods for assessing material characteristics and consolidation effects on stone and mortar. *J. Geophys. Eng.* 10, pp. 6, doi:10.1088/1742-2132/10/6/064005.

CIRCULAR FOUNDATION PARAMETERS OPTIMIZATION BY METHOD OF BOUNDARY ELEMENTS

Alla Morgun, Ivan Met and Roksolana Malachkovska

Vinnitsia National Technical University, Faculty Building, Power Engineering and Gas Supply, Department of Construction, Municipal Engineering and Architecture, Vinnitsia, Khmelnytske shose95, Ukraine; alla@morgun.com.ua, vanmet@ukr.net, roksimalachkovska@gmail.com

ABSTRACT

The types of structures, for construction of which it is expedient to use circular foundations, are considered. The advantages of the circular foundations as compared with other types of foundations are determined. Applying the method of boundary element (MBE), the search of optimal ratio of the internal and external diameters of circular foundation is performed to obtain maximum carrying capacity of tower drier circular foundation. The comparison of the numerical studies with the experimental data is carried out, carrying capacity of tower drier circular foundation in case of rational relations of its internal and external diameters is determined. The technique of non-linear behaviour of the circular foundation under loading as the most economically efficient type of foundation construction for ring in plan buildings is developed.

KEYWORDS

Circular foundation, Stressed-strained state, Carrying capacity, Method of boundary elements (MBE)

INTRODUCTION

Foundations are structural elements which transmit load from the construction to the ground. For the reliable transmission of these loads the foundations must be designed in such a way that avoid their excessive subsidence and provide sufficient sliding and sloping stability [2].

Besides the most investigated foundations (strip foundations, rectangular foundations, ring foundations) circular foundations are more suitable and economically efficient to provide the support of axially-symmetrical constructions such as tower silo, water-cooling towers, chimneys, transmission towers, television aerials, radar installations, smoke stacks, piers, underground parkings, water towers, shaft storage facilities and storage tanks [4].

For such constructions circular foundations are better due to the complete usage of the carrying capacity of soil basis. They are often used for the building of large and high constructions to resist lateral loadings and increase the resistance to overturning. Besides, circular foundations enable to decrease the amount of the material, used for the construction and the cost of the construction that is also very important for the investor.

Ukraine also refers to the countries where circular foundations are used in construction sphere. Characteristic trend for modern agricultural brand of our country is the necessity to construct grain complexes – dryeration bins, where the circular foundations are used, as they have higher specific carrying capacity than the spread foundations [8].

With the growing usage of such foundations in numerous important projects, the interest to their behaviours grew. Such behaviours comprise the response to loading and maximum carrying capacity. Distribution of stresses in the basis of foundations of circular shape has qualitative and quantitative differences from the analogue foundations with the continuance bottom (ring, rectangular, strip foundations). Stressed-strained state of structures foundations depends on the form of the foundations in the plan [4].

It was found that there is no sufficient literature where the results and methods of the design for the calculation of circular foundations carrying capacity are presented. The existing methods of circular foundations calculation do not have the reliable normative base, that substantially restricts the possibilities of their rational design and usage and restrain their wide implementation, although for certain structures (smoke stacks, water cooling towers, silvers, television towers, etc.) the application of circular foundations is most expedient.

Thus, the development of reliable, scientifically substantiated methods of their stressed-strained state determination is an urgent problem for foundation construction.

PROBLEM DEFINITION

The necessity of the solution of problems, connected with the assessment of the strength and soil deformability is dictated by the requirements of engineering practice. Deformative properties of the foundation, upper structure of the tower type and soil base have different order. The characteristic feature of such structures (elevator, smoke stacks, water towers, bridge piers) is extremely high rigidity of the above-foundation part, Figure 1. They do not bend and provide gradual settling as a single mass. Conditions of such structures operation greatly depend on the soil base. Nowadays foundations of greater part of circular structures are designed in the form of shallow depth foundations.

In the given research, more accurate preconditions for the description of circular foundations behaviour, taking into account matching deformation of the foundation and nonlinear deformations of the base complex engineering-geological conditions are suggested.

Calculations of circular foundation settling [Figure 1 b] are carried out, applying modern numerical method of boundary elements and latest achievements in the sphere of dispersive soils mechanics. Spring-plastic model, based on the plastic flow theory in the form of non-associative law was elaborated.

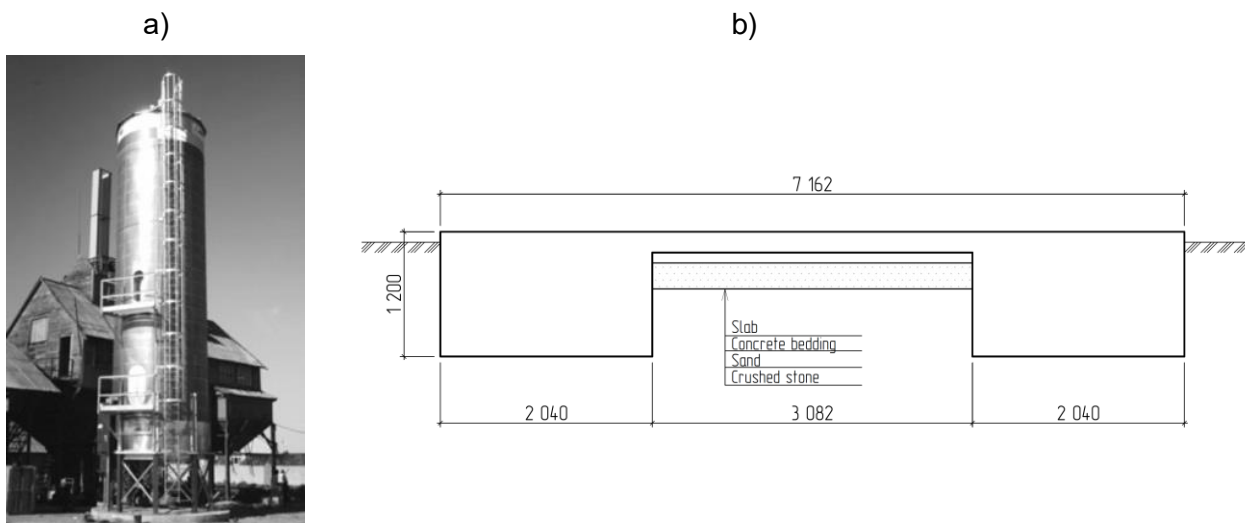


Fig. 1 – a) Tower drier; b) Geometrical characteristics of the circular foundation

Dilatancy relations of dispersive soil grounds of V.N. Nikolaevsky and I.P. Boiko, the procedure of step-by-step loading, applying the O.A. Ilushin method of spring solutions were used. As the criterion of soil transition into plastic state Mises-Shleier-Botkin criterion was used. As the values of safe loading and boundary carrying capacity are formed by soil strength characteristics are used in the developed model, determination of these characteristics is performed by experimental standard triaxial studies of soil specimen: $E=9800$ kPa; $\rho=1.96$ t/m³; $\rho^{\min}=1.64$ t/m³; $\rho^{\max}=2.21$ t/m³; $\vartheta=0.35$; $e=0.67$; $\varphi=26^\circ$; $c=17.2$ kPa; $p_0=-1900$ kPa.

According to the existing Building Regulations (1) carrying capacity of the circular foundation consists of the soil resistance under the footing, the first component in (1) and force of friction on the lateral surface, the second component in (1).

$$F = \gamma_c \cdot (R \cdot A \cdot \gamma_{cr} + U \sum f_i \cdot h_i \cdot \gamma_{cf}) \quad (1)$$

where R, f_i – is the calculated soil resistance under the footing and on the lateral surface, correspondingly; A – is the area of the foundation footing; $U \sum h_i$ – is the area of the lateral surface.

For determination of operating surfaces areas of the ring and circular foundations (Figure 2) the following dependences are used:

- for the ring foundation:

$$S = 2\pi R \cdot H + \pi R^2, \quad (2)$$

where $A = \pi R^2$, $U \sum h_i = 2\pi R \cdot H$.

for circular foundation carrying capacity was determined as the sum of lateral resistances on the internal and external lateral surfaces of the circular foundation and soil compression strength under the footing of the circular foundation:

$$S = 2 \cdot 2\pi R \cdot H + \pi R^2 - \pi r^2 \quad (3)$$

where the area of the foundation footing $A = \pi R^2 - \pi r^2$, area of the lateral surface $U \sum h_i = 2 \cdot 2\pi R \cdot H$.

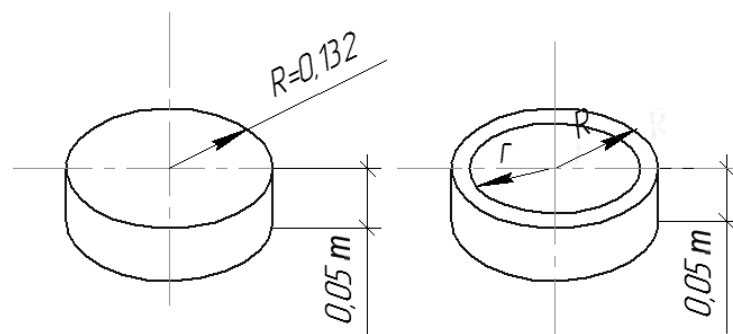


Fig. 2 – Schemes of the studied models of the circular foundation

THEORETICAL CALCULATIONS BY METHOD OF BOUNDARY ELEMENTS

Data for the calculation of working surfaces (lateral surfaces and footing) for the considered models of circular foundations are given in Table 1. For obtaining optimal ratio r/R method of gradient descent is used. Gradient of the ratio of total working surfaces of the circular foundations to the ring foundations increases to $r/R = 0,4$ and then decreases. Calculation data are given in Figure 3.

Tab. 1 – Data for calculation of the working surfaces of the circular foundations models

Ratio R/r	r (m)	R (m)	Area of lateral surfaces, (m ²)	Ratio to the ring foundation to lateral surfaces	Area of the point, (m ²)	Ratio to ring foundation to the point	Total working surface (m ²)	Ratio of total working surfaces of the circular foundations to ring foundations
0		0,132	0,04147	1	0,0547	1	0,09617	1
0,2	0,0264	0,132	0,0497	1,198	0,05255	0,96	0,1023	1,15
0,4	0,0528	0,132	0,05806	1,4	0,04598	0,84	0,10404	1,176
0,6	0,0792	0,132	0,06635	1,6	0,03503	0,64	0,10138	1,024
0,8	0,1056	0,132	0,0747	1,8	0,1972	0,36	0,09443	0,648

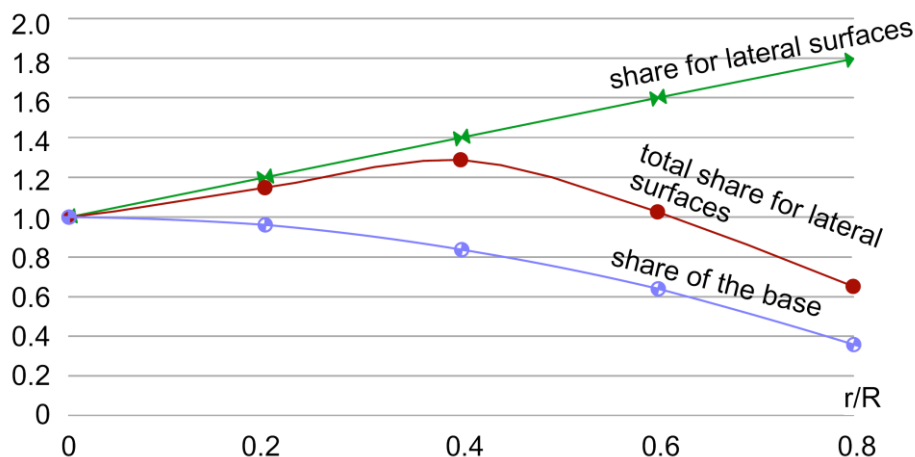


Fig. 3 – Dynamics of the indices of the circular foundation working surface change relatively the working surface of the ring foundation, depending on r/R

Elastic-plastic model, that was used, gave the basis the numerical analysis of the obtained data of the forecasting character of circular foundations deformation [5].

As the considered problem is non-linear, the step-wise iteration process is used, because step-wise procedure was and remains the integral part of finite element analysis. At each step linear problem was solved, applying O. A. Ilushin method of elastic solutions.

MBE reduces the calculation system of differential equations to the integral equation (Brebbia, 1987):

$$\left. \begin{aligned} \sigma_{ij,j} + b_j &= 0 \\ \varepsilon_{ij} &= \frac{1}{2}(u_{i,j} + u_{j,i}) \\ \sigma_{ij} &= C_{ijkl} \varepsilon_{kl} \end{aligned} \right\} \Rightarrow C_{ij}(\xi)u_j(\xi) + \int_{\Gamma} p_{ij}^*(\xi, x)u_j(x)d\Gamma(x) = \int_{\Gamma} u_{ij}^*(\xi, x)p_j(x)d\Gamma(x), \quad (4)$$

where $\sigma_{ij,j} + b_j = 0$ are the static equilibrium equations; $\varepsilon_{ij} = \frac{1}{2}(u_{i,j} + u_{j,i})$ – are the geometrical equations; $\sigma_{ij} = C_{ijkl} \varepsilon_{kl}$ – are the physical equations of the environment.

In the process of the consideration of the non-linear problem integral equation obtained by K. Brebbia [3] has the form:

$$c_{ij}u_j + \int_{\Gamma} \rho_{ij}^* u_{ij} d\Gamma = \int_{\Gamma} u_{ij}^* \rho_i d\Gamma + \int_{\Omega} \dot{\sigma}^* \varepsilon_{jk}^p d\Omega \quad (5)$$

where u – is the set vector of displacements on the contact boundary of the foundation construction; p – is the target vector of the stresses on the boundary; u^* , p^* , σ^* – are the kernels of the boundary equations (5) or MBE impact function, kernels are fundamental solutions of a boundary value problem corresponding to a source function given in the form of Dirac delta function [5]. In the boundary element method, this is R. Mindlin's solution for displacements and stresses due to the action of a unit force $P = 1$ in space and they are marked with an asterisk.

Kernels of the integral equation characterize the studied environment: c_{ij} – is constant, it is determined from the conditions of the body motion as a whole, it appears in the process of the transition of the boundary problem to the integral equation (4) for the obtaining the single solution; Γ , ξ , x , Ω – are correspondingly boundary surface of the foundation construction, point of the disturbance, point of the observation and boundary of the triangle sections of active zone of the soil [3].

In the process of numerical realization (5) only the contact surface of the foundation and soil was discretized, contact boundary was divided into a number of boundary linear elements, expected active zone of the base deformation was discretized by the triangled sections.

ANALYSIS OF RESULTS

The results of the studies show that the most optimal from the point of view of carrying capacity must be the circular foundation with $r/R=0.4$, as it has the maximum total working surface.

For the verification of the obtained data, the calculation of the models of the circular and ring foundations, the dimensions of which are given in Table 1, is carried out by MBE, using the developed elastic-plastic model of the soil base. Calculation data and the comparison with model experimental studies are shown in Figures 4, 5.

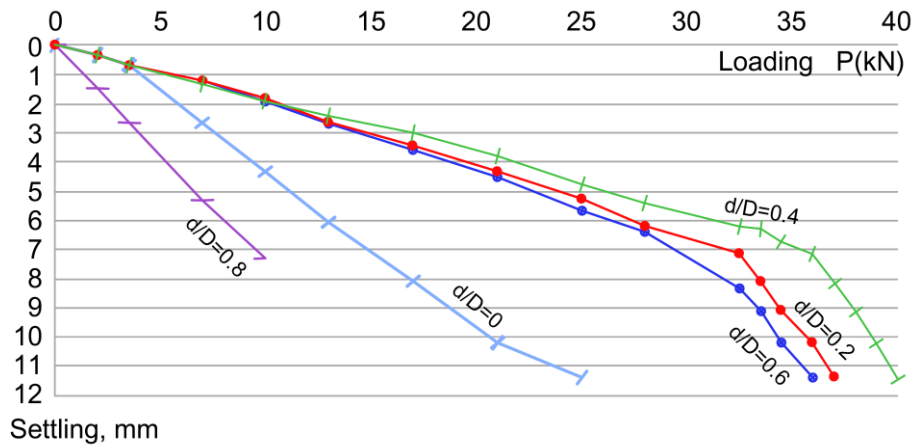


Fig. 4 – Data of the numerical forecast by MBE of carrying capacity of the ring and circular foundations with the same contact area

Analysis of the dependences in Figure 3 allows to make a conclusion that in case of the same contact surface minimal carrying capacity is inherent to the ring with $d/D = 0,8$, where, according to Table 1, total working surface is the smallest. Maximum value of carrying capacity has the test ring plate with $d/D = 0,4$ (43 kN), its total working surface (Table 1) is the largest. Proceeding from the obtained conclusions, the ratio $d/D = 0,43$ is suggested to be taken as the circular foundation of the tower drier (Figure 1b).

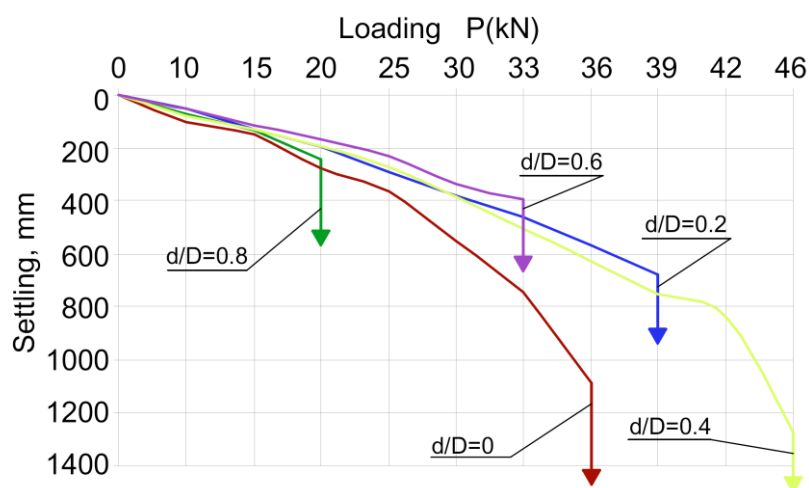


Fig.5 – Experimental studies of the test plates of the circular and ring forms with the same contact area and different d/D ratios

Modern calculations requirements comprise the requirements to provide the complete information regarding the functioning of the construction at all the stages of deformation, including

the stage of destruction. Figure 6 shows the graph “loading-settling”, obtained by MBE, as the physical process of stressed – strained state change of the circular foundation construction of the tower drier.

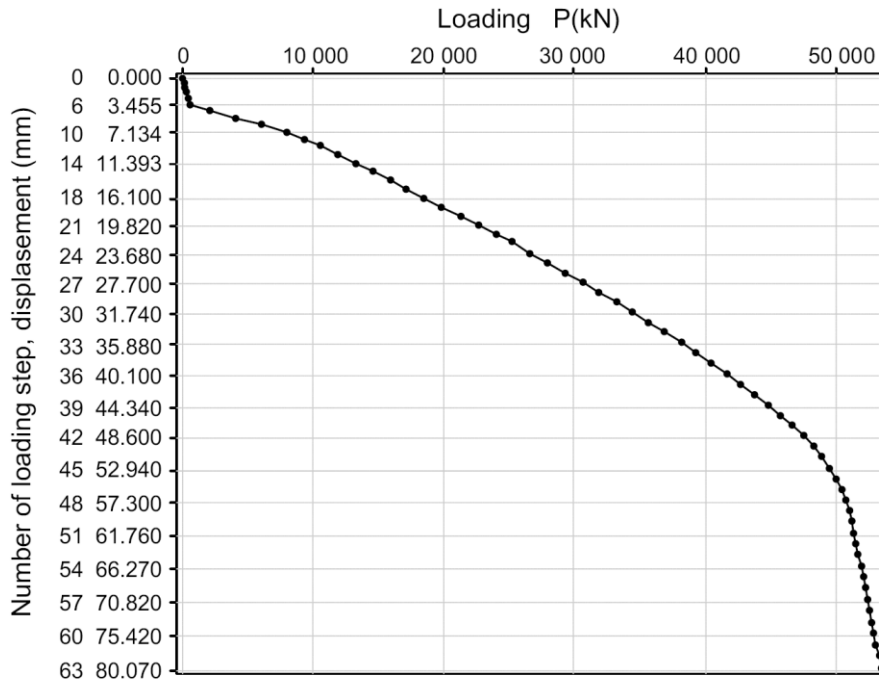


Fig. 6 – Graph “loading-settling” of the circular foundation of tower drier

When the tower drier of 5400 kN of the weight is loaded settling is 8 cm, it is less than admissible 10 cm. In the process of dryeration bin construction (Figure 1) and transmission on the foundation the loading of 5400 kN, the value of settling was 7,2 cm.

CONCLUSION

Displacement of foundation constructions in dispersive soil bases under the action of force impacts causes the change of its physical-mechanical properties, that influences their carrying capacity.

Non-linear model of soil base behaviour, developed by MBE, enables to describe the behaviour of the circular foundation with the sufficient for practical needs accuracy, providing economic effect.

The suggested dilatancy model and MBE enables at the stage of design to forecast geoengeering situation of circular foundation behaviour, state of foundation structure in the specific engineering-geological conditions that allows to improve the quality of design calculation, possibility to increase the terms of construction functioning by means of its stressed-strained state regulation.

REFERENCES

- [1] State building norms of Ukraine (2009). Bases and fundamentals of the buildings. Main principles of the design, Kyiv, Minregionbuild of Ukraine, 2009
- [2] G.Mase, Theory and problems of continuum mechanics, Moscow, Mir, 1974

- [3] Brebbia K., Teles J., Vroubel L. (1987) Methods of boundary elements. Moscow: Mir. Publishing House.
- [4] Cherkashin A. V., Druzhkin S. I, Strulev V. M. (2007). Experimental Research of the Ring and Circular Foundations Settling on Sand Basis. *TSTU: Proceedings of Scientific Papers of Young Scientists and Students*. 20, 224 – 228.
- [5] C. Brebbia, S Walker, “Application of the boundary element method in engineering”, Moscow, Mir, 1982
- [6] Nikolaevskiy V. N., (1975). *Determining Laws of Soils Mechanics*: Moscow: Stroiyizdat Publishing House.
- [7] Boiko I. P. (1985) Theoretical Fundamentals of Pile Foundations on Elastic-Plastic Base. Bases and foundations, №18: (11-18).
- [8] R. Timchenko, V. Sedin, D. Krishko, calculation of foundations-covers for constructions of tower type on the impact of uneven subsidence of base, *Bulletin of the Pridneprovsk State Academy of Civil Engineering and Architecture*, 2015, No. 10 (211): 29-35

GROUTED SLEEVE CONNECTION FOR PRECAST CONCRETE MEMBERS

Kulondwa Kahama Espoir , Xie Fuzhe and Geng Haojie

*Jiangsu University, School of Civil Engineering and Mechanics, Department of Civil Engineering,
301 Xuefu Rd, Jingkou District, Zhenjiang, Jiangsu, China Zhenjiang, China. ;
espoirkulondwa@gmail.com, xiefuzhe@ujs.edu.cn, g_hj007@163.com*

ABSTRACT

Precast concrete structures have gained preference in the modern construction industry because of the multiple advantages they offer. The connection of precast members is an important aspect to consider in the design of structures with precast components. Grouted Sleeve connection, one of the famous connector types, is made of the trio of reinforced bars, high strength grouting materials and a ductile iron cylinder. This article compares the finding of recent experimental research findings on grouted sleeve connection and establishes the relationship between the three components of the connector to enhance the performance of the splicing agent. It is found that the tensile performance of the connector increases with the embedded length of the bar for a normal sleeve. An effective embedded length set between 6 and 8 times the diameter of the bar will maximize the tensile performance of the connector. The increase in diameter of the sleeve cylinder, the compressive strength of the grout and the length of the bar embedded and its surface will affect the bond performance and the mode of failure under tensile load.

KEYWORDS

Precast concrete, Sleeve connector, Bond strength, Embedded length

INTRODUCTION

Precast Concrete (PC) is a currently promoted technology in concrete structures. It is believed that PC technology has been used in ancient Rome for tunneling. The current PC technology commonly used was first used by Alexander Brodie, a British engineer in 1905. In the USA the technology was used in the construction of a Bridge in Pennsylvania after the World War II [1, 2]. The most developed countries have embraced the technology with Japan and China also being among the beneficiaries of the invented technology. The concrete members are prefabricated far from or near the site and have relatively gained preference over cast-in-situ concrete most especially for high raised buildings, multi-storied car parking, highway bridge supports among others [3, 4].

There are many listed benefits of using PC over the cast on-site concrete. Some of the benefits include the reduction in construction's required time, avoidance of unnecessary delays caused by extreme weather conditions, decreased environmental pollution, enhances architectural ventures which could not be possible with the traditional technology, a limited number of laborers on site. In addition, the new technology decreases the risks of site-related accidents and labor cost and offers the ability to produce very good quality concrete with high strength in the controlled environment [5, 6].

Due to the ability to produce very high strength concrete in a controlled environment, structural engineers picked interest to maximize the use of precast elements for structures which are expected to support the heavy load. It is now a matter of knowing how to connect the different PC structural members safely together [6].

CONNECTIONS FOR PRECAST CONCRETE

Briefing on precast connection

A connection in reference to precast concrete structure means a construction between two or several precast concrete components. It can, therefore, comprise multiple joints [7].

Connections are critical structural elements in precast concrete construction. Beside influencing the type of frame to use and the erection process they are responsible for proper transmission of the loads between structural elements and ensure the robustness of the structure in the overall continuity. It is evident that the main difference between precast and traditional cast on-site concrete lies on the continuity of the structure at the nature of the connection between different members [8]. The traditional cast on-site concrete has the continuity of the structure at the connection as the result of the site set up of the reinforcement bars encored together in the foam work before casting and vibration of fresh concrete. For the PC structure gets its continuity from a good link between two or more structural members being erected on site.

Precast concrete members are linked to each other by a mean of connections. There is ongoing research on the various types of connections to confirm the reliability of the performance of these connections to ensure the integrity and safety of the structure. It is crucial to understand that a lot of reactions that are responsible for structural stability happen at a junction between two different structural members.

Design consideration and criteria of PC connections

The main role of a connection for both precast structures and cast in situ structures is to provide adequacy in structural loads transferring without undergoing any considerable deformation [9]. For precast structures, a connection ensures members are safely linked, provides the support during the erection of other members, and accounts for the integrity of the final structure's performance. In the whole process, the structural engineer ensures the connections serve for the continuity of the structure as a whole. Any bridging gap at the joint in the connection will compromise the structural integrity to an extent [4].

While ensuring the structural integrity at the connection, it is also important to acknowledge that the conception of the connection should always be simple in order to facilitate the erection process and enable final loads transmission [5]. The designer should consider the connection's design criterion, the ease of mounting members on-site, the strength, the durability, the fire resistance and the most importantly the material which is preferably ductile with high strength in most cases [1, 5]. There is a diversity of connections that link precast concrete elements together.

After manufacturing the different components of the precast concrete structures, engineers have a task to mount the different parts together while ensuring structural integrity. Currently, there are many ways of connecting the precast components together in order to form a performing structure. Advancement in research on connections discovered the feasibility of a hybrid structure which is the combination of steel structure and PC reinforced structure to provide safe links between members. In this document, we will focus on one of the common types of connection used in the precast structure.

Characterization of connections

The connections between the precast elements are either wet or dry. Wet connections rely on the splice of the reinforcement bars. They're usually achieved by a reinforcement lapping setting and an onsite concrete fill in the lapping dowel [10, 11]. Though wet joints involve extra cost and time they enhance good ductility of the connection and do not hamper important movement in the connection [12]. In 2019 Scholars in Japan rate the performance of the wet as better or similar to the monolithic cast-in-situ intersection [13]. The dry connections are set up by means of the steel materials and are in most cases used for fixed connections [10, 12]. Dry connections can be achieved in practical by bolting, anchoring or welding on site. In times of overstress, they have a brittle failure [11, 12] and hidden cracks can develop below the anchorage without being noticed [14]. Much as [15] reports a good performance of the joints, wet connections are more preferable than the dry connections. In other cases, the connections in precast structures are classified differently. Based on the elements they connect we have shear wall connections, slab connections, walls connections, beam to column connections, beam to beam connections, column to columns connections, column to foundation columns [8, 11]. Other scholars have classified the precast connections according to the major force actions which they convey. We, therefore, have shear connections, tensile connection and compression connection [7]. Much as there may be the presence of torsion action in the working of connection, its influence is relatively minimal and not an object of focus considered in concrete structures unless for special cases. It is important to therefore notice that connections are designed in consideration of the members that are to be connected.

Thus, a satisfactory connection between precast components can be achieved in several ways which in most cases include bolting and threading, mechanical connectors, anchors, bar couplers, special insert, shims, welding, grouting and etc. In the diversity of connections settings, the structural engineer should remain innovative in adapting the chosen connection set up to his site and have sufficient information about the working of that connection in particular [8].

GROUTED SLEEVE SPLICE (GSS)

Grouted splice is one of the preferred precast mechanisms to link two different members. Alfred A. Yee invented it in 1960, GSS is a hollow cylinder made with ductile materials of iron, where two reinforcement steel bars are connected together [16-19].

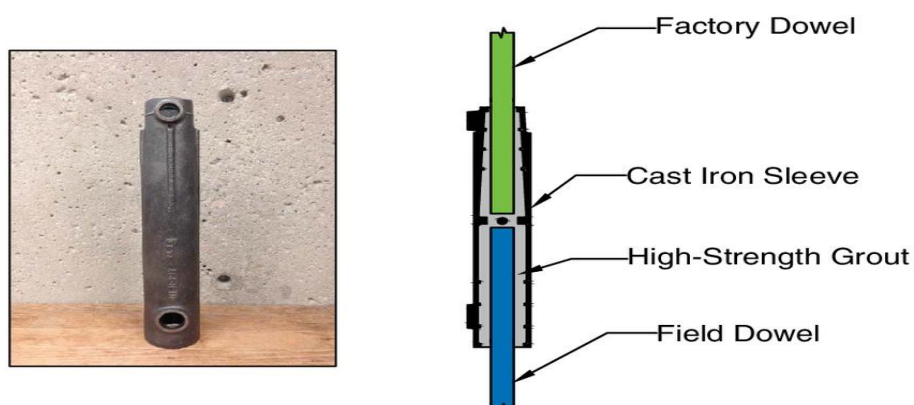


Fig.1- Elements of the GSS connector

In Figure 1, the image also used in [20] provides a pictorial understanding of the connection set up of grout sleeve itself on the left and the description and details of the components of a full grouted sleeve with the trio component of sleeve, bar and grout.

To achieve a proper bonding capacity of the rebars, high strength grouting materials are inserted in the sleeve. Grouted sleeve connection is used in precast concrete to connect a column to column, beam to column connection, column to foundation connection as well as shear walls connections.

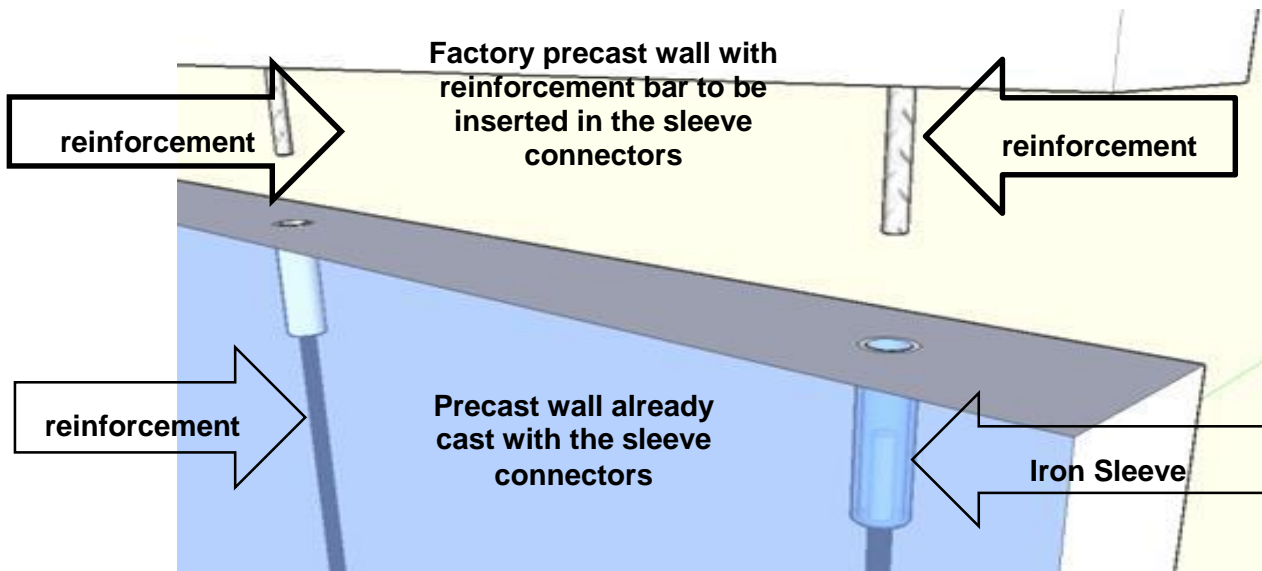


Fig.2 - Erection of Precast members using grouted sleeve connector

The edited image extracted from [21] captures two wall panels yet to be connected together by a grouted GSS, an illustration of the in-situ erection setting.

A grouted sleeve connection used for precast members splicing comprises of a cylindrical duct sometimes made of steel, the reinforcements bars and the grout. It is important to understand that the composite materials of each one of the trio components of the sleeve matters for a good performance of the connector [22]. The sleeve enhances the grout confinement around the steel reinforcements [6]. It serves as a connecting agent between the field's reinforcement and the factory member's reinforcements during the erection process, keeps reinforcements in proper alignment and holds the connection components together while allowing the inflow of grouting material in the sleeve through the two holes [23]. As illustrated in Figure 2, the two reinforcement that participates in the connection of the walls have their lapping inside the connector. The reinforcements and inserted grout enhance, therefore, the continuity of the structure at the connection inside the GSS connector [16]. The grout is a high strength concrete material that fills the void space between the bars and the inner surface of the sleeve connector. The grout confinement in the sleeve serves as a bond between the two reinforcement bars being connected [16, 24].

Factors influencing the performance of the sleeve

The performance of the GSS connector under loading highly depends on the strength of the grouting materials and their confinement inside the connector [25-27]. The appropriate grout material is preferably a high compressive strength material which has non shrink property [28]. Insufficient grouting and the presence of grouting defects in the steel sleeve will decrease the load load-bearing capacity at the connection and will lead to the premature failure of the set up [28, 29]. Defects in grouting materials will also damage the adhesion between the grout and sleeve inner walls and bar surface which is paramount in the connection proper performance. A 30 percent ratio of the defect in grout for a sleeve will lead to premature failure of the connector [19, 29]. There is a

strong agreement between the deliverables and findings of the existing experimental research by deferent authors on the impact of the grouting defects in relation to the confinement of the grout in the sleeve and the performance of the connector. But the gap between the research specimen set up with artificial defects and the suspected existing defects in the connection set up is relatively big. Up to now, the research on grouting defects within the connector does not reflect the real case. Detection of small defects in the sleeve by means of nondestructive tests was proved inefficient and not accurate in defects sizing within the sleeve[30, 31]. The research conducted by [29] used soil and foam as the defects while [28] without specifying the nature of defects in his experiment, he affirms to have defects in the vertical plane of the sleeve along the path of the upper embedded length. His defects are in different sizes. We can make an observation that both of the experimental work later experimental works do not reflect the ideal scenario faced on site. There is a need to pursue the in-depth study on grouting materials ,their propagation in the sleeve and the way they perform with the connector's other components [32].

The bond strength between the bar and the grout also depends on the bar structure, the grout's compressive strength, its chemical adhesion and the diameter of the steel sleeve, The bar's roughness and the bearing of the steel bar [33]. Most experimental work use 28 days normal aged grout of strength varying between 58 Kpa in [34] up to more than 80 Kpa in [28]. The highest compressive strength grout is the most preferred in the field and hence much more used for many experimental works and field works. The findings after the experiment conducted in [25] establish that the strength of the bond between the reinforcement bars and the steel sleeve increases proportionally with the compressive strength of the grout. Hence the compressive strength of the grout will increase the bond performance of the connector. The mechanism of load transfer by grouted sleeve connector depends on the bond between all the components involved which is provided by the grouting materials [18].

$$u = \frac{P}{\pi d_b l_e} \tag{1}$$

The Equation (1) also used in [25, 34, 35] can find the average bond stress when the connector is subjected to a load. P is the force in the bar, πd_b is the nominal perimeter of the bar and l_e is the embedded length of the bar.

The data from the experimental study [36], were used to plot the graph in Figure 3. A selection of data with different bars diameter respectively 16,18 and 20 were picked under different embedded length with other parameters constant to study the grout bond response.

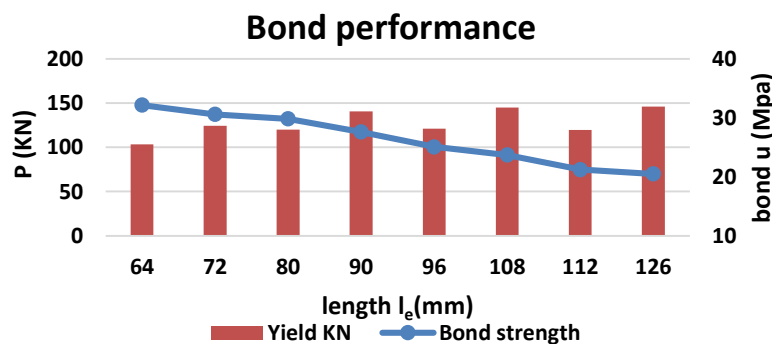


Fig. 2- Behaviour of bond strength under increasing embedded length

The bond strength u is indirectly proportional with the embedded length l_e . It can be observed from the graph that the difference in the bar diameter has no impact on the sloping line of the bond strength under the increasing embedded length of the reinforcements. The tensile capacity of the connector is not linked to the bond strength only but varies according to both the

bond and the embedded length. It is a result of a good set up of all the features in the sleeve [25]. Regardless of the bar diameter in the sleeve and increase in l_e will weaken the bond. The deduction from the above graph is that the bond strength of the grout within the connector will decrease with the embedded length of the bar. The bonding mechanism within the connector is enhanced by the confinement of grout within the connector therefore, an increase in embedded length will decrease the confinement of grout within the connector and hence compromising the bonding strength [16].

There is an existing link also between the surface' nature of reinforcement bar and the connection performance. The need to find the anchorage of the bars have lead researchers to investigate the type of bond existing between the grout and the reinforcements [34, 37]. It was found that bars with a smooth surface have a weak bond with the grout. In an experiment conducted by [35], a specimen with the reinforcement with rough circumference had a good grout bond capacity and failed by bar fracture while the smooth bar failed by bar pull out of the sleeve. The interdependence of bond adhesion of the grout and the bar in relation with the bar's roughness is mentioned as well in [33]. This behavior is justified by the additional frictional resistance that the ribs on the rough surface of the bar make with the grout. Other researchers managed to get an expression that links the embedded length of the bar to the performance of the sleeve under loading conditions [18].

The alignment of the two bars being connected within the sleeve is crucial for a good performance of the connector. Misalignment of the reinforcement in the sleeve bar will compromise the distribution of the tensile stress within the connector [6, 21, 25]. The impact of the alignment on the performance of the connector is emphasized in [3, 6]. The same issue may aggravate deformations in the connector and weakens the surrounding grouts in times of load application. The same can precipitate the failure of the connection [37].

The diameter of the bar increases linearly with the tensile capacity of the connector [24, 32]. It is logic to establish a linear relationship between the tensile performance of the GSS connector and the diameter of the reinforced bar if the set-up of components of the connector are all carefully integrated since the same relationship exists between the diameter and the tensile performance of the reinforcement bar.

To determine the total embedded length of the bar the following expression can be used:

$$l_e = \frac{P}{\pi d_b u} \quad (2)$$

l_e is the embedded length, P is the applied force, d_b is the bar diameter, and u is the bond strength between the bar and surrounding grout [3, 26].

In his experimental work [24] established the relationship between the length and the tensile behavior of the grouted sleeve connector.

From their experimental findings in [26, 34] it can be established that the expression $l_e = 16d_b$ where l_e is the length of the sleeve and d_b the diameter of the bar can be used without any weakening of the sleeve performance. Further investigations on the right length being eight and twelve times the diameter of the bar were also proven safe to use [34]. The safe embedded depth of the bar should be selected in consideration of the type of the sleeve being used. Headed couplers require a shorter embedded length than the normal sleeve.[34]. [35],[25] and [21]on the other side after their experiment realized that the expressions $l_e = 6d_b$ and $l_e = 7d_b$ will give the sleeve the tensile strength performance exceeding the requirement in ACI 318. The same expression was approved by scholars in China and the United Kingdom in 2019 after their experimental work on grouted sleeve splice with wedges [6]. There is a complete disagreement of research on the proper embedded length to use inside the steel connector. It is valuable to understand that, though the length of the bar has a linear relationship with the tensile performance

of the connector, the embedded length is not the only parameter on which the tensile depends on. In [34] it is also agreed that the nature of the grout-bar bond, sleeve-grout bond and the compressive strength of the grout will have an influence on the tensile performance of the connector. Different setting of the connector will require different embedded length of the bar but the normal sleeve largely used will perform well at the embedded length between 6 and 8 times the bar diameter.

The data from [38] after the experiment were used to produce the following chart below showing the relationship between the embedded length of a 16mm diameter, the bond strength and tensile strength capacity.

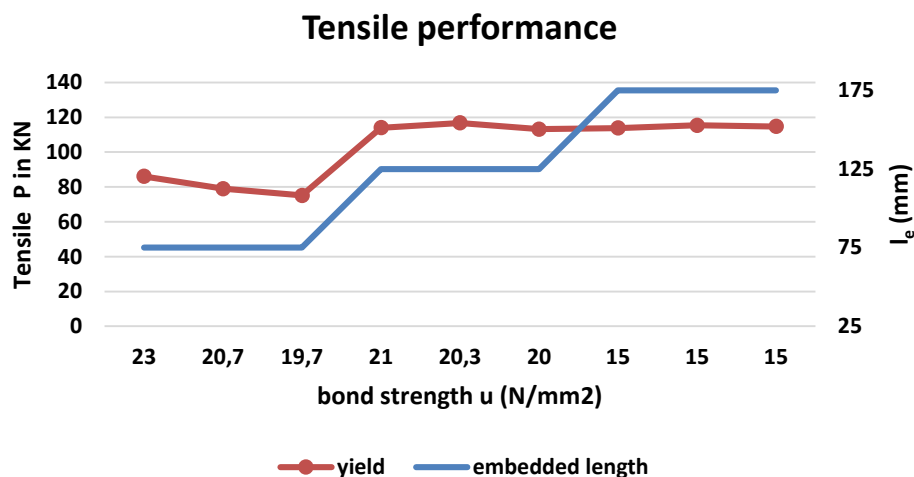


Fig. 3- Tensile performance for different embedded lengths

In Figure 4, decreasing bond strength at the same embedded length of the bar will decrease the tensile capacity. The increase of the anchorage length to the effective one will slightly decrease the bond capacity but significantly increase to the maximum the tensile capacity of the connector. Any additional length beyond the required embedded length of the bar will only decrease the bond capacity u without any effect on the tensile load-bearing capacity P .

The steel or iron sleeve should be able to ensure very good quality of bond strength [18, 32]. The structural and economical influence of the type of connector cannot be negligible. Different connectors influence both the embedded length and the grout bond strength depending on whether the sleeve is threaded or not, headed, wedged and etc. [21, 34]. The performance of the bonding grout with the sleeve depends on the nature of the inner surface of the steel or iron sleeve. Ribbed surfaces provide better bonding than smooth surfaces just like for the surface properties of the bar [24, 35]. Better bond performance of ribbed or threaded sleeve inner surface was reported by [26] in his conclusion. Sleeves with a threaded inner surface can increase the tensile performance of the connector. It was found in [38] that the tensile capacity of the threaded sleeves outperforms the performance of the normal sleeve with a smooth inner surface by about 36KN. The threads and ribs will enhance proper adhesion and improve the sleeve-bond strength hence creating a frictional resistance during the tensile test.

The ratio of the sleeve diameter to the bar diameter d_s / d_b counts also for the grout confinement effect of the sleeve and should lie between 2.66 and 3.55 [34]. The ideal ratios for specific bars were tabulated in the same document after experiment [34]. It is more preferable to have a tolerance of about 2.5 cm around the bars within the sleeve [3, 34]. An experimental study found that selecting a lower size of the sleeve diameter will improve the confinement in the sleeve enhance a better performance of the connector [37, 38].

Selecting the data from [6] in his experiment conducted in 2019, the chart below was plotted to mark the relationship between the bond strength, the sleeve diameter and the tensile performance of the sleeve.

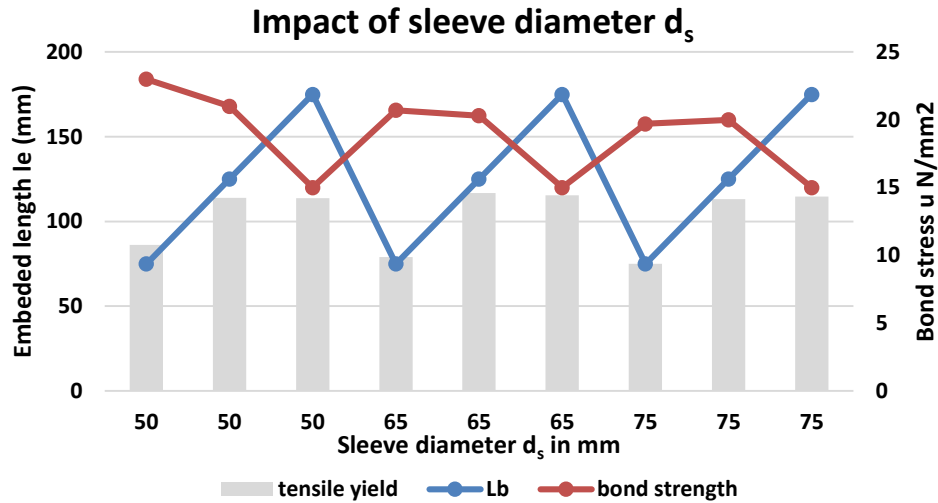


Fig.4- The impact of the diameter of the sleeve cylinder

At the same sleeve diameter and increase in l_e will decrease the bond. Likewise, at the same embedded length, and increase in the sleeve diameter will decrease the bond strength. The tensile capacity increases with the length up to the safe embedded length. Any additional length is unnecessary. A larger sleeve diameter will weaken the bond and cause a slight regress in the tensile capacity.

The data in the experimental work tabulated in [38] were selected to illustrate the relationship between the diameter of the sleeve and the bond at a different embedded length of the bar. ($d_b=18\text{mm}$)

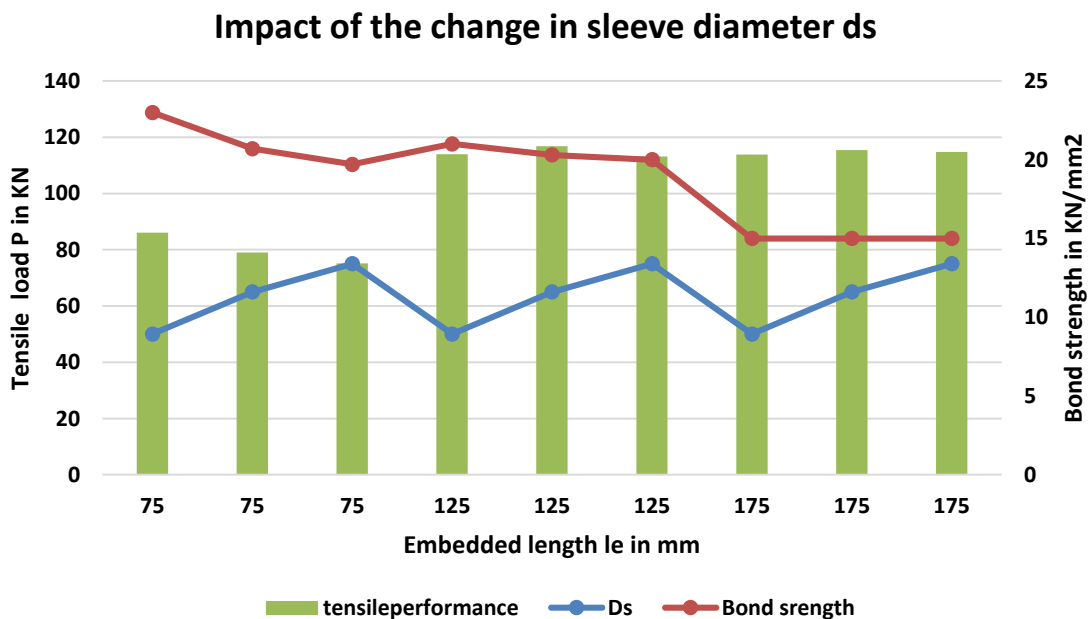


Fig. 5 - Impact of sleeve diameter

From the above chart, an increase in the sleeve diameter will result in a decrease of the bond strength under the same embedded length of the bar or even a shorter embedded length. The tensile performance increases significantly with the embedded length up to the required embedded length for this case 125mm which is about $6.9d_b$. Despite the decrease in sleeve diameter, an increase in embedded length still reduces the bond strength. An increase in sleeve diameter and in embedded length will both decrease the bond strength until the minimum bond strength where no further weakening of the bond is observed. The tensile capacity is maximum at the embedded length 125mm. No further improvement in performance both on the bond and tensile is not possible.

Mechanical interlocks play a key role in case of bond failure the performance of the connector relies on frictional resistance and mechanical interlocks [39].

Performance of the grouted sleeve connection

It is reported that the PC had poor performance in seismic regions and was therefore previously used consciously in seismic regions with a lot of precautions and relatively high risks [11]. The grouted sleeve connection was found through much experimental work to withstand several earthquakes without undergoing any major deformation [35]. The wet connections are more preferred more than the wet in seismic zones because of their ability to allow movements within the connection setting [10]. No wonder, the PC structures now exist in seismic zones of Japan, China, Canada and etc. The nature of the connection allows to the connection very high ductility there hence there is displacement inside the connection due to apply load before the ultimate load that causes the connection to fail. The load displacement curve of the grouted sleeve connector is homogeneous and the connection does not register a brutal failure before yield [24]. This accounts for the good ductility of the connector previously mentioned. An experiment conducted by [17] on columns with grouted sleeve splice confirmed that grouted sleeve connection is safe to withstand earthquakes. The homogeneity and the non-brutal failure of the sleeve in the load displacement curve of a grouted sleeve connection is an indicator of good confinement and proper bonding between the two reinforcement being connected [24]. The good tensile performance of the grouted sleeve connection is proven by the bar fracture outside the sleeve during the tensile test experiments [16, 38].

In his experimental research, [39] found out that grouted sleeve connections allow axial movement and have very good energy dissipation without undergoing considerable deformation. The same author highlights poor response to critical rises in temperatures. The poor thermal conductivity within the connected components is also confirmed in [40].

The poor performance of the connection when subjected to high temperature is the disadvantage of the connection [41]. Though proper link can be achieved by the GSS, in case of a fire outbreak, the connection will be weakened. At temperatures above 500°F , the steel materials in the structure will start losing their strength properties [42]. Concrete cover on top of the sleeve connector made also out of steel should be enough in order to provide adequate protection of the connection. Isolation of the connection and its protections should be a priority while setting up the connection. Investigations should also be carried out and confirm the fire endurance of the connection the point at which the weakening of the GSS connector will compromise the load-bearing capacity of the connector. The later compromise may cause the collapse of the structure.

Improvements of the sleeve

Some engineers use a spirally confined lap which is a new technology proposed and being assessed to improve the confinement in the connector for the precast members intended to carry heavy structural loads [18]. This improvement meanwhile is achieved outside the connector but is meant to enhance the compressive performance of the connection.

Further ongoing improvements of grouted sleeve connection range from half grouted sleeve with mechanical interlocks where one part of the sleeve is grouted and another end is fixed. In Beijing, there has been the creation of a grouted sleeve with threaded and multiple shear keys [6, 43]. Threaded sleeves have been observed to have a considerable improvement in tensile performance. The new technology of incorporating a shear key in the connector is reported to improve the grout-pipe bond failure by preventing it with a minimum of three shear keys [21]. A modification of the sleeve with wedges and other tapered head have been used to conduct an experiment that found an improvement in the performance of the modified sleeve.

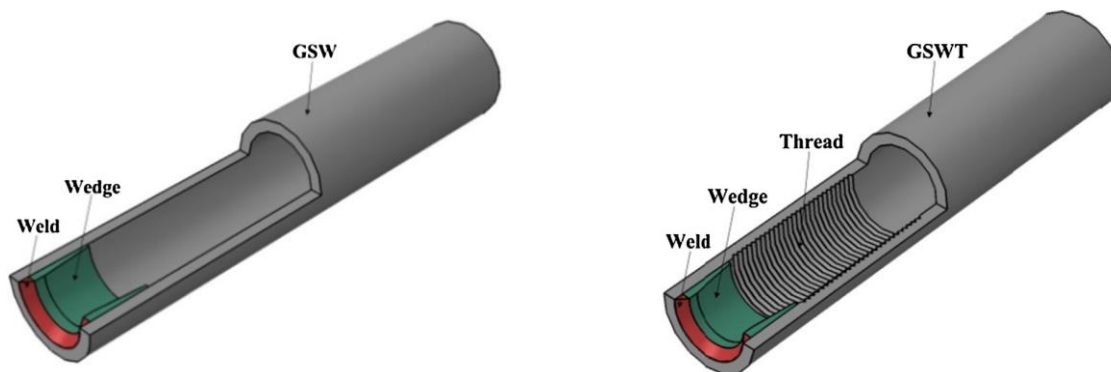


Fig.6- Sleeve cylinder with wedge and with wedge and threads

All improvement and customized sleeve should, therefore, be subjected to experimental tests of their ability to convey structural loads before they can be used. Other researches on the improvement and customized sleeve connector remain confidential and private.

CONCLUSIONS

Many experiments conducted on grouted sleeve splice approved the working and the performance of the connector under loading conditions. A good combination and a proper set up of the trio components in the right geometry and specified properties will enhance a safe connection. The GSS has three major modes of failures that are reported in the experimental works reviewed: bar bond failure also referred to as bar pullout, bar fracture outside the sleeve, and grout- sleeve bond failure [16, 32, 44].

The bar pullout case has been common in the specimen with weakened bond strength as a result of poor adhesion between grout and rebars. Much as there is gap in studying the distribution of the grouting materials inside the sleeve, it can be realized that the additional length of the bar anchored in the sleeve beyond the effect which is placed between 6 and 7 times the diameter of the bar will weaken the bond without additional tensile capacity [6, 18, 26]. Excessive length beyond the required will be the cause of bar pulling out of the sleeve.

Bar fracture is the best mode of failure for a sleeve connector. This failure means that the connector setting outperforms the tensile capacity of the bar. The connector's tensile performance is 1.25 times the tensile performance of the bar inserted. This means the connection achieves the tensile requirement of the connector. The impact of the tensile yield capacity of the reinforced bar is not assessed by many scholars yet believed to have a considerable impact by [45, 46].

A safe length of the embedded portion of the bar with rough surface inside a steel sleeve with a small sleeve diameter d_s and the ribbed inner surface will make a better set up for a good performance of the splicing agent.

Grout to sleeve bond failure is the least common type of failure. It is the type of failure resulting from a poor bonding between the sleeve and the grout. Usually common with sleeve without proper interlocking mechanisms and smooth surfaces [21, 26]. A small diameter sleeve will enhance good bonding than a wider diameter of the sleeve [45].

Research derivable reported the good performance of the connection in earthquakes and good capacity of energy absorption. Under fire outbreaks, the connection is weak due to poor thermal conductivity.

FURTHER RESEARCH

We recommend that the distribution of grouting materials in the sleeve and their impacts on the connector's performance should be clearly understood. The impact of their various confinement in the sleeve should resort in order to improve the safety of the connection.

We advise conducting a study that should focus on increasing the bond together with the length of the bar then assess the tensile capacity of the connector. Otherwise, provide clear concepts and equations that explain the existing trend of inverse proportionality between the bond and the embedded length of the bar.

Scholars should link the tensile yield of the reinforcing bar to the overall performance of the sleeve connector with an emphasis on the tensile contribution of the bar [46].

Many studies were done on GSS connection focus on bond strength, which is key, but a study on the contribution sleeve material on the tensile performance would be more insightful.

ACKNOWLEDGEMENT

The authors appreciate the supports from the National Natural Science Foundation of China under Grant No. 51608234 and the Jiangsu Province Science Foundation Grant No. BK20160534.

REFERENCES

- [1] Martin, L.D. and C.J. Perry, *PCI design handbook: precast and Prestressed concrete*. Vol. 1. 2004: Prestressed Concrete Inst.
- [2] Taylor, G.R., I.D. Neu, and I.D. Neu, *The American railroad network, 1861-1890*. 1956: University of Illinois Press.
- [3] Henin, E. and G. Morcou, *REINFORCING BAR SPLICE SLEEVE FOR PRECAST CONCRETE CONSTRUCTION*.
- [4] Yuan, Z., C. Sun, and Y. Wang, *Design for Manufacture and Assembly-oriented parametric design of prefabricated buildings*. Automation in Construction, 2018. **88**: p. 13-22.
- [5] Mohammed, H.A., *Precast Concrete Precast Building System Solutions*.
- [6] Lu, Z., et al., *Mechanical behaviour of grouted sleeve splice under uniaxial tensile loading*. Engineering Structures, 2019. **186**: p. 421-435.
- [7] Elliott, K.S., *Precast concrete structures*. 2016: Crc Press.
- [8] Engström, B., *Structural connections for precast concrete buildings*. FIB: Commission C, 2008. **6**.
- [9] Darwin, D., C.W. Dolan, and A.H. Nilson, *Design of concrete structures*. 2016: McGraw-Hill Education.
- [10] Breccolotti, M., et al., *Wet-joint techniques for the construction of precast concrete pipe rack structures in remote seismic zones*. PCI Journal, 2017.
- [11] Prasad, C. and P. Patchigolla, *Structural Connections for Precast Concrete Buildings-Review of Seismic and Other Design Provisions in Various International Codes-An Overview*. The Masterbuilder, 2015: p. 46-52.
- [12] Nimse, R.B., D.D. Joshi, and P.V. Patel, *Behavior of wet precast beam column connections under progressive collapse scenario: an experimental study*. International Journal of Advanced Structural Engineering (IJASE), 2014. **6**(4): p. 149-159.
- [13] Cai, G., et al., *A Demountable Connection for Low-Rise Precast Concrete Structures with DfD for Construction Sustainability-A Preliminary Test under Cyclic Loads*. Sustainability, 2019. **11**(13): p. 3696.
- [14] TAHER, S.E.-D., A. ATTA, and A.E.-D. SHARKAWI, *WET VS. DRY TECHNIQUES IN CONNECTING PIECEWISE PRECAST REINFORCED CONCRETE BEAM-COLUMN ELEMENTS IN MOMENT RESISTING FRAMES*.

- [15] Metelli, G. and P. Riva. *Behaviour of a beam to column “dry” joint for precast concrete elements*. in *The 14th World Conference on Earthquake Engineering October*. 2008.
- [16] Alias, A., et al., *Structural performance of grouted sleeve connectors with and without transverse reinforcement for precast concrete structure*. *Procedia Engineering*, 2013. **53**: p. 116-123.
- [17] Lu, Z., et al., *Studies on seismic performance of precast concrete columns with grouted splice sleeve*. *Applied Sciences*, 2017. **7**(6): p. 571.
- [18] Hosseini, S.J.A., *Bond Behaviour of Grouted Spiral and Splice Connection Under Direct Axial and Flexural Pullout Load*. 2015, Universiti Teknologi Malaysia.
- [19] Qiong, Y. and X. Zhiyuan, *Experimental study of grouted sleeve lapping connector under tensile load*. *Građevinar*, 2017. **69**(06.): p. 453-465.
- [20] Pantelides, C.P., M. Ameli, and L.D. Reaveley, *Evaluation of Grouted Splice Sleeve Connections for Precast Reinforced Concrete Bridge Piers*. 2017.
- [21] RAHMAN, A.B.A. and O.H. YEE, *Grout Filled Steel Pipe Integrated With Shear Key for Precast Concrete Connection*.
- [22] Levitt, M., *Precast concrete: materials, manufacture, properties and usage*. 1982: CRC Press.
- [23] Hua, L.J., et al., *PERFORMANCE OF CS-SLEEVE UNDER DIRECT TENSILE LOAD: PART I: FAILURE MODES*. *Malaysian Journal of Civil Engineering*, 2008. **20**(1).
- [24] Lin, F. and X. Wu, *Effect of sleeve length on deformation properties of grouted splices*. *Građevinar*, 2017. **69**(07.): p. 537-546.
- [25] Einea, A., T. Yamane, and M.K. Tadros, *Grout-filled pipe splices for precast concrete construction*. *PCI journal*, 1995. **40**(1): p. 82-93.
- [26] Henin, E. and G. Morcous, *Non-proprietary bar splice sleeve for precast concrete construction*. *Engineering Structures*, 2015. **83**: p. 154-162.
- [27] Kim, H.-K., *Bond strength of mortar-filled steel pipe splices reflecting confining effect*. *Journal of Asian Architecture and Building Engineering*, 2012. **11**(1): p. 125-132.
- [28] Zheng, G., et al., *Mechanical performance for defective and repaired grouted sleeve connections under uniaxial and cyclic loadings*. *Construction and Building Materials*, 2020. **233**: p. 117233.
- [29] Xu, F., et al., *Experimental bond behavior of deformed rebars in half-grouted sleeve connections with insufficient grouting defect*. *Construction and Building Materials*, 2018. **185**: p. 264-274.
- [30] Li, Z., et al., *Ultrasonic Detection Method for Grouted Defects in Grouted Splice Sleeve Connector Based on Wavelet Pack Energy*. *Sensors*, 2019. **19**(7): p. 1642.
- [31] Yan, H., B. Song, and M. Wang, *Ultrasonic Testing Signal of Grouting Defect in Prefabricated Building Sleeve*. *Ekoloji*, 2019. **28**(107): p. 945-953.
- [32] Wang, J., et al. *Experimental study on Bond slip relationship of Steel sleeve*. in *MATEC Web of Conferences*. 2016. EDP Sciences.
- [33] Sayadi, A.A., et al., *The relationship between interlocking mechanism and bond strength in elastic and inelastic segment of splice sleeve*. *Construction and Building Materials*, 2014. **55**: p. 227-237.
- [34] Brenes, F.J., S.L. Wood, and M.E. Kreger, *Anchorage requirements for grouted vertical-duct connectors in precast bent cap systems*. 2006.
- [35] Zheng, Y., Z. Guo, and X. Ming. *Pullout Bond Properties of Grout-Filled Mechanical Splice for Precast Concrete Construction*. in *5th International Conference on Civil Engineering and Transportation*. 2015. Atlantis Press.
- [36] Zheng, Y., et al., *Parametric study on a novel grouted rolling pipe splice for precast concrete construction*. *Construction and Building Materials*, 2018. **166**: p. 452-463.
- [37] Ling, J.H., A.B.A. Rahman, and I.S. Ibrahim, *Feasibility study of grouted splice connector under tensile load*. *Construction and Building Materials*, 2014. **50**: p. 530-539.
- [38] Ling, J.H., et al., *Behaviour of grouted pipe splice under incremental tensile load*. *Construction and Building Materials*, 2012. **33**: p. 90-98.
- [39] Zhao, X.-L., P. Grundy, and Y.-T. Lee. *Grout sleeve connections under large deformation cyclic loading*. in *The Twelfth International Offshore and Polar Engineering Conference*. 2002. International Society of Offshore and Polar Engineers.
- [40] Zhao, X.L., et al., *Behaviour of grouted sleeve connections at elevated temperatures*. *Thin-walled structures*, 2006. **44**(7): p. 751-758.
- [41] Gustaferro, A.H. and L.D. Martin, *Design for fire resistance of precast prestressed concrete*. 1989: Prestressed Concrete Institute.

- [42] Rini, D. and S. Lamont. *Performance based structural fire engineering for modern building design*. in *Structures Congress 2008: Crossing Borders*. 2008.
- [43] Wu, Y.C., L.P. Sheng, and W.J. Zhao. *Research and Development Status of Grouted Splice Sleeve in Precast Concrete Structure*. in *E3S Web of Conferences*. 2018. EDP Sciences.
- [44] Elsayed, M., M.L. Nehdi, and F. Ghrib, *Predicting Behavior of Grouted Dowel Connections Using Interfacial Cohesive Elements*. *Applied Sciences*, 2019. **9**(11): p. 2344.
- [45] Alias, A., et al., *Performance of grouted splice sleeve connector under tensile load*. *Journal of Mechanical Engineering and Sciences (JMES)*, 2014. **7**: p. 1096-1102.
- [46] Kuang, Z. and G. Zheng, *Computational and experimental mechanical modelling of a composite grouted splice sleeve connector system*. *Materials*, 2018. **11**(2): p. 306.

PRINCIPLES AND INSTRUCTIONS FOR COMPLEX PROTECTION OF HISTORIC BUILDINGS WITH VAULTED STRUCTURES FROM THE EFFECTS OF DYNAMIC LOADS

Jiří Witzany

CTU in Prague, Faculty of Civil Engineering, Department of Building Structures, Prague, Thákurova 7, Czech Republic; witzany@fsv.cvut.cz

ABSTRACT

Historic buildings located in areas exposed to dynamic effects caused by natural or technical seismicity are one of the most vulnerable types of structures. Masonry buildings often have timber-ceiling structures with insufficient rigidity and not fully functional system of wall and beam ties, therefore being extremely sensitive to the dynamic effects caused by natural or technical seismicity. Main focus of the article is the outline of possible rehabilitation and restoration design approaches for strengthening of historic buildings in terms of dynamic loads. Brief information about the research performed in the field of masonry vaults' reinforcement due to the dynamic loading is presented.

KEYWORDS

Masonry, Vaults, Dynamic effects, Historic structures, Strengthening

INTRODUCTION

Seismic waves due to earthquakes (natural seismicity) are usually complex continuous movements, similar to the oscillations characterized by its period, amplitude, velocity and acceleration (Figure 1a). To simplify this, the movement during an earthquake is normally assumed to be a simple harmonic motion. The effect of seismic waves in the subsoil directly in contact with the structure is first transmitted to the foundations of the building, exerting cyclical horizontal displacement of the foundation due to the repeated movements of the subsoil, which are then transmitted to above ground structure through the underground (lowest) floor. The type and magnitude of the horizontal displacement depends mainly on the shear and flexural stiffness of the individual floors' structure or the substructure (Figure 1b). The highest values of stresses or horizontal (shear) deformations related to the distribution of the load-bearing system's stiffness along the height of the building can be expected on the lowest floors between the foundations and the superstructure, or in the substructure. In this perspective, the systems with a relatively low stiffness on these floors – e.g. spacious halls, temple naves, etc. - represent the weakest, critical point, usually with the lowest resistance to seismic effects [1,2]. The movement of the Earth's surface during an earthquake in horizontal direction reaches approx. 0.3 to 0.5 times the gravitational acceleration. The horizontal component is the one that has the most severe impacts on buildings. A frequent cause of failures of masonry structures is the relatively low tensile strength of masonry and low ductility, which is the cause of considerable sensitivity of these materials (masonry structures) to the effects of forced deformations. The consequences of this property are, in many cases, manifested locally in the places of stress states with a significant tensile

component. Figure 2 illustrates this fact by comparing the working diagrams of masonry, concrete and steel.

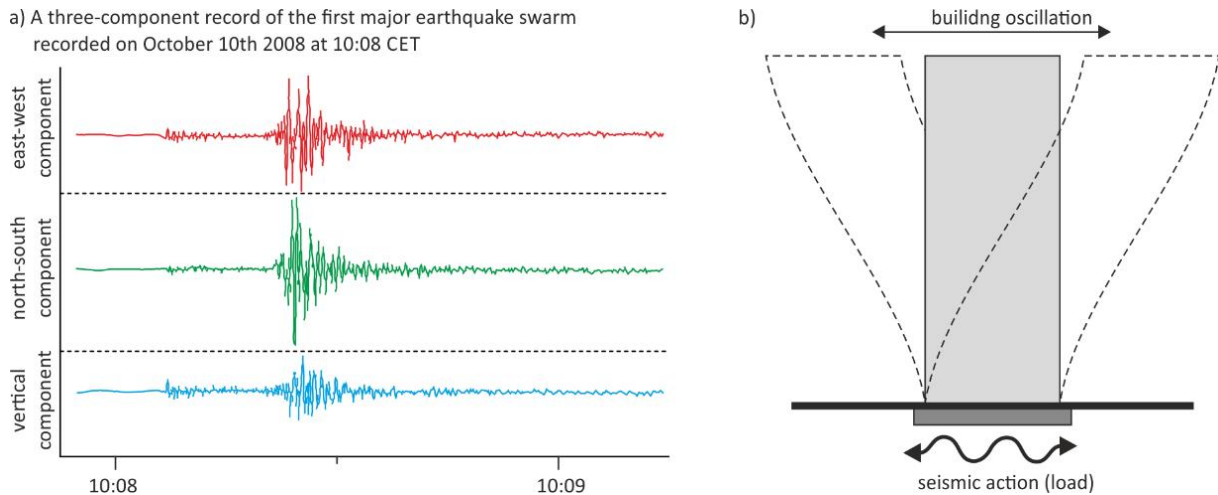


Fig. 1 – a) Record of seismic excitations during earthquake swarm in 2008 (West Bohemia, Czech Republic), b) Response of the structure to seismic loading

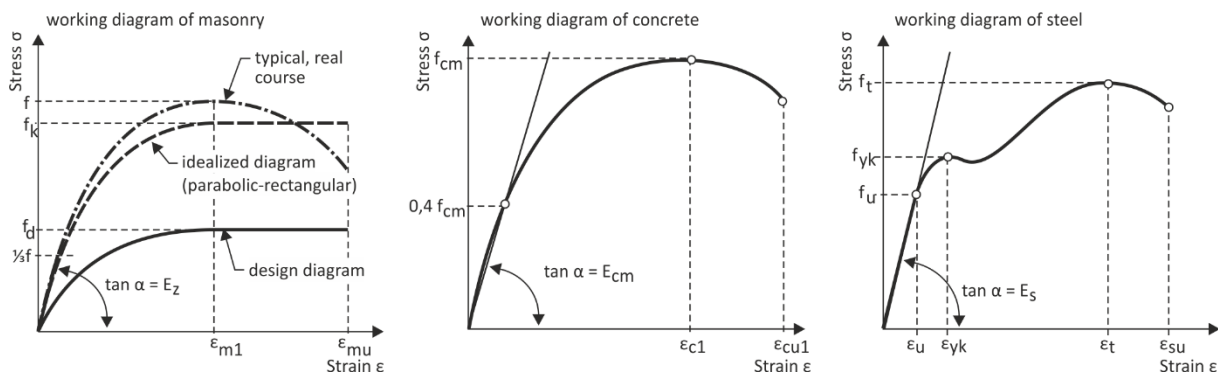


Fig. 2 – Load-displacement diagrams of masonry, concrete and steel

The severity and intensity of seismic (dynamic) effects, which spread through the soil, caused primarily by natural seismicity, depends, among other things, on the execution method and the properties of the foundation structures of the building. The magnitude of vibrations from the subsoil is mainly affected by its geological composition and mechanical properties. Propagation of vibrations through the subsoil depends directly on the natural frequencies of soils of the overlying formations on the bedrock. In the conditions of the Czech Republic, the usual thickness of soils on the bedrock is 2-4 m. In such a case, the natural frequencies of the soil may be very close to the natural frequencies of buildings [3]. Due to this, the transmission of vibrations into building structures can be amplified by the so-called resonance effect [4]. Secondary excitation of subsoil movements near non-stabilized geological conditions may also lead to failure of masonry structures.

The structures with limited spatial stiffness and insufficiently rigid foundation structures tend to be highly susceptible to dynamic effects due to technical and natural seismicity [5]. Typical masonry buildings, often without fully functional system of wall and beam ties, with beam ties anchored in degraded masonry, with an inadequately rigid vaults' supports system, buildings with "soft" timber ceilings, with shallow or non-rigid foundations and unsuitable or degraded foundation

subsoil are extremely sensitive to these effects [6,7]. The type of masonry failure under dynamic loading caused by vibrations is essentially a brittle fracture. At relatively low vibrations, the masonry breaks due to fatigue not only in the joints, but also in masonry units. Vertical cracks occurring in the perimeter walls of castle and church towers are also, in many cases, caused by seismic effects (including low-cyclic effects of temperature and dynamic effects of heavy bells) [7]. Low resistance of masonry structures to seismic effects can lead to severe damage or even collapse of these structures [8,9], many of which are buildings with national or even international heritage protection.

Current research in the field of masonry structures' response to dynamic effects is focused mainly on experimental and theoretical analyses of the behaviour of main structural parts (walls, columns, vaults) under seismic action (horizontal loads) and on the possible methods of rehabilitation, restoration, strengthening and stabilization of these structures. The in-plane displacement capacity of masonry structures is considered one of the most important factors for evaluating their resistance to seismic loads [10,11]. In the field of strengthening, different materials and reinforcing methods are being tested. The use of high strength composites based on carbon, glass, basalt and steel fibers and epoxy resins (FRP) or cementitious matrices (FRCM) is often preferred. The experimental and theoretical research is primarily focused on the determination of optimal placement of the strengthening measures [12,13], verification of bond properties of reinforcing measures [14], verification of novel types and shapes of FRP reinforcement (Ω -Wrap [15]), use of different materials (for example polyparafenilenbenzobisoxazole fibre reinforced cementitious matrix - PBO-FRCM [16,17], Anorganic Matrix composite Grid [18] and others) or even modification of the strengthening composite properties by nanomaterials [19]. Experimental research of masonry structures (mainly vaults) is also focused on verification of seismic performance of reinforced structures [20-23]. Integral part of the research is numerical modelling of reinforced structures using advanced, non-linear approaches and their evaluation against the experimental results [8,24-26]. The use of textile based reinforcements (TRM) and steel reinforced grouts (SRG) is often found to be favourable compared to traditional FRP reinforcement, due to the more ductile behaviour, better compatibility with historic masonry materials, reversibility, lower costs, lower diffusion resistance and better fire resistance [21,22, 27-32].

REHABILITATION AND RESTORATION DESIGN OF A HISTORIC BUILDING IN TERMS OF DYNAMIC LOADS

The rehabilitation design of a historic masonry building situated in a seismically "hazardous" foundation soil, near the tectonic faults, in burrowed under areas, not fully consolidated made-up ground and slope covers, in the sloping terrain, in areas of geological faults exposed to dynamic effects and shocks must be elaborated with special care. It is necessary to assess the execution and condition of foundations and the substructure, the quality and workmanship of load-bearing masonry, the stiffness and effectiveness of the system of tendons, the transfer of horizontal forces exerted by vaulted structures, the stiffness of the supporting system and the stiffness of the floor structures in their planes.

Results of extensive analysis of the damaged to historic masonry buildings in seismically active regions [3] can be summarized as follows:

- a) Due to the seismic activity of earthquake swarms, the buildings made of classic stone, brick and mixed masonry are notably more endangered, compared to, for example, the wall structures of prefabricated concrete buildings erected in the same area in last century.
- b) The degree and magnitude of damage to masonry buildings, which do not undergo regular maintenance and repair of the damage caused by dynamic effects of previous seismic activity, is more severe compared to undamaged buildings. The stress redistribution and dissipation from parts of the masonry structure with damage to intact parts is too small and therefore the

extent and intensity of the damage gradually increases. The area of the undamaged masonry structure with the ability to absorb the seismic energy without failure is reduced, which leads to lower resistance of the masonry structure.

- c) Masonry buildings with binder based of cement mortar have higher stiffness, compared to buildings with binder based on lime, and, at the same time, due to the low tensile strength of the masonry, cracks of larger widths appear and a more significant deflection of damaged parts occurs, which makes subsequent masonry repairs difficult. In contrast, the masonry with a softer binder based on lime dissipates the fracture energy in the binder part of the masonry and, as a result, more frequent and smaller (thinner) cracks appear, with a less pronounced effect on the overall stability of the masonry structure.

Preventive measures in historic masonry buildings with vaulted structures in regions with increased seismicity include:

The assessment or execution of adequate modifications to ensure the stiffness and strength of the foundation structure, such as the strengthening of foundation masonry, tying of foundation structures with bracing strips, tie rods, etc., securing the participation of foundations in response to the dynamic loads and stress redistribution caused by a change in the shape of the foundation subsoil.

The reinforcement of vertical masonry columns and walls (concreting, shotcreting, steel bandage, reinforcement with FRP composites), strengthening and stiffening of floor structures (reinforcement with additionally installed steel beams, tie rods, bracing, overconcreting), deepening and bracing of foundations, all these measures increase the overall resistance of masonry structures to dynamic and seismic effects.

Additional stiffening of the load-bearing structure situated at the foundation and floor slabs' levels, vertical pre-stressing of walls and columns with the foundation structure (Figure 3), activation of tie rods together with delimiting "spacers", reinforcement of vaults with pre-stressed lamellas based on high-strength fibers situated on the extrados and pre-stressing of supports or interconnection of foundations are the most effective measures.

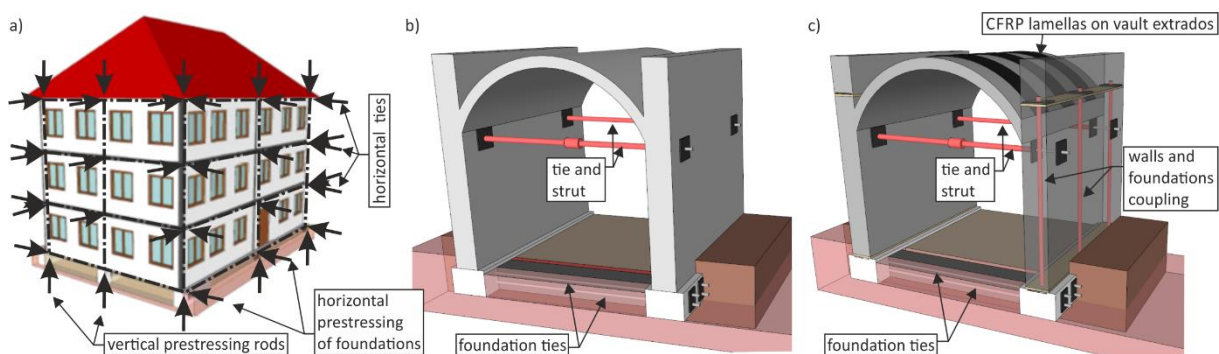


Fig. 3 – a) Prestressing of the load-bearing masonry structures and foundations vertical and horizontal direction, b) Additional vault ties and foundation coupling, c) Stiffening the vault structure by CFRP lamellas, vault ties and foundation coupling

In masonry buildings with wooden ceilings, the stiffness of the floor structure must be secured, above all, by functional wall and beam ties, or by additionally executed ring beams and by masonry bracing at the floor structure level, additional masonry reinforcement (in both horizontal and vertical directions).

In addition to the horizontal bracing of the masonry structure by a system of ties (wall, vault, beam ties), the masonry can also be additionally reinforced by vertical steel ties, which vertically tie individual parts of the building – e.g. anchoring of the wooden structures of trusses, baroque

towers and domes. Wooden vertical tie rods may also be used, beam tie rods are anchored to the floor beams. Similarly, cornices, stone slabs of balconies, bay windows, suspended staircases can also be anchored by vertical steel tie rods, and the masonry can be strengthened in places where the bed joints may open.

The analysis of the response to dynamic effects in the vault structure requires special attention. The type of the vault impost mounting in the masonry of the abutments mostly corresponds to partial embedding of the vaults in the abutments. The vaults gradually or continuously enlarged in the impost cross-sections in which full embedding can be assumed may be an exception to this rule. In contrast to the “simple” mounting of a vault with a bowstring on the abutments (statically determinate system), vaults with a partial or full embedding are very sensitive to deformations of the supporting system which are transferred to the vault structure, and due to dynamic loads they may cause the vault failure (e.g. in the case of semicircular vaults most often in the crown part, but in some cases near the abutments).

Securing the vault stability requires a functional and effective tie rod, beam tie system, or a stable supporting system (massive retaining walls of Romanesque buildings, supporting system of Gothic cathedrals, etc.). Vault ties and tie rods secure the transfer of the horizontal component of the resultant support forces in the mounting of vaults onto the supporting structure and, to some extent, the vault shape. Similar to the arched supporting system of Gothic buildings, vault ties reduce the requirements for the bending stiffness of the supporting structure (columns, walls) allowing their more subtle design. Their absence, insufficient dimensions or effectiveness are the most common causes of failure in vaults.

The reinforcement (strengthening) of the vault by overall reinforcement, or by additionally installed monolithic, precast and steel strips, or strips of high-strength FRP composites installed along the whole length on the back of the vault and anchored to the vertical supporting structure increases the resistance of the vault to dynamic effects. To achieve the required effectiveness of the vault reinforcement by additionally installed strips the immovability and stability of the supports and the foundation structure is necessary (see Figure 3c).

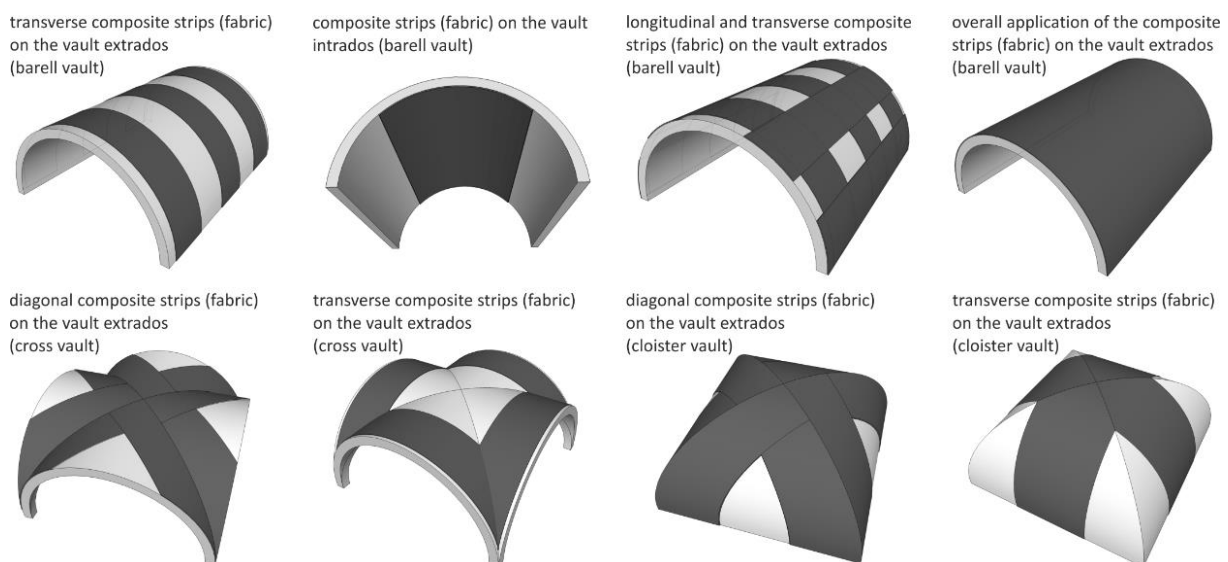


Fig. 4 – Schematic representation of the reinforcement of vaulted structures using carbon (glass, aramid etc.) fabrics based composites

By applying FRP composites based on high-strength fibers, the resistance (load-bearing capacity, stability) of reinforced vaulted structures to dynamic effects can be increased. This property may be advisably used to increase the resistance of mainly historic vaults of e.g. sacral

buildings exposed to dynamic effects due to technical and natural seismicity in seismically active regions, or to increase the resistance of structures to the effects of extreme loads (Figure 4 and Figure 5). Composites (strips of fabric made of CFRP or GFRP fibers, or carbon lamellas bonded and glued with epoxy adhesives) should be applied on the back of vaulted structures along the whole length of the vault, or locally on the face of the vault in areas of tensile stresses (Figure 6). Similarly, the overall stiffening of the system of supports or the building can be achieved by carbon lamellae situated around the perimeter of the building, installed flatly in shallow grooves or inserted in grooves in the masonry (e.g. in places of bed joints).

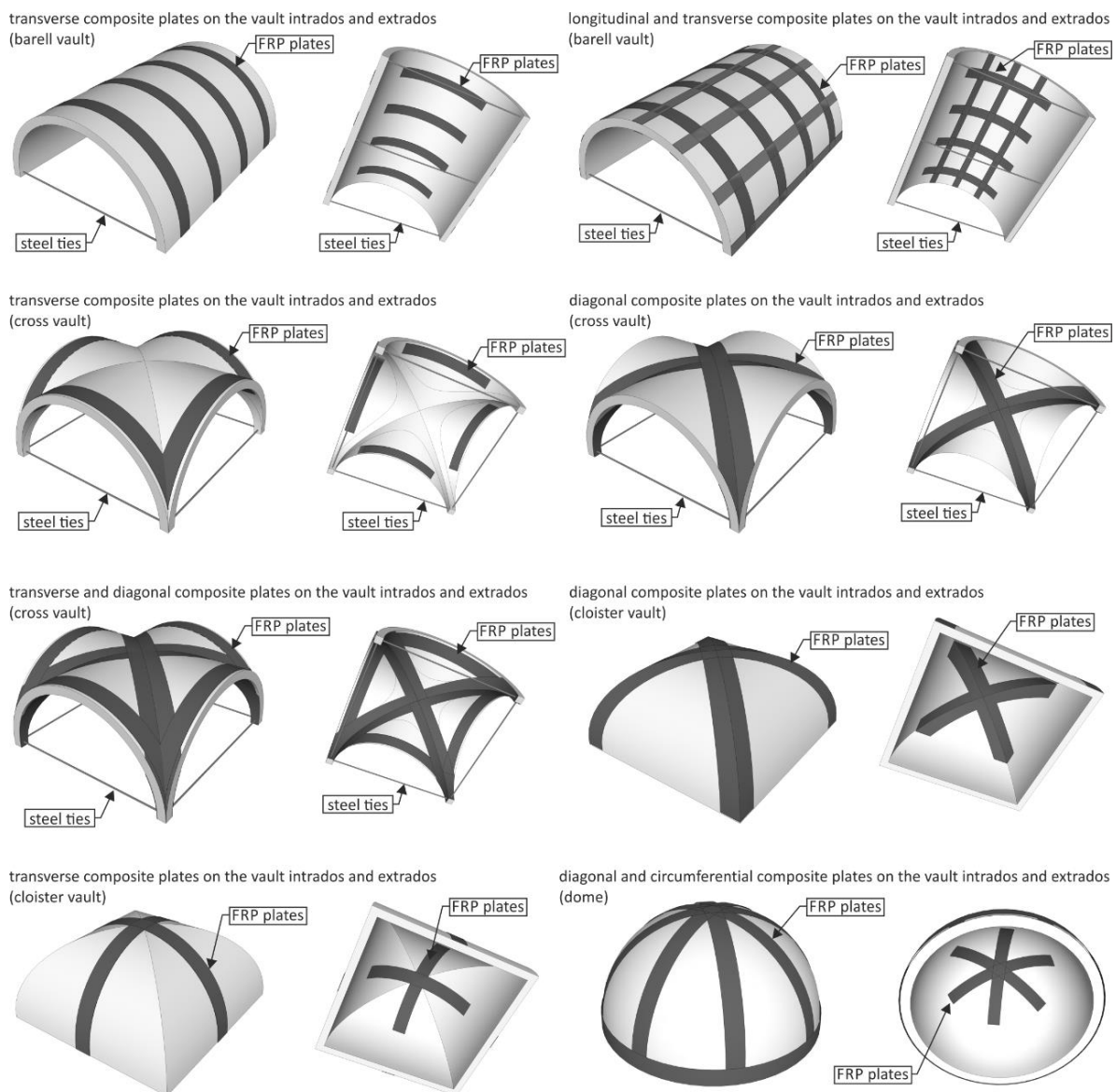


Fig. 5 – Schematic representation of the reinforcement of vaulted structures using carbon plates and steel ties due to the seismic loads and extrados using high strength strips (plates, lamellas)

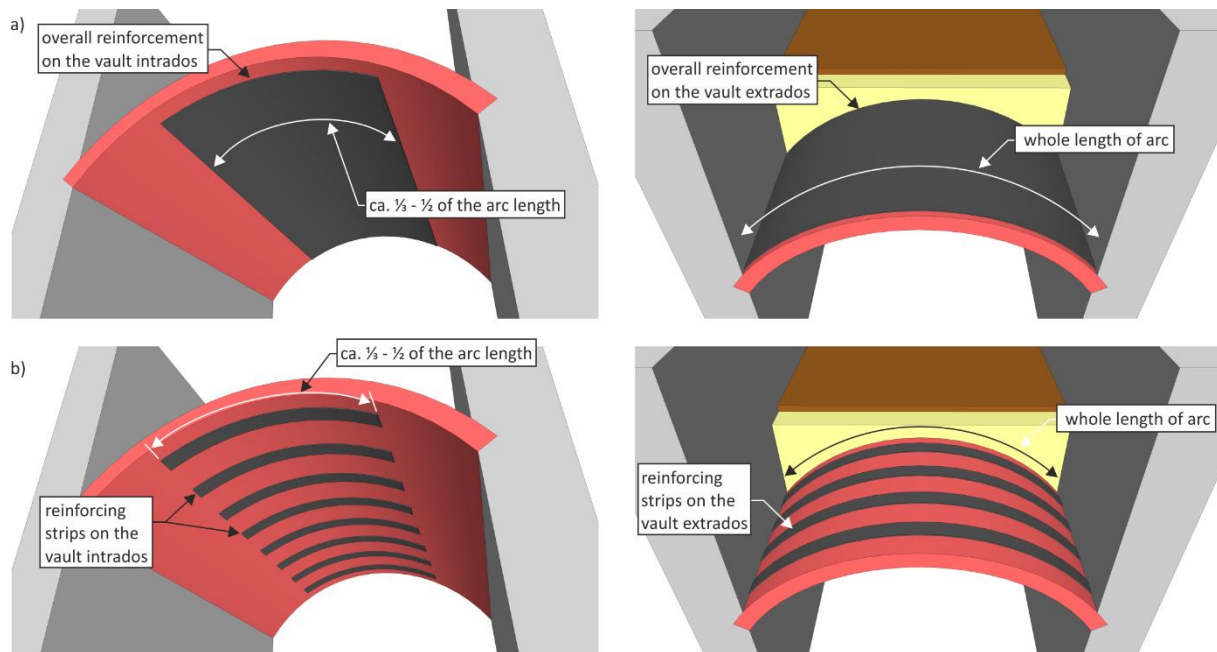


Fig. 6 – Optimal arrangement of reinforcing composites based on high-strength fabrics and lamellas on barrel vault, a) Overall reinforcement of the barrel masonry vault on the intrados and extrados (using high strength fabrics), b) Reinforcement of the barrel masonry vault on the intrados

Partial reinforcement of the vault can be achieved by additional execution of vault backings. Vault backings built, as a rule, to 1/3 to 2/3 of the vault extrados height, especially at higher vaults, favourably affect the pressure line course and effectively secure the foot joint and hazardous cross-sections at the back of semicircular barrel vaults against opening and deflection (transforming the vault with a rise $v/l > 0.3$ into a vault with a lower rise, e.g. $v/l < 0.2$). The backing must have sufficient stiffness and strength to be able not only to withstand but also to react immediately to horizontal deformations of the vault in the so-called hazardous cross-section areas, and, particularly, to an increase in the horizontal force at the “toe” of the transformed vault due to the effect of dynamic loads and thus enhance the vault stability and resistance.

Additional insertion of dampening devices and elements between the foundations and the masonry superstructure (systems with a controlled response) requires very complex technological solution when applied on existing buildings. Therefore, passive systems are often used as the basic protective measure against the effects of seismicity in historic and heritage buildings, including a number of measures focused on preventive strengthening of the structure to avoid its damage.

Note: Load-bearing systems with a “controlled response” (stiffness of individual floors), with inserted elements and devices for the dissipation of energy and reduction of dynamic effects caused by dynamic loads can be designed:

- on the principle of passive or active elements reducing the risks of structural damage or a complete building’s collapse during an earthquake,
- by inserting active elements and components which detect (record) the foundation subsoil movement induced by seismic or extreme wind effects (wind blasts) and actively respond to it.

BEHAVIOR OF BARREL VAULTS UNDER SEISMIC LOADING

A frequent cause of vault failures in regions with increased risk of natural seismicity is their inelastic response to dynamic effects (Figure 7). Experimental research [13, 33] has manifested a decrease in the vault stiffness due to repeated dynamic loads - seismicity, traffic impacts, mining, etc. - which, in the interaction with e.g. a permanent vertical load, gradually cause the appearance and development of microcracks and cracks, the growth and propagation of cracks arising usually due to other permanent and cyclic loads, up to the failure of the structure – by a gradual increase in deformations in individual load cycles. The velocity of this process, the gradual decrease in the vault stiffness, depends on the intensity of the vaulted structure response during the occurrence of repeated dynamic loads. The decrease in the vault stiffness (Figure 8a) due to the growing vault damage is accompanied by a decrease in the vault natural frequencies (Figure 8b).



Fig. 7 – Examples of the failure of a barrel masonry vault with vaulted openings and cross vault of a historic building (Loretto near Bor u Tachova, West Bohemia, Czech Republic, 17th cent.)

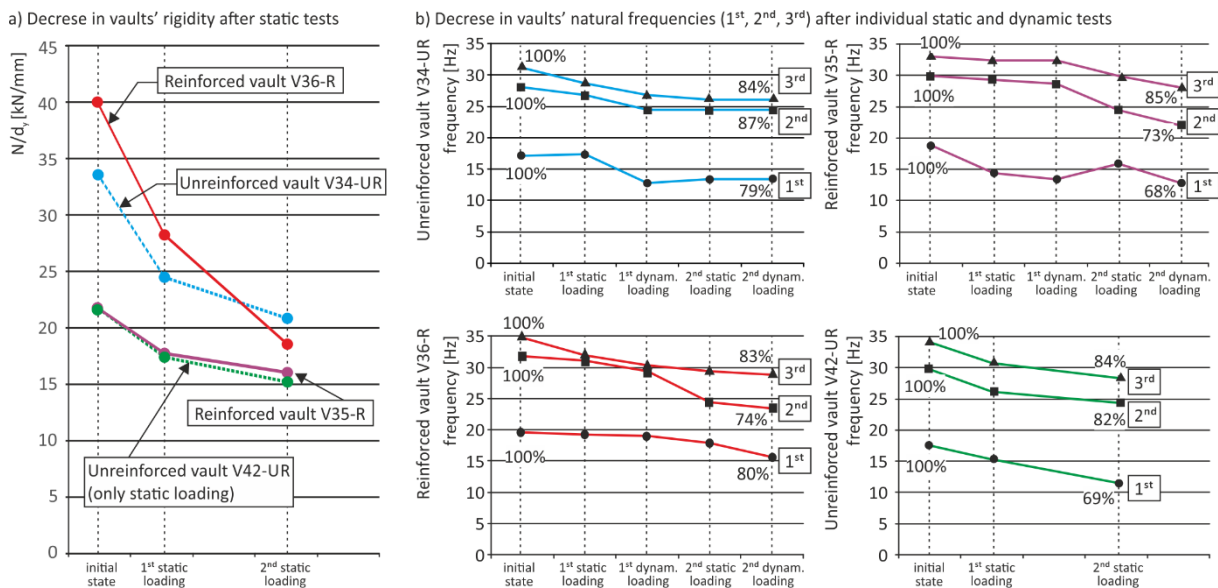


Fig. 8 – a) Experimentally determined decrease in the stiffness of vault structures, b) Experimentally determined decrease of natural frequencies (1st – 3^d)

The results of experimental research [13,33] have shown a decrease in the stiffness of a masonry barrel vault with a tendon after each load “cycle” of static and dynamic loading, which was reflected in the overall increase in deformations and a lowering of natural frequencies and, in some cases, even in an increase in internal damping. The cause of a change in the vault stiffness was the formation of microcracks, the development and propagation of cracks and, in the first load cycles, also the vault consolidation, especially by additional compression of contact joints (mortar - masonry unit) in the bed joints of the vault masonry. The obtained results are extremely important for the evaluation of the residual life of primarily the vaults of historic buildings located in seismically active regions or in places with intensive technical and induced seismicity (mining activity, quarrying, traffic etc.).

Note: The dynamic response can be utilized to determine potential damage to the structure that may be complicated to detect in other ways. Assuming a low level of dynamic (i.e. non-destructive) excitation, the principle of such tests is to compare the dynamic characteristics of the structure. The characteristics most often refer to resonant frequencies and their respective oscillation shapes. A change in the frequency, most often a decrease, may be a sign of the appearance of internal cracks in the tested vault. A change in the shape of the oscillation then indicates its global failure.

CONCLUSIONS

The rehabilitation design of a historic masonry building with vaults exposed to dynamic effects in terms of its overall protection against the occurrence of failures and damage requires a detailed analysis of the supporting system of the historic building, including its adjoining structures, and, based on the overall assessment, the execution of appropriate modifications, rehabilitation and additional measures to secure the supporting system. The analysis and design of complex measures for the protection of the building must be preceded by a detailed survey. The scope of individual protective measures depends on the specific situation, design and condition of the historic building

ACKNOWLEDGEMENTS

The article was written with support from the NAKI DG16P02M055 project “Development and Research into Materials, Procedures and Technologies for Restoration, Conservation and Strengthening of Historic Masonry Structures and Surfaces and Systems of Preventive Care of Historic and Heritage Buildings Threatened by Anthropogenic and Natural Risks”.

REFERENCES

- [1] Elghazouli, A. (Ed.), 2009 *Seismic Design of Buildings to Eurocode 8*. Publisher: CRC Press, London, UK.
- [2] Lorant, G., *Seismic Design Principles*. Available online: <https://www.wbdg.org/resources/seismic-design-principles> (accessed on 21. 3. 2018).
- [3] Witzany, J., Zigler, R., Čejka, T., Libecajtová, A, 2019. Complex Static and Dynamic Protection of Historic Buildings From the Effects of Natural Seismicity, *Civil Engineering Journal* 3, 320-330, art. no. 26, DOI: 10.14311/CEJ.2019.03.0026
- [4] Makovička, D.; Makovička, D., jr., 2009. Response Analysis and Vibroinsulation of Buildings Subject to Technical Seismicity, In: *Earthquake Resistant Engineering Structures VII*. Publisher: WIT Press, Southampton, UK, pp. 197-205, DOI: 10.2495/ERES090181
- [5] Celep, Z., İncencek, M., Pakdamar, F., 2008. Structural and earthquake response analysis of the Muradiye mosque, 14 WCEE, Beijing, China Conference: *Proceedings of the 14th World Conference on Earthquake Engineering*.

- [6] Borri, A., Corradi, M., Vignoli, A., 2002. New materials for strengthening and seismic upgrading interventions, International Workshop Ariadne 10, Arcchip, Prague, Czech Republic.
- [7] Ravikumar, C.S., Thandavamoorthy, T.S., 2014. Application of FRP for strengthening and Retrofitting of civil engineering structures, *International Journal of Civil Structural, Environmental and Infrastructure Engineering, Research and Development (IJCSIEIRD)*, 4(1), pp. 49 – 60.
- [8] Mahinia, S.S., Eslamib, A., Ronagh, H.R., 2012. Lateral performance and load carrying capacity of an unreinforced CFRP-retrofitted historical masonry vault – A case study. *Construction and Building Materials* 28, 146-156, DOI: 10.1016/j.conbuildmat.2011.08.013
- [9] Anania, L., D'Agata, G., 2017. Limit analysis of vaulted structures strengthened by an innovative technology in applying CFRP. *Construction and Building Materials* 145, 336-346, DOI: 10.1016/j.conbuildmat.2017.03.212
- [10] Rossi, M., Calderini, C., Lagomarsino, S., 2016. Experimental testing of the seismic in-plane displacement capacity of masonry cross vaults through a scale model. *Bulletin of Earthquake Engineering* 14, 261-281, DOI: 10.1007/s10518-015-9815-1
- [11] Misseri, G., Rovero, L., 2017. Parametric investigation on the dynamic behaviour of masonry pointed arches. *Archive of Applied Mechanics* 87, 385-404, DOI: 10.1007/s00419-016-1199-4
- [12] Oliveira, D. V., Basilio, I., Lourenço, P.B., 2010. Experimental Behavior of FRP Strengthened Masonry Arches. *Journal of Composites for Construction*, 14, DOI: 10.1061/ASCECC.1943-5614.0000086
- [13] Witzany, J., Zigler, R., Čejka, T., Makovička, D., Urushadze, S., Pospíšil, S., 2015. Experimental research into dynamic characteristics of masonry segment barrel vaults, In: Proceedings of SMAR 2015, The Third Conference on Smart Monitoring, Assessment and Rehabilitation of Structures. Publisher: ITU, Istanbul, Turkey, pp. 1-8.
- [14] Caggegi, C., Carozzi, F.G., De Santis, S., Fabbrocino, F., Focacci, F., Hojdis, L., Lanoye, E., Zuccarino, L., 2017. Experimental analysis on tensile and bond properties of PBO and aramid fabric reinforced cementitious matrix for strengthening masonry structures. *Composites Part B: Engineering* 127, 175-195, DOI: 10.1016/j.compositesb.2017.05.048.
- [15] Anania, L., Badalà, A., D'Agata, G., 2013. The post strengthening of the masonry vaults by the Ω-Wrap technique based on the use of C-FRP. *Construction and Building Materials* 47, 1053-1068, DOI: 10.1016/j.conbuildmat.2013.05.012
- [16] Alecci, V., Misseri, G., Rovero, L., Stipo, G., De Stefano, M., Feo, L., Luciano, R., 2016. Experimental investigation on masonry arches strengthened with PBO-FRCM composite. *Composites Part B: Engineering* 100, 228-239, DOI: 10.1016/j.compositesb.2016.05.063
- [17] Alecci, V., Focacci, F., Rovero, L., Stipo, G., De Stefano, M., 2016. Extrados strengthening of brick masonry arches with PBO–FRCM composites: Experimental and analytical investigations. *Composite Structures* 149, 184-196, DOI: 10.1016/j.compstruct.2016.04.030
- [18] Giamundo, V., Lignola, G.P., Maddaloni, G., Balsamo, A., Prota, A., Manfredi, G., 2015. Experimental investigation of the seismic performances of IMG reinforcement on curved masonry elements. *Composites Part B: Engineering* 70, 53-63, DOI: 10.1016/j.compositesb.2014.10.039
- [19] Cakira, F., Uysal, H., Acar, V., 2016. Experimental modal analysis of masonry arches strengthened with graphene nanoplatelets reinforced prepreg composites. *Measurement* 90, 233-241, DOI: 10.1016/j.measurement.2016.04.061
- [20] Corradi, M., Borri, A., Castori, G., Coventry K., 2015. Experimental Analysis of Dynamic Effects of FRP Reinforced Masonry Vaults. *Materials* 8, 8059–8071, DOI: 10.3390/ma8125445
- [21] Garmendia, L., Larrinaga, P., San-Mateos, R., San-José, J.T., 2015. Strengthening masonry vaults with organic and inorganic composites: An experimental approach. *Materials and Design* 85, 102-114, DOI: 10.1016/j.matdes.2015.06.150
- [22] Bilotta, A., Ceroni, F., Nigro, E., Pecce, M., 2017. Experimental tests on FRCM strengthening systems for tuff masonry elements. *Construction and Building Materials* 138, 114-133, DOI: 10.1016/j.conbuildmat.2017.01.124

- [23] Valvona, F., Toti, J., Gattulli, V., Potenza, F., 2017. Effective seismic strengthening and monitoring of a masonry vault by using Glass Fiber Reinforced Cementitious Matrix with embedded Fiber Bragg Grating sensors. *Composites Part B: Engineering* 113, 355-370, DOI: 10.1016/j.compositesb.2017.01.024
- [24] Bertolesi, E., Milani, G., Carozzi, F.G., Poggi, C., 2018. Ancient masonry arches and vaults strengthened with TRM, SRG and FRP composites: Numerical analyses. *Composite Structures* 187, 385-402, DOI: 10.1016/j.compstruct.2017.12.021
- [25] Milani, G., Valente, M., Fagone, M., Rotunno, T., Alessandri, C., 2019. Advanced non-linear numerical modeling of masonry groin vaults of major historical importance: St John Hospital case study in Jerusalem. *Engineering Structures* 194, 458-476, DOI: 10.1016/j.engstruct.2019.05.021
- [26] Grillanda, N., Chiozzi, A., Milani, G., Tralli, A., 2019. Collapse behavior of masonry domes under seismic loads: An adaptive NURBS kinematic limit analysis approach. *Engineering Structures* 200, DOI: 10.1016/j.engstruct.2019.109517
- [27] Kouris, L.A.S., Triantafillou, T.C., 2018. State-of-the-art on strengthening of masonry structures with textile reinforced mortar (TRM). *Construction and Building Materials* 188, 1221-1233, DOI: 10.1016/j.conbuildmat.2018.08.03
- [28] Alecci, V., De Stefano, M., Focacci, F., Luciano, R., Rovero, L., Stipo, G., 2017. Strengthening Masonry Arches with Lime-Based Mortar Composite. *Buildings* 7, DOI: 10.3390/buildings7020049
- [29] De Santis, S., 2017. Bond behaviour of Steel Reinforced Grout for the extrados strengthening of masonry vaults. *Construction and Building Materials* 150, 367-382, DOI: 10.1016/j.conbuildmat.2017.06.010
- [30] Carozzi, F.G., Poggi, C., Bertolesi, E., Milani, G., 2018. Ancient masonry arches and vaults strengthened with TRM, SRG and FRP composites: Experimental evaluation. *Composite Structures* 87, 466-480, DOI: 10.1016/j.compstruct.2017.12.075
- [31] De Santis, S., Roscini, F., de Felice, G., 2018. Full-scale tests on masonry vaults strengthened with Steel Reinforced Grout. *Composites Part B: Engineering* 141, 20-36, DOI: 10.1016/j.compositesb.2017.12.023
- [32] Zampieri, P., Simoncello, N., Tetougueni, C.D., Pellegrino, C., 2018. A review of methods for strengthening of masonry arches with composite materials. *Engineering Structures* 171, 154-169, DOI: 10.1016/j.engstruct.2018.05.070
- [33] Witzany, J., Pirner, M., Zigler, R., Urushadze, S., 2020. Experimental research into the response of segmental barrel vaults to repetitive static and dynamic loads, *Engineering Structures* 208, art. no. 110342, DOI: 10.1016/j.engstruct.2020.110342

PREDICTION OF TBM PENETRATION RATE OF WATER CONVEYANCE TUNNELS IN IRAN USING MODERN METHODS

Alireza Afradi, Arash Ebrahimabadi and Tahereh Hallajian

Department of Mining and Geology, Qaemshahr Branch, Islamic Azad University, Qaemshahr, Iran; A.Ebrahimabadi@Qaemiau.ac.ir

ABSTRACT

TBM has been used extensively in civil engineering activities and plays an important role in tunnelling projects. Hence, the penetration rate of these machines plays a crucial role in the success of their application. Therefore, in order to predict the TBM penetration rate in this study in several water conveyance tunnels including the tunnels of Karaj, Ghomrood, Golab, Nosoud and Sabzkooh, four intelligence techniques including multiple linear and nonlinear regression analysis, Gene Expression Programming (GEP) method, and Support Vector Machine (SVM) were applied. The obtained values of R^2 and RMSE included 0.43 and 3.08 for linear regression, 0.68 and 2.3 for nonlinear regression, 0.74 and 2.09 for GEP method and 0.97 and 0.6 for SVM method, respectively which were utilized to predict TBM penetration rate. By investigating the tunnels database, the results indicated that the SVM method had the most accurate prediction of penetration rate (in terms of R^2 and RMSE) and the maximum amount of R^2 and the minimum amount of RMSE among all predictive modelings. Finally, respecting the amount of R^2 and RMSE, the other methods like GEP method, nonlinear regression, and linear regression are listed to have the required accuracy in predicting penetration rate.

KEYWORDS

Linear regression, Non-linear regression, Gene expression programming, Support vector machine

INTRODUCTION

Nowadays, the application of mechanized tunnelling has been extensively developed around the world. Due to ever-increasing advance of studied or constructed tunnelling projects (e.g. water conveyance tunnels, subway tunnels and road tunnels), and also the importance of construction time, the use of mechanized tunnelling has been important [1]. The proper use of these tunnelling devices would only be feasible by considering a number of factors including the selection of an appropriate tunnel boring machine, technology transition system, excellent management and project condition as well [2]. Thus, Tunnel Boring Machines (TBMs) would be a significant option for every tunnelling project due to their capabilities and high advancement rates [3]. In the beginning, the only capability of a mechanized excavation tool has been boring and advancement. In the course of time and through the increased need for high boring and advancement rates, several lateral capabilities such as the conveyor system for evacuating muck, temporary and permanent support of excavated areas have been added [4]. In empirical modelling of TBM performance, the machine and ground have been assumed as a continuous system which simultaneous effects on the machine's performance were not so precise and detailed rather it might have been entered to the model unknown [5]. The other category of empirical models was mainly developed by some experimental studies based on one or several parameters of rock or through the prediction index of rock

performance. Due to the similarities of TBM disc cutter mechanism to one or few numbers of the tests by prediction indices, there is a close relationship between the results and disc (or generally TBM) penetration rate [6]. This group of predictive models are basically different from the other categories since the prediction indices depend on some experimental studies which are generally carried out for the purpose of simulating rock cutting process. Hence the prediction of TBM penetration rate or the cutting forces are associated to the cutting process. The penetration tests can be an example of this kind. The indices might be used in some empirical field modelling along with other parameters [7]. Forecasting TBM penetration rates is one of the issues that has received considerable attention for estimating the timing of a project. Many researchers have proposed several methods to estimate TBM penetration rate [8]. In many models, only a few basic parameters are used to analyze the model and the influence of other parameters is ignored [9]. In the present study, TBM penetration rate was investigated by four different approaches including linear and nonlinear regression, Support Vector Machine (SVM) and Gene Expression Programming (GEP) algorithm.

MATERIAL AND METHODOLOGY

Ghomrood water conveyance tunnel

Ghomrood water conveyance tunnel is located 25 km southeast of Aligudarz city in Lorestan province [10].

Golab water conveyance tunnel

The Golab water conveyance tunnelling project was proposed by Isfahan province in order to transfer the drinking water of Kashan [11].

Karaj water conveyance tunnel

Regarding the administrative divisions of Iran, the range of the Karaj water conveyance tunnel project has been located in the north of Tehran which is considered as the mountainous regions of the south of Alborz mountain range.

This tunnel has been located in Alborz formation which the constitutive rocks of the region mainly consist of pyroclastic sedimentary rocks including green tuff, shear tuff, silty tuff of sandstone tuff and intrusive masses of Monzodiorite and Monzogabbro. The largest fault of the region in the tunnel route is Purkan-Vardij fault [12].

Nosoud water conveyance tunnel

The Nosoud water conveyance tunnel, with a length of 49 km, is part of a large tropical water supply plan for the western part of the Iran [13].

Sabzkooh water conveyance tunnel

The Sabzkooh water conveyance tunnel is located in the vicinity of Sakiabad village within a distance of 7 km to Choghakhor dam and 68 km to Shahr-e Kord in Chaharmahal and Bakhtiari Province. The route of Sabzkooh tunnel is oriented in the north margin of Zagros mountain ranges in the high central sections of the structural Zagros zone and passes through the north edge of the Sabzkooh syncline. The geology of the region consists of sedimentary rocks which have been occurred as folded zones, faults, shear zones and sutured and altered surfaces [14].

Regression

Regression is the statistical analysis technique which is used in the most engineering and non-engineering analyses. This approach is extensively utilized to ensure data validity and the results of modelling, which is evaluated by the determination coefficient (R^2). The determination coefficient (R^2) represents the accuracy of the graph and data validation. Regression analysis is used to determine the contribution of independent variables for predicting the dependent variable [15]. In regression analysis, the objective is to predict dependent variable changes with respect to independent variables. Multivariate regression analysis is well suited to study the effects of independent multivariate variables on the dependent variable. [16].

Gene Expression Programming (GEP)

One of the branches of evolutionary processing is gene expression programming. In gene expression programming, we try to use computer genetics algorithms, and the concepts of decomposition trees for specific applications, instead of writing the required program code, allowing the computer to know the program just by knowing the general meaning of the work. In fact, we give a high-level command to the computer and the computer itself prepares the necessary program to run the program, then runs the program and provides us with the desired output. Genetic expression programming, abbreviated GEP, uses genetic algorithms to write computer programs. In this case, the variables are programming structures, and the output is the program's ability to achieve goals. Minor changes are needed in genetic algorithm operations such as mutations, reproduction, and cost function assessment to use them in GEP. In fact, GEP is a computer program that writes other computer programs. In order to develop and run the models based on GEP, Genexpro tools are applied in the current study. The mentioned program was based on GEP. The GEP is the newest revision of the genetic programming which analyzes different computer programs. One of the GEP advantages is that the genetic diversity indicators are very simple, thus genetic operators act in chromosome level [17]. Moreover, another advantage of this technique is the unique nature of multigene, which could prepare the evaluation process of the complicated models including the parameters listed below. Table 1 indicates the GEP parameters.

Tab. 1 - GEP parameters

Head size	10
Chromosomes	30
Number of genes	4
Mutation rate	0.00138
Inversion rate	0.1
One-point recombination rate	0.00277
Two-point recombination rate	0.00277
Gene recombination rate	0.00277
IS transposition rate	0.00546
RIS transposition rate	0.00546
Gene transposition rate	0.00546
Fitness function	RMSE
Linking function	(+)

Support Vector Machine (SVM)

SVM is a classifier or a border which determines the best classification and separation among the data by utilizing the support vectors [18]. In the SVM, the principles of the learning machine and creating a model is the only data placed in the support vectors [19]. This algorithm is not sensitive to the other points, and it aims to find an optimal line of data so that it has the maximum allowable distance with regard to all classifications (the support vectors) [20]. In a simple way, the support vectors are a set of points in n-dimensional space of data which determine the border of classifications, so that the data classification could be carried out. The classification output can be changed as a result of moving one of the vectors [21]. The specification of SVM used in predicting penetration rate was listed in Table 2.

Tab. 2 - SVM parameters

Model type	ϵ -SVR
Kernel function	Gaussian function (Radial basis function (RBF))
Degree	2
ϵ	0.1
C	1000
s	0.5

Evaluation parameters

In this paper, the determination coefficient (R^2) and root-mean-square error (RMSE) have been utilized to evaluate the parameters. The determination coefficient (R^2) indicated a tiny percentage of the independent variable changes which was determined by a dependent variable. The best value for the coefficient of determination varies between one and zero. Thus, the closer to the one, the better results will be achieved. RMSE is the standard deviation of the predicted amount by a model or the statistical estimator and the real (measured) amount [22].

The data

The input and output variables of the predictive modelling of TBM penetration rate are illustrated in Table 3. In this step, the data of the five mentioned tunnels (the case studies) are merged which the descriptive statistics of the data which are represented in Table 4. The description of the projects is shown in the Table 5.

Tab. 3 - Input and output variables of predictive modeling of TBM penetration rate

	Variable type	Symbols used in the model
Input variable	Uniaxial Compressive Strength	UCS
	Brazilian Tensile strength	BTS
	Rock Quality Designation (RQD)	RQD
	Cohesion	C
	Elasticity Modulus	E
	Poisson's ratio	ν
	Density	D
	Joint angle	JA
	Joint spacing	JS
	Output variable	Penetration rate

Tab. 4 - Descriptive statistics of the data used in the five tunnels

	UCS (MPa)	BTS (MPa)	(RQD)(%)	C (MPa)	E (GPa)	v	D (g/cm ³)	JA (Deg.)	JS (m)	PR(m/hr)
Mean	60.0981	9.6179	54.28	2.3001	8.9689	0.2859	2.5556	31.3686	0.7563	8.0513
N	491	491	491	491	491	491	491	491	491	491
Std. Deviation	43.41903	2.78877	18.038	3.82586	7.95887	0.05486	0.11110	7.80257	0.39740	4.10796
Minimum	5.36	5.00	20	0.20	0.50	0.20	2.30	14.00	0.17	0.74
Maximum	199.60	15.00	95	23.89	62.00	0.40	2.84	57.00	1.60	26.62
Variance	1885.213	7.777	325.352	14.637	63.344	0.003	0.012	60.880	0.158	16.875
Harmonic Mean	30.2964	8.7910	46.56	0.5817	3.8961	0.2749	2.5507	29.4610	0.5387	5.9592
Geometric Mean	43.7932	9.2053	50.71	1.0390	6.3386	0.2805	2.5531	30.4146	0.6453	7.0690
Std. Error of Mean	1.95947	0.12586	0.814	0.17266	0.35918	0.00248	0.00501	0.35213	0.01793	0.18539

Tab. 5 - The description of the projects

No	Project	TBM type	TBM diameter (m)	Lithology
1	Karaj water conveyance tunnel, Lot 1 (Iran)	Double shield (Herrenknecht)	4.65	Tuffs, Shaly and Sandy Tuffs, Agglomerate
2	Ghomrood water conveyance tunnel, Lots 2, 3 & 4 (Iran)	Double shield (Wirth)	4.525	Limestone, Shale and sandstone, Slate, Phyllite, Schist with quartzitic veins
3	Nosoud water conveyance tunnel, Lot 2(Iran)	Double shield (Herrenknecht)	6.73	Limestone, Shale and Limy Shales
4	Sabzkooch water conveyance tunnel, (Iran)	Double shield	4.5	Limestone, Dolomite
5	golab water conveyance tunnel, (Iran)	Double shield (Wirth)	4.53	Phyllite, sandstone, conglomerate, shale

RESULTS

TBM penetration rate prediction in the five tunnels using linear regression model

In order to TBM penetration rate prediction for single tunnels, the assumptions used in the predictions are kept, and the data of each five tunnels are merged. Therefore, the prediction of TBM penetration was carried out on the overall database. Table 6 represents the coefficient of determination related to the multivariate linear regression modeling which is applied for predicting TBM penetration rate in database.

The values of regression coefficients related to predictive modeling of the penetration rate are also shown in Table 7. Furthermore, the nonlinear relationship, created by the coefficients, between the independent variables and the penetration rate are described in Equation 1. Additionally, using the predictive modelling, the Dispersion diagram and Coordination diagram of the measured and the predicted values of penetration rate have been illustrated in figures 1 and 2, respectively.

Tab. 6 - The coefficient of the determination of the linear regression for predictive modeling of TBM penetration rate in the tunnels database

Model Summary

Model	R	R Square	Adjusted R Square	Std. Error of the Estimate
1	.660 ^a	.436	.425	3.11377

a. Predictors: (Constant), UCS (MPa), BTS (MPa), RQD (%), C (MPa), E (Gpa), V, Density (g/cm3), Joint Angle (Deg.), Joint_Spacing(m)

Tab. 7 - Coefficients of linear regression for predictive modelling of the penetration rate in the five tunnels

Coefficients^a

Model		Unstandardized Coefficients		Standardized Coefficients	t	Sig.
		B	Std. Error	Beta		
1	(Constant)	.818	.841		.972	.331
	UCS (MPa)	-.008	.005	-.077	-1.576	.116
	BTS (MPa)	.241	.028	.577	8.629	.000
	RQD(%)	-.053	.012	-.215	-4.297	.000
	C (MPa)	-.088	.024	-.154	-3.683	.000
	E (Gpa)	-.100	.025	-.264	-4.047	.000
	V	-.024	.024	-.071	-.982	.326
	Density (g/cm3)	3.097	.417	.328	7.434	.000
	Joint Angle (Deg.)	.126	.013	.395	9.521	.000
	Joint_Spacing(m)	-1.779	.237	-.293	-7.494	.000

a. Dependent Variable: PR (m/h)

$$PR = 0.818 - 0.008 * UCS + 0.241 * BTS - 0.053 * RQD - 0.088 * C - 0.1 * E - 0.024 * V + 3.097 * D + 0.126 * JA - 1.779 * JS \quad (1)$$

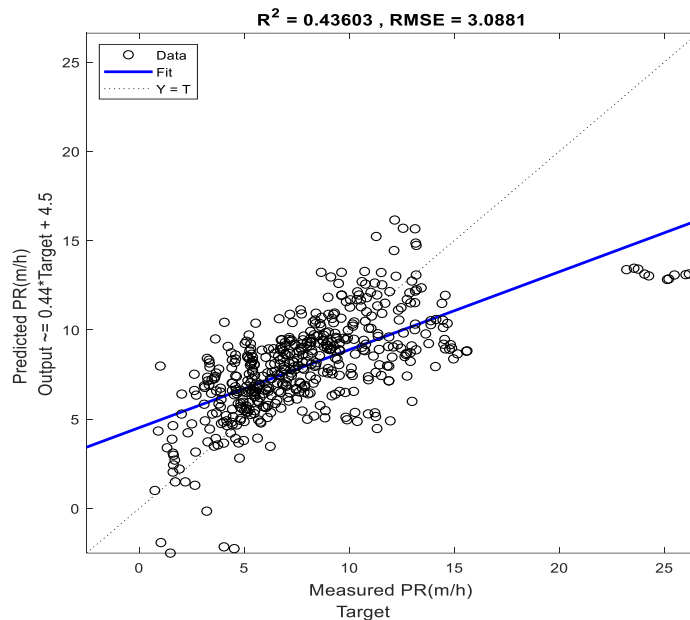


Fig. 1 – Dispersion diagram for five tunnels using linear regression model

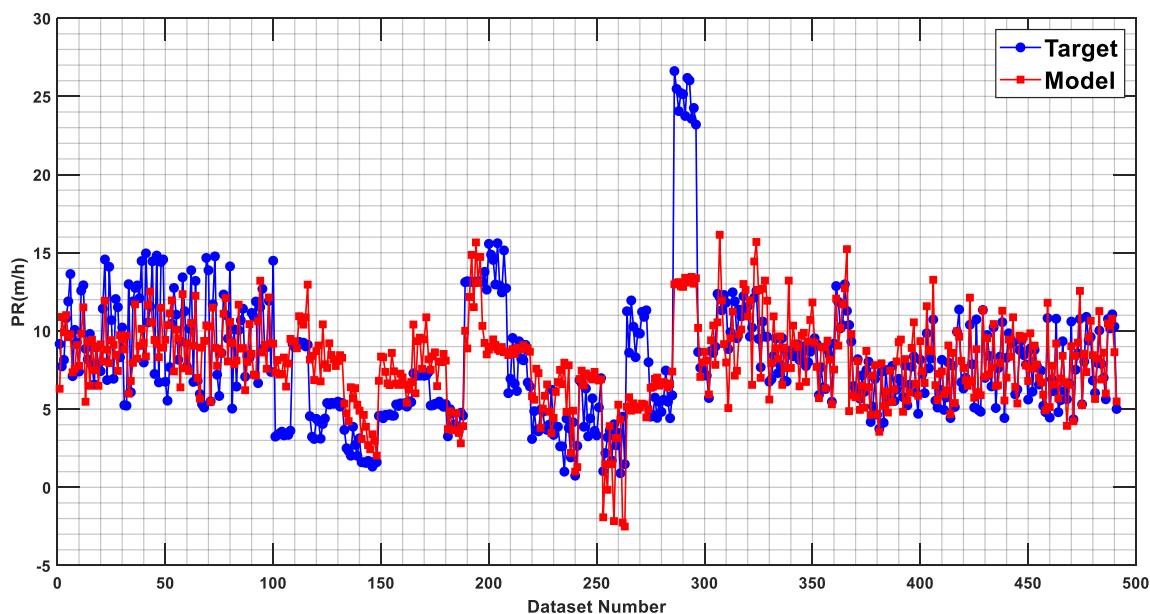


Fig. 2 – Coordination diagram for five tunnels using linear regression model

TBM penetration rate prediction in the five tunnels using nonlinear regression model

For predicting the penetration rate in the single tunnels, the assumptions used in the prediction were kept, and the related information of each five tunnels were merged. Table 8 represents the coefficient

of determination related to multivariate nonlinear regression modeling which is applied for the predicting TBM penetration rate in the five tunnels. Also, the values of regression coefficients related to the predictive modeling of the penetration rate in these five tunnels are shown in table 9. Furthermore, the nonlinear relationship, created by the coefficients, between the independent variables and the penetration rate are described in Equation 2. Additionally, the Dispersion diagram and Coordination diagram of the measured and the predicted values of penetration rate using the predictive modeling have been illustrated in figures 3 and 4, respectively.

Tab. 8 - The coefficient of determination of the nonlinear regression for predictive modeling of TBM penetration rate in the five tunnels

Model Summary

Model	R	R Square	Adjusted R Square	Std. Error of the Estimate
1	.827 ^a	.685	.679	2.32887

a. Predictors: (Constant), UCS(MPa)(cub), BTS(MPa)(cub), RQD (%) (exp), C(MPa)(inv), E(GPa) (quad), V(pow), Density(g/cm3) (cub), JA(Deg.) (cub), JS(m) (inv)

Tab. 9 - Coefficients of nonlinear regression for predictive modeling of penetration rate in the five tunnels

Coefficients^a

Model		Unstandardized Coefficients		Standardized Coefficients	t	Sig.
		B	Std. Error	Beta		
1	(Constant)	-24.746	2.607		-9.494	.000
	UCS(MPa)(cub)	.598	.043	.386	13.779	.000
	BTS(MPa)(cub)	-.096	.035	-.096	-2.723	.007
	RQD(%) (exp)	.506	.130	.129	3.904	.000
	C(MPa)(inv)	.683	.099	.217	6.869	.000
	E(GPa) (quad)	-.150	.112	-.039	-1.337	.182
	V(pow)	.838	.192	.157	4.368	.000
	Density(g/cm3) (cub)	1.067	.143	.240	7.441	.000
	JA(Deg.) (cub)	.079	.011	.237	7.388	.000
	JS(m) (inv)	.659	.053	.380	12.373	.000

a. Dependent Variable: PR (m/h)

$$\begin{aligned}
 PR = & -39.9 + 0.29UCS - 0.004UCS^2 + 0.066BTS \\
 & - 0.04BTS^2 + 0.0001BTS^3 + 5.51e^{-0.009RQD} + \frac{1.14}{C} + 0.04E \\
 & - 0.0009E^2 + 5.64e^{0.008V} + 28.16D - 11.47D^2 + 1.58D^3 \\
 & - 0.05JA + 0.001JA^2 + \frac{0.274}{JS}
 \end{aligned}
 \tag{2}$$

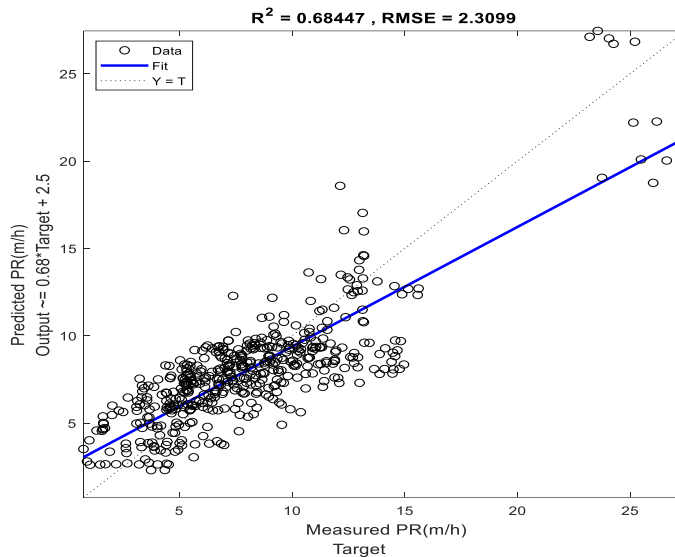


Fig. 3– Dispersion diagram for five tunnels using nonlinear regression model

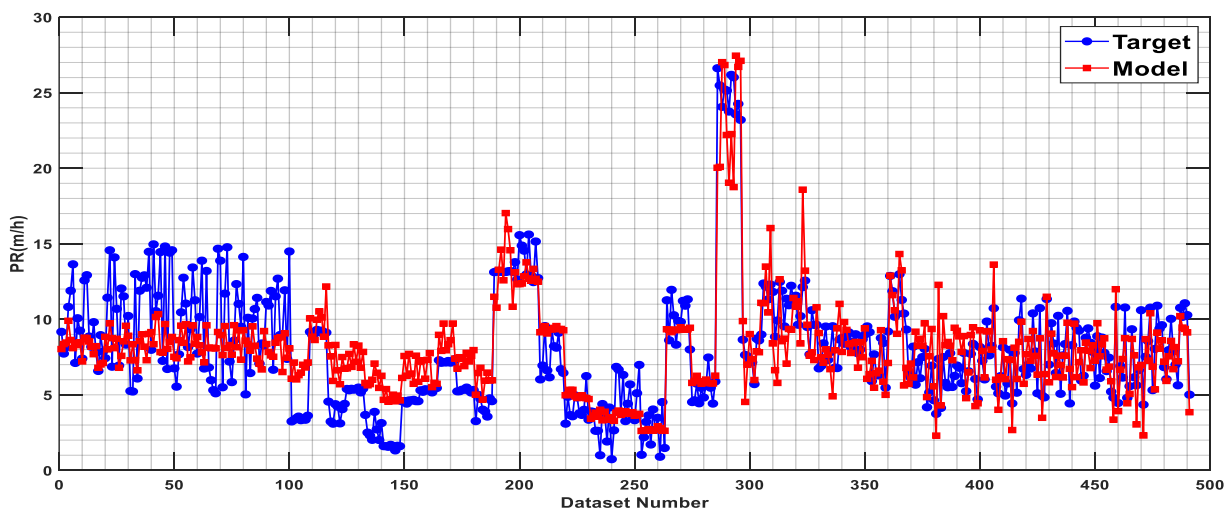


Fig. 4– Coordination diagram for five tunnels using nonlinear regression model

Prediction of TBM penetration rate in the five tunnels using Gene Expression Programming (GEP) method

To predict the TBM penetration rate related to the single tunnels, all the assumptions used in the predictive models were kept, and the data of each five tunnels were merged. Figure 5 shows R^2 , RMSE and Dispersion diagram related to Gene Expression Programming (GEP) which are used to predict TBM penetration rate in the five tunnels. Besides, Coordination diagram of the measured and predicted values of penetration rate using GEP predictive modeling have been represented in Figure 6. Binary expression tree of predictive modeling of the penetration rate in the tunnels, created by GEP model, between the input

variables and penetration rate have been illustrated in Figure 7. Also, the equation of GEP model is described in Equation 3.

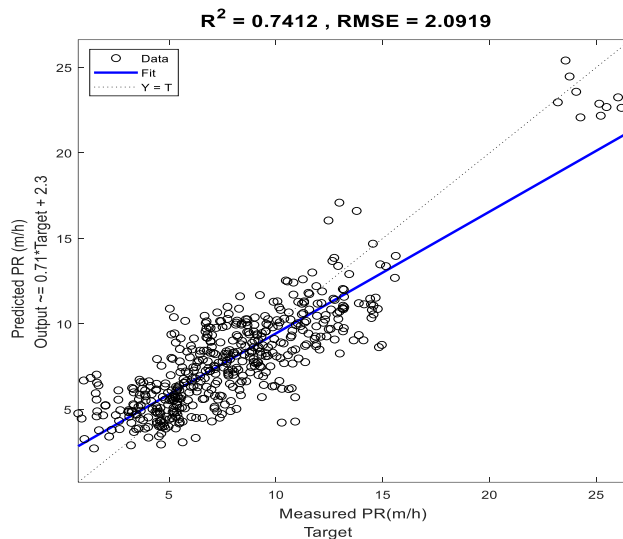


Fig. 5 – Dispersion diagram for five tunnels using GEP model

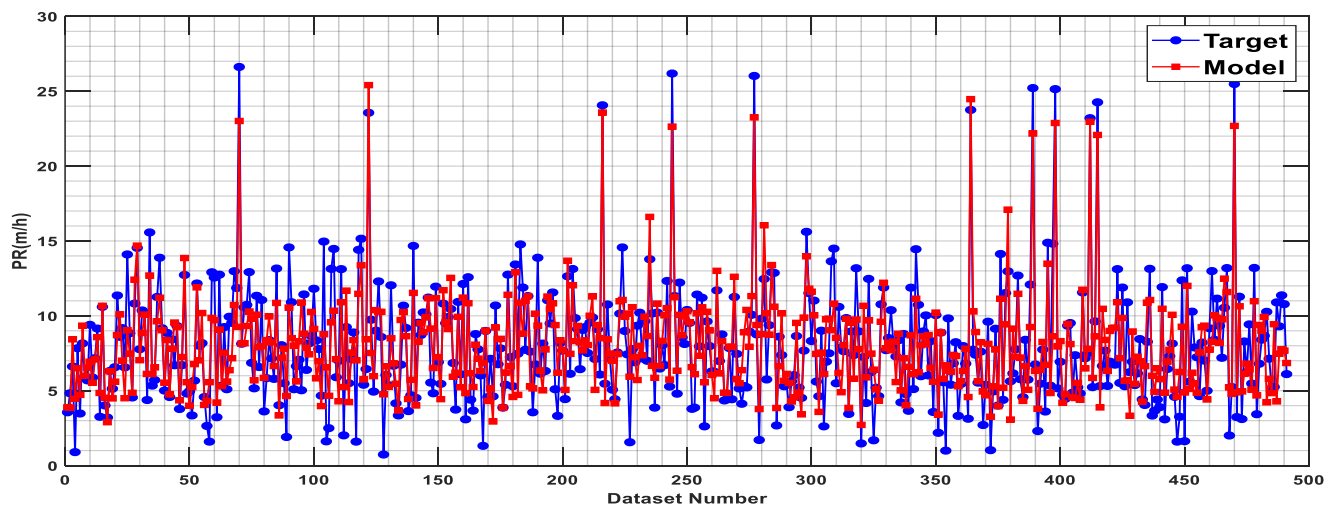
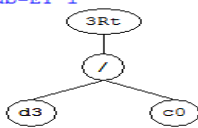


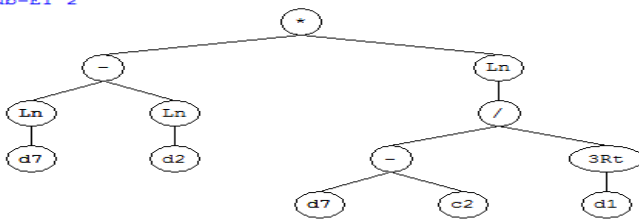
Fig. 6 – Coordination diagram for five tunnels using GEP model

$$\begin{aligned}
 ET1 &= \sqrt[3]{\frac{C}{0.69}} \\
 ET2 &= (\ln(JA) - \ln(RQD)) * \ln\left(\frac{JA - 2.8}{\sqrt[3]{BTS}}\right) \\
 ET3 &= \sqrt{\frac{BTS + D}{JS + v}} - \frac{JA}{(-7.73C) - \sqrt{BTS}} \\
 ET4 &= \frac{-3.84}{C^3 - \ln(JS) - 0.51 + \ln(JS + D)}
 \end{aligned}
 \tag{3}$$

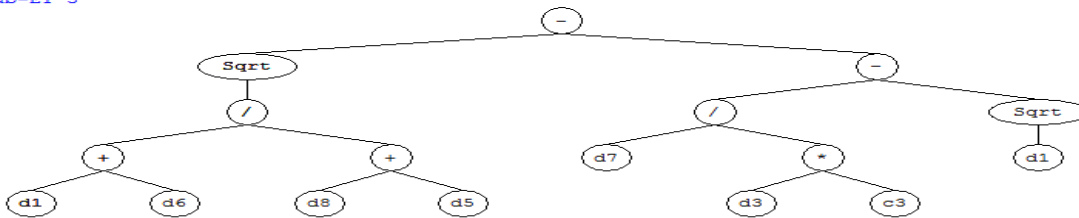
Sub-ET 1



Sub-ET 2



Sub-ET 3



Sub-ET 4

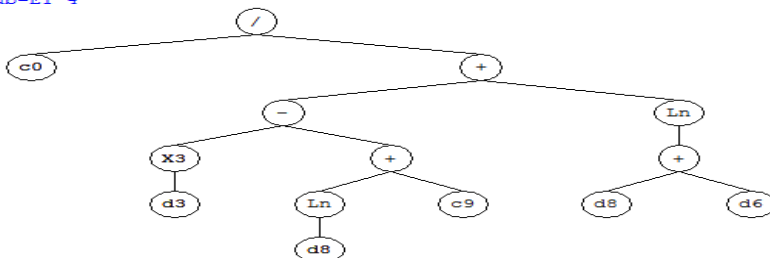


Fig. 7 – Binary expression tree of predictive modeling of the penetration rate using GEP model in the five tunnels

Prediction of penetration rate in Sabzkooh water conveyance tunnel using Support Vector Machine (SVM) method

In order to predict the TBM penetration rate for the single tunnels, the assumptions used in the prediction were kept, and the data of each five tunnels were merged. R^2 , RMSE and Dispersion diagram relating Support Vector Machine (SVM) model have been presented in figure 8. They were used to predict TBM penetration rate in the five tunnels. This figure indicated a fitting line between the measured values and the best fitting curve ($y=x$). As can be seen in figure 8, most of the predicted and measured values except some points were fitted on the bisection line, which implied the equality of the measured and predicted values based on the line $y=x$. Moreover, figure 9 presented the Coordination diagram of the measured and predicted values of penetration rate using the SVM method.

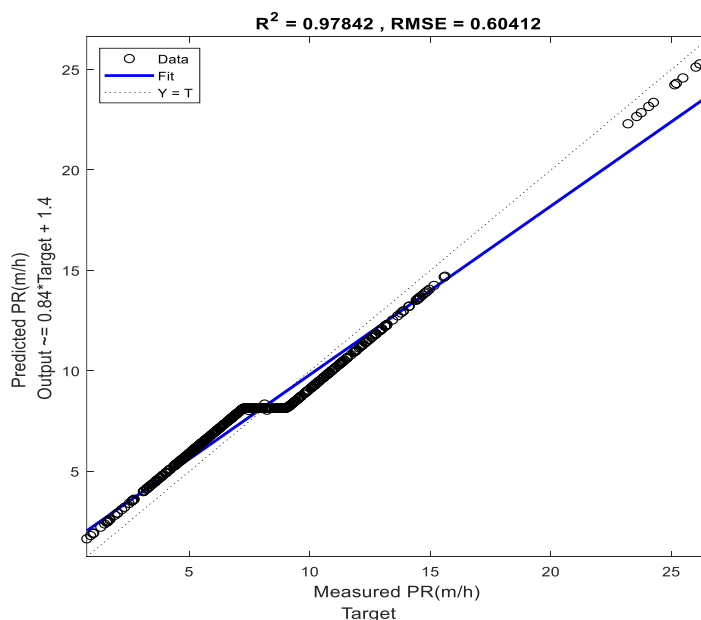


Fig. 8 – Dispersion diagram for five tunnels using SVM model

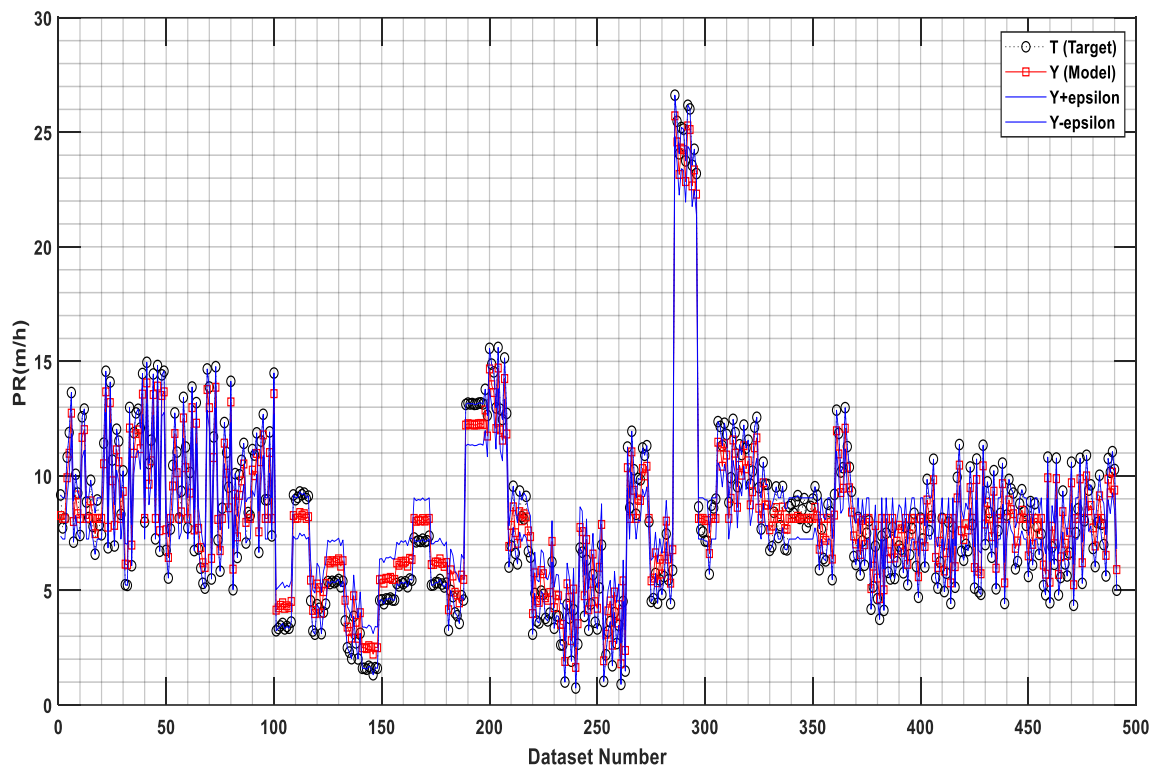


Fig. 9 – Coordination diagram for five tunnels using SVM model

CONCLUSION

Over the past three decades, many models have been proposed to predict the performance TBM based on theoretical and empirical research. All of these models are intended to accurately estimate TBM penetration rate and how the rock mass interacts with the specifications of TBM. In a realistic model, rock mass characteristics and TBM specifications must be considered to evaluate TBM performance. One of the significant parts of every tunnelling project is related to the study of TBM performance which plays a key role in selecting the method and TBM. Hence, a feasibility study of predicting TBM penetration rate using effective parameters was carried out. In order to predict TBM penetration rate, several methods including multiple linear and nonlinear regression analysis, GEP and SVM have been utilized. As a result, to achieve an acceptable relationship, nine effective parameters including field data and machine parameters were considered as the independent variables, and TBM penetration rate (PR) has been assumed as the dependent variable. Also, a linear or nonlinear relationship between the independent variables and TBM penetration rate was obtained. In this paper, R^2 and RMSE have been applied to estimate the accuracy and the efficiency of the predictive modeling of TBM penetration rate. The obtained values of R^2 and RMSE included 0.43 and 3.08 for linear regression, 0.68 and 2.3 for nonlinear regression, 0.74 and 2.09 for GEP method and 0.97 and 0.6 for SVM method, respectively. The results indicated that in most cases, Gene Expression Programming (GEP) method had higher accuracy and efficiency (in terms of R^2) and RMSE) than the multivariate linear and nonlinear regression in predicting TBM penetration rate. It was remarkable

to note that Gene Expression Programming (GEP) method required a basic knowledge to realize the concept of this method and the capability of interpreting specific outputs compared to the linear and nonlinear regression techniques. The analyses represented that the Support Vector Machine (SVM) method showed better performance (in terms of R^2) and RMSE) with regard to the other techniques (linear and nonlinear regression method and GEP algorithm). In addition, the maximum amount of R^2 and the minimum amount of RMSE were allocated to the SVM method among all predictive modeling.

REFERENCES

- [1] Bruland, A., 2000. Hard rock tunnel boring: advance rate and cutter wear. The Norwegian Institute of Technology, Trondheim, Norway. <https://doi.org/10.13140/2.1.3050.3204>
- [2] Sapigni, M., Berti, M., Bethaz, E., Busillo, A., Cardone, G., 2002. TBM performance estimation using rock mass classifications. *International Journal of Rock Mechanics and Mining Sciences*, 39(6):771–788, [https://doi.org/10.1016/S1365-1609\(02\)00069-2](https://doi.org/10.1016/S1365-1609(02)00069-2)
- [3] Benardos, A.G., Kaliampakos, D.C., 2004. Modelling TBM performance with artificial networks. *Tunnelling and Underground Space Technology*, 19:597–605, <https://doi.org/10.1016/j.tust.2004.02.128>
- [4] Ribacchi, R., Lembo Fazio, A., 2005. Influence of rock mass parameters on the performance of a TBM in a Gneissic Formation (Varzo Tunnel). *Rock Mechanics and Rock Engineering*, 38(2):105–127, <https://doi.org/10.1007/s00603-004-0032-5>
- [5] Zhao, Z., Gong, Q.M, Zhang, Y., Zhao, J., 2007. Prediction model of tunnel boring machine performance by ensemble neural networks. *Geomechanics and Geoengineering*, 2:123–128, <https://doi.org/10.1080/17486020701377140>
- [6] Gong, Q.M., Zhao, J., 2009. Development of a rock mass characteristics model for TBM penetration rate prediction. *International Journal of Rock Mechanics and Mining Sciences*, 46(1):8–18, <https://doi.org/10.1016/j.ijrmms.2008.03.003>
- [7] Hamidi, J.K., Shahriar, K., Rezai, B., Rostami, J., 2010. Performance prediction of hard rock TBM using Rock Mass Rating (RMR) System. *Tunnelling and Underground Space Technology*, 25(4):333–345, <https://doi.org/10.1016/j.tust.2010.01.008>
- [8] Gholamnejad, J., Tayarani, N., 2010. Application of artificial networks to the prediction of tunnel boring machine penetration rate. *Mining Science and Technology*, 20(5):727–733, [https://doi.org/10.1016/S1674-5264\(09\)60271-4](https://doi.org/10.1016/S1674-5264(09)60271-4)
- [9] Yagiz, S., Karahan, H., 2011. Prediction of hard rock TBM penetration rate using particle swarm optimization. *International Journal of Rock Mechanics and Mining Sciences*, 48(3):427–433, <https://doi.org/10.1016/j.ijrmms.2011.02.013>
- [10] Cheraghi seifabad, M., 2013. Engineering geology of ghomroud tunnel with emphasis on water inflow-a case study, *Electronic Journal of Geotechnical Engineering*, 18:45-54.
- [11] Sadeghi, M. Narimani, R., 2016. Using In situ penetration tests to improve the performance of TBM in long tunnels-Case study of Golab water transfer Tunnel, Conference Paper.
- [12] Hassanpour, J., Rostami, J., Khomehchiyan, M., Bruland, A., Tavakoli, H. R., 2010. TBM Performance Analysis in Pyroclastic Rocks: A Case History of Karaj Water Conveyance Tunnel. *Rock Mechanics and Rock Engineering*, 43(4):427–445 <https://doi.org/10.1007/s00603-009-0060-2>.
- [13] Fahimdanesh, Sh., HafeziMoghaddas, N., 2014. Tunneling machine selection model based on geologic parameters using ahp method. *Indian Journal of Scientific Research*, 9 (1): 137-145. <https://doi.org/10.5958/2250-0138.2014.00022.4>
- [14] Talary, G.A., Rahimi, E., Abbasi, M., 2016. Seismotectonics and earthquake risk analysis in the area of Sabzkooh-Choqakhor water conveyance tunnel. Thirty-fourth gathering and second international congress of geosciences.
- [15] Wang, S., Zheng, L. and Dai, J., (2014). Empirical Likelihood Diagnosis of Modal Linear Regression Models. *Journal of Applied Mathematics and Physics*, 2(10): 948-952, <https://doi.org/10.4236/jamp.2014.210107>.
- [16] Brimacombe, M., 2016. Local Curvature and Centering Effects in Nonlinear Regression Models. *Open Journal of Statistics*, 6(1): 76-84. <https://doi.org/10.4236/ojs.2016.61010>.

- [17] Ferreira, C., 2002. Gene Expression Programming in Problem Solving. In: Roy R., Köppen M., Ovaska S., Furuhashi T., Hoffmann F. (eds) *Soft Computing and Industry*. Springer, London. https://doi.org/10.1007/978-1-4471-0123-9_54
- [18] Vapnik, V., 1995. *The nature of statistical learning theory*, Springer, New York, <https://doi.org/10.1007/978-1-4757-3264-1>.
- [19] Vapnik, V., (1998). *Statistical learning theory*, Wiley, New York.
- [20] Afradi, A., Ebrahimabadi, A., Hallajian, T., 2019. Prediction of the Penetration Rate and Number of Consumed Disc Cutters of Tunnel Boring Machines (TBMs) Using Artificial Neural Network (ANN) and Support Vector Machine (SVM)-Case Study: Beheshtabad Water Conveyance Tunnel in Iran. *Asian Journal of Water, Environment and Pollution*, 16 (1): 49-57. <https://doi.org/10.3233/AJW190006>.
- [21] Afradi, A., Ebrahimabadi, A., Hallajian, T., 2020. Prediction of TBM Penetration Rate Using Support Vector Machine. *Geosaberes*, 11:467 - 479. <https://doi.org/10.26895/geosaberes.v11i0.1048>
- [22] Afradi, A., Ebrahimabadi, A., Hallajian, T., 2020. Prediction of tunnel boring machine penetration rate using ant colony optimization, bee colony optimization and the particle swarm optimization, case study: Sabzkooh water conveyance tunnel. *Mining of Mineral Deposits*, 14(2):75-84. <https://doi.org/10.33271/mining14.02.075>

SEISMIC DAMAGE FIELD OBSERVATION AND VULNERABILITY ANALYSIS OF MULTILAYER REINFORCED CONCRETE FRAME STRUCTURE

Siqi Li^{1,2}, Tianlai Yu^{1} and Jianqiang Yu¹*

1. Northeast Forestry University, School of Civil Engineering, Harbin 150040, China; 79654127@qq.com, tianlaiyu@126.com, 31017548@qq.com
2. The Open University of Harbin, No. 259, Yiman Street, Harbin City, China

ABSTRACT

To research the seismic damage characteristics, mechanism and vulnerability of multi-storey reinforced concrete (RC) frame structures, statistics and analysis, were made on 930 RC frame structures in Dujiangyan during Wenchuan earthquake, China. Firstly, seismic damage of RC frame structure in Dujiangyan is investigated comprehensively. According to the investigation results, easily damaged locations of this kind of structural system are: infilled wall, frame column, beam-column, joints and stairs. However, a large number of RC frame structures are basically intact or slightly damaged. By using the method of numerical statistical analysis, the non-linear relationship model and the fitting curve of seismic damage investigation samples under multiple seismic damage grades are given. Considering the number of stories, multiple ages and seismic fortification influencing factors, the empirical seismic damage situation of structures under each factor is analyzed, and the non-linear regression curve is developed. The empirical seismic vulnerability matrix and continuous regression function model and curve of RC frame structure in multi-intensity region are established. A calculation model of mean seismic damage index (MSDI) is proposed, and the vulnerability matrix and regression curve based on this parameter are given in combination with the empirical seismic damage investigation data. The above research results can provide a basic reference for vulnerability analysis and intensity scale revision of RC structures.

KEYWORDS

RC frame structure, Seismic damage field observation, Vulnerability analysis, Mean damage seismic index (MDSI), Seismic intensity

INTRODUCTION

On May 12, 2008, at 14:28:4, Ms8.0 earthquake occurred in Wenchuan County, Sichuan Province, China. The instrument epicentre was located in Baihua Town, Wenchuan County, Aba Prefecture. The seismographs fault was located in the Longmenshan fault. The macro epicentre was located in Yingxiu Town, with a focal depth of 14km. The absolute disaster area reached 100,000 square kilometers. Earthquakes were felt in Southern China, Japan, Thailand and the Philippines [1]. Tsinghua University, etc. [1], has carried on the investigation of earthquake damage to RC frame structure, analyzed the damage characteristics of non-structural components such as enclosure structure and infilled wall. The causes of serious damage caused by poor construction quality and complicated structure layout are analyzed, and the seismic measures to improve the structure are put forward. Li Hongnan et al. [2], carried out on-site seismic damage observation on

engineering geology seismic damage, structural earthquake damage and lifeline project seismic damage. Three main damage characteristics of RC frame structure were given. Sun Baitao et al. [3], analyzed the damage characteristics and causes of multiple types of structures in Wenchuan earthquake, field investigated 5000 structural damage samples, and gave the failure characteristics of RC structures mainly in the maintenance structure, the junction of filling walls and beams and columns. Li et al. [4], through investigating and analyzing multiple typical seismic damaged structures in Wenchuan earthquake, the failure characteristics and causes of typical structures are given. Li et al. [5], Combined with 2178 bottom frame seismic wall structures in Dujiangyan City, conducted seismic damage investigation and analysis, and gave typical failure characteristics of this type of structure.

Manfredi. et al. [6], damage characteristics of RC frame structures in Emilia earthquake in Italy in 2012 are analyzed, and the intensity evaluation and vulnerability analysis of RC frame structures are carried out by using EMS-98 intensity scale. Westenenk.et al. [7], the damage analysis of frame shear wall structure in the 2010 Concepción earthquake in Chi Chi was carried out, and the failure proportions of the structure under N-S and E-W ground motions were given. Lin. et al. [8], the site investigation of the structural damage in Lushan earthquake in 2014 was carried out. The damage investigation pictures of column foot, joint, short column and masonry wall of RC frame structure were given. The acceleration time history curve was given based on the actual ground motion parameters. Maeda.et al. [9], combined with the seismic damage survey data from north-eastern Japan in 2011, carried out in-depth research. Considering the instrumental intensity theory, the acceleration time history curve and the acceleration response spectrum curve of 5% damping are given by using the ground motion parameters measured by different stations, and the vulnerability relationship between the seismic damage parameters and the seismic damage grade is established. Eleftheriadou.et al [10], collected the data of structural seismic damage investigation in southern Europe, established the vulnerability matrix based on 178578 buildings, calculated and gave the relative and cumulative frequency of each structural type and damage grade according to the damage ratio, obtained the vulnerability probability matrix (DPM) of RC frame structure, masonry structure and other typical structures.

In the field investigation, it is not comprehensive to select only some discrete survey points for structural seismic damage analysis and vulnerability study. In order to comprehend more accurately and comprehensively the damage characteristics of RC structures in a multi-intensity region, a vulnerability matrix based on empirical seismic damage is established and a typical region is selected. It is necessary to conduct comprehensive seismic damage investigation.

FIELD OBSERVATION OF RC FRAME STRUCTURE

According to the analysis of the results of seismic damage investigation of RC frame structure in Dujiangyan city, this kind of structure is extensively used because of its flexible layout, easy to take large bays, strong practicability and mature construction technology. Therefore, the author and the relevant seismic damage investigators carried out a detailed investigation of the above vulnerable locations.

Failure of filled wall

The failure of infilled wall is the most prominent in the investigation of seismic damage of RC frame structure. In the lower intensity zone, the horizontal earthquake action destroys the connection of frame column, beam and infilled wall, produces horizontal and vertical cracks around the extended infilled wall, as shown in Figure1.

In higher intensity zone, X-shaped cross-inclined cracks or unidirectional inclined cracks appear in the filling wall due to the reciprocating effect of ground motions. This phenomenon is more obvious at the opening of the tunnel, as shown in Figure 2. When the seismic parameters reach the peak value, the infilled walls absorb a lot of energy, and even collapse locally or wholly.

As shown in Figure 3, the main reason is the lack of effective tie with columns and beams. Plane instability occurs first under seismic action, which cannot well resist seismic action together with the main bearing members.



Fig. 1 – Cracks around filling wall

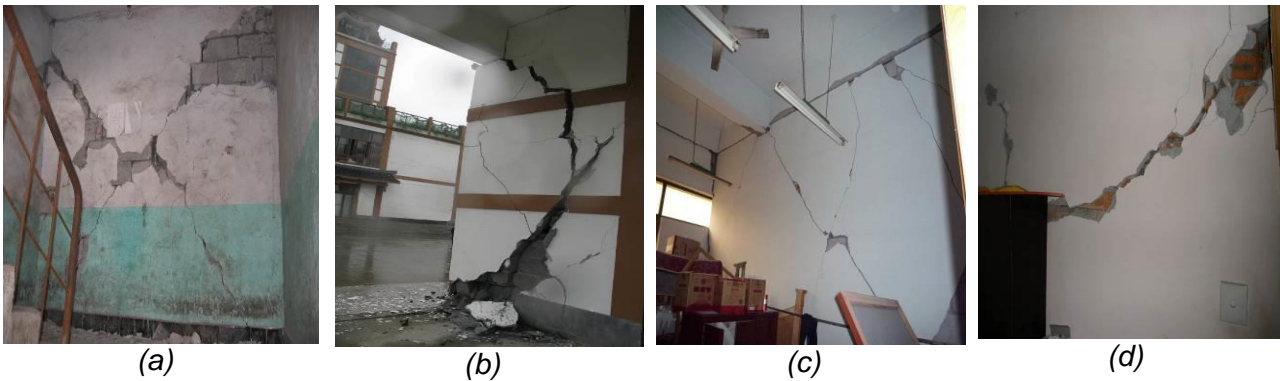


Fig. 2 – Filling wall cracks: (a) (b) (c) filling wall cross-oblique cracks; (d) opening unidirectional cracks



(a) Partial collapse of bottom filling wall

(b) Integral collapse of second-story filling wall

Fig. 3 – Filling wall collapse

However, from the analysis of the effect of the infilled wall, it has become the first seismic defence line of the whole RC frame structure to a certain extent, absorbed part of the vibration energy and played the role of energy dissipation and shock reduction. Therefore, the damage of the main structure has been delayed, especially in the higher intensity zone, which has played a role of protection for the principal structure in a certain sense. In seismic design, full consideration should be given to the anti-seismic effect of infilled walls to enable them to more accurately estimate the anti-seismic capacity of RC frame structures. The stiffness ratio between layers should be reasonably controlled to prevent damage caused by too weak bottom.

Failure of frame columns, beams and joints

Depending on the results of seismic damage investigation of RC frame structure in Dujiangyan city, the damage characteristics of beams, columns and joints are basically the same as those of Muisne in 2016 and Emilia in 2012. Damage of frame columns is more serious than that of beams. Because of the complex force on the top of the column, under the coupling action of shear force, bending moment and axial force, brittle failure of concrete at the end, longitudinal buckling of reinforcing bars, failure of stirrups, inclined cracks and yielding of longitudinal bars often occur. Due to improper setting of stirrups on the top of the column, most of them are 90 degree bending hooks [10], incongruity effectively cooperate with the longitudinal bars to resist earthquake, and the stirrups of the column are insufficiently allocated or anchored, resulting in damage. As shown in Figure 4. The phenomenon of "strong beam and weak column" appears. Considering the effect of floor space and distributed reinforcement, and the excessive reinforcement of the beam, it contributes to the beam to a certain extent, resulting in lighter damage of the beam than that of the column. However, also a few cases of negative bending moment near the end of the beam, which leads to shear failure at the end of the beam, as shown in Figure 5. Under the influence of reciprocating seismic excitation, the beam-column joints are in the state of shear-compression composite stress, the concrete at the top of the column is peeled off, the steel bar is bent and exposed, and the crack damage occurs at the end of the beam, as shown in Figure 6. The low ratio of stirrups at joints leads to brittle failure. The poor quality of concrete pouring constitutes one of the factors leading to joint failure due to the dense arrangement of reinforcement at joints. The mechanism of beam hinges and "strong columns and weak beams" should be studied in depth to ensure that the structure has sufficient shear resistance and ductility, to control the axial compression ratio of frame columns, to consider appropriate enlargement of the design cross-section size of the bottom frame columns, to ensure their strength, and to ensure that the stirrup spacing at the top of the columns is small enough to ensure that the bottom has sufficient overall stiffness.



Fig. 4 – Failure of frame beams and columns



Fig. 5 – Failure of frame beams end



Fig. 6 – Failure of joint

Staircase damage

The investigation found that staircase damage occurred in multi-intensity zones. Some outdoor staircase steps were broken into several sections, Steel bars were exposed and distorted and yielded, staircase platform beams and stirrups were broken. As shown in Figure 7, concrete was crissed and the protective layer was severely peeled off, staircase panels were broken, as shown in Figure 8, a large number of staircase walls were cracked and damaged, as shown in Figure 9. The function of stairs is not considered in the calculation and analysis of seismic system of RC frame structures, but the investigation of empirical seismic damage shows that stairs increase the lateral stiffness of structures to a certain extent and contribute to seismic resistance. Stairs and staircases are subjected to considerable shear force and bending moment under reciprocating earthquake action. Serious damage often occurs at the end of staircase beams, slabs, and the middle part of the span. Steel bars leak out, buckle, and concrete to crumble. The

seismic design of stairs in RC frame structures should be considered reasonable to effectively improve the overall connection with the main frame.



Fig. 7 – Fracture of stair platform beam



Fig. 8 – Stairboard midspan breakage and failure



Fig. 9 – Cracking of staircase wall

Structural collapse

In the investigation of seismic damage in high intensity regions, it was found that some RC frame structures without seismic design and poor construction quality had partial or overall collapse, which was more prominent in the Kashmir earthquake in Pakistan in 2005 and Simav earthquake in Turkey in 2011. The main reasons for the damage are that the structure layout is relatively complex. Some of these structures are generally located in township areas, built by the residents themselves, lack of formal design and construction supervision, random material selection and structural form, poor construction quality and high intensity regions, which to some extent aggravate the damage degree of the structure, such as Figure 10 shows. It is necessary to pay full attention to the seismic design of this kind of structure in township areas, and strictly follows the design specifications for construction in order to improve the quality of engineering structures.



(a) Partial collapse



(b) Ensemble collapse of bottom layer

Fig. 10 – Collapse failure

Basically intact

In the investigation of RC frame structures, most of the buildings suffer less seismic damage, even almost intact. Most of these structures are multi-storey RC frame structures in earthquake regions. Even in the high intensity region of XI degree, there is still quite a number of such structures which have been designed aseismic. The damage grade is slight damage or basically intact. According to seismic fortification of VII degree in Dujiangyan city, this kind of structure shows great aseismic potential, as shown in Figure 11.



Fig. 11 – RC frame structure after seismic design basically intact

FIELD OBSERVATION DATA ANALYSIS

The seismic damage investigation team conducted a total sampling survey of 8625 buildings in Dujiangyan city, and assessed the seismic damage grade of each building. The main structural types of the city: masonry structure (MS), bottom frame-seismic wall masonry structure (BFM), reinforced concrete frame structure (RC), single-storey concrete and brick workshop (SSB), and other types of buildings (OS). Figure 12 displays the number distribution of structural types in the city. According to the Chinese Seismic Intensity Scale (GB/T 17742-1999) and Appendix A1.2 of GB/T 1828.3-2000, the seismic damage grades of structures are classified into five criteria: destroyed (D5), severely damage (D4), moderately damage (D3), slightly damage (D2), and basically intact (D1). As shown in Table 1, seismic damage grades of structures are evaluated. In order to ensure that the records of seismic damage investigation more standard, the seismic damage grades are expressed by 51, 41, 42, 43, 31, 32, 33, 21 and 11, respectively. Due to the great difference of damage degree between D3 and D4 buildings, for better evaluation of the detailed seismic damage situation under the same seismic damage grade, the two grades are refined within their grades (31, 32, 33), (41, 42, 43), respectively. RC frame structure is widespread used in the developed and developing countries in the world, and the data are comprehensive. The number of seismic damage survey samples accounts for a certain proportion. In this paper, the seismic damage investigation and survey data of RC frame structures in multi-intensity regions are summarised and analysed.

Data statistics and numerical analysis

Statistical analysis of seismic damage of 930 RC frame structures in Dujiangyan City is carried out, as shown in Figure 13. Figure 14 shows the damage of proportional distribution of the structure under multiple seismic damage grades. 72% of the structures are in D1 and D2. Most of these buildings can be designed and constructed in accordance with the applicable chapters of the Code for Seismic Design of Buildings (GB50011-2001, GBJ11-89), showing good seismic performance. RC frame structures of D3, D4 and D5 are mostly self-built buildings without seismic design or are located in high intensity regions, and the seismic action is relatively large. Through program editing and analysis, the Polynomial cubic and Gaussian quadratic fitting curve of the non-linear model can continuously approximate the discrete points of RC frame structure samples, the R^2 value is above 0.98, therefore, we develop them as nonlinear vulnerability regression function models, two non-linear functional model, such as Formula (1) and (2), can be established to obtain the relationship between the seismic damage grade (R_D) and the number of seismic damage

investigation samples (N_D), among them, a, b, c, d, m_1, m_2 are the regression parameters of the model. In which R_D refers only to the 9 seismic damage grades defined in this section. According to the empirical seismic damage survey sample data, using the above two non-linear models for regression, the empirical functional model and its fitting curve based on the grade of seismic damage and the number of seismic damage samples in the region are obtained, as shown in Formula (3), (4) and Figure 15. The investigation team found that the number of stories, construction age and seismic fortification factors of RC frame structure have a significant impact on the structural damage.

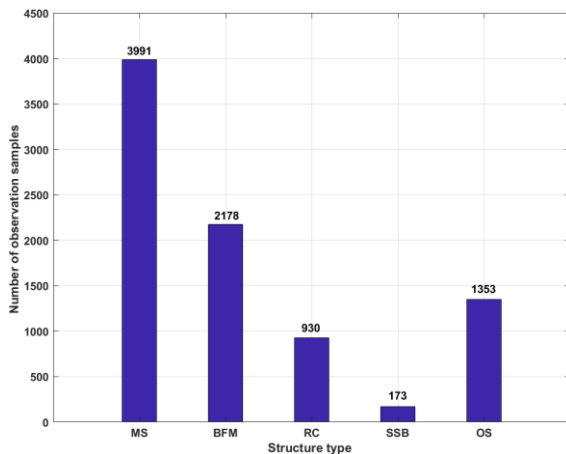


Fig. 12 – Quantity distribution of structural types in Dujiangyan city

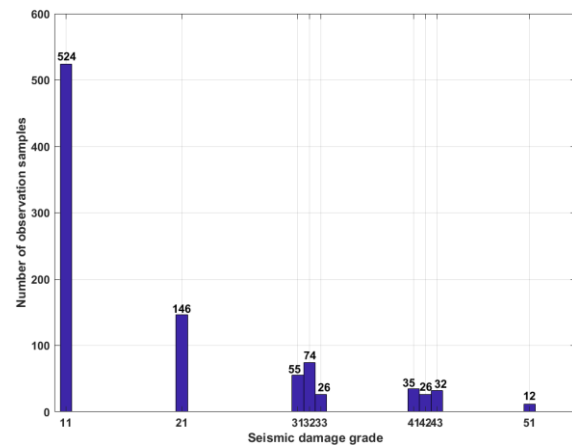


Fig. 13 – Statistical analysis of seismic damage of RC frame structure

Tab. 1: Quantification of provisions on seismic damage grades

Seismic damage grade	Quantitative description of provisions
D1	Bearing and non-bearing components intact, or individual non-bearing elements of slight damage, without repair can continue to use
D2	Individual bearing components have visible cracks and non-bearing components have obvious cracks. continue to use without repairs or minor repairs
D3	Most load-bearing components have slight cracks, some have obvious cracks, and individual non-load-bearing components are severely damaged, which can be used after general repair.
D4	Most of the load-bearing components are damaged seriously, and the non-load-bearing components collapse locally, so it is difficult to repair the buildings.
D5	Most of the load-bearing components were seriously damaged and the house structure was on the verge of fall or collapse.

$$N_D = aR_D^3 + bR_D^2 + cR_D + d \tag{1}$$

$$N_D = m_1 e^{-\frac{(R_D - n_1)^2}{p_1}} + m_2 e^{-\frac{(R_D - n_2)^2}{p_2}} \tag{2}$$

$$N_D = -0.0216R_D^3 + 2.55R_D^2 - 100R_D + 1340 \tag{3}$$

$$N_D = 1.166 \times 10^{17} e^{-\left(\frac{R_D + 492.5}{87.59}\right)^2} + 23.58 e^{-\left(\frac{R_D - 37.64}{15.81}\right)^2} \quad (4)$$

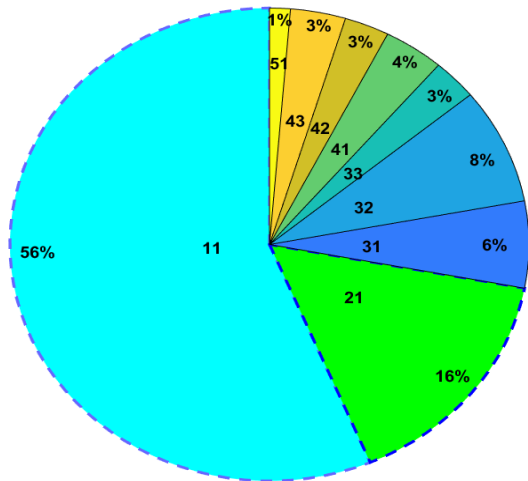


Fig. 14 – Proportion distribution of seismic damage grade of RC frame structure

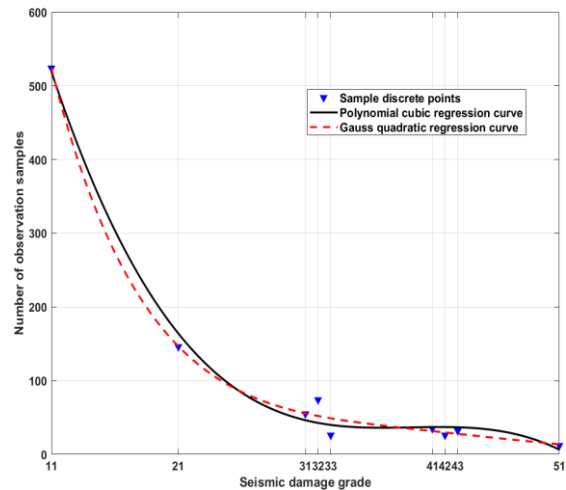


Fig. 15 – Nonlinear model curves of sample number and seismic damage grade

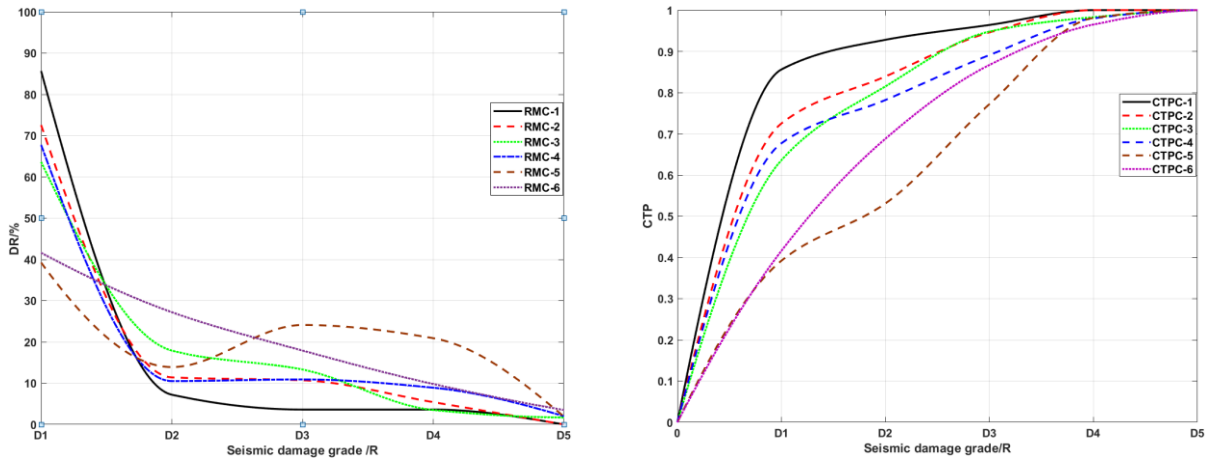
According to the visual inspection sample, the author carries on the statistical analysis separately. RC frame structure in this city, is mostly 6-storey and below buildings. Therefore, only 6-storey and below houses are analysed, which is representative to extent. A vulnerability matrix considering the floor number factor is established, as shown in Table 2. Figure 16 shows the damage ratio (DR) regression model curve (RMC) and cumulative transcendental probability curve (CTPC) of the structure considering story factor. The seismic damage of the first story RC frame structure is obviously lighter than that of other multi-story structures. On the overall trend, the damage grades of D3 and D4 increase with the increase of storeys. However, it is noteworthy that the seismic damage of a six-storey structure is weaker than that of five-storey, but more serious than that of other floor structures. Considering the sudden change of floor stiffness and the attenuation of ground motion, the mechanism of seismic damage is relatively complex, which should be paid attention to, and it is necessary to perform in-depth study.

Tab. 2 - Empirical seismic vulnerability matrix considering storey number factor (%)

Structural floor number	D1	D2	D3	D4	D5
1	85.6	7.2	3.6	3.6	0
2	72.5	11.4	10.7	5.4	0
3	63.6	17.9	13.3	3.5	1.7
4	67.7	10.5	10.9	8.9	2
5	39.2	13.9	24.1	20.9	1.9
6	41.6	27.2	17.9	9.8	3.5

The influence factors of multiple ages of RC frame structure on the seismic damage of the structure remarkable discrepancy. 905 samples (25 unknown age buildings were excluded from 930) are divided into RC frame structures built before 1990, 1991-2000 and after 2001 according to the years, the empirical seismic vulnerability matrices based on the above ages are established,

respectively, as shown in Table 3. Figure 17 shows the damage ratio and cumulative transcendental probability regression model curves considering the age-dependent factors, respectively. The RC frame structure constructed before 1990 has the greatest damage rate. With the increase of the years, the damage rate of the structure decreases obviously.

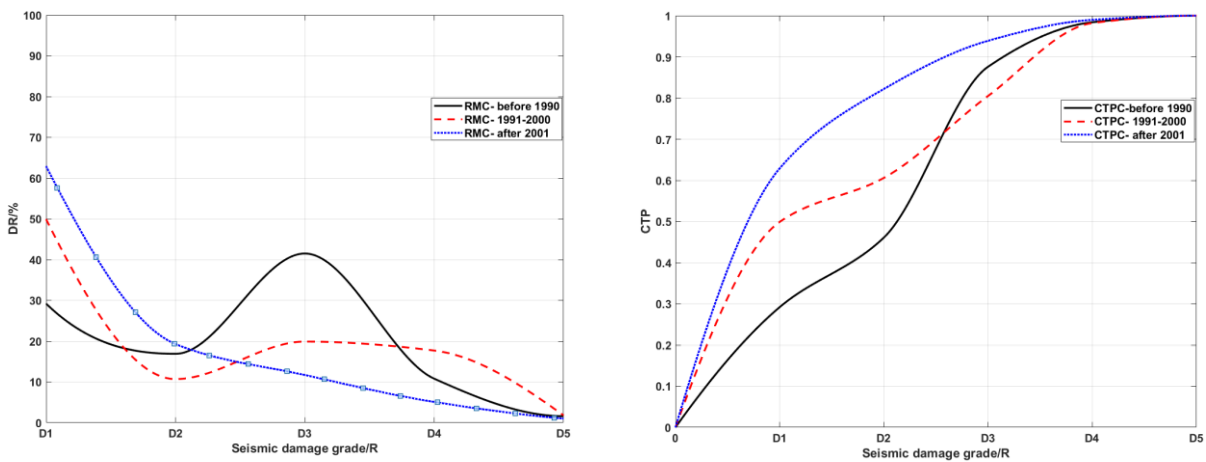


(a) Damage ratio regression model curve (b) Cumulative transcendental probability curve

Fig. 16 – Vulnerability curve considering floor factor

Tab. 3 - Empirical seismic vulnerability matrix considering chronological factor (%)

Age	D1	D2	D3	D4	D5
Before 1990	29.2	16.9	41.5	10.8	1.6
1999-2000	49.9	10.7	19.9	17.7	1.8
After 2001	62.9	19.3	11.7	5.1	1.0



(a) Damage ratio regression model curve (b) Cumulative transcendental probability curve

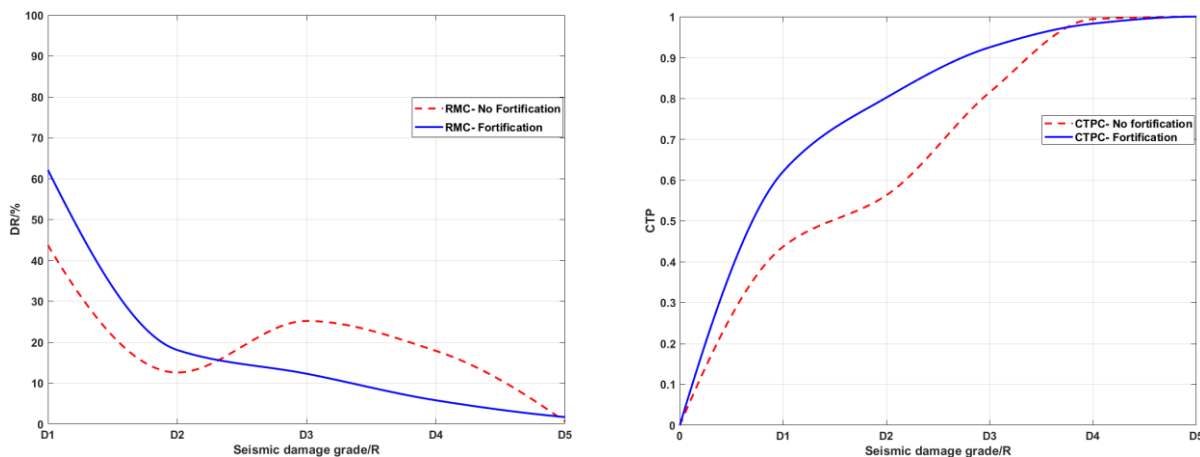
Fig. 17 – Vulnerability curve considering age factor

Whether the seismic fortification factor is taken into account in RC frame structures in the seismic damage investigation area has a relatively prominent impact on their damage. 904 buildings (26 buildings under reinforcement and construction are excluded from 930 samples) of the holistic field inspection sample are summarized, and the empirical regional seismic vulnerability

matrix based on this factor is established, as shown in Table 4. The numerical regression analysis is carried out and the curve of the non-linear regression model is given, as shown in Figure 18. The structure fortified according to the intensity of fortification in this zone is apparent superior to the structure constructed by township residents without considering seismic fortification. Most RC frame structures in the main urban area of Dujiangyan city can consider the impact of seismic factors on the structure. However, generous private buildings in towns and villages around the city, which do not consider the factors of seismic fortification, and bring about seriously damaged. The number of samples of RC frame structure D5 is scarce, so the regression curve is not remarkable for considering the difference of seismic fortification factors. To some extent, it also shows the seismic performance of RC frame structure in this huge earthquake.

Tab.4 - Empirical seismic vulnerability matrix considering seismic fortification factor (%)

Seismic fortification	D1	D2	D3	D4	D5
No fortification	43.7	12.6	25.2	17.9	0.6
fortification	62.1	18.1	12.3	5.8	1.7



(a) Damage ratio regression model curve (b) Cumulative transcendental probability curve

Fig. 18 – Vulnerability curve considering fortification factor

Vulnerability analysis of empirical seismic damage

Vulnerability of building structures refers to the probability of various degrees of damage when structures are subjected to multiple earthquake actions. Vulnerability analysis is also called earthquake damage prediction in some literature. Vulnerability analysis can be split into empirical statistical method, theoretical calculation method and simple method based on seismic code according to the characteristics of the methods used [11]. In this paper, empirical analysis method is utilized to analyse the masonry structure of Dujiangyan city. Sampling method for seismic damage investigation is to take all samples from this city. Vulnerability analysis is mainly based on vulnerability curve and vulnerability matrix, while vulnerability matrix research is relatively less due to the larger sample size. This paper evaluates all RC frame structural samples of Dujiangyan city by using the quantitative standard of structural seismic damage clause in China Seismic Intensity Scale (GB/T17742-1999). Combining with probability theory model, structural vulnerability is analysed. The empirical seismic damage matrix of the structure type is established, as shown in

Table 5, SIR in the table represents the seismic intensity region. Considering that controversy in the initial delimitation of seismic intensity, the seismic damage in the region of VI degree is also considered in the investigation of seismic damage, and the probability curve of empirical seismic vulnerability is given, as shown in Figure 19. Figure 20 shows the structural damage under different seismic damage levels in multiple intensity regions.

Seismic intensity and damage grade are given as discrete integers in the application of structural damage assessment. It is difficult to achieve a more meticulous evaluation of seismic intensity and structural damage in a certain zone. Reference [12] establishes the attenuation model of seismic intensity and displacement, magnitude and regression curve to realize the continuous evaluation of seismic intensity. In reference [13], a vulnerability matrix based on the actual damage survey data of Athens earthquake in Greece in 1999 is established. The non-linear model curves between ground motion parameters (actual peak acceleration and reference acceleration ratio) and collapse ratio are given, and the continuous relationship between discrete ground motion parameters and collapse ratio is established. A continuous model of seismic damage grade and intensity should be considered, the seismic damage samples of 930 RC frame structures distributed discretely in multi-intensity areas in the city are analysed numerically. The Exponential quadratic fitting model is determined. However, the dispersion and variance of VIII and IX degree regions larger, and the fitting degree flat. Therefore, Polynomial quadratic fitting model is selected to model in these two intensity regions, as shown in formula (5-6). In the formula P_I represents the empirical damage rate of seismic damage under different damage grades in the I intensity region, and R_D represents the seismic damage grade. $f, g, h, i, j, k, l, o, p$ represent regression parameter factors. Based on the regression analysis of the actual seismic damage survey data in the multi-intensity area, the parameter factors are determined, and the empirical vulnerability non-linear function model of the multi-intensity area in the city is established. As shown in Table 6 and Formula (7-12), the continuous distribution curve (CDC) is obtained, as shown in Figure 21. To a certain extent, the curve of the continuous model can realize the evaluation of the continuous seismic damage grade.

Tab.5 - Empirical seismic vulnerability matrix in multi-intensity regions (%)

SIR	D1	D2	D3	D4	D5
VI	89.2	9.7	1.1	0	0
VII	68.1	21.6	10.1	0.2	0
VIII	22.8	41	25.7	10.5	0
IX	9.8	15.1	21	42.6	11.5
X	6.2	8.1	12.4	21.8	51.5
XI	1.4	3.3	7.1	16.8	71.4

$$P_I = fe^{(gR_D)} + he^{(iR_D)} \tag{5}$$

$$P_I = jR_D^4 + kR_D^3 + lR_D^2 + oR_D + p \tag{6}$$

Tab.6 - Nonlinear continuous model of P_I and R_D in multi intensity zones

SIR	Continuous model of nonlinear function	
VI	$P_I = -0.01285e^{(0.2397R_D)} + 817.9e^{(-2.216R_D)}$	(7)
VII	$P_I = -0.03742e^{(0.7047R_D)} + 201.2e^{(-1.085R_D)}$	(8)
VIII	$P_I = -1.208R_D^4 + 17.68R_D^3 - 92.64R_D^2 + 190.5R_D - 91.5$	(9)
IX	$P_I = -3.479R_D^4 + 37.31R_D^3 - 136.6R_D^2 + 206R_D - 93.5$	(10)
X	$P_I = 4.603e^{(0.2573R_D)} + 0.03909e^{(1.358R_D)}$	(11)
XI	$P_I = 0.6716e^{(0.7849R_D)} + 1.816 \times 10^{-6} e^{(3.368R_D)}$	(12)

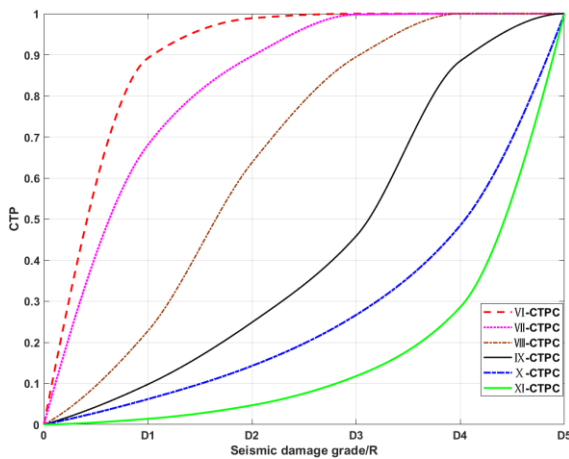


Fig. 19 – Vulnerability curve in multi-intensity regions

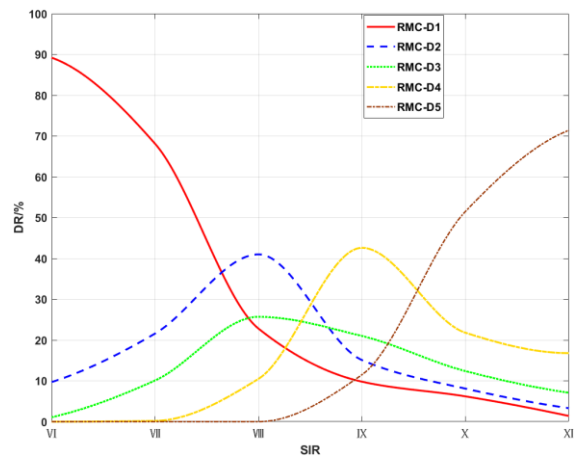


Fig. 20 – Seismic damage grades curve in multi-intensity regions

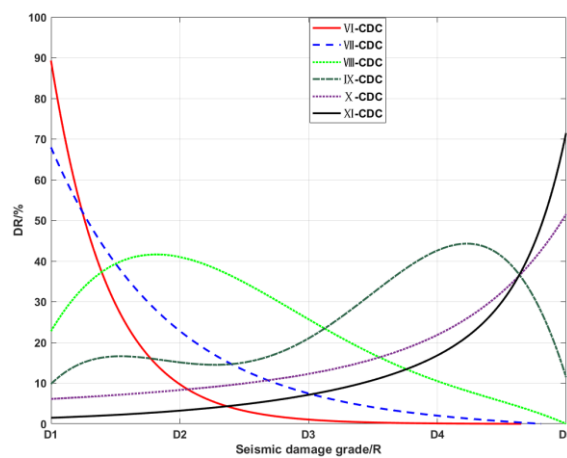


Fig. 21 – Continuous Model curve of Nonlinear Function n multi-intensity regions

Seismic damage index analysis

To evaluate the overall damage of typical structures in a certain region more accurately, the concept of seismic damage index is introduced. Considering structural displacement, energy dissipation, structural modal, stiffness and site factors, 0-1 is used as a quantitative index to express the degree of structural damage. Among them, 0 represents no damage or failure, and 1 represents complete damage or failure [14]. In reference [15], the seismic damage index interval is split into [1,7], which represents the seismic damage of structures in multiple intensity regions. Reference [16] uses EMS-98 intensity scale to carry out structural vulnerability analysis, defines the seismic damage index as [0,5], establishes a functional model between vulnerability ratio, intensity and displacement, and applies it to the seismic damage index analysis in multiple intensity regions.

According to the empirical situation of seismic damage in Dujiangyan city, the seismic damage index (d_i) used in this paper is a number between 0 and 1 to express the degree of seismic damage of structures from light to heavy [17]. The proportion of buildings damaged by earthquakes at all grades in empirical seismic damage investigation and the corresponding seismic damage index is calculated by a weighted average method. As shown in formula (13), the numerical value is called the mean seismic damage index (MSDI).

$$MSDI = \sum_{i=1}^5 d_i \cdot \eta_i \tag{13}$$

Tab.7 - Relationship between seismic damage grade and seismic damage index [14,17]

Damage grade	Median	d_i
D1	0.05	$0.00 \leq d_i < 0.10$
D2	0.20	$0.10 \leq d_i < 0.30$
D3	0.425	$0.30 \leq d_i < 0.55$
D4	0.70	$0.55 \leq d_i < 0.85$
D5	0.925	$0.85 \leq d_i \leq 1.00$

In the formula, the value of d_i is determined according to 5 seismic damage grades ($i = 1, 2, 3, 4, 5$) and the Chinese seismic intensity scale. As shown in Table 7, η_i represents the ratio of the number of damages in the i th seismic damage grade to the total number of samples for a certain type of structure in a specific intensity region. According to the MSDI model and the vulnerability matrix established by the empirical seismic damage investigation, the matrix model of formula (13) is analysed and the MSDI matrix model is obtained, as shown in formula (14-16) where η_{ji} is the quantity damage ratio of RC frame structure in the state of damage grade i , when the seismic intensity (SI) = j . $MSDI_j$ represents the d_i of a certain type of structure in i intensity region. By selecting the median and limit values of the d_i in Table 7 and combining with the empirical seismic damage matrix of RC frame structure, the vulnerability matrix of the structure based on the MSDI is given, as shown in Formula (17).

$$[MDI] = [d_i] \times [\eta_{ji}] \quad (14)$$

$$[MSDI] = \begin{bmatrix} d_1 \\ d_2 \\ \vdots \\ d_i \end{bmatrix} \times \begin{bmatrix} \eta_{61} & \eta_{62} & \cdots & \cdots & \eta_{6i} \\ \eta_{71} & \eta_{72} & \cdots & \cdots & \eta_{7i} \\ \eta_{81} & \eta_{82} & \cdots & \cdots & \eta_{8i} \\ \vdots & \vdots & \ddots & & \vdots \\ \eta_{j1} & \eta_{j2} & \cdots & \cdots & \eta_{ji} \end{bmatrix} \quad (15)$$

$$[MSDI] = \begin{bmatrix} MDI_6 \\ MDI_7 \\ MDI_8 \\ \vdots \\ MDI_j \end{bmatrix} \quad (16)$$

$$[MSDI] = \begin{bmatrix} 0.0687 \\ 0.1216 \\ 0.2761 \\ 0.5289 \\ 0.7010 \\ 0.8155 \end{bmatrix} \quad (17)$$

Figure 22 shows the regression curves of the MSDI in the multi-intensity region of the city. The empirical MSDI in the VI and IX regions is higher than the average values of D1 and D3 of d_i respectively, while the VII, VIII and IX regions are obviously lower than the slight damages and damages, and the MSDI in the X region is approximately equal to the average value of the d_i . The model analysis is basically consistent with the empirical observation damage investigation, which verifies the application value of the model to a certain extent.

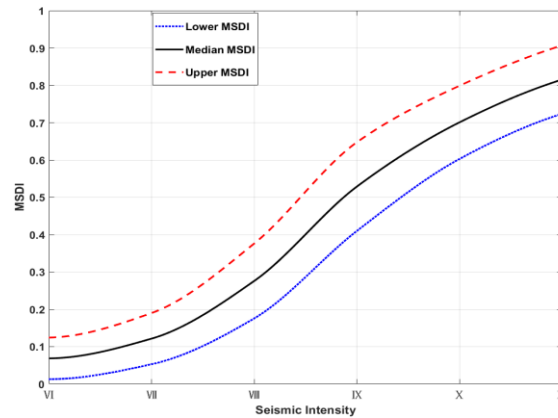


Fig. 22 – Regression curve of MSDI in multiple intensity regions

CONCLUSION

To examine the seismic damage and vulnerability of multi-storey RC frame structures in multi-intensity regions, this paper investigates 930 such buildings in Dujiangyan city, Wenchuan earthquake China, a typical seismic zone with multi-intensity and ground-spanning. Structural vulnerability analysis is deeply studied and the following main conclusions are drawn:

- (1) 930 RC frame structures in Dujiangyan City were investigated and analysed for seismic damage. Typical damage locations were cracking or collapse of filling walls, beam-column and joints of frames, staircases, and local collapse or floor seating of individual structures in the high intensity region. However, a large number of buildings that have been fortified according to VII, showing good seismic performance.

(2) Statistical analysis of RC frame structure survey samples is carried out, and the overall seismic damage proportional distribution of the structure is given. The non-linear fitting model between the seismic damage grade and the number of damage samples is obtained, and the regression analysis is performed with the empirical seismic damage investigation data. Considering the influence of floor number, age and seismic fortification factors on structural damage, the vulnerability matrices of different factors are established, and the regression analysis curves are given. The vulnerability matrix based on the empirical seismic damage characteristics of Dujiangyan city is established. A theoretical method of continuous function non-linear model is advanced. Continuous non-linear relationship is established between diverse seismic intensity, multiple damage grade and failure ratio, and curve models are given, respectively.

(3) Applying the theory of SDI analysis, combining the empirical seismic damage vulnerability matrix of the multi-intensity regions of the city and the Chinese seismic intensity scale (GB/T 17742-1999), a matrix model based on the MSDI is proposed. The MSDI matrix of RC frame structure in the multi-intensity regions is obtained by using the vulnerability matrix of the zone for model analysis and calculation, and the regression curve of the MSDI is bestowed. Lines to verify the applicability of the matrix model.

ACKNOWLEDGEMENTS

The basic data used in this paper are from the Dujiangyan city seismic damage field observation team of the Institute of Engineering Mechanics (IEM), CEA. The results of this investigation are greatly appreciated by more than 30 scientific research workers from universities and research institutes in China who have been investigating the structural damage of Dujiangyan city in the past two months.

REFERENCES

- [1] Civil and Structural Groups of TSING Hua University., Xi Nan Jiao Tong University., Bei Jing Jiao Tong University., 2008. Analysis on seismic damage of buildings in the Wen chuan earthquake. *Journal of building structures*, vol. 29: 1-9.
- [2] Li H N, Xiao S Y, Huo L S., 2008. Damage investigation and analysis of engineering structures in the Wen chuan earthquake. *Journal of Building Structure*, vol. 29: 10-19.
- [3] Sun B T, Zhang G X., 2012. Statistical analysis of the seismic vulnerability of various types of structures in Wen chuan M8.0 earthquake. *China Civil Engineering Journal*, vol. 45: 26-30.
- [4] Li S Q, Yu T L, Chen Y.S., 2019. Comparative analysis of the empirical seismic vulnerability of typical structures in multiple intensity zones. *Archives of Civil Engineering*, vol. 65(3):167-183.
- [5] Li S Q, Yu T L, Jia J F., 2019. Investigation and analysis of empirical field seismic damage to bottom frame seismic wall masonry structure. *International Journal of Engineering Transactions B: Applications*, vol. 32(8):1082-1089.
- [6] Manfredi G, Prota A, Verderame G M, et al., 2014. 2012 Emilia earthquake, Italy: reinforced concrete buildings response. *Bulletin Earthquake Engineering*, vol. 12: 2275-2298.
- [7] Westenek B, Delallera J C, Jünemann R, et al., 2013. Analysis and interpretation of the seismic response of RC buildings in Concepción during the February 27, 2010, Chile earthquake. *Bulletin Earthquake Engineering*, vol. 11: 69-91.
- [8] Lin X C, Zhang H Y, Chen H F, et al., 2015. Field investigation on severely damaged aseismic buildings in 2014 Ludian earthquake. *Earthquake Engineering & Engineering Vibration*, vol. 14: 169-176.
- [9] Maeda M, Ai-washali H, Suzuki K, et al., 2012. Damage of RC building structures due to 2011 east Japan earthquake In: *Proceedings of the 2012 Structures Congress*. Chicago, 1023-1034.
- [10] Eleftheriadou A K, Karabinis A I., 2013. Evaluation of damage probability matrices from observational seismic damage data. *Earthquakes and Structures*, vol. 4: 299-324.

- [11] Li S Q, Chen Y S, and Yu T L. Comparison of macroseismic-intensity scales by considering empirical observation of structural seismic damage. *Earthquake Spectra*, 2020, DOI: 10.1177/8755293020944174.
- [12] Musson R M W., 2005 Intensity attenuation in the U.K. *Journal of Seismology*, vol. 9: 73-86.
- [13] Eleftheriadou A K, Karabinis A I. 2011 Development of damage probability matrices based on Greek earthquake damage data. *Earthquake Engineering and Engineering Vibration*, vol. 10: 129-141.
- [14] Li S.Q., and Chen Y.S., 2020. Analysis of the probability matrix model for the seismic damage vulnerability of empirical structures. *Natural Hazards*, 104(1):705-730.
- [15] Zobin V M., Ventura-ramírez F., Gutiérrez -andrade C L., et al., 2006 The Mw 7.4 Colima, Mexico, Earthquake of 21 January 2003: The Observed Damage Matrix in Colima City and its Comparison with the Damage Probability Matrix. *Natural Hazards*, vol. 38: 391-410.
- [16] Ferreira T M., Vicente R, Mendesdasilva J A R, et al. 2013 Seismic vulnerability assessment of historical urban centres: case study of the old city centre in Seixal, Portugal. *Bulletin Earthquake Engineering*, vol. 11: 1753-1773.
- [17] Li S Q, Yu T L, Zhang M., 2020. Vulnerability analysis of multi-storey RC frame structures in multi-intensity zone under empirical seismic damage. *Journal of Dalian University of Technology*. vol. 60(2):200-208.

DEVELOPMENT OF RURAL ARCHITECTURE – DESIGN AND CREATION OF A WEB DATABASE

Petr Soukup and Kryštof Sýkora

Czech Technical University in Prague, Faculty of Civil Engineering, Department of Geomatics, Prague, Thákurova 7/2077 166 29 Prague 6 Dejvice, Czech Republic; soukup@fsv.cvut.cz; krzysztof.sykora@gmail.com

ABSTRACT

The article deals with the design of database structures of a web application for the presentation of information about the development of rural architecture in the 19th and 20th centuries in the territory of today's Czech Republic. The processes of data structure design, description of the chosen solution and method of implementation are presented. The solution used is based on freely available technologies and applied to the creation of a smaller web portal. The described methods can be inspiring for similar types of web presentations, which are a frequent output of many activities and projects.

The created web application contains various types of data: maps of selected villages, spatial models of selected rural buildings, their floor plans, created orthophoto, photo gallery, and other textual and graphical information documenting the development of rural architecture. Objects of interest are located on the used interactive map. The application allows users to search and filter the required data. The technological solution is based on the PostgreSQL database and the PHP Nette framework. The created portal presents interesting information about important values of rural architecture, which can be considered as a part of the cultural heritage. The web portal can be used by experts and the general public.

KEYWORDS

Database, Data model, Web portal, Rural architecture

INTRODUCTION

Modern web portals provide users with a large amount of information that is stored in various data files and formats. The tool for effective management and analysis of differentiated and content-structured information is a geographic information system (GIS). It is based on a database that has effective tools for all necessary data operations (editing, backup, history tracking, secure access, etc.). An important aspect of the creation of every GIS application is the design of a suitable data structure of this database. The design of a suitable structure for a database of documents relating to the development of rural architecture is the subject of this article.

Development of rural architecture

The transformation of Czech rural architecture in the 19th and 20th centuries has been the subject of growing expert interest in recent years. This time period is specific for intense social and economic changes (e.g. industrialization, migration, the influence of the First and Second World Wars, population change by political intervention, central socialist planning, etc.), which were also reflected in the architectural development of the villages [1].

Experts from the Institute of Art History of the Czech Academy of Sciences (ÚDU), in cooperation with the Department of Geomatics, Faculty of Civil Engineering, CTU in Prague, are trying to contribute to the development of knowledge in this area. The subject of their research is

the development of urban planning of selected municipalities and art historical studies of selected houses in rural regions. The aim of the research is to map and promote the significant values of rural architecture and thus contribute to their preservation for future generations. The results of the research should also support the general debate on the need for more consistent monument protection of rural architecture, which would prevent the gradual devastation of its urban and stylish structure.

The changes in rural architecture that took place in the last two centuries are documented in many ways and forms. An important source of information about the development of rural localities are old maps, later black and white aerial survey photos, currently colour orthophotos. Historical drawings, later photographs, plans, results of geodetic surveying by various methods, possibly audio or video recordings, today also digital spatial models may be available for the study of important buildings. Across time and type of subject of interest, a number of verbal descriptions in the form of written or printed documents can be a valuable source of information.

In terms of building development, a total of 39 villages evenly distributed throughout the Czech Republic (three villages in each region) were processed within the mentioned research. In 13 of them (one in each region) detailed maps were prepared, clearly showing the built-up area development and the digital spatial models were made for 13 selected village buildings.

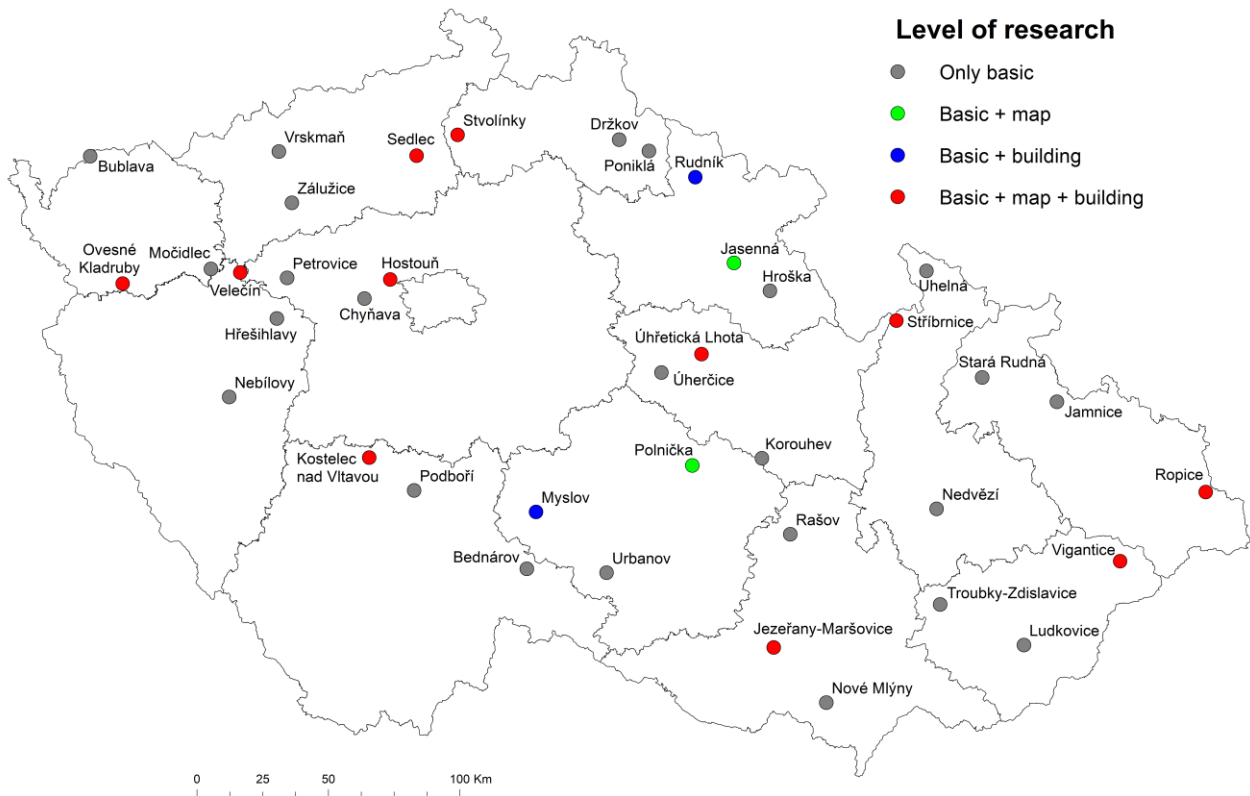


Fig. 1 – Location of selected villages and buildings

The selection of villages was made with regard to the historical significance of architecture. Locations that were so far outside the main interest of experts were selected for the research. Selected buildings represent characteristic historical buildings of the region, which have not yet been subjected to detailed architectural and historical research and show a high degree of originality. The location of selected villages and buildings is shown in Figure 1.

The built-up area development can also be monitored on archival aerial survey photos (LMS). Based on them, a set of orthophotos was created for three selected villages (Hostouň, Ropice, Držkov).

DATASETS

The collected and sorted material, as well as all processing results, must be systematically managed in a suitably selected system (database). An important element of the concept of such a system is an effectively designed structure, with respect to the type of data and the relationship between them. The following is an overview of the main data sets used and their brief characteristics.

Maps of built-up area development

The maps of built-up area development were created on the basis of detailed analyzes of archival and current maps [2] and they show the development of buildings in the period from the mid-19th century to the present. In the database, maps are stored in the PDF vector files (divided into thematic layers) and in the PNG raster files. All processed maps are presented interactively on the page <http://venkov.fsv.cvut.cz/projekt/vesnice.html>.

Spatial models

The modelling of all objects was based on data obtained by survey of objects [3]. A combination of geodetic and photogrammetric methods was used. The creation of the exteriors of the models was done in the form of vectorization of a point cloud; the interiors were modelled on the basis of the floor plans. The database stores models in the 3D PDF format and raster previews of models in the PNG format. All processed models are presented interactively on the page <http://venkov.fsv.cvut.cz/projekt/modely.html>.

Floor plans

For the geodetic survey of the ground floor plans of the modelled buildings, the method of constructional measures supplemented by cross measures was used. The floor plan drawings correspond to their real model geometrically and dimensionally with sufficient accuracy. It is therefore possible to determine control measures retrospectively, e.g. lengths and angles, between building structures that are not easily detectable in reality. The connection of the drawings to the state reference coordinate system was performed using current cadastral maps. In the database, floor plans are stored in the PDF format.

Orthophotos

Orthophotos were processed on the basis of archival aerial survey photos (LMS) and the current digital relief model (DMR 5G). A sufficient number of naturally signalled ground control points were used to make orthophotos, the coordinates of which were obtained from the current maps. The accuracy of the resulting orthophotos was verified at checkpoints and is in the interval 1 - 1.5 m according to the age and quality of the LMS used [4]. In the database, the created orthophotos are saved as TIF files with georeferencing in TFW files.

Other text and graphic documents

The database includes other various text and graphic files (articles, photographs, plans, sketches). In general, these materials can be divided into two groups according to the date of

origin: archival and contemporary. They are stored in the database in various formats depending on the type of data.

METHODS AND TECHNOLOGIES

Interactive websites presenting various documents can be based on many technologies. Simpler content can be effectively presented without the use of sophisticated database tools [5]. In current practice, still popular and much used systems based on the traditional relational database model (RDBMS) are used to manage a common documentation pool. These systems are mostly based on the client-server architecture, where the client communicates with the server component using the Structured Query Language (SQL).

The relational database model, as practice shows, is not ideal in all cases [6], [7]. For large amounts of data (so-called “big data”) or data that do not fit into the relational model due to their structure, database systems are used, which are in many respects more advantageous for the management of such data. These systems include so-called NoSQL (not-only SQL) databases [8], [9].

In addition to the efficiency of storing and modifying the content of documents, a key element in the design of the database is the ability to index their content for full-text search. Another important feature may be the ability to track changes in document content over time (similar to versioning systems). The choice of the used database system is essential for the long-term sustainability and extensibility of the proposed information system. The following text describes the design and implementation of a specific database, including the relevant web application.

Application design

The initial task was to create a database system with an appropriate web interface to facilitate the storage, sorting and representation of the data used. In this section, these tasks are looked at individually, with a strong accent on data presentation in the database design process.

The first order of business was to formulate an appropriate technical solution for the task at hand. The first task was to create a system that would suitably present a complex sets of data regarding to selected municipalities and buildings in the Czech Republic. First of all, detailed discussions about proper data presentations were conducted. Then a database model was devised. The initial data presentation was to create tables for each specific entity (such as buildings, municipalities, documents, maps, etc.), that would be linked together in a parent-child type of relationship. This way, all documents would correspond to a building, all buildings to municipality, those then to a district, and so forth.

After the principal guidelines were defined, the tasks moved to create a user interface. Several technologies to base the application on were considered. One of the primary options was the Java Spring framework coupled with a front end powered by such technologies as react.js. A more high-level language approach would make the applications design more robust and modular. In the end the PHP and Nette framework was selected, as PHP was a technology more familiar to the production team. The Nette framework was an added value that could give the solution a more high-level design such as Java Spring framework.

During this time, a number of similar projects were reviewed to gain inspiration for website design. The subject of interest was the website, which contains an interactive map connected with other information about selected thematic objects displayed on the map. There is a large number of such web portals - they differ in the technologies used and the implemented functionality. The biggest conceptual inspiration was the website presenting the Archaeological Atlas of the Czech Republic (archeologickyatlas.cz). Using the knowledge gained through an extensive research, the original web database application was developed.

Principal usage

The website has the following basic uses: data presentation, storage and categorization. The first, the presentation, refers to the ability of all visitors to view the content of the web portal. Essentially, anyone can come to the web application and view all the published materials. The filtering feature makes it possible for researchers and the general public to find materials related to their interest or work.

The filter allows users to sort entities according to two basic attributes: entity type and keywords. A potential user can select what type of entity searches for, e.g. maps, documents or entire municipalities. The second filtering attribute lets the user select what keywords he wants to look for. A typical use case would be to find an archival document and specify the keyword type to be a map.

For other users - the maintainers, the website in addition to representation of their work, also serves in the storage and categorization portions. All registered users of the website can add and manage their own work. The web application provides a clear overview of the presented work results. A preview of the available user rights is shown in Figure 2.

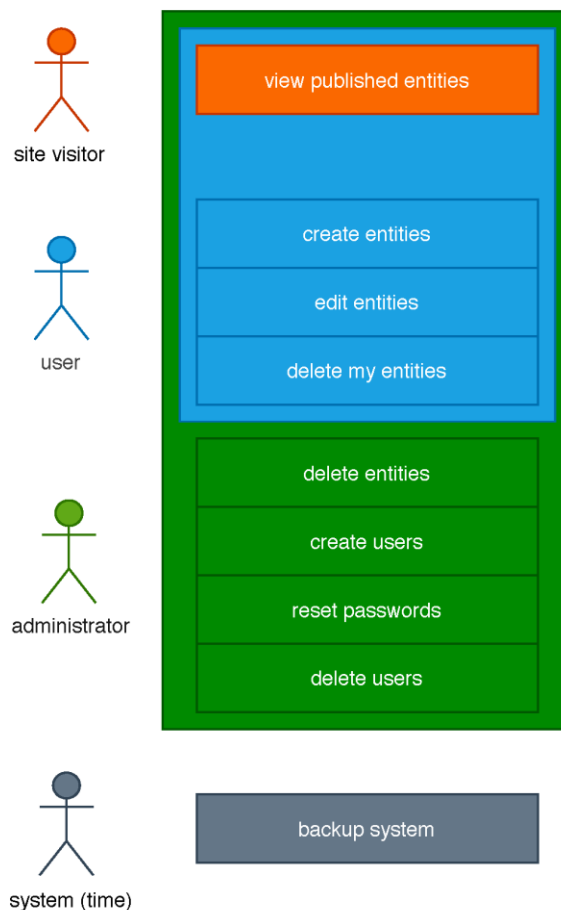


Fig. 2 – Use-case diagram

The basic use of the application remains the same for all users. All entities are created and stored under their respective parent entities. To find an entity, the search function can be used or the map, or simply navigate to the appropriate parent entity. If one is looking for data from a given district, he simply finds the region and selects the district to see all municipalities that contain some

data. Alternatively, the filter form can also be used to enter such a query. This can be done by all users. But only the registered users can create new entities, keywords and edit the data.

To create something new, it is needed to navigate to the appropriate parent entity. For example, to add a new building, one does so from the page of the municipality the building belongs to. If the municipality is not listed, one must navigate to the district of municipality (all of which are listed for registered users) and first create the municipality. Editing an entity is performed at the site that actually represents it (in contrast to creation, which is done from the entities parents' page).

Technological approach

Web application technical design can be divided into two sections, database design and user interface design. The database uses the PostgreSQL v. 11 application. The web app runs on Apache webserver with PHP 5. The web application itself runs on the PHP Nette framework. The whole system is deployed on a virtual machine, running Debian Buster. Deployment diagram is seen in Figure 3.

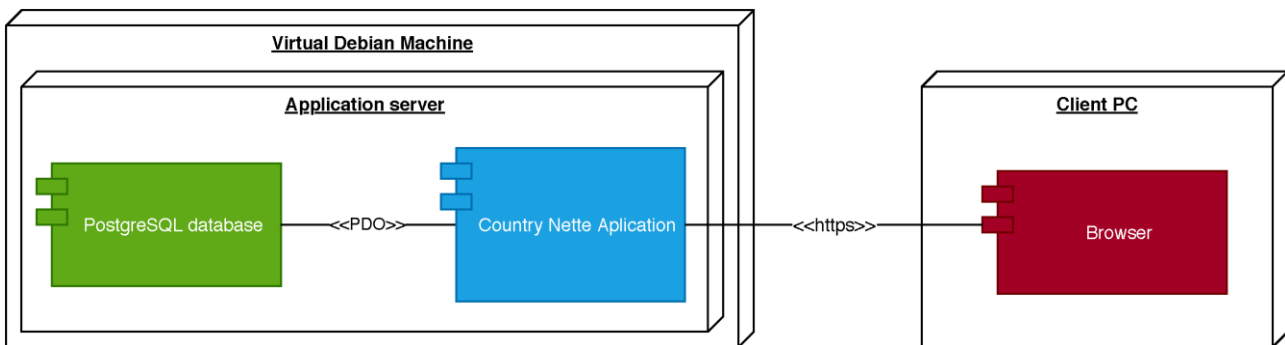


Fig. 3 – Deployment diagram

As mentioned previously, the Nette framework was chosen to provide a more high-level support to the project. Unlike plain PHP, Nette is designed to facilitate web application design, handle several security problems, improve the code reusability and add various functionalities for handling database objects. The result is that using the framework, the application could be designed using a more industry standard template format. This proved a great help in the process of development as changes in ever larger application scaled very well.

The choice of PostgreSQL as the database client was motivated in part by the existence of the PostGIS spatial database extender. The motivation was, that as an application partially used for storing geo-informatics data, the addition of such functionality would be useful. While the PostGIS add-on is currently not used (as the only localisation of data stored in the database are GPS coordinates of municipalities and buildings - of which are in database terms few), it remains a good option for future expansion.

An important part of the website is the background map which indicates by the mark the location of processed municipalities and buildings. Location data (GPS coordinates) of elements can be entered into the database graphically by clicking on the location on the map, or by numerical values of coordinates from the keyboard. The map and database information are linked in both directions. Clicking on a marker on the map will display information about that feature. Similarly, selecting an element in the database displays the position of the element on the map. For example, when selecting a region, the location of all database elements located in the given region is displayed in the map with a marker.

The map server mapy.cz is used as a base map. It provides a detailed map with a resolution of the individual buildings displayed, including descriptive numbers. It is thus easy to locate individual buildings registered in the database on the map accurately. The map server

contains a detailed documented application programming interface (API) that can be freely used for the development of publicly accessible user applications.

Database model

The data are represented as a set of texts, files, and attributes pertaining to various objects, such as municipalities, buildings, etc. A database system that was put forward resembled a knowledge tree, as most objects belonged to some parents and themselves had several children. Such as a municipality containing a number of buildings, the buildings having a large gallery are associated with them.

By the end of the process, the reflection was, that a graph database such as MongoDB might have been a better choice for representing this data structure, but due to familiarity with and general lack of system taxing database tree traversing operations, the selected SQL database system proved sufficient.

The original design did not change significantly. All objects or entities as they began to be called remained mostly unchanged. The major difference was that all the entities became represented primarily by one table (class), as seen in Figure 4. After some evolution, all entities proved to benefit from some common attributes (such as a name, description, etc.), that it was decided, the tree structure and common data for all entities, be represented in a single table - entity.

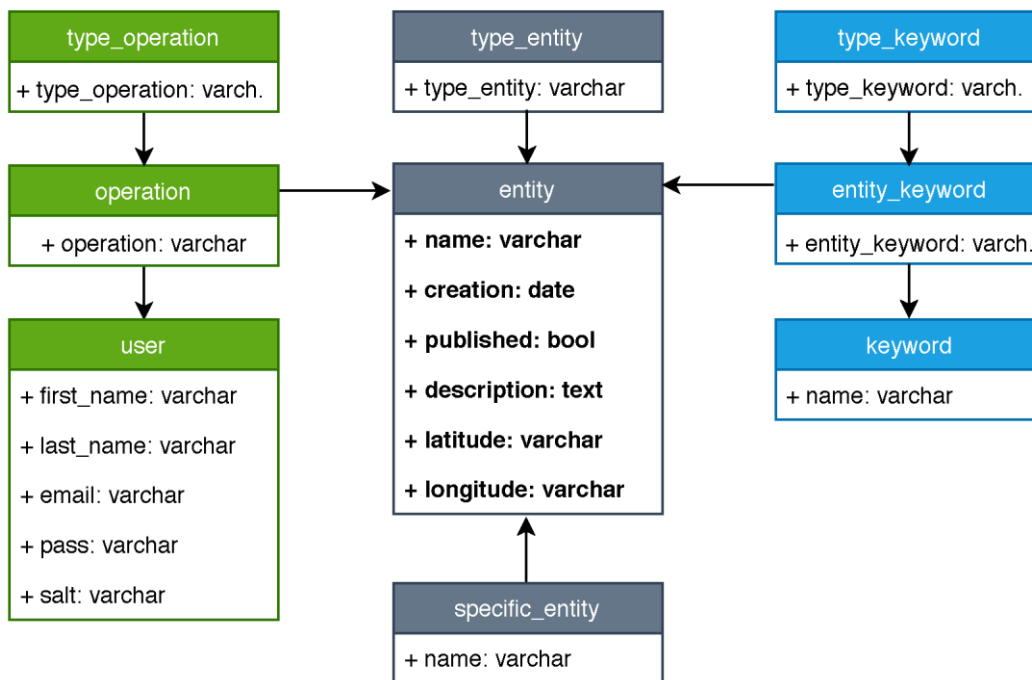


Fig. 4 – Domain model

A significant aspect of the entity design in the database model is the inclusion of keywords. Several types of keywords can be related to given entity types. Such as a building having the “type of building” or a photo of a building might have the “exterior type” keyword. These are used for description but primarily filtering. If someone is looking for a photo containing doors, beams, or renovated floors, one can simply filter for such images. The keywords also help to maintain a unified approach to categorization. Any registered user can create new keywords, but this practice will be later restricted. The flexible database design also enables to modify easily what keywords

can be assigned to which entities, as this design configuration had to be changed several times during development.

The last notable part of the general domain model is the part documenting user actions. Every action in the system (creation, editing, deleting) is documented.

The following Figure 5 shows an overview of all used entities. These being the keywords, attributes, and general tree structure of all entities in the database application. The individual table attributes are accompanied by their data type.

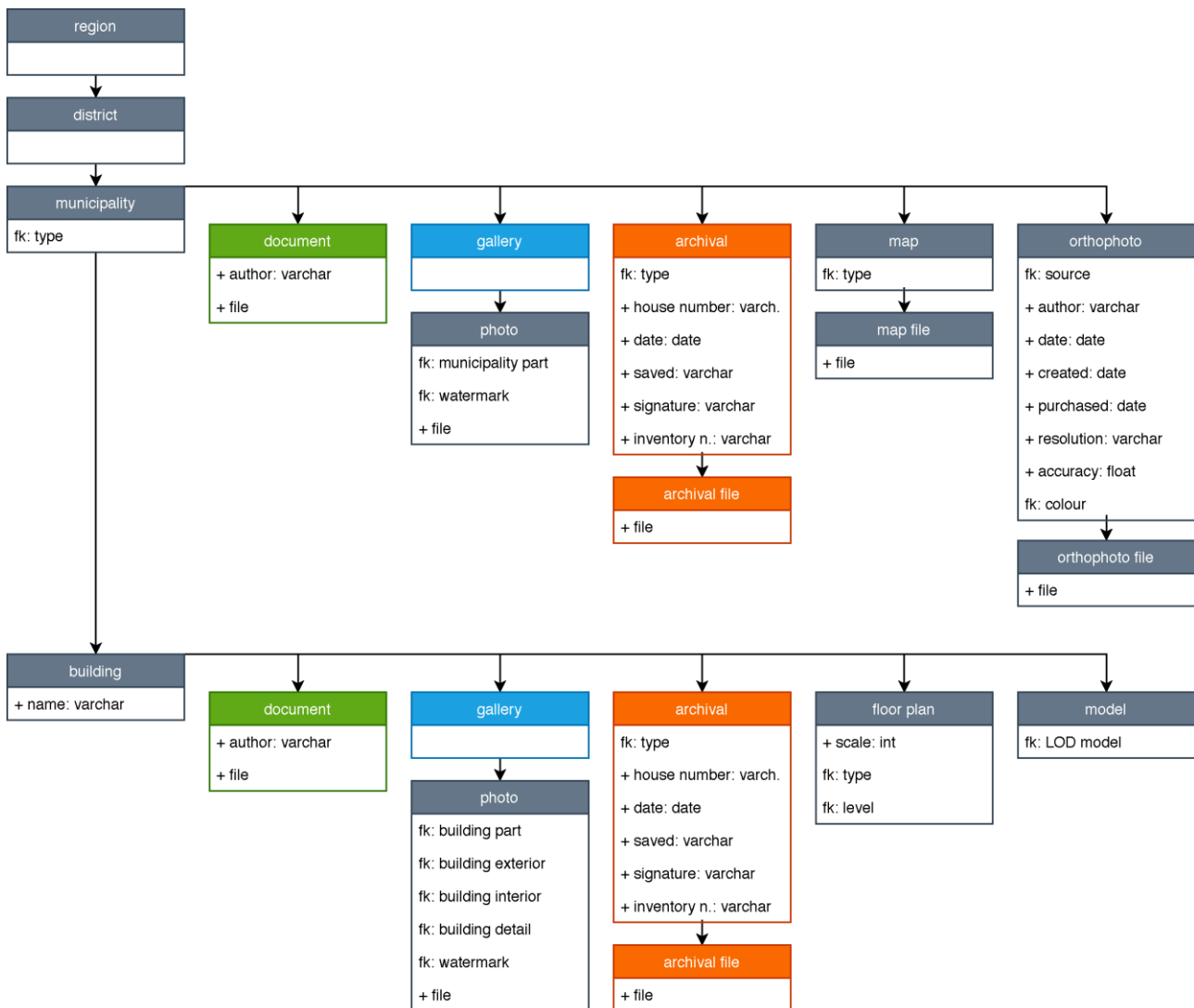


Fig. 5 – Application entities

Acronym FK in this context means a foreign key usually to a set of keywords. It is the unique use of keywords being kept in this way at the database level. One may add keywords but only in a global context - for all entities with the given keyword type. then the keywords can be only assigned to individual entities. This is done so that individual users are discouraged from coming up with new keywords whenever they want and to rely more on a standardized set. Arrows represent the three like relations of the various entities in the application. The same coloured entities represent the duplication – e.g. the entities that can belong to both, a municipality or a building.

Finally, take note that while some entities contain a file as an argument (such as a document entity), entities such as archival or map can contain several files. These files are stored in the server file system. Upon upload to server all files are renamed using a unique identifier. This is done to prevent overriding existing files with new ones (user uploading file called map.pdf twice). Their original name is stored as entity name in the database. The name of the entity can be changed for the purposes of the website itself, but the file once downloaded keeps its original name.

The application, its database and uploaded files are subject to regular backups. These backups are facilitated using a bash backup script while the application is in development. Backups will be replaced by a fully automated system once the application is moved to the final production server after development is concluded.

Copyright must be strictly observed during the public presentation of documents on the website. The data used (archive maps, aerial survey photos, etc.) must contain information about the data provider. According to the license conditions, their presentation on the website is often conditioned by the use of a watermark with the abbreviation of the relevant organization. The documents used and created (photographs, maps, orthophotos, studies, etc.) must include the author's name and the type of license. This information is an integral part of the documents in the created web application.

RESULTS

Two teams of experts participated in the development of the described application. Experts in rural architecture (ÚDU) and specialists in geoinformatics (CTU). The usual problems in communication between members of differently oriented teams (caused by different professional vocabulary) occurred mainly in the initial phases of the cooperation. The ideas of ÚDU experts were transformed by the CTU team into the environment of the used technological tools. The concept of the proposed solution had to be modified several times with regard to new requirements.

The used data storage based on a classic relational database is sufficiently powerful and provides all the necessary functionality. For a larger amount of data with a looser structure, it would be possible to consider using a NoSQL database.

The NoSQL document database MongoDB was tested in the phase of finding suitable tools. Due to the relatively small amount of processed data and their quite unambiguous interconnection, the concept of a traditional relational database was finally chosen. The PostgreSQL database was selected, which is one of the most used freely available relational databases. The described solution based on the use of keywords is sufficiently powerful and flexible.

The application is currently in the testing phase of the final version, which will be then released as a production version. Through a web application, the database is filled with real data. Therefore, all subsequent fixes and enhancements to the application must be already made with a respect to the entered data. The application contains considerable potential for further development. Planned modifications include the implementation of a module for user management (so far implemented manually), expansion of search options, as well as optimization of the connection with the navigation map and improvement of a web design. A trial version of the application is available at <https://country.fsv.cvut.cz/>.

CONCLUSION

The created web portal organized presents information about the development of rural architecture in the 19th and 20th centuries in selected localities in the territory of today's Czech Republic in one place. Maps of built-up area development, floor plans and spatial models of buildings, orthophotos, photo galleries and a number of archival materials are available at the portal, all of them were supplemented by expert studies of the results of art historical research.

Some of the materials posted to the web server are not publicly accessible (e.g. due to copyright or data volume) and are used only for the needs of registered users of the portal.

The target group of users of the portal is the general public, but experts in the field of rural architecture will also find inspiring and new knowledge here. The information presented on the web portal serves to discover and better understand the values of the cultural heritage that rural architecture contains.

ACKNOWLEDGEMENTS

This work was supported by the Ministry of Culture of the Czech Republic from the Program for the Support of Applied Research and Development of National and Cultural Identity for the Years 2016-2022 (NAKI II), grant project "The Transformation of Rural Architecture with Emphasis on the Development in the 19th and 20th Centuries", No. DG16P02H023. More information about the grant can be found on the project's website <http://venkov.fsv.cvut.cz/projekt>.

REFERENCES

- [1] Hůrková L., Mezihoráková K. (eds.), 2018. Proměny venkovské architektury s důrazem na vývoj v 19. a 20. století I. Texty: Ludmila Hůrková, Klára Mezihoráková, Dalibor Prix, Tomáš Valeš, Marie Platovská, Kateřina Dolejší, Jan Uhlík, Markéta Svobodová, Pavel Vlček. First edition in Czech, English summary, 311 pp. Prague, Artefactum 2018, ISBN: 978-80-88283-14-0
- [2] Poloprutský Z., Soukup P., Gruber J., 2017. Development of rural settlements in the 19th and 20th centuries: creation of analytical map outputs. In: 18th International Conference Dějiny staveb 2017. Pilsen, Czech Republic, 2017, 235–243, in Czech. ISBN 978-80-87170-52-6.
- [3] Poloprutský Z., 2018. Metric Survey Documentation as a Basis for Understanding the Development of Rural Architecture. The Civil Engineering Journal, Prague 2018, 27(1), 48-59. ISSN 1805-2576. DOI 10.14311/CEJ.2018.01.0005.
- [4] Hodač J., Zemánková A., 2018. Historical Orthophotos Created on Base of Single Photos - Specifics of Processing. Civil Engineering Journal, Prague 2018, 3, 425-438. ISSN 1805-2576. DOI 10.14311/CEJ.2018.03.0034.
- [5] Jílková P., Cajthaml J., 2019. Database of Historical Atlases: An Interactive Web Application. In: Proceedings of the International Cartographic Association. Tokyo: International Cartographic Association, 2019, vol. 2. ISSN 2570-2092.
- [6] Liu F., Yu C., Meng W., Chowdhury A., 2006. Effective keyword search in relational databases. In: Proceedings of the 2006 ACM SIGMOD international conference on Management of data (SIGMOD '06). ACM, New York, NY, USA, 563-574. DOI 10.1145/1142473.1142536.
- [7] Padhy R. P., Patra M. R., Satapathy S. C., 2011. RDBMS to NoSQL: Reviewing some Next-Generation Non-Relational database's. International Journal of Advanced Engineering Science and Technologies, 11(1), 015 – 030, ISSN: 2230-7818.
- [8] Hills T., 2016. NoSQL and SQL Data Modeling: Bringing Together Data, Semantics, and Software, ISBN 9781634621113 Technics Publications.
- [9] Cattell R., 2011. Scalable SQL and NoSQL data stores. SIGMOD Rec. 39, 4 (May 2011), 12-27. DOI: <https://doi.org/10.1145/1978915.1978919>.

MEASUREMENT OF TRAFFIC CONGESTION FOR INDORE

H.S. Goliya¹, Kundan Meshram², Suchetan Mahapatra¹

1. CE-AMD, Shri G. S. Institute of Technology & Science, Indore, M.P., India
2. Department of Civil Engineering, Guru Ghasidas University Bilaspur (C.G.), India; kundan.transpo@gmail.com

ABSTRACT

Traffic congestion is caused due to an imbalance of transportation demand and supply. Traffic congestion is not only responsible for harming our health but also for not gaining full potential in our economic sector. Traffic congestion is an obstacle to the development of any country as it creates a huge amount of economic costs, discomfort cost, and alike. In the current scenario Indore city also prevails such a condition, some intersections of the city are badly affected by traffic congestion which causes potential hazard and delays so traffic congestion study is much needed at some potential road intersections. Several parameters like segmental delay, delay ratio, and relative delay ratio have been used to effectively measure traffic congestion at some potential sections taken for 6 locations. A model developed for segmental delay (Vehicle-second), segmental delay (person-second), delay rate, and relative delay Rate.

KEYWORDS

Segmental delay, Delay rate, Relative Ddelay rate, Traffic congestion

INTRODUCTION

Transportation contributes to the social, economic, industrial, and cultural development of any country. Every product whether it is food, medicine, clothes, industrial items, or other essential commodities needs transport facility at all stages to get supply thoroughly throughout the country, which in term helps the country to uplift its economy and development hand to hand.

But in recent years, the usage of transportation facilities has been increased drastically. Many of the cities experiencing a huge number of traffic flow which leads to a system break down in some cases, in talking about India, considerable numbers of cities facing a huge transportation management problem, as a result, the movement of vehicle, speed characteristics have been observed not up to the mark.

Due to incessant increase in population, increase in household incomes and its resultant increase in the level of car usage coupled with poor land-use planning, poor transport design and planning. In urban areas, the problem of traffic is observed in road intersections for most of the cases [5]. Road intersections consist of too many actual and potential conflict points [4]. This is because at intersections, vehicular flows from several directions approaches making either left-turn, through and right-turn movements seek to occupy the same physical space at the same time. In addition to these vehicular flows, pedestrians also seek to use this space to cross the street and thereby worsening the already bad traffic situation.

Traffic congestion is the result of the gap between transportation demand and supply [2]. It may be said that traffic jam is killing our time only but that will be wrong. Traffic congestion can be held responsible not only for harming our health but also for not gaining full potential in our economic sector [1]. The transportation system has now become the spider that is sitting in the

centre of a development web in which every web string controls almost every development process of a country. Traffic congestion is an obstacle to development of any country as it creates a huge amount of economic costs, discomfort costs, and so on [3]. Because of traffic congestion, companies that are related with the public transport system cannot achieve their targeted profit.

In the current scenario Indore city also prevails such a condition, some intersections of the city are poorly affected by traffic congestion which causes potential hazard and delays so traffic congestion study is much needed at some potential road intersections. The aim of the study is measure effective congestion at potential sections by using segmental delay, delay ratio, relative delay ratio techniques.

STUDY AREA

The National Highway-3 also known as Agra Bombay Road is one of the prime and important road networks which pass through Indore, connecting Agra and Mumbai. The study area concerns some potential sections of this road in between the city named

- a. Section 1 (Palasia Square to Industry House)
- b. Section 2 (Industry House to LIG Square)
- c. Section 3 (LIG Square to Rasoma Chouraha)
- d. Section 4 (Rasoma Chouraha to MR9 Chouraha)
- e. Section 5 (MR9 Chouraha to Vijayanagar Square)
- f. Section 6 (Vijayanagar Square to Satya Sai)

The AB road consists of two way with 6 meters of road width at Palasia square and Industry House sections. LIG square, Rasoma Chouraha, and MR9 sections have a lane width of 7 meters. Vijayanagar section consists of 7.5 meters of lane width. The city transport authority also established a BRTS system in between the road section at the central position as public transport facilitation. The studied section has a capacity of approx. 4000 PCU/hr.

The study area consists of total 3.5 km stretch starting from Palasia square to Vijayanagar square.

DATA COLLECTION

Traffic Flow

The method of obtaining traffic flow data in this study was using standard video recording procedure. This is however essentially a manual method. Traffic flow was analyzed from a video recording of the studied sites themselves. This includes the entire count of the vehicle over the recorded time at peak hours. The classification of vehicles, their quantity and direction were also observed from the recordings at laboratory.

Speed

Speed could be recorded in three distinct ways

- a. Space mean speed
- b. Time means speed
- c. Spot speed

The short base speed that is the speed at a particular section (spot speed) can be used but the proper instrument has to be used. While taking the speed of the vehicle every time it was ensured that it should be free from the influence of traffic signalling or any other factors such as

inclined terrain, junction effect, etc. In this study time mean speed or the average speed has been taken into consideration as it can be obtained by two observers, one in starting position and another at the end position of the stretch, besides this can also be cross-checked in the laboratory from the video recordings. Over all this method of obtaining the speed of any vehicles is easy to apply, economical and collected data can be subjected to statistical procedures.

Travel Time

Travel time data is very crucial to calculate traffic congestion, time taken to travel a particularly known length of section is measured for every types of vehicle. The data includes travel time during free-flow condition and peak hour flow at congestion like situations. This is totally a manual and field observation method but video recordings also can be useful in some cases.

Geometric Characteristics

Geometric measurements were obtained in the field by the means of simple tape measurement. The degree of accuracy was nearest to 10 cm. The data were recorded in the rough notebook.

DATA REDUCTION PROCESS

Video recording was carried out continuously over the predefined period of the time at peak hours at every section. To produce the variables much needed for the analysis, in the next step the raw data have been retrieved. Raw data that were collected and recorded in the field included traffic flow, vehicle types, passage time of the vehicles, and occupancy per vehicle over the measurement lines. The video recorded data were retrieved in the laboratory and transcribed in the computer files. There after further processing of the data has been carried out using a standard spread sheet, statistical software packages and some computer macros. The first and foremost task was to convert the passage time into travel time and eventually measure the speed of each category of the vehicle, the time data included normal passage time and passage time during congestion like situation. Obviously, the speed that came up from the data should include free-flow speed and congested speed of the different categories of the vehicles, using the particular studied section. Thereafter, the speed data were inspected for each site if there were any outliers or other unusual values.

When retrieving data from the video clips, few incidences that were suspected to be true value have been noticed and neglected. The vehicles that were moving slowly due to some influence were treated as valid for sampling and some fast-moving vehicles that stopped due to some personal reason or unnecessarily has been taken as invalid, besides these few incidences like slowing down of vehicle due to running out of fuel or some mechanical problem encountered, also taken as an invalid and neglected simultaneously.

Generally, results required from the data reduction process for the studied sites were as follows:

- a. 16 hrs. data to obtain the peak periods of traffic flow and identify the congestion timing.
- b. Traffic flow and composition for a period of 15 minutes, for each site and each direction.
- c. Space mean speed, over 5 minutes' period for each and every class of vehicles at each site and each direction.
- d. Free-flow speed and congested speed based upon time calculation over a known length of stretch of 20 meters.

RESULTS AND DISCUSSION

The process to estimate the traffic congestion, measurement of traffic flow in the section should be carried out accurately. The travel time analysis also plays a crucial role in this case. The proper analysis of traffic and design of the road should thoroughly study to make an effective conclusion which may further used for future design and implementation. Before proceeding to the analysis part there need to be discussed some conceptual definitions and theory related topics.

Flow Measurement

Traffic composition of different vehicles has been determined and their proportion has been calculated as mentioned earlier. As per IRC:106-1990[6], PCU conversion is done by using proper factors to get an equivalent flow estimation. A proper example of PCU conversion is shown in Table 1 for an individual section.

Tab. 1- Traffic Flow for all Sections at Peak Hour

Locations	Flow (PCU/hr.) towards Dewasnaka	Flow (PCU/hr.) towards Bhawarkuan
Section 1	3472	3225
Section 2	2837	2747
Section 3	4142	3605
Section 4	3035	3207
Section 5	3248	3305
Section 6	3738	4004

Segmental Delay

Segmental delay is the measurement of overall time consumption due to the bad condition of traffic flow. Congestion increases the time consumption of traveling for a particular distance than the usual traffic condition which causes delay. In the delay analysis the excess time lost per vehicle and per person has been quantified at each section in terms of Vehicles-second and person-second. A relative comparison has been made to identify which section is most affected by congestion and which one has less effect of congestion. Speed comparison at various sections is shown in Figure 1 and Figure 2.

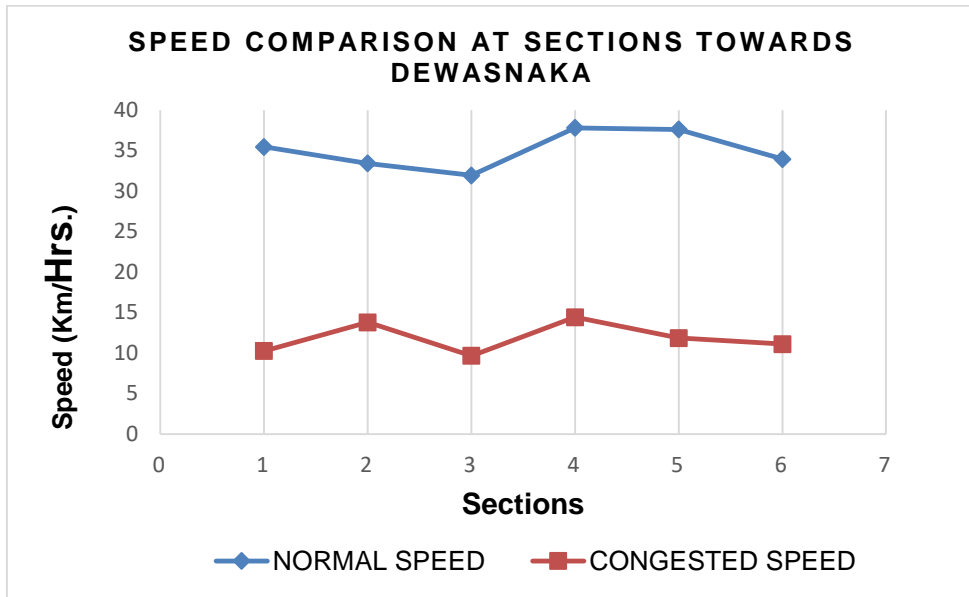


Fig. 1- Speed comparison at sections towards Dewasnaka

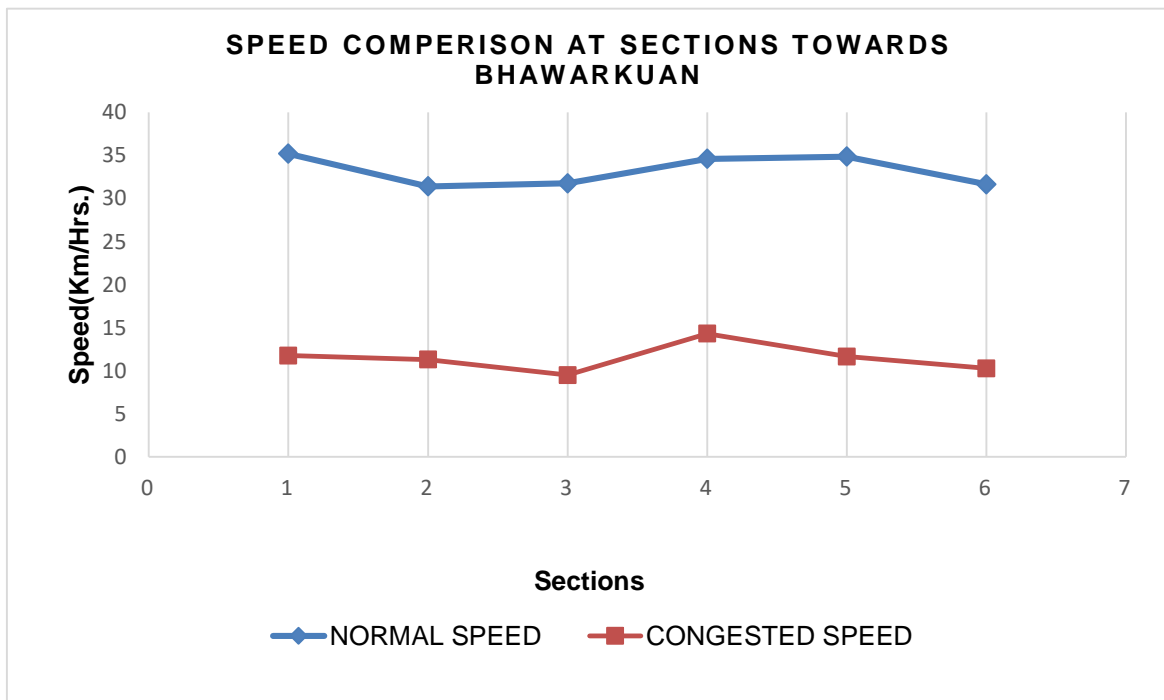


Fig. 2- Speed comparison at sections towards Bhawarkuan

Multiple regression analysis has been carried out for Segmental delay (Vehicle-second) and Segmental delay (person-second), as shown in Table 2.

Tab. 2- Model for Segmental delay (Vehicle-second) and Segmental delay (person-second)

S.N.	Model	R ²	RMSE
1.	$D = -19176.4 + 3738.815 * T_C - 2922.22 * T_a + 4.699241 * V_p$	99%	1.1027E-11
2.	$D' = -69855 + 7414.247 * T_C - 6022.11 * T_A + 9.31578 * V_p + 16330.11 * V_{OC}$	99%	2.31043E-11

Where,

D = Segmental delay (Vehicle-second), D' = Segmental delay (person-second),

T_a = Acceptable travel time over a defined section (second), T_C = Congested travel time over a defined section (second), V_p = Vehicle volume in peak period (PCU/hr.), V_{OC} = Vehicle occupancy (persons/ vehicle), R^2 = Coefficient of correlation, $RMSE$ = Root Mean Square Error

Delay Rate

Delay rate is the difference between the rate of travel of congestion situation and normal situation. The rate of travel can be measured as the time required to travel a particular segment length. It is the inverse of the velocity at any section, measured as Sec per meter. Relative delay rate can be explained as the ratio of delay rate to acceptable (normal) travel rate. A regression model has been developed for delay rate and relative delay rate, as shown in Table 3.

Tab. 3- Model for delay rate and relative delay rate

S.N.	Model	R ²	RMSE
1.	$D_R = -0.02631 + 0.948524 * T_{R_c} - 0.63062 * T_{R_a}$	99%	2.80432E-16
2.	$R_{D_R} = -0.03035 + 1.029935 * \left(\frac{D_R}{T_{R_a}}\right)$	98%	5.1279E-16

Where,

D_R = Delay rate, R_{D_R} = Relative Delay Rate, T_{R_c} = Travel Rate at congestion (sec / meter), T_{R_a} = Acceptable Travel Rate (sec / meter), R^2 = Coefficient of correlation, $RMSE$ = Root Mean Square Error

CONCLUSIONS

- I. Section 3 and Section 6 accommodates the highest number of traffic flow among all the sections. However, in section 3(LIG square) lowest speed has been observed during congestion.
- II. Section 1 has less a flow of traffic than section 6 but still section 1 has a higher segmental delay. This variation was observed due to the high value of merging traffic to straight moving traffic ratio, due to the rotary effect at Vijayanagar streaming of traffic is quite good.
- III. Segmental delay is maximum at section 3, traffic flowing towards Dewasnaka and for traffic towards Bhawarkuan, the segmental delay is maximum at section 6. But the relative delay rate is maximum in section 1, traffic flowing towards Dewasnaka.

- IV. Section 3 experience worst traffic congestion at the Level of Service of E and V/C ratio tends to unity. However, Section 1 and section 4 also have a bad flow condition and LOS obtained there is E. Section 6, section 2 and section 5 has favourable flow condition.

REFERENCES

- [1] Dadić, I., Kos, G., Poić, K. and Gašparac, E., 1999. Measures for reducing traffic congestion in cities. *PROMET-Traffic & Transportation*, 11(1), 15-19.
- [2] Aderamo, A.J., and Atomode, T.I., 2012. Traffic congestion at road intersections in Ilorin, Nigeria. *Mediterranean Center of Social and Educational Research*, 3(2),201-213.
- [3] Rahane, S.K. and Saharkar, U.R., 2014. Traffic congestion-causes and solutions: a study of Talegaon Dabhade City. *Journal of Information, knowledge, and research in civil engineering*, 3(1),160-163.
- [4] Pro than, J.I.J., Islam, M., Rahman, A. and Pramanik, A., 2017. Transportation System Analysis at the Major Road Intersection in the CBD Area of Rangpur City, Bangladesh. *International Journal of Transportation Engineering and Technology*, 3(4), 74-82.
- [5] Marfani, S., Shihora, D., Kanthariya, C., and Kansara, H., 2018. Traffic Improvement for Urban Road Intersection, Surat. *Traffic*, 5(03), 2966-2970.
- [6] IRC: 106-1990. Guidelines of Capacity of Urban Roads in Plain Areas. Indian Road Congress, New Delhi.

STUDY ON THE INFLUENCE OF CABLE/SLING DAMAGE ON THE NATURAL VIBRATION CHARACTERISTICS OF SPECIAL-SHAPED CABLE-STAYED ARCH BRIDGE WITHOUT BACK CABLE

Kexin Zhang¹, Tianyu Qi¹, XingWei Xue¹, Zhimin Zhu², Quansheng Sun³

- 1. School of traffic engineering, Shenyang Jianzhu University, Shenyang, 110168, China; jt_zkx@sjzu.edu.cn*
- 2. Liaoning Urban Construction Design Institute Co. LTD, Shenyang, 110000, PR of China; minzdragon@126.com*
- 3. Department of Civil Engineering, Northeast Forestry University, Harbin, 150040, China; hrbsqs@126.com*

ABSTRACT

In order to study the influence of cable/sling damage on the natural vibration characteristics of a special-shaped cable-stayed arch bridge without back cable. The natural vibration characteristics of the bridge with different cable/sling damage and their different damage degree are analysed. According to the characteristic of self-vibration of cable-stayed arch bridge without back cable, the structural health of bridges can be diagnosed and evaluated.

KEYWORDS

Cable-stayed arch bridge without back cable, Natural vibration frequency, Stay cable, Mode of vibration, Sling

INTRODUCTION

Cable-stayed arch bridge without back cable is a new type of bridge structure which combines backless a cable-stayed bridge with an arch bridge. It has the characteristics of backless cable-stayed bridge and arch bridge, and its unique shape gives people a unique aesthetic feeling [1-3]. The cable-stayed structure can balance the dead weight of the main girder by the inclined bridge tower and enhance the longitudinal bending resistance of the main girder. The special-shaped arch structure ensures the transverse mechanical properties of the broad beam and makes the whole structure work harmonically [4-5]. Due to the material characteristics of cable or sling and the impact of the natural environment, the probability of cable or sling damage will be greatly increased. It is necessary to study the influence of the damage on the performance of the cable-stayed arch bridge without back cable. The damage of the cable or sling will lead to the change of the natural vibration characteristics of the structure. It is a simple and effective method to judge the health condition of cable-stayed arch bridge with the change of the natural frequency of the needle [6-7].

BACKGROUND

A bridge is a cooperative system of cable-stayed bridge without back cable and special-shaped arch bridge. The span arrangement is 40 m+90 m=130 m for two spans, and the bridge is 39 m ~ 43 m wide, See Figure 1 to Figure 2. The main girder and the bridge tower adopt prestressed concrete structure and reinforced concrete structure respectively, both of which are made of C50 concrete. The sling is made of steel strand extrusion, and the standard tensile strength is 1860 MPa. A total of 19 pairs of slings are arranged longitudinally, two of which are to be pulled against each other. The spacing of arch rib slings is 4.25 m. A total of 8 cables are arranged longitudinally with a cable spacing of 8.5m. The finished cable is made of galvanized steel strand and the standard tensile strength is 1860 MPa. Steel box structure is adopted in the arch ribs, and concrete is poured only at the arch foot. The bridge has a height of 25.8 m above the deck and a cable distance of 4.25 m. The bridge has 38 slings. The substructure is bored pile foundation and light abutment. The elevation and cross-section of the bridge are shown in Figure 1 and Figure 2.

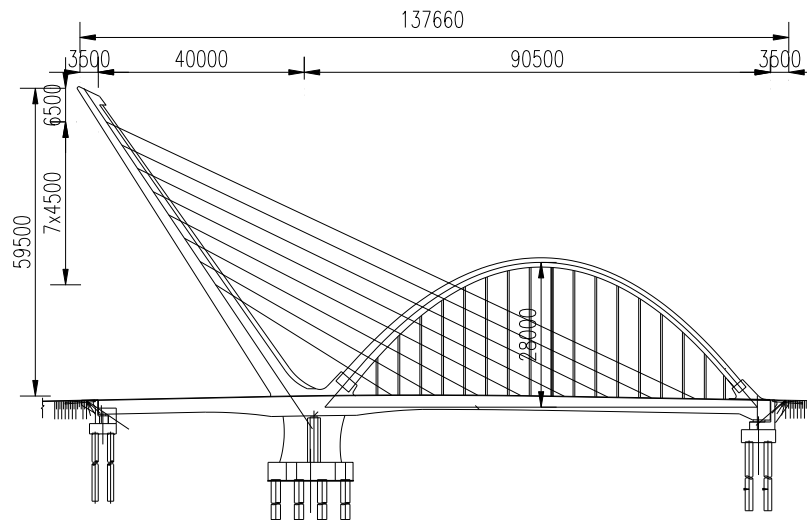


Fig. 1 - Vertical view

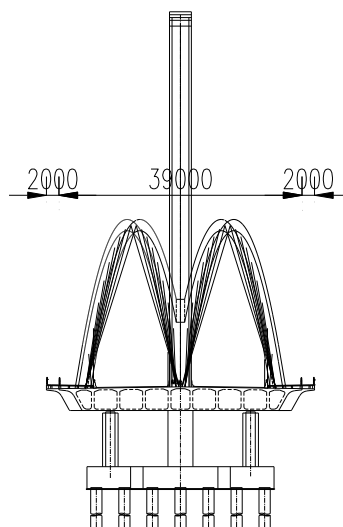


Fig. 2 - Cross section drawing

The finite element software Midas/Civil 2019 was used to establish the analysis model of the cable-stayed arch bridge without back cable. A total of 904 nodes and 1182 units were established, and piers and beams are a consolidated system. The pier, tower, beam, arch and transverse brace are simulated by beam element, while the cable and sling are simulated by truss element. The finite element model of the whole bridge is shown in Figure 3.

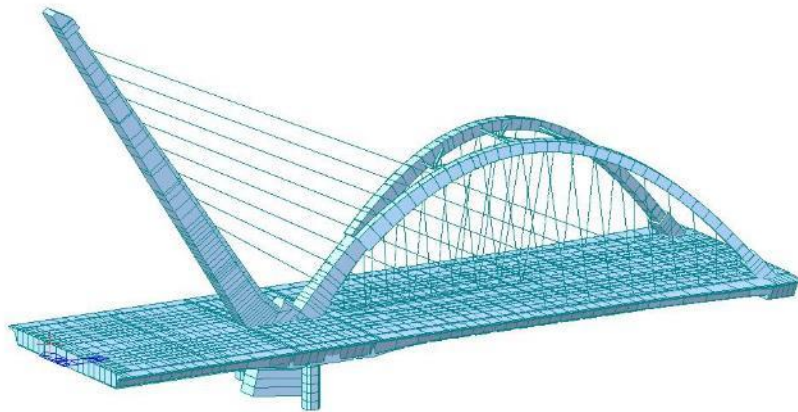
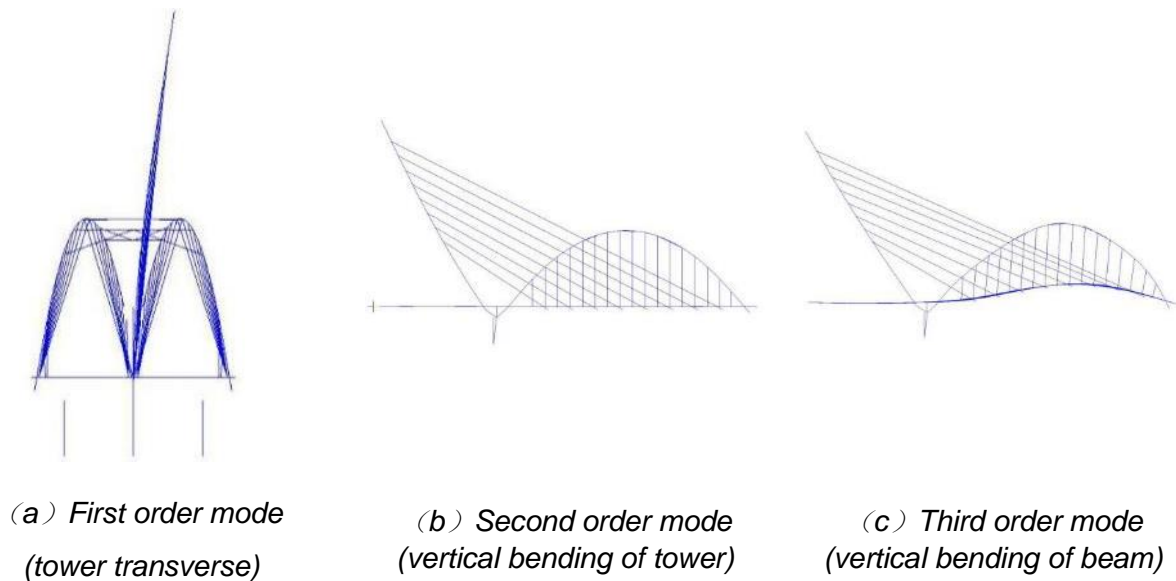
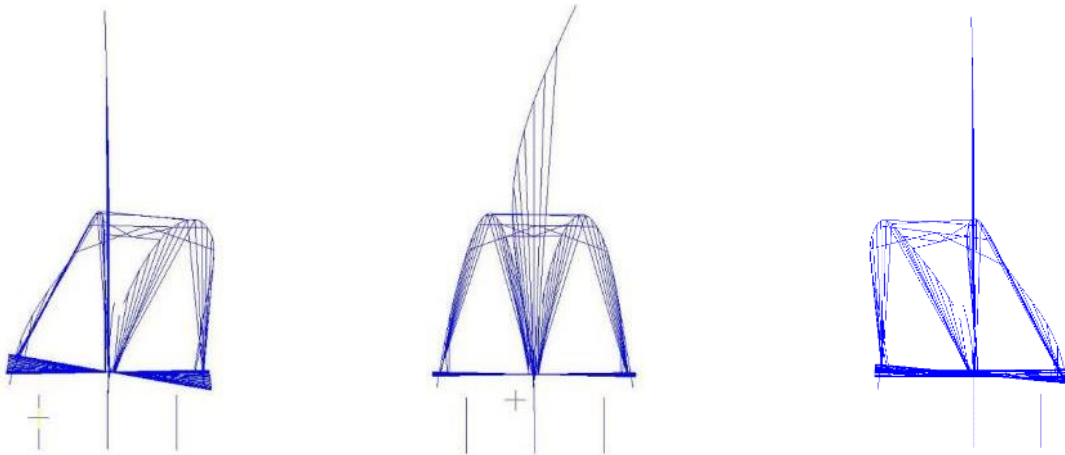


Fig. 3 - Finite element model of bridge

ANALYSIS OF BRIDGE VIBRATION CHARACTERISTICS

In dynamic analysis, the natural frequencies and main modes of the bridge structure are the most important parameters. The change of bridge stiffness will lead to the change of structural frequency, which is of the great significance to the health of cable-stayed arch bridges without back cables. Figure 4 shows the six main modes of vibration in front of a cable-stayed arch bridge without back cable.





(d) Fourth order mode (arch transverse)

(e) Fifth order mode (tower transverse)

(f) Sixth order mode (arch transverse)

Fig. 4 - Modal figure

Generally, the first few frequencies play an important role in bridge structure. The first 8 frequencies and modes of natural vibration of the cable-stayed arch bridge without back cables are shown in Table 1.

It can be seen from Table 1, in the first six modes, except the third mode which is the vertical bending mode of the beam, the other modes are the tower bending mode and the arch bending mode. The main beam has a wide cross section and poor transverse stiffness. However, due to the large transverse stiffness provided by the shaped arch, the torsional stiffness of the main girder of the cable-stayed arch bridge without back cable is large, and it has a good resistance to torsional deformation.

Tab. 1 - Material properties

Modal number	Period /s	Vibration mode shape	Modal number	Period /s	Vibration mode shape
1	0.5116	Column transverse bending	5	2.5661	Column transverse bending
2	0.9425	Vertical bending of tower	6	2.8959	Transverse arch bending
3	1.8163	Vertical bending of beam	7	2.8979	Vertical bending of beams + Vertical bending of towers
4	2.0269	Transverse arch bending	8	3.3851	Vertical bending of beams + Vertical bending of towers

ANALYSIS OF THE INFLUENCE OF CABLE DAMAGE ON THE BRIDGE'S NATURAL VIBRIATION CHARACTERISTICS

Natural vibration characteristics under different cable damage

The bridge has a total of 8 pairs of cables, cable specifications are GJ15-25, GJ15-31. The cables are numbered from the short cable to the long cable, which are S01 ~ S08 respectively. The specification of S01~S06 is GJ15-31, and that of S07~S08 is GJ15-25. The damage of each cable was simulated by reducing the elastic modulus. S02 represented the short cable, S04 and S06 represented the medium cable, and S08 represented the long cable. The elastic modulus of the

cable after damage is 1×10^{-5} MPa. Statistical frequency variation after cable damage, frequency variation rate = (frequency value after damage - no damage frequency value)/no damage frequency value. The values of frequency and frequency amplitude after damage are shown in Table 2, and the frequency amplitude after cable damage is shown in Figure 5. It can be seen from Table 2 and Figure 5. The cable damage has the greatest influence on the frequency variation of the 1st order transverse and 1st order vertical bending of the main tower of cable-stayed arch bridge, but it has little influence on the beam bending and arch bending modes. As shown in Figure 6 and Figure 7, the 1-order transverse bending frequency of the main tower and the 1-order vertical bending frequency of the main tower were calculated under different cable damage conditions. With the increase of the damage cable number, the natural vibration frequency of the 1st order transverse bending of the girder decreases linearly. When S8 cable is damaged, the 1st order transverse bending natural vibration frequency of the main tower is the smallest, which is 0.3175 Hz, but the change rate is the largest, which is -37.9%. When cable S1 is damaged, the 1st order transverse bending natural vibration frequency of the main tower is the largest, which is 0.506Hz, and the change rate is -1.09%. With the increase of damage cable number, when S8 is damaged, the first-order vertical bending frequency of the main tower is 0.5134, the frequency change rate is -42.35%, and the first-order vertical bending natural vibration frequency of the main tower is linearly decreasing. When cable S1 is damaged, the first-order vertical bending frequency of the main tower is the largest, which is 0.9318 Hz and the rate of change is -0.9318%.

Tab.2 - Frequency and frequency amplitude under cable damage

Order number	Primary frequency /Hz	Frequency after cable damage/Hz				Frequency variation after cable damage /%				Vibration mode shape
		S2	S4	S6	S8	S2	S4	S6	S8	
1	0.5116	0.4994	0.4535	0.3887	0.3175	-2.39	-11.35	-24.02	-37.94	Tower of transverse bending
2	0.9425	0.9160	0.8287	0.6937	0.5434	-2.81	-12.08	-26.40	-42.35	Tower vertical
3	1.8163	1.8139	1.7116	1.6435	1.7480	-0.13	-5.76	-9.51	-3.76	Beam vertical
4	2.0269	2.0204	2.0189	2.0213	2.0237	-0.32	-0.39	-0.28	-0.16	Arch transverse bending
5	2.5661	2.3391	2.3320	2.5643	2.2818	-8.85	-9.12	-0.07	-11.08	Tower of transverse bending
6	2.8959	2.8114	2.7780	2.8463	2.7248	-2.92	-4.07	-1.71	-5.91	Arch transverse bending
7	2.8979	2.8738	2.8940	2.8954	2.8955	-0.83	-0.14	-0.09	-0.08	Beam column vertical bending
8	3.3851	3.1570	3.0430	3.3352	3.0877	-6.74	-10.11	-1.47	-8.79	Beam column vertical bending

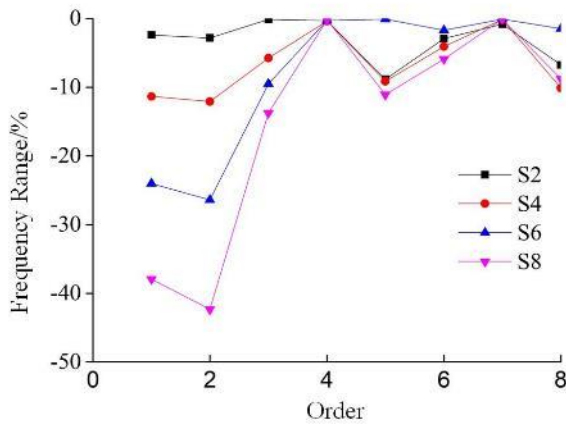


Fig.5 - Frequency variation under different main cable damage

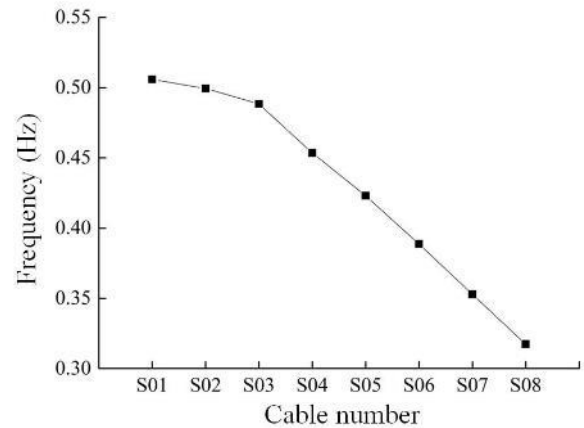


Fig.6 - First order transverse bending frequency of tower under different cable damage

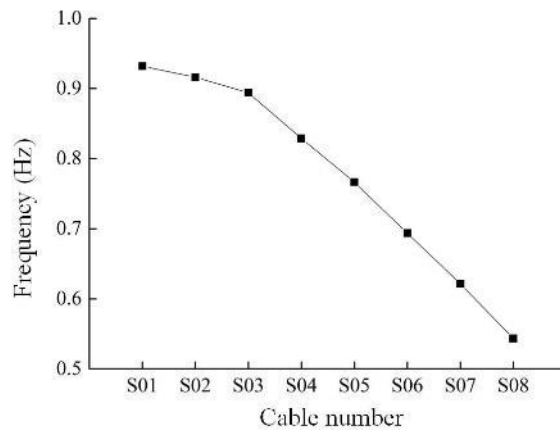


Fig.7 - First order vertical bending frequency of main tower under the different cable damage

Natural vibration characteristics of cables under different damage degrees

In order to explore the influence of different damage degree on bridge natural vibration frequency, three kinds of cable damage of different length were analysed. S01 and S02 were taken as the short rope representatives, S04 and S05 as the middle long rope representatives, S07 and S08 as the long rope representatives. The damage degree was 25%, 50%, 75% and 100% respectively, and the elastic modulus was 1.5×10^5 MPa, 1×10^5 MPa, 0.5×10^5 MPa and 1×10^5 MPa respectively. Figure 8, Figure 9 and Figure 10 are the frequency values of short, medium and long cables under different damage degrees. Figure 11, Figure 12 and Figure 13 show the variation amplitude of different damage degrees of S01, S04 and S07 cables. It can be seen from the figure that: under different damage conditions of short cables, the frequency values show regular changes. The damage is mainly reflected in the first-order vertical bending mode of the main tower, and the frequency variation becomes larger and larger with the increase of damage degree. It has little effect on the bending modes of beams and arches.

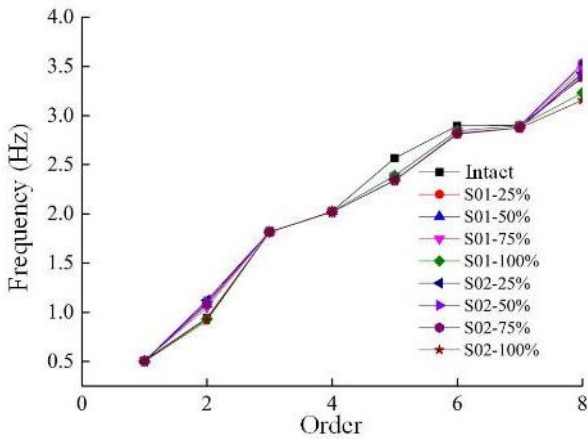


Fig. 8 - Different damage frequency of cables S01 and 02

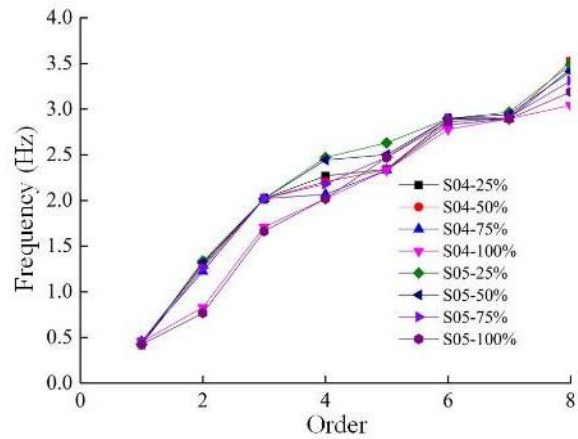


Fig. 9 - Different damage frequency of cables S04 and S05

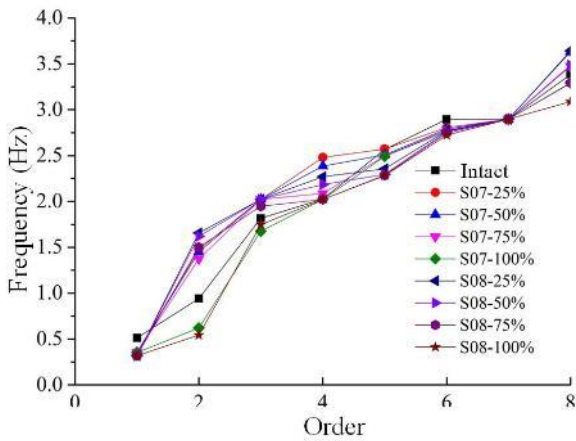


Fig. 10 - Different damage frequency of cables S07 and S08

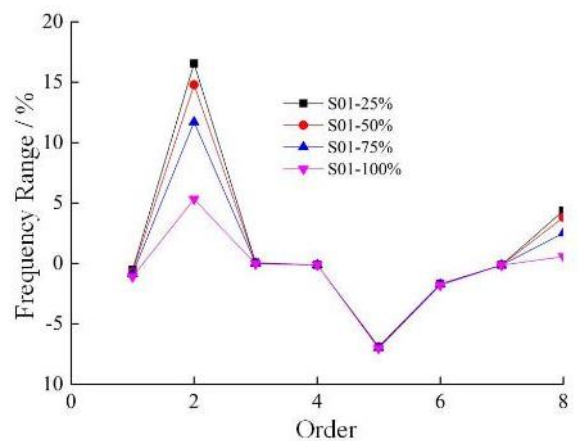


Fig. 11 - Frequency variation of cable S01 with different damage degree

It can be seen from Figure 9 and Figure 12, the frequency of medium and long stay cables varies regularly under different damages. The damages are mainly reflected in the first-order vertical bending mode of the tower, the first-order transverse bending mode of the arch and the second-order transverse bending mode of the arch. It has little effect on other modes.

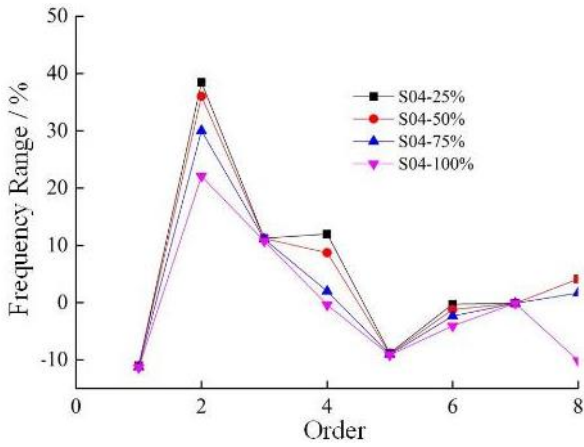


Fig. 12 - Frequency variation of cable S04 with different damage degree

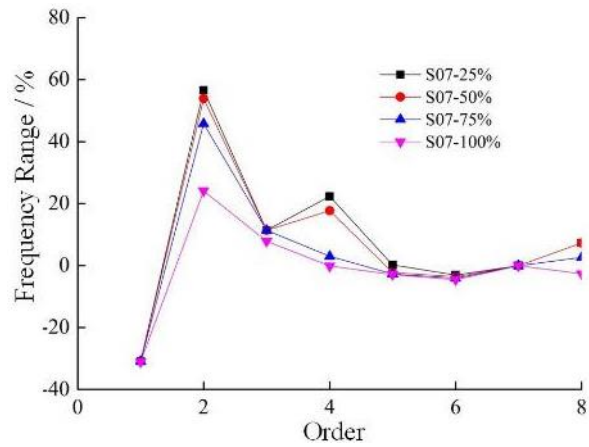


Fig. 13 - Frequency variation of cable S07 with different damage degree

It can be seen from Figure 10 and Figure 13; the frequency of the long stay cables varies regularly under different damages. The damages are mainly reflected in the one-order vertical bending mode of the tower and the one-order transverse bending mode of the arch, which have little influence on the beam bending mode and the tower transverse bending mode.

The bridge has 17 pairs of slings, which are numbered from the bridge tower to the abutment, and are D1 ~ D17 respectively. The elastic modulus of 1×10^5 MPa was used to simulate D1-D3, D4-D6, D7-D9, D10-D12, D13-D15 sling damage, and the frequency amplitude after the sling damage was calculated. The frequency amplitude of the sling was = (the value of the natural vibration frequency after the damage - the value of the natural vibration frequency without damage)/the value of the natural vibration frequency without damage. As shown in Figure 14, the frequency variation amplitude of the boom sling after injury shows a linear increase under different sling injuries. It can be seen from the figure that sling damage has almost no effect on the first-order transverse bending natural vibration frequency of the main tower of cable-stayed arch bridge.

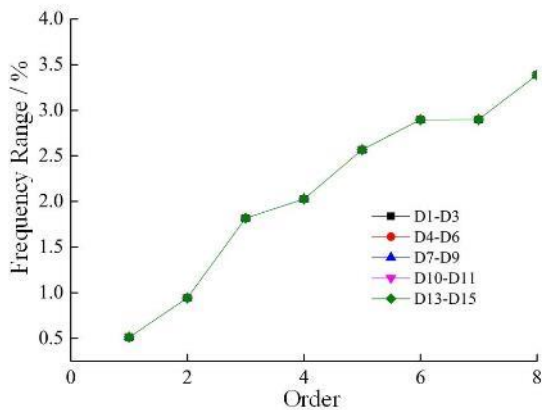


Fig. 14 - Frequency variation under different sling damage

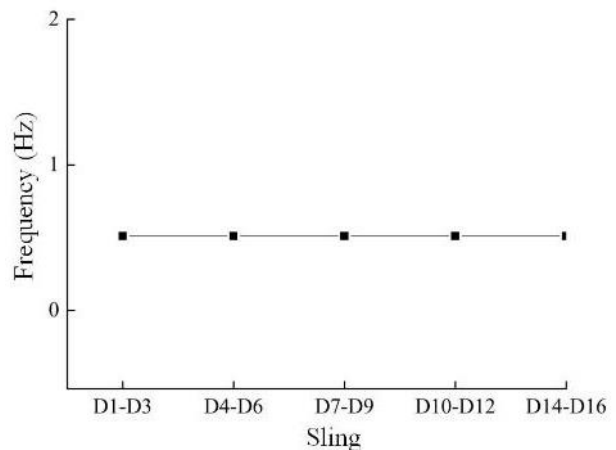


Fig. 15 - First order transverse bending frequency of main tower under different cable damage

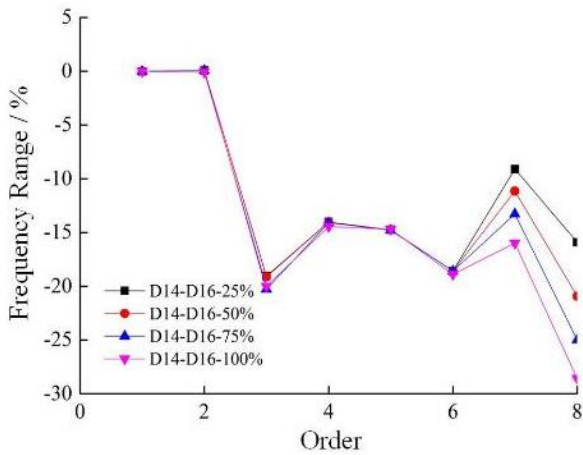


Fig. 16- Different damage frequency variation of slings D1-D3

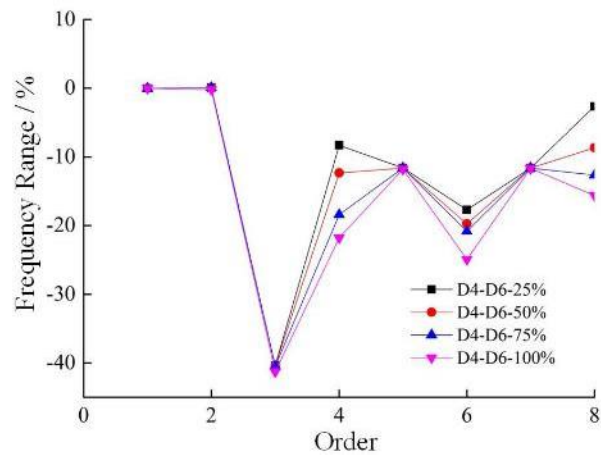


Fig. 17- Different damage frequency variation of slings D4-D6

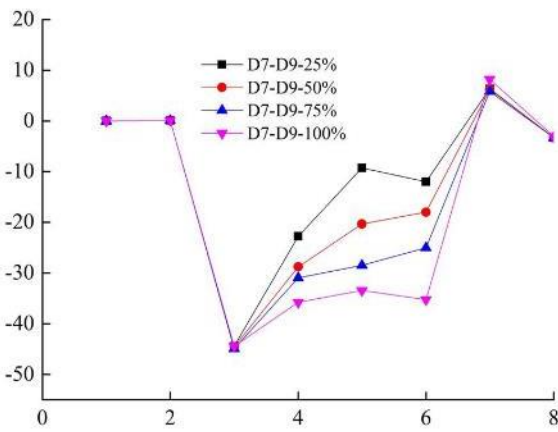


Fig. 18 - Different damage frequency variation of slings D7-D9

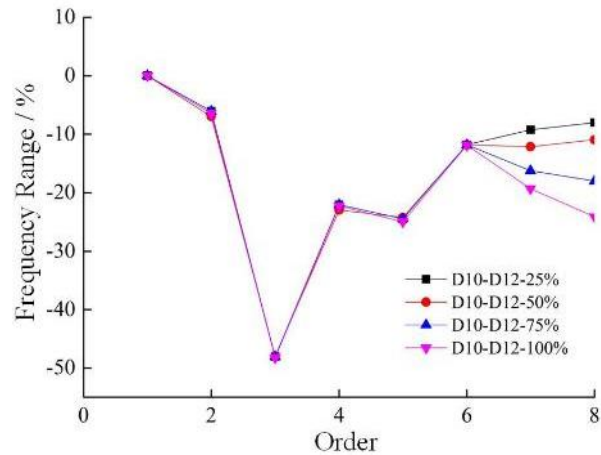


Fig. 19 - Different damage frequency variation of slings D10-D12

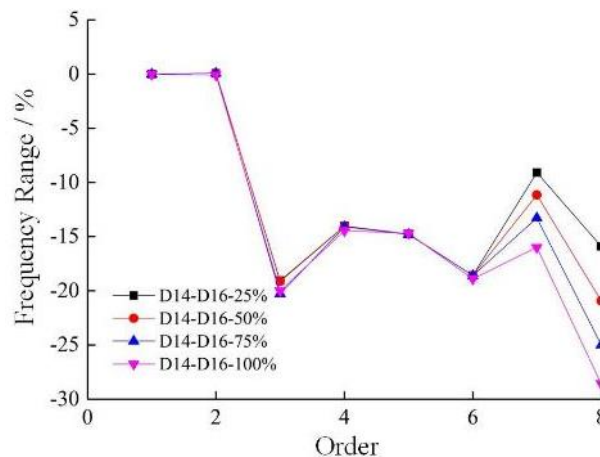


Fig. 20 - Different damage frequency variation of slings D14-D16

In order to explore the influence of different damage degrees of cables on the bridge's natural vibration frequency, D1-D3, D4-D6, D7-D9, D10-D12 and D14-D16 for short cables, middle short cables, middle cables, middle long cables and long cables were taken to analyze the natural vibration characteristics under different damage degrees respectively. When the damage degree

are 25%, 50%, 75% and 100% respectively, the elastic modulus are taken as 1.5×10^5 MPa, 1×10^5 MPa, 0.5×10^5 MPa and 1×10^5 MPa respectively.

After the short cables D1-D3 damage, the frequency variation of three pairs of cables under different damage degree is shown in Figure 16. After the middle long cables D4-D6 damage near the cable tower, the frequency of three pairs of cables D4-D6 under different damage degrees is shown in Figure 17. When the middle arch rib long cables D7-D9 are damaged, the frequency of three pairs of cables D7-D9 under different damage degrees is shown in Figure 18. The frequency of long cables D10-D12 in the far tower under different damage degrees is shown in Figure 19. The frequency variation of short cables D14-D16 under different damage degrees is shown in Figure 20. As it can be seen from Figure 16, under the condition of short cable damage near the tower, the frequency variation amplitude presents a parabolic change of the upper opening. Under different damage degrees, the variation effect is mainly reflected in that the transverse bending mode of the arch (the 4th mode) and the transverse bending mode of the tower (the 5th mode) have almost no effect on the beam mode. As it can be seen from Figure 17, when the long cables D4-D6 near the tower are damaged, the frequency changes irregularly. Under different damage degrees, the variation effect is mainly reflected in the transverse and flexural modes of the arch (the fourth and fifth modes), and it has almost no effect on the beam mode and tower mode. As it can be seen from Figure 18, when the long cables D7-D9 near the tower are damaged, the variation of frequency presents a parabolic change of the upper opening. Under different damage degrees, the influence of variation is mainly reflected in the transverse bending mode of the tower and the transverse bending mode of the arch. As can be seen from Figure 19 and Figure 20, under the condition of damage to the long cable away from the tower and the short cable away from the tower, the frequency variation amplitude presents irregular changes. Under different damage degrees, the variation effect is mainly reflected in the beam tower vertical bending mode (mode 7 and mode 8), and it has almost no effect on the arch mode.

CONCLUSION

In this paper, the self-vibration characteristics of the cable/sling under the damage of the cable-stayed arch bridge without back cable are analysed. The natural vibration frequency and its variation rule of bridges with different cable/sling damage and different cable damage degree are studied. The results of the study are as follows:

- (1) There is no torsional mode in the first several modes of the bridge. It is shown that the special-shaped arch boom ensures the transverse mechanical performance of the broad section main beam, and makes the main beam of the cable-stayed arch bridge have a large torsional rigidity and a good ability to resist torsional deformation.
- (2) With the increase of damage cable number, the frequency of 1st order vertical bending of main beam and the frequency of 1st order vertical bending of main tower are linearly decreasing, and the natural vibration frequency of bridge is the smallest when S9 cable is damaged. With the increase of the number of the damage sling, the frequency of the 1st order vertical bending of the main beam and the frequency of the 1st order vertical bending of the main tower are linearly increasing.
- (3) The frequency of the short cable varies regularly under different damage conditions, and the damage is mainly reflected in the vertical bending mode of the low-order main beam (the second mode). Under the different damage of the middle length cable, the damage is mainly reflected in the 1st order vertical bending mode of the tower, the 1st order transverse bending mode of the arch and the 2nd order transverse bending mode of the arch. The damage of long stay cable is mainly reflected in the first order vertical bending mode of the tower and the first order transverse bending mode of the arch. With the increase of damage degree, the frequency variation

amplitude becomes larger and larger, which has little effect on the beam bending mode and the tower transverse bending mode.

(4) The vertical stiffness of the main tower and the transverse stiffness of the wide main beam should be taken into account in the design of the bridge with no back cable and arch combination structure. Special attention should be paid to the construction and maintenance of long stay cables, which will affect the performance of the whole bridge. It is better to scatter the suspends of the arch to increase the transverse stability of the main beam.

REFERENCES

- [1] Sun Quansheng, Han Hongguang. Analysis of Mechanical Behavior of Cable-stayed Arch Bridge Without Back Cable [J]. The Chinese and Foreign Road, 2015,35(1):204-208.
- [2] Wang Lianxiang, Zhou Shuixing. The cable-stayed arch composite bridge in putrajaya city, Kuala Lumpur, Malaysia[J]. World Bridges, 2004(4)
- [3] Ge Junying, Su Mubiao. The Method of Cable Damage Simulation for Cable-stayed Bridges and Its Influence on the Distribution of Cable Force and Defection. [J]. China Railway Science,2016,37(3):30-37.
- [4] Sun Quansheng, Zhang Kexin. Analysis of the Influence of Cable Damage on the Vibration Characteristics of Backless Cable-stayed Bridges[J]. The Chinese and Foreign Road,2016,36(1):144-148.
- [5] Xuan Jiming, Shen Fuxing. Research and engineering application of bridge detection technology [J]. Bridge Construction,2007:158-162 .
- [6] Xiang Haifan. Theory of Higher Bridge Structure[M]. BeiJing: China Communications Press, 2007 .

APPLICATION OF GEOMATICS METHODS IN THE RESEARCH OF STRUCTURES OF HISTORICAL KITCHENS

Miroslava Cejpová¹, Zdeněk Poloprutský², Štěpánka Poučová¹, Adam Bujok¹ and Michael Rykl¹

1. CTU in Prague, Faculty of Architecture, Department of Architectural Conservation, Thákurova 9 166 29 Prague 6 Dejvice, Czech Republic
2. CTU in Prague, Faculty of Civil Engineering, Department of Geomatics, Thákurova 7/2077 166 29 Prague 6 Dejvice, Czech Republic; zdenek.poloпрutsky@fsv.cvut.cz

ABSTRACT

The article deals with metric survey documentation of medieval and early modern kitchens preserved in various types of buildings in the Czech Republic. Historic kitchens are important but still neglected technical monuments in terms of knowledge of their functional and structural aspects. As part of the student scientific project, surveys and metric survey documentation were carried out, which are the bases for the creation of diagrams of the spatial and structural arrangement of medieval and early modern kitchens. For the article, five very well-preserved kitchens were selected which represent three construction types of historical kitchens. For selected examples, their current metric survey documentation was evaluated. According to its quality and according to the character of a particular kitchen, the method of new metric survey documentation was chosen – 3D geodetic measurement (total station), Terrestrial Laser Scanning (point cloud and 3D model) and close range photogrammetry (point cloud and textured 3D model). The aim was to test and evaluate the informative possibilities of these technologies. Outputs are the description and the metric survey documentation of the selected kitchens. These outputs will be used in the passports of individual buildings to evaluate their construction development. The documentation will also allow the creation of generalizing schemes of spatial and structural arrangement of the individual types of kitchens.

KEYWORDS

3D modelling, Building Archaeology Survey (BAS), Computer Aided Design (CAD), Close-range photogrammetry, Geographic Information Systems (GIS), Historical kitchens, Terrestrial Laser Scanning (TLS)

INTRODUCTION

The article deals with metric survey documentation for research of historical kitchens in the Czech Republic. For a deeper knowledge of these parts of historical buildings, it is first necessary to obtain credible metric survey documentation that will allow the recognized facts to be correctly interpreted. As these are spatially complex systems, interdisciplinary cooperation is a necessity. Therefore, the article also evaluates the specifics and possibilities of application of digital 3D technologies in evaluating the spatial and structural arrangement of five selected kitchens. The outputs will be used as bases for passports of the individual buildings, for the evaluation of building development and the typology of the kitchens and for the presentation of results.

In terms of knowledge of their functional and structural aspects, the historical kitchens are important but still neglected technical monuments. Food preparation, its quality, quantity, level of

processing and culture of serving, in the past as well as today, have always been, still are and probably will be one of the main ways to present one's social status, etc. Therefore, the kitchen was an important place of a house or a residence, which was repaired, improved and modernized.

So far, the metric survey documentation of kitchens in the Czech Republic has been carried out mainly within the documentation and focus of the entire building or area. Therefore, only the basic documentation of floor plans, in some cases sections and views, and photo documentation prevails. Detailed metric survey documentation of the historical kitchen was carried out, for example, in the area of Grabštejn Castle as part of a university thesis in 2016 [1]. At present, the rapid development of technologies for documentation and visualization of monuments enables the creation of digital 3D models. For example, the kitchen of the ruins of Roupov Castle was processed in 2017. Schemes of the spatial and structural arrangement of medieval and early modern kitchens have so far been solved and presented abroad in the framework of popular-science literature or installations and sightseeing tours on specific buildings.

This article presents the specifics and pitfalls of surveying of historical kitchens and the possibilities of current measurement technologies for their documentation.

Types of structures of historical kitchens

Research into the functioning and construction development of kitchens and their documentation has not been at the forefront of research interest yet. The author dealt with the kitchens at medieval castles in Bohemia and France as a part of her studies and professional practice [2, 3]. In the Czech Republic, historians have been dealing with this issue since the 1990s. The initial interest in the study of court society [4–9] was transferred to the kitchens themselves [9–11] and attention was paid to them in the study of structural design of buildings [12].

The chosen method of smoke extraction had the greatest influence on the construction of the kitchens. Unfortunately, they are the vaults and chimneys that disappeared on the ruins soon after the trusses had collapsed, and on standing buildings they are often repaired or rebuilt after the onset of draft chimneys. Within the Czech Republic, only a few historical kitchens have been preserved without major reconstructions to this day. To determine the method of the smoke extraction from the kitchen, our team studies and compares individual kitchens and creates generalized schemes of their spatial and structural arrangement. So far, six basic types of smoke extraction have been defined¹:

Type 1: Kitchen, where the vault of the smoke-part of the kitchen forms the smoke-part of the chimney.

Type 2: Kitchen, where the smoke-part of the chimney passes through the ceiling of the kitchen and extends into the floor above the kitchen.

Type 3: Large kitchen with several chimneys located around the perimeter of the room on the floor above the kitchen.

Type 4: Large kitchen vaulted with 4-6 fields of cross vault, i.e. to 1-2 on pillars or columns. One vaulted field was omitted and replaced by a smoke-part of the chimney.

Type 5: Kitchen, where vault contributes to the direction of smoke into the chimney, e.g. a slightly rising barrel vault.

Type 6: Kitchen, in which the so-called Collar (Mantel) caught and discharged smoke into the chimney.

1 These conclusions were presented at the Castrum Bene 16 conference [13], the proceedings are in press currently.

The article presents five examples of very well-preserved kitchens, which illustrate the three types of structures of historical kitchens.

METHODS

For the research of medieval and early modern kitchen, the quality metric survey documentation is essential. This is also irreplaceable when comparing individual buildings and determining the development of both entire kitchens and certain structural elements. The metric survey documentation of the examined kitchen could usually be obtained in several ways:

1. Archival survey – finding available metric survey documentation
2. New detailed survey
3. Addition of older metric survey documentation with a new more detailed survey²

Since different types of data sets were combined with each other, it was necessary to establish uniform reference scale. The reference scale was selected 1: 50, which is most often used and can be very effectively applied when processing a 2D survey documentation (drawings), 3D point clouds or models [14–18].

Archival survey

We always start our work by finding and collecting archival metric survey documentation (most often in the archives of the territorially relevant heritage institute or building office or in the state archive). However, the accuracy of older plans is proportional to the time of origin and purpose of the acquisition, and thus requires a critical analytical approach³. While the plans from the 18th and 19th century mainly provide information on the construction development of the building, the plans from the second half of the 20th century tend to be of very high quality. Even here, however, we encounter problems, because the space of the kitchen is not often surveyed in detail enough or the situation has changed since the time of the survey. In such cases, it is usually sufficient to perform a detailed survey of the monitored area only and thus subsequently supplement the older metric survey documentation. If the older metric survey documentation does not exist or cannot be used, a new detailed survey must be performed.

Geographic Information System (GIS)

Digitized archival metric survey documentation can be transformed into any coordinate system, which is defined by a sufficient number of identical points. For georeferencing scanned plans, the *affine transformation* [19] can be selected, which takes into account the different distortion of the plan sheet in the longitudinal and transverse direction⁴. If the number of identical points is excessive (more than 3), the accuracy of the transformation can be estimated and the deviations in the position of the identical points can be compensated by the *least squares method*. Due to the fact that cadastral maps are available in digital vector form for almost the entire territory of the Czech Republic today [20], it was possible to georeference the archival metric survey documentation into

2 It was a detailed survey of the kitchen, for its location within the building, we used an older metric survey documentation.

3 The requirements and the most common shortcomings of metric survey documentation for the needs of heritage preservation are described in [14].

4 The use of a higher degree of transformation leads to smaller deviations at identical points, but to larger local deformations.

the S-JTSK system (EPSG: 5514). The corners of the building were chosen as identical points or the network of crosses was used, if available. We successfully used GIS software ArcMap, v. 10.7.1 [21] to process these data sets.

Computer Aided Design (CAD)

Current CAD software solutions enable vector drawing and direct modelling of spatial objects. They contain specialized functions for this purpose. They also support the layering of a drawing or 3D model into thematic data layers. We successfully used AutoCAD [22] and MicroStation [23] software solutions for vectorization of georeferenced archival metric survey documentation and for the elaboration of new plans⁵.

New detailed survey

Ideally, the detailed survey was carried out so that it is divided into two parts taking place in parallel, which allows their mutual coordination and complementarity:

1. New detailed survey, i.e. instructed 3D geodetic measurement of the building, according to [14].
2. Identification, photo documentation, description and dating of building structures, according to [24].

The first point is based on the geodetic measurements with the total station, which is used to determine the spatial coordinates of points of interest⁶. Their coordinates are calculated by the *spatial polar method* [25]. Other alternatives or extensions are Terrestrial Laser Scanning (TLS) and Close-range photogrammetry (Crp). The second point is based on a tour of building structures and an understanding of their functions within a specific architectural solution.

Terrestrial Laser Scanning (TLS) and Close-range photogrammetry (Crp)

TLS is automated, i.e. non-selective, spatial data collection process – point cloud⁷. 3D laser scanners of various designs are used for this purpose. Data collection, i.e. measurement, takes place non-selectively, therefore it is necessary to select objects of interest during post-processing. At present, it is popular to use TLS, among other things, in heritage preservation [17, 18].

Crp is currently applied by solutions, i.e. procedures and systems, that allow, among other things, to process a coloured point cloud and a textured 3D model [16, 26, 27]. This makes them an alternative to TLS. In our cases, commercial photogrammetric software was used – Agisoft Metashape Professional, v. 1.6.4 [28].

RESULTS

The final outputs of the metric survey documentation, including individual types of the kitchens, are presented in the following sections.

5 Typically, these are floor plans, vertical sections, views or orthophotomosaics (final adjustment).

6 That is, the points of interest are selected selectively during the survey and their coordinates X, Y and Z are measured at the same time. The calculations use the spatial polar method, whose mathematical foundations are well described in the literature, e.g. [25].

7 A set of points with known X, Y, Z coordinates, colours, etc.

The first type of the historical kitchens

The first type of historical kitchens are kitchens, where the vault of the smoke-part of the kitchen forms the smoke-part of the chimney. It was supported by peripheral walls or an arched waist, which divided the kitchen space into a smoke-part and a clean-part. The clean-part of the kitchen used to be vaulted or flat-ceilinged. The chimney could be plastered on the outside or covered with gutter-tiles, plastering is more likely in the case of reinforcement of the chimney ribs on the outside. There were no more floors above the kitchen. A protruding or monastery vault was used for the construction of the smoke-part of the chimney.

The monastery vault was used in the **St. Agnes Monastery in Prague**. The protruding vault was in the shape of a regular octagonal truncated pyramid, a regular quadrilateral truncated pyramid, or an irregular quadrilateral truncated pyramid. We documented the asymmetrical irregular four-sided vault of the kitchen in the **Old Palace in Jindřichův Hradec**. The construction of regular chimneys is the same as the construction of helmets used to roof the towers.

St. Agnes Monastery in Prague

St. Agnes Monastery is situated on the right bank of the Vltava river, in Old Town area called „Na Františku“. The monastery of Poor Clares of the Order of Saint Clare and Franciscans was founded around 1231. The kitchen, based on a square floorplan with the monastery vault and ribs connecting on a chimney at the top, was built between 1238–1245 [29, 30]. The kitchen has been recognized in the past and today it is a part of the exhibition. The chimney on the vault is a new formation, the original has not been preserved. This kitchen belongs to the few medieval kitchens frequented in the literature.

At present, it is a popular tourist attraction. Therefore, it was necessary to carry out the detailed survey outside the opening hours and in the shortest possible time. For detailed survey, we used Crp and TLS. For post-processing, we used RealityCapture software [31] and Metashape Professional software [28].

Old Palace in Jindřichův Hradec

The area of Jindřichův Hradec Castle and Château, which has grown to the area of today's three and a half hectares over the centuries, was gradually built on the site of an older Slavic fortified settlement, documented by archaeological research since the 10th century. The construction of a medieval castle, called "Novum castrum" (New Castle) in the oldest historical report from 1220, is associated with the name of Jindřich Vítkovec [32].

The so-called **Old Palace** is partly basement, it has three floors and two mezzanines. It has undergone a complex construction development. Around 1400, the kitchen was established during the building alterations that took place on the north-west side of the palace in a place where it is close to the round bergfrit. The older part of the palace was followed by a tract, which joined the tower on the north side. Above the kitchen, a massive chimney was topped by a decorative head. Sometime before 1492, the youngest tract of the **Old Palace** was raised by another floor. This new floor was located roughly at the height of the kitchen. This enabled its reconstruction. The older small kitchen became part of the chimney and the kitchen itself was moved to a newly built room, from which the entrance to the palace was established. Access to the kitchen for cooks and catering was through the porch.



Fig. 1 – Kitchen in the area of the St. Agnes Monastery in Prague, exterior, view to the North



Fig. 2 – Kitchen in the area of the St. Agnes Monastery in Prague, interior, orthophotomosaic, view to the North



Fig. 3 – Jindřichův Hradec, chimney of the castle kitchen in the Old Palace, exterior, view to the West



Fig. 4 – Jindřichův Hradec, kitchen in the Old Palace, interior, floor plan from TLS

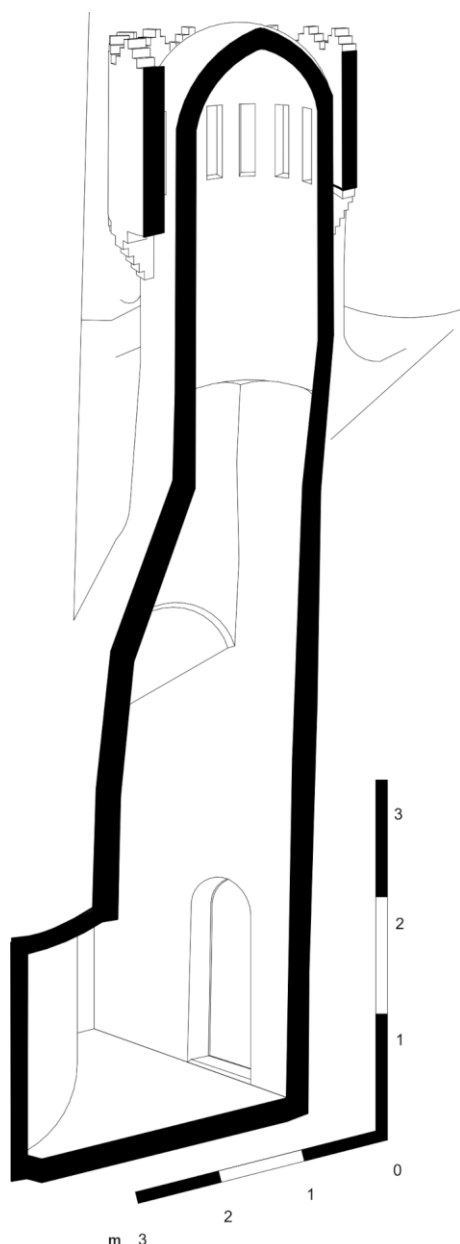


Fig. 5 – Jindřichův Hradec, axonometric section through the chimney of the kitchen in the Old Palace, state of knowledge and interpretation of found situations as of 11/2020

Again, it is a popular tourist attraction. Therefore, it was necessary to carry out detailed survey outside the opening hours and in the shortest possible time. For detailed survey, we used TLS, which we supplemented operationally with Crp. Geomagic Wrap 2017 software [35] and Metashape Professional software were used for post-processing.

The so-called Old Palace is partly basement, it has three floors and two mezzanines. It has undergone a complex construction development. Around 1400, the kitchen was established during the building alterations that took place on the north-west side of the palace in a place where it is close to the round bergfrit. The older part of the palace was followed by a tract, which joined the tower on the north side. At the time of construction, this tract was one floor lower than the older part of the palace. In the space of its attic, the small kitchen was inserted into the narrow space between the northern part of the palace and the bergfrit, connected by a door to the third floor of the original palace. Above the kitchen, a massive chimney was topped by a decorative head. Sometime before 1492, the youngest tract of the Old Palace was raised by another floor. This new floor was located roughly at the height of the kitchen. This enabled its reconstruction. The older small kitchen became part of the chimney and the kitchen itself was moved to a newly built room, from which the entrance to the palace was established. Access to the kitchen for cooks and catering was through the porch.

Again, it is a popular tourist attraction. Therefore, it was necessary to carry out detailed survey outside the opening hours and in the shortest possible time. For detailed survey, we used TLS, which we supplemented operationally with Crp. Geomagic Wrap 2017 software [33] and Metashape Professional software were used for post-processing.

Křivoklát

The Křivoklát Royal Castle was founded at the beginning of the second quarter of the 13th century, the first stage of its construction lasted until the 1380s. A major reconstruction took place under Wenceslas IV. (1378-1419). After the great fire of 1422, it was only temporarily repaired and a major construction intervention was carried out here by Jiří Poděbradský (1458-1471). It was magnificently rebuilt during the reign of Vladislav Jagellonský from the late 1470s to the 1520s. In 1643, the castle was destroyed by fire. In 1658, the heavily damaged castle was

pawned and sold shortly afterwards. A brewery was developed in the Lower Castle; the rest of the castle was only maintained. Another great fire damaged the castle in 1826. In the second half of the 19th century and the first third of the 20th century, the castle was restored. In 1970s, heritage modifications and surveys were started.

We know the kitchens in Křivoklát from the Vladislav reconstruction only. Until now, a small kitchen is preserved on the first floor of the tower Huderka. From the status of the castle before and after the fire of 1643, it is known the form of two kitchens in the northern front of the Lower Castle

[34]. The first completely disappeared. The second is partially preserved in the mass of the house No. 132, which is adjacent to the complex of palaces of the Upper Castle.

The BAS [35] was carried out for the house, which was deepened by our team members as part of the preparation of the scheme. In the part of the building where the kitchen was, there is a shop with a warehouse currently, so the rooms are filled with furniture and goods. Therefore, we used the quality metric survey documentation of the castle from 1966-67 to create plans [36].

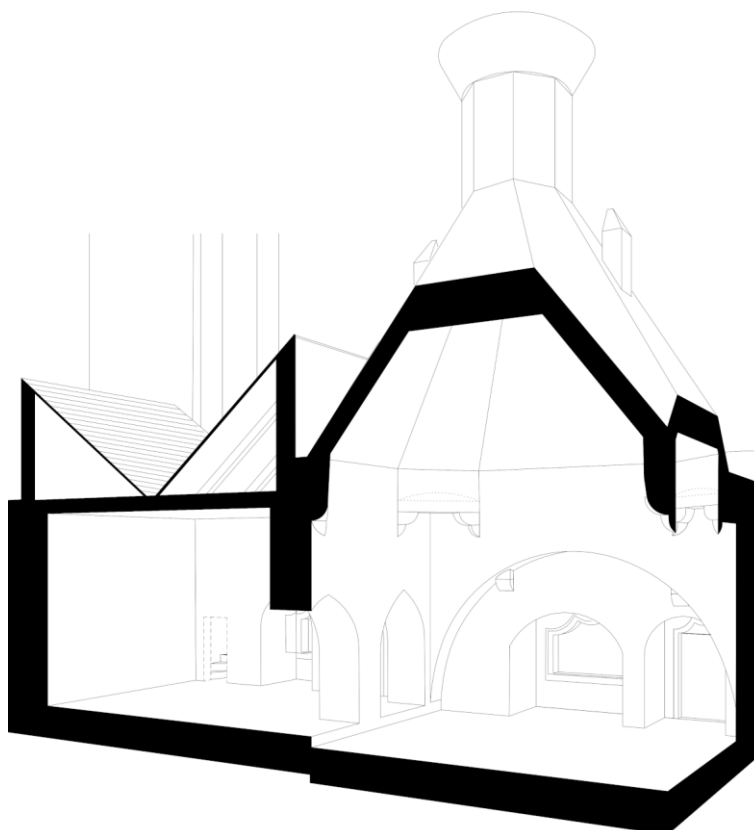


Fig. 6 – Křivoklát, axonometric section through the kitchen, reconstruction of the original appearance, state of knowledge and interpretation of found situations as of 11/2020

The second type of the historical kitchens

The second type of historical kitchens are kitchens, where the smoke-part of the chimney passes through the ceiling of the kitchen and extends into the floor above the kitchen. These kitchens are so large that the central chimney could not cover their entire space. In that case, the open fire-platform was located in the centre of the room. There were columns or pillars⁸ around it. Waists or lintels were mounted on them, which carried the chimney, so that the fire-platform was accessible from all sides. The smoke-part of the chimney penetrated the floors above the kitchen. Structurally, it was a regular quadrilateral truncated pyramid formed by a protruding vault. An example is the kitchen at the castle in **Brtnice**.

⁸ For the older period, we have documented 4, for the younger period, we have documented up to 6.

Brtnice

The château in Brtnice stands on the site of a late Gothic castle, which was first mentioned in 1436. The extensive layout surrounds three courtyards and is surrounded by Gothic-Renaissance fortifications. The château buildings were built gradually. The late Gothic castle was rebuilt and completed in the Renaissance style, the expansion continued in the late Renaissance. Renovations of the château took place after the Thirty Years' War, after 1760, when the château burned down [37], and before the middle of the 19th century [38]. During the renaissance reconstruction, the kitchen was inserted into the ground floor of a Gothic tower in the wing separating the first and second courtyards. It was completed before 1604.

At present, it is not so frequented tourist attraction, i.e. with occasional tourist tours. This condition provided enough time for detailed survey and allowed the application of all measurement methods. Archival metric survey documentation from 1967-9 in the reference scale of 1 : 100 was georeferenced in the current cadastral map in GIS software. Using the archival metric survey documentation, it was possible to connect a new detailed survey with a total station to the S-JTSK (EPSG: 5514). The output of the detailed survey was the current floor plan in the reference scale of 1:50 and the coordinates of the control points for Crp and TLS. In this case, it was desirable to document also on the adjacent surroundings of the kitchen, i.e. selected adjoining rooms. TLS was used for this. Furthermore, it was desirable to document the interior of the kitchen using Crp in order to create orthophotomosaics capturing the vertical structures of the fireplace. From the point clouds created by TLS and Crp, a combined point cloud was created, which was used to drawing the new floor plan.

The third type of the historical kitchens

The third type of historical kitchens are large kitchens with several chimneys located around the perimeter of the room on the floor above the kitchen. The kitchen is vaulted, in the corners or in the centres of the sides of the kitchen there are openings in the vault, which led smoke into the chimneys located on the outside of the perimeter walls of the building. The so-called **Menhartka in Jindřichův Hradec** (around 1500), probably the most famous Czech castle kitchen, has chimneys in the corners. It functioned unchanged until the 19th century.

Menhartka in Jindřichův Hradec

The mass of the Menhartka tower, in which the kitchen is located, contains three vertical parts of approximately the same height. The plinth section has heavier masonry projecting 90 cm in front of the middle part. The protrusion is terminated by a sloping flat covered with gutter-tiles and stone slabs. The middle part is architecturally divided by corner chimneys of the kitchen and bays. The upper part consists of a tent roof covered with gutter-tiles. The plinth and middle part form the space of the kitchen. In the upper part, a representative room called "Courtroom" was, according to the fresco decoration [39].

Detailed survey was carried out during the same campaign as in the Old Palace. We used TLS for detailed survey. Due to the fact that it was a high building with black ceilings (from soot) and insufficient lighting⁹, it was the only measuring technology that made sense to apply under the given conditions. Geomagic Wrap 2017 software was used for post-processing.

⁹ It was a combination of insufficient natural light and the unavailability of sufficient artificial lighting.

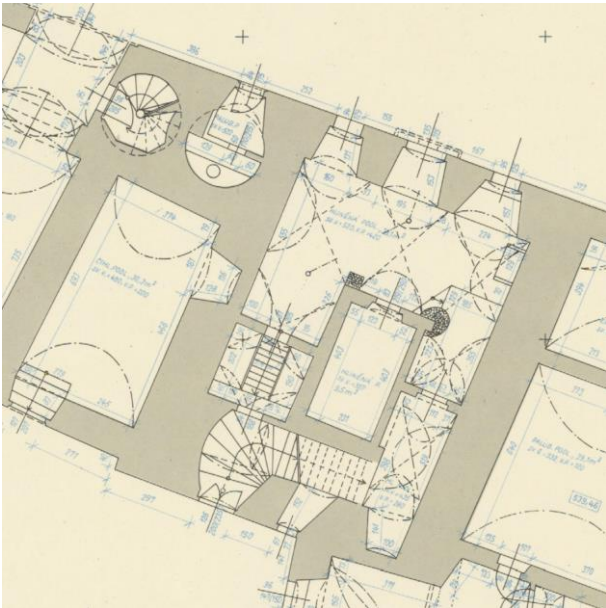


Fig. 7 – Kitchen in Brtnice - floor plan 1:100, 1967-1969

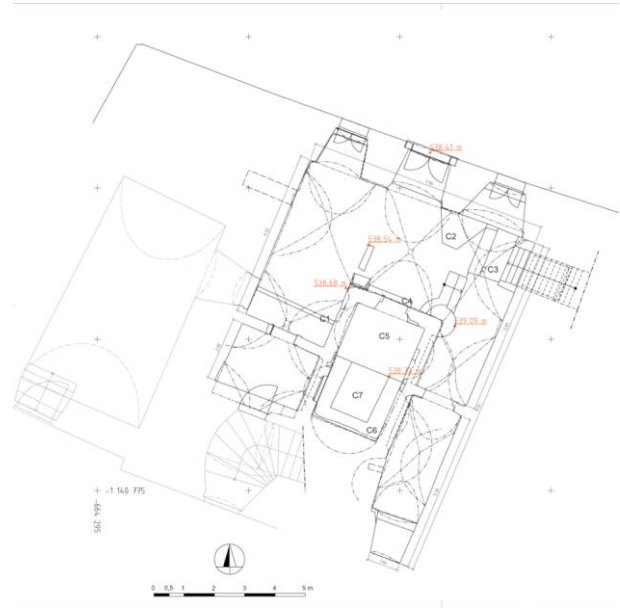


Fig. 8 – Kitchen in Brtnice - floor plan 1:50, present



Fig. 9 – Kitchen in Brtnice, orthophotomosaic 1:20 - view to the East

CONCLUSION

During the solution of our project, our own work-flow for the implementation of metric survey documentation and selection of measurement technologies proved to be successful:

1. The aim of the archival survey is to find and collect suitable archival metric survey documentation.
 - a) There is a high-quality archival metric survey documentation¹⁰ that can be georeferenced into the reference coordinate system, and which can be further used as a basis, only supplemented by additional surveys of some details, see **Křivoklát**.
 - b) There is a quality archival metric survey documentation that can be georeferenced to the reference coordinate system. However, its Level of Detail in the monitored kitchen-space is not sufficient. Therefore, it is necessary to supplement it with further detailed survey. The type of this survey depends on the character of the documented space, see **Brtnice**.
 - c) There is no suitable archival metric survey documentation, see **St. Agnes Monastery in Prague, Old Palace** and **Menhartka in Jindřichův Hradec**.
2. The aim of the detailed on-site survey is to get to know the object and, as a result, may influence the way of surveying.
 - a) The existing archival metric survey documentation¹¹ is used, see **Křivoklát**.
 - b) The existing archival metric survey documentation is supplemented, see **Brtnice**.
 - c) A new 3D geodetic survey of the building¹² is being implemented, see **St. Agnes Monastery in Prague, Old Palace** and **Menhartka in Jindřichův Hradec**.
3. The aim of the post-processing of the detailed survey is to create comprehensive sets of spatial data that can be further analysed according to the purpose of acquisition, see Figure 4 and Figure 11.
4. The aim of processing of final outputs is to create a comprehensive set of outputs that concisely describe and display the examined space, see Figure 5, Figure 6, Figure 8, Figure 9, Figure 11 and Figure 12.

The detailed on-site survey can be usually complicated in several types of building spaces:

- inaccessible spaces – an example is the middle vertical part of **Menhartka**, where it is not visible through the ledge and into the chimney orifices, so terrestrial measurements cannot be used.
- confined spaces where it is not possible to get a sufficient distance, see **Old Palace** and **Křivoklát**

10 Ideally, we were looking for older metric survey documentation processed by the measuring group of SÚRPMO, or another organization according to the requirements of SÚRPMO employees, because it is usually of high quality.

11 According to the evaluation of the documented space, it is necessary to choose the method of supplementing - updating or correcting the older metric survey documentation or creating a new one, if the older one is not usable.

12 The construction of some buildings may be such that the total station is the most efficient for the survey, i.e. buildings in good construction and technical condition without major reconstructions. For others, it may be the most effective to perform the survey using TLS or Crp.



Fig. 10 – Jindřichův Hradec, Menhartka kitchen, exterior, top view to the North-West

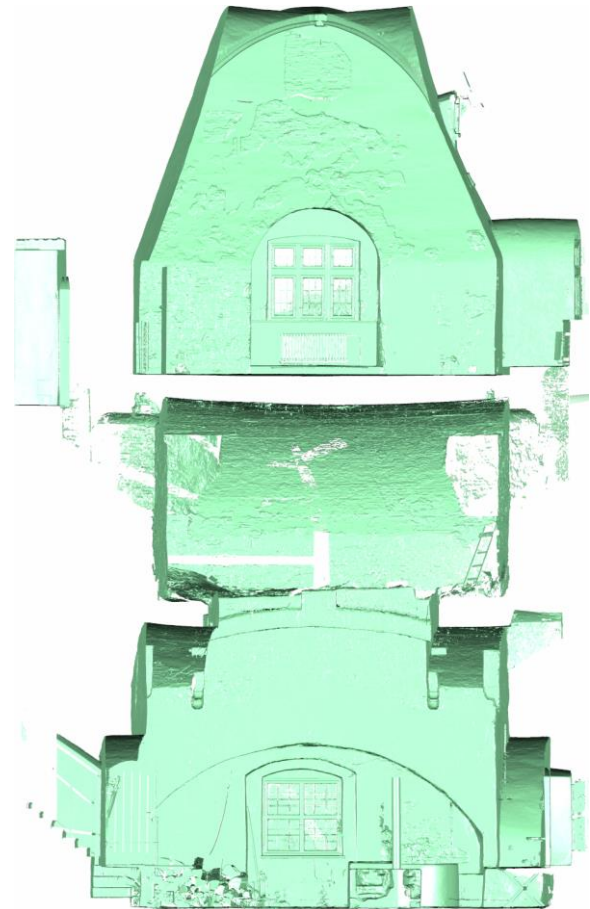


Fig. 11 – Jindřichův Hradec, Menhartka kitchen, interior, vertical section of 3D model from TLS, view to the North-West

- used spaces, i.e. living rooms, warehouses or shops, where spaces are cramped due to furniture, goods, etc., see **Křivoklát**
- spaces with dark to black walls – generally, complicate targeting when surveying with a total station and form monochromatic spaces, which are unsuitable for close photogrammetry; examples are the lower and middle vertical part of **Menhartka** and some parts of **Brtnice**
- spaces with significant architectural elements – examples can be, for example, vaulted ribs in the **St. Agnes Monastery in Prague**

Detailed survey using the total station is a universal solution. It is advantageous to apply it in cases where the required outputs are drawings – floor plans, etc., because it allows adapting the workflow of the survey to the desired output. When surveying larger or more complex buildings and combining different measurement technologies, it is necessary to create a uniform spatial framework, i.e. a survey net, for the whole campaign. When archival metric survey documentation is used, it is possible to focus on identical points in this way, which will enable the connection of data and surveys in GIS. In cases, where TLS or Crp is used, it is possible to measure the control points in this way. Its disadvantage is the time-consuming process of the survey, so its larger application is not advantageous in time pressure.

Detailed survey using the TLS is a fast automated solution that offers high demands on detailed shape fidelity during time pressure for the survey. Its advantages are the possibility of independent application without the support of other technologies, independence from lighting

conditions when surveying and a colour of the scanned object. In some cases, it may be advantageous to measure several identical or control points in order to be able to connect to the survey with archival metric documentation or other performed surveys. Confined and inaccessible spaces and spaces with dark to black walls are usually advantageous to survey using TLS. There are usually crucial a shape and a structure of constructions not colour. Its disadvantage is the time-consuming post-processing of large amounts of spatial data. Furthermore, in some cases, the export of bases for the elaboration of drawings¹³ – floor plans, vertical sections, etc. can be complicated.

Detailed survey using the Crp is an alternative to TLS. In our practical experience, it is advantageous if the control points are measured using the total station. Its disadvantages are the dependence on the lighting conditions during the survey and colour of the photographed object, when monochromatic surfaces are problematic. On the contrary, its advantage is that it allows the creation of orthophotomosaics, which can be supplemented with drawings. This is especially true for vertical views and sections, which thus increase their informative value.

The historical kitchens, together with smoke-extracting structures, are spatially very complex. In addition, due to frequent modifications, the found situations in the kitchens are also very complicated. The presented detailed surveys show that it is possible to create clear 3D models and provide documentation with maximum data retention.

The detailed metric survey and the clarification of constructions will allow defining basic features of historical kitchens, which can be recognized both in the ruins (especially castles, fortresses) and in a standing but rebuilt building. This will then assist in the identification of the remains of the original kitchens during the Building Archaeology Surveys (BAS) of the buildings as well as in the design of building modifications and repairs.

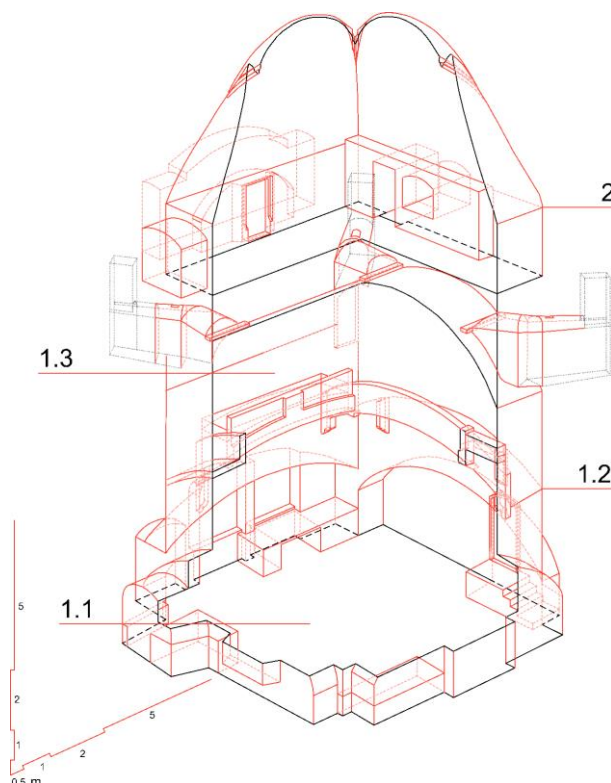


Fig. 12 - Jindřichův Hradec, axonometric section of Menhartka kitchen (1.1 - space under segmental waists; 1.2 - waists; 1.3 - chimney orifice; 2 - Courtroom), state of knowledge and interpretation of found situations as of 11/2020

¹³ Historical buildings usually have an irregular floor plan. In the metric survey documentation of historical buildings for the needs of heritage preservation, it is a common practice that to increase its informative value, vertical sections of the building are inclined in floor plan, e.g. parallel to the selected wall, or divided into partial parts, which are shifted relative to each other in floor plan.

ACKNOWLEDGEMENTS

This work was supported by the Grant Agency of the Czech Technical University in Prague, grants No. SGS19/116/OHK1/2T/15. We would also like to thank our colleague Jaroslav Šedina² for processing Figure 4 and Figure 11.

REFERENCES

- [1] PEXA, Ladislav. *Grabštejn castle (Liberec) - metrical documentation of selected part*. Prague, 2016. BACHELOR THESIS. FCE CTU in Prague, Departments of Geomatics.
URL: <https://dspace.cvut.cz/handle/10467/78841>
- [2] CEJPOVÁ, Miroslava. Nástin vývoje české hradní kuchyně. In: *XVIII. celostátní konference středověké archeologie: Archaeologia Historica*. Brno: Muzejní a vlastivědná společnost, 1987, 367–374. ISBN 0231-5823.
- [3] CEJPOVÁ, Miroslava. Topenišťe dochovaná v hradních kuchyních. In: *1. konference SHP – Vývoj a funkce topenišť, 4. – 6. června 2002, Zahrádky u České Lípy: Sborník příspěvků z 1. konference stavebně historického průzkumu 4. - 6. 6. 2002 v Zahrádkách u České Lípy. Vývoj a funkce topenišť: věnováno památce Romana Kursy*. Praha: Unicornis, 2003, 85–94. ISBN 978-80-86562-00-1.
- [4] BŮŽEK, Václav, ed. Život na dvoře a v rezidenčních městech posledních Rožmberků. *Opera historica: časopis pro dějiny raného novověku*. 1993, **3**. ISSN 1805-790X. URL: <https://www.opera-historica.com/>
- [5] BŮŽEK, Václav, ed. Poslední páni z Hradce. *Opera historica: časopis pro dějiny raného novověku*. 1996, **6**. ISSN 1805-790X. URL: <https://www.opera-historica.com/>
- [6] BŮŽEK, Václav, ed. Aristokratické rezidence a dvory dvory v raném novověku. *Opera historica: časopis pro dějiny raného novověku*. 1999, **7**. ISSN 1805-790X. URL: <https://www.opera-historica.com/>
- [7] BŮŽEK, Václav, ed. Slavnosti a zábavy na dvorech a v rezidenčních městech raného novověku. *Opera historica: časopis pro dějiny raného novověku*. 2000, **8**. ISSN 1805-790X. URL: <https://www.opera-historica.com/>
- [8] HRDLIČKA, Josef. *Hodovní stůl a dvorská společnost: strava na raně novověkých aristokratických dvorech v českých zemích*. Vyd. 1. České Budějovice: Historický ústav Jihočeské univerzity, 2000. Monographia historica, sv. 1. ISBN 978-80-7040-462-1.
- [9] DUCHOŇOVÁ, Diana a Tünde LENGYELOVÁ. *Hradné kuchyne a šľachtické stravovanie v ranom novoveku: radosti slávností, strasti každodennosti*. Bratislava: Veda, vydavateľstvo SAV, 2016. ISBN 978-80-224-1538-5.
- [10] KORBELÁŘOVÁ, Irena, Miroslava CEJPOVÁ, Hana FABIÁNOVÁ, Petra KANIOVÁ, František KOLÁŘ, Barbara MARETHOVÁ, Kateřina BŘEČKOVÁ, Dalibor PRIX, Romana ROSOVÁ, Hedvika SEDLÁČKOVÁ a Romuald TURAKIEWICZ. *S knížaty u stolu kuchyně a kultura stolování na středověkých vévodských dvorech v Opavě a Ratiboři*. Ostrava, Czech Republic: Národní památkový ústav, 2018. ISBN 978-80-88240-08-2.
- [11] ŠTAJNOCHR, Vítězslav. *Zámecké kuchyně: zámecké kuchyně v kontextu evropského vývoje*. Praha: Národní památkový ústav, 2017. ISBN 978-80-7480-093-1.
- [12] ŠKABRADA, Jiří. *Přehled vývoje historických stavebních konstrukcí*. Pardubice: Univerzita Pardubice, 2016. ISBN 978-80-7395-992-0.
- [13] CEJPOVÁ, Miroslava. Die Bauform der Burgküchen in den böhmischen Ländern im 13. – 16. Jahrhundert. In: *The 16th International Castellological Conference: Castle and Economy: Castrum Bene 16 - Castle and Economy: Book of Abstracts and Fieldtrip Guides*. Kutina – Sisak, Croatia: Muzej Moslavine Kutina, Povijesna udruga Moslavina (PUM), 2019. ISBN 978-953-7135-62-1.
URL: http://www.ffzg.unizg.hr/pov/pov2/files/10obavijesti/2019/castrum_bene_final.pdf
- [14] VESELÝ, Jan. *Metric survey documentation of historic buildings for use in heritage management*. Prague: National Heritage Institute, 2014. ISBN 978-80-86516-79-0.

- [15] PÖCHTRAGER, M., G. STYHLER-AYDIN, M. DÖRING-WILLIAMS a N. PFEIFER. AUTOMATED RECONSTRUCTION OF HISTORIC ROOF STRUCTURES FROM POINT CLOUDS – DEVELOPMENT AND EXAMPLES. *ISPRS Annals of Photogrammetry, Remote Sensing and Spatial Information Sciences*. 2017, **IV-2/W2**, 195–202. ISSN 2194-9050. DOI: 10.5194/isprs-annals-IV-2-W2-195-2017
- [16] CHIABRANDO, F., M. LO TURCO a F. RINAUDO. MODELING THE DECAY IN AN HBIM STARTING FROM 3D POINT CLOUDS. A FOLLOWED APPROACH FOR CULTURAL HERITAGE KNOWLEDGE. *ISPRS - International Archives of the Photogrammetry, Remote Sensing and Spatial Information Sciences*. 2017, **XLII-2/W5**, 605–612. ISSN 2194-9034. DOI: 10.5194/isprs-archives-XLII-2-W5-605-2017
- [17] TOMMASI, C., C. ACHILLE a F. FASSI. FROM POINT CLOUD TO BIM: A MODELLING CHALLENGE IN THE CULTURAL HERITAGE FIELD. *ISPRS - International Archives of the Photogrammetry, Remote Sensing and Spatial Information Sciences*. 2016, **XLI-B5**, 429–436. ISSN 2194-9034. DOI: 10.5194/isprs-archives-XLI-B5-429-2016
- [18] LUHMANN, T., M. CHIZHOVA, D. GORKOVCHUK, H. HASTEDT, N. CHACHAVA a N. LEKVEISHVILI. COMBINATION OF TERRESTRIAL LASERSCANNING, UAV AND CLOSE-RANGE PHOTOGRAMMETRY FOR 3D RECONSTRUCTION OF COMPLEX CHURCHES IN GEORGIA. *ISPRS - International Archives of the Photogrammetry, Remote Sensing and Spatial Information Sciences*. 2019, **XLII-2/W11**, 753–761. ISSN 2194-9034. DOI: 10.5194/isprs-archives-XLII-2-W11-753-2019
- [19] LUHMANN, T., Stuart ROBSON, Stephen KYLE a Jan BOEHM. *Close-range photogrammetry and 3D imaging*. Berlin: De Gruyter, 2014. De Gruyter textbook. ISBN 978-3-11-030269-1.
- [20] CZECH OFFICE FOR SURVEYING, MAPPING AND CADASTRE. *Atom download service* [online]. 2018 [2018-05-16]. URL: <http://atom.cuzk.cz/>
- [21] ESRI. *ArcMap: ArcGIS Desktop* [online]. 2020 [2020-09-02]. URL: <http://desktop.arcgis.com/en/arcmap/>
- [22] AUTODESK. *Autodesk Knowledge Network* [online]. 2020 [2020-09-02]. URL: <https://knowledge.autodesk.com/>
- [23] BENTLEY SYSTEMS. *Bentley - Infrastructure and Engineering Software and Solutions* [online]. 2020 [2020-09-02]. URL: <https://www.bentley.com/en>
- [24] BERÁNEK, Jan a Petr MACEK, ed. *Building Archaeology Survey: A Methodology*. Prague: National Heritage Institute, 2015. ISBN 978-80-7480-037-5.
- [25] MCCORMAC, Jack, Wayne SARASUA a William J. DAVIS. *Surveying: 6th Edition*. Hoboken, N.J.: Wiley, 2013. ISBN 978-0-470-49661-9.
- [26] MARČIŠ, Marián a Marek FRAŠTIA. Photogrammetric Measurement of a Wooden Truss. *Slovak Journal of Civil Engineering*. 2018, **26**(4), 1–10. ISSN 1338-3973, 1210-3896. DOI: 10.2478/sjce-2018-0022
- [27] WESTOBY, M.J., J. BRASINGTON, N.F. GLASSER, M.J. HAMBREY a J.M. REYNOLDS. ‘Structure-from-Motion’ photogrammetry: A low-cost, effective tool for geoscience applications. *Geomorphology*. 2012, **179**, 300–314. ISSN 0169555X. DOI: 10.1016/j.geomorph.2012.08.021
- [28] AGISOFT. *Agisoft Metashape User Manual: Professional Edition, Version 1.6* [online]. 2020 [2020-09-02]. URL: https://www.agisoft.com/pdf/metashape-pro_1_6_en.pdf
- [29] WIKIPEDIA. *Convent of Saint Agnes (Prague)* [online]. 2020 [2020-10-01]. URL: [https://en.wikipedia.org/w/index.php?title=Convent_of_Saint_Agnes_\(Prague\)&oldid=947230221](https://en.wikipedia.org/w/index.php?title=Convent_of_Saint_Agnes_(Prague)&oldid=947230221)
- [30] SOUKUPOVÁ, Helena. *Anežský klášter v Praze*. Praha: Odeon, 1989. ISBN 978-80-207-0046-9.
- [31] CAPTURING REALITY. *RealityCapture: Mapping and 3D Modeling Photogrammetry Software* [online]. 2020 [2020-10-01]. URL: <https://www.capturingreality.com/>
- [32] NATIONAL HERITAGE INSTITUTE. *Jindřichův Hradec: Official web presentation* [online]. 2020 [2020-10-02]. URL: <https://www.zamek-jindrichuvhradec.cz/en>
- [33] 3D SYSTEMS. *Geomagic Wrap 3D Scanning Software* [online]. 2020 [2016-02-22]. URL: <http://www.geomagic.com/en/products/wrap/overview>
- [34] DURDÍK, Tomáš. *Ilustrovaná encyklopedie českých hradů*. Praha: Nakladatelství Libri, 2009. ISBN 978-80-7277-402-9.
- [35] LÍBAL, Dobroslav a A. LIŠKOVÁ. *Státní hrad Křivoklát. Stavebně historický průzkum. Dům čp. 132, 133*. Strojopis. 1985

- [36] ÚSTAV GEODÉZIE A KARTOGRAFIE PRO KRAJ STŘEDOČESKÝ A HL. M. PRAHY. STŘEDISKO MAPOVACÍ. *Křivoklát hrad. Zaměření. 1:50.* 1967
- [37] PLAČEK, Miroslav. *Hrady a zámky na Moravě a ve Slezsku.* Praha: Libri, 1996. ISBN 978-80-85983-08-1.
- [38] MĚŘÍNSKÝ, Zdeněk, Daniela NOVOTNÁ a Martina STRAKOVÁ. *Brtnice: rodiště Josefa Hoffmanna.* Brtnice: Město Brtnice, 2006. ISBN 978-80-254-1426-2.
- [39] VILÍMKOVÁ, Milada, Jan MUK a Jiřina MUKOVÁ. *Jindřichův Hradec, zámek. Stavebně historický průzkum.* Strojopis. 1976



EFFECTS OF LARGE-SCALE UNLOADING ON EXISTING SHIELD TUNNELS IN SANDY GRAVEL STRATA

WU Hao¹, MIAO Miao¹, ZHOU Hui^{1,2}, FENG Zhi-hua^{1,3}

1. Chang'an University, School of Highway, Xi'an, Shanxi, China; miaomiao@chd.edu.cn
2. CCCC Highway Consultants CO., Ltd., Beijing, China; 571493995@qq.com
3. Bridge and tunnel branch institute, Hebei Provincial Communications Planning and Design Institute, Shijiazhuang, Hebei, China; 1216819601@qq.com

ABSTRACT

The influence of large-scale unloading of soil on existing metro tunnels is a difficult problem in the operation of Metro in sandy gravel strata. In order to predict and control the tunnel deformation and ensure the safety and normal operation of the metro, three-dimensional numerical models are proposed in this study. These models based on the line 5 of Chengdu subway engineering and the adjacent unloading projects analyse the deformation and stress characteristics of existing metro tunnels under large-scale unloading of soil. In conclusion, after comprehensive reinforcement measures such as advanced tubal curtains and horizontal beams, anti-floating anchor cables, the elastic modulus of strata is improved to a certain extent, and the rebound of pit bottom soil is effectively reduced. After the excavation of the foundation pits are completed, the maximum longitudinal uplift of left and right tunnel is 8.33 mm and 9.56 mm under reinforced condition, which is less than the control standard value of 10 mm.

KEYWORDS

Shield tunnel, Pit excavation, Sandy gravel statement-floating stability measures, Numerical modelling

INTRODUCTION

Foundation pit projects in the dense urban areas frequently are constructed on existing subway tunnels. These large-scale unloading will break the original mechanical balanced state, cause rebound deformation and settlement of the surrounding soil, which will lead to additional stress and deformation of adjacent existing metro[1-4]. Increasing concerns have been raised about the effects of large-scale unloading on the existing subway tunnels in urban underground projects. A large number of scholars have used a variety of methods to study the effects of foundation pit

excavation on adjacent subway structures, including centrifuge tests [5-7], field tests [8-10] and numerical simulations [11-13].

Through physical model tests, the effects of unloading conditions on stress-strain of existing tunnels are studied. Kusakabe et al. [14-15] based on model tests, the influence of excavation unloading of soil in sandy soil on existing tunnels is studied. Field measurement is the most direct method to study the proximity between unloading project and existing metro tunnel. Sharma et al. [16-17] installed a precise monitoring system in a tunnel in Singapore to monitor the effect of large excavation on the deformation of adjacent tunnels. With the growing number of such cases, predicting the tunnel's displacements has been increasingly important to reduce the risk of excavations. Most researchers simulated the interaction behaviour between tunnels and excavation by using numerical methods. Chakeri et al. [18-20] took foundation pits crossing subjacent tunnels as an engineering background, and established three-dimensional numerical models for analysis by using the finite difference software FLAC3D. Some semi-analytical methods to evaluate the heave of underlying tunnel induced by adjacent excavation are presented and verified by field measurement results [21-23].

However, the previous practice and theoretical research are lacking in the analysis of the deformation and loading condition of existed metro tunnels under large-scale unloading in the sandy gravel strata [24-27]. Sandy pebbles are the products of long-term transport of rocks interacting with flowing water and riverbed. Sandy gravel strata are generally composed of cohesive soil or sand-pebble, coarse sand and pebble, which are characterized by loose structure, uneven distribution, low cohesion, low plasticity, great compressive stress but little tensile stress and strong discreteness [28-30]. The line 5 of Chengdu subway engineering located in the sandy gravel strata of Chengdu Plain, China, which will be put into use in the end of 2019. When the metro is completed, the municipal tunnel above the metro will be constructed, and this adjacent unloading project will have an impact on the existing metro tunnel.

ENGINEERING OVERVIEW

Engineering geology

The planned construction between Saiyuntai Station and Dafeng Station of line 5 of Chengdu Metro is located at the main trunk of the traffic, which has dense surface buildings and complex underground stilts. According to geological survey, the top-down distribution of strata in the study area is shown in Figure 1.

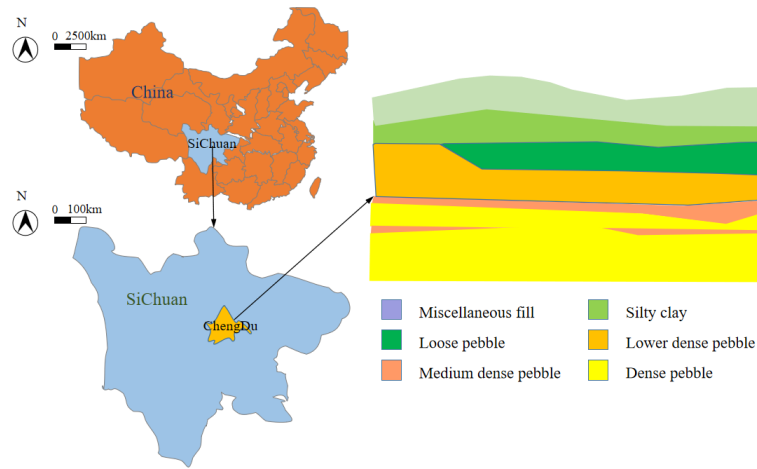


Fig.1-Geological profile

Introduction of Engineering

The total length of line 5 of Chengdu Metro is about 49 kilometres. The section works between Saiyuntai Station and Dafeng Station whose stake is from K0+760 to K0+800 underneath pass throat area of Baoji-Chendu railway, and the building map diagram is shown in Figure 2. The relative spatial position of the municipal tunnel and line 5 of Chengdu Metro is shown in Figure 3. The municipal tunnel will be constructed by cut-and-cover method and divided into two parts: the south side foundation pit and the north side foundation pit. The foundation pit on the south side has been excavated before the excavation on Line 5 of Metro, so the unloading of the foundation pit on the north side will affect the structure of the lower subway.

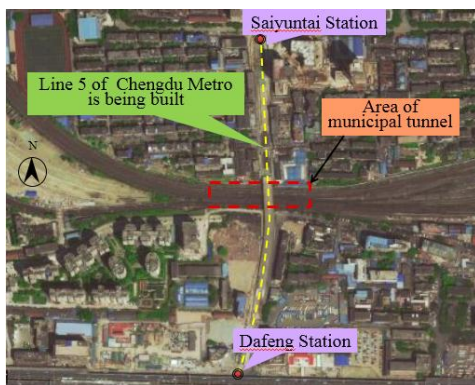


Fig.2 - Plane position sketch of subway shield zone

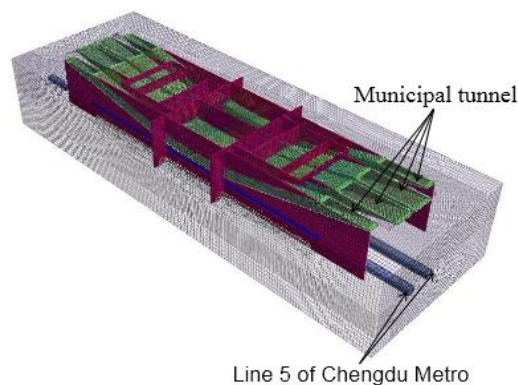


Fig.3 - Diagram of relative position between municipal tunnel and line 5

The relative horizontal position and vertical position of the municipal tunnel and line 5 of Chengdu Metro are shown in Figure 4. The plane dimension of the north side foundation pit is 35m×59m, including the west side relief road, the main foundation pit I, the main foundation pit II and the east side relief road. The foundation pit excavation unloading depth is about 12m, and the minimum distance from the bottom of the foundation pit to the vault of the shield tunnel below is only

2m. The burial depth of shield tunnels is 10.8 to 17.8 m, in which inside diameter is 6 m and outside diameter of 6.4 m.

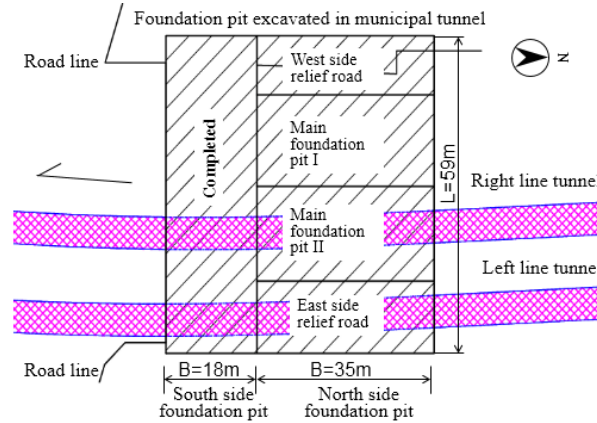


Fig.4 - Plane Position Diagram

In this project, the unloading of a large range of soil will affect the tunnel below [31]. Considering the lack of construction experience of short distance unloading above Metro in gravel strata, the safety control standard of Chengdu Metro Line 5 is formulated in combination with the Technical Specification for Monitoring Urban Rail Transit Engineering.

Tab.1 - Safety control standards of Chengdu Metro line 5

Monitoring items and scope	Shield tunnel in operation
Horizontal and vertical displacement of tunnel	$\leq 10\text{mm}$
Radial convergence of tunnel	$\leq 10\text{mm}$
Deformation curvature radius of tunnel	$R \geq 1500\text{m}$
Deformation relative curvature of tunnel	$\leq 1/2500$
Opening of segment joints	$< 2\text{mm}$
Lateral height difference of track	$< 4\text{mm}$
Void content of track bed	$\leq 5\text{mm}$
Crack width of structure	$\leq 0.2\text{mm}$

COMPREHENSIVE REINFORCEMENT MEASURES

Advanced Tubal Curtains and Horizontal Beams

In order to reduce the influence of municipal tunnel construction unloading on the additional deformation and internal force of the existing shield tunnel structure, the soil above the arch of line 5 of Chengdu Metro shield tunnel is strengthened by using the joint support of advanced tubal curtains and horizontal beams. There are two layers of advanced tubal curtains, the lower side advanced tubal curtains whose longitudinal length is 51.5 m, diameter is 800 mm and

circumferential distance is 850 mm are semi-circular along the tunnel vault, and the upper side advanced tubal curtains are horizontally placed under the bottom of the municipal tunnel, which layout diagram is shown in Figure 5. The advanced tubal curtains that use locks to ensure the stability of the interface are 67. After the construction of the advanced tubal curtains is completed, the micro-expansion concrete is filled to enhance the longitudinal bending stiffness of the advanced tubal curtains.

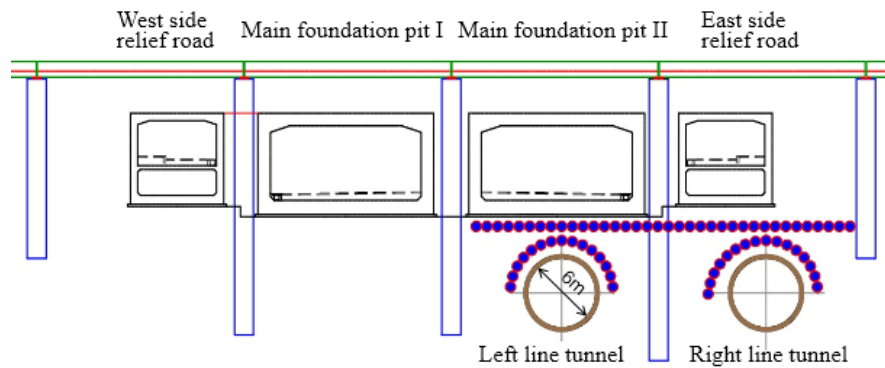


Fig.5 - Strengthened sketch of advance tubal curtains and horizontal beams

Anti-floating Anchor Cables

In order to further strengthen the safety of the subway operation, the prestressed anchor cables and the tunnel segments are connected to control the floating of the shield tunnel. The affected area under the foundation pit of the municipal tunnel and within 100m of the longitudinal tunnel segment, the prestressed anchor cables are arranged at the bottom and side of the tunnel segments and the layout of anchor cables of each ring tunnel segment is shown in Figure 6. Seven tension points are set for each segment, a total of 933 tension points are set in the range of 100 m. Each prestressed anchor cable is about 10m, the anchor end is about 8m, and the free end is 2m. Through mechanical analysis, the prestressed anchor cable that is flexible structure is composed of 3 steel strands whose diameter is 15.2mm and pre-stress force is 200 kN.

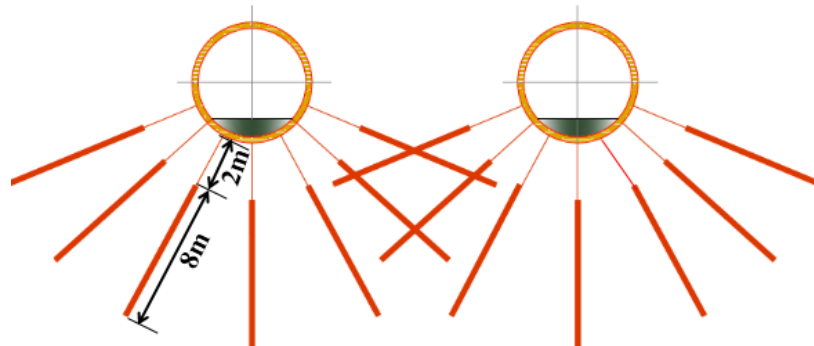


Fig.6 - Layout of anti-floating anchor cables

NUMERICAL MODELLING

Finite Element Model and Selected Parameters

The excavation foundation pit of the municipal tunnel, which is 12m high, 59m long and 35m wide, is built above line 5 of Chengdu Metro. The numerical calculation model was established by using Midas NX finite element software. The length was 180m (X direction), the width was 130m (Y direction), and the calculated depth was 50m (Z direction), which can eliminate the influence of boundary conditions. The overall model is shown in Figure 7(a). The modified Mohr-Coulomb constitutive relation is adopted in the model. The model soils are simulated by solid elements, the tunnel segments adopt the shell elements, the foundation pit retaining structures are simplified to be equivalent to the 2D plate elements, the advanced tubal curtains and internal supporting structure of steel pipe are made of beam element, and the anti-floating anchor cables are simulated by embedded truss. The reinforcement structures are shown in Figure 7(b-d). The boundary conditions restrict the normal displacement, the bottom boundary restricts the vertical displacement, and the upper boundary is the free surface.

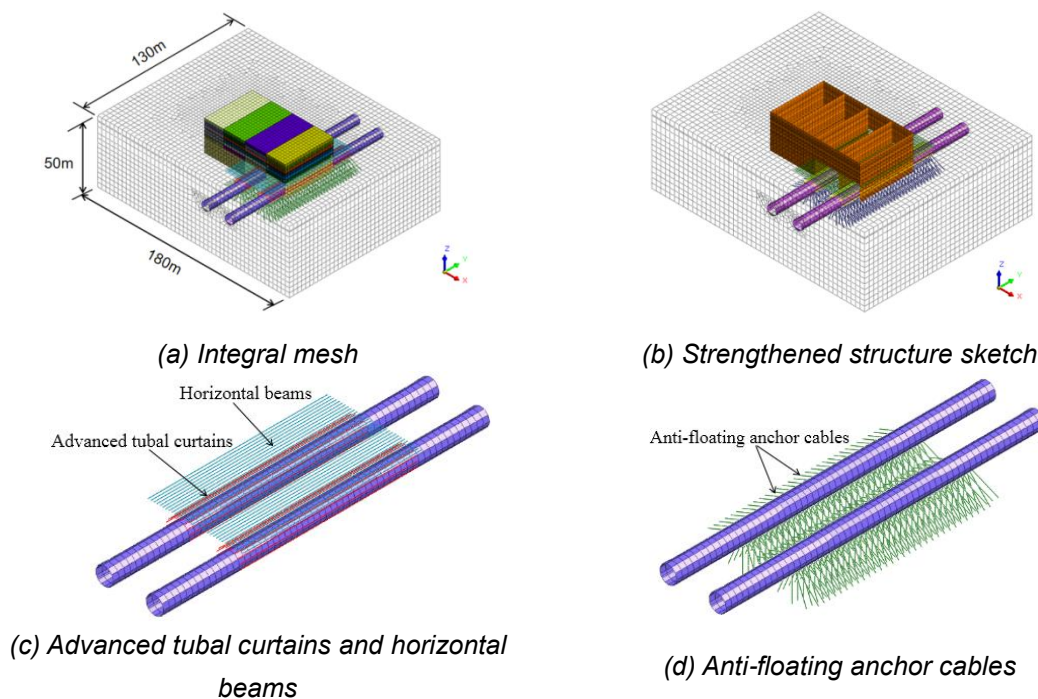


Fig.7 - Computational model and strengthened structural diagram

The specific soil and structure parameters were determined by the "Special Exploration Report of sandy gravel strata of Shield Tunnel of Line 5 of Chengdu Metro " and the empirical values of mechanical calculation parameters of each rock layer in Chengdu area. Detailed formation mechanics calculation parameters and structural parameters are shown in Tables 2 and 3.

Tab.2 - Physico-mechanical parameters of soil

Types	γ (kN·m ⁻³)	ν	c (kPa)	φ (°)	E_{50}^{ref} (MPa)	E_{oed}^{ref} (MPa)	E_{er}^{ref} (MPa)	K_0	H (m)
Miscellaneous fill	18	0.2	8	10	8	8	24	-	3
Silty clay	19.5	0.3	37.1	17.	6	6	18	0.40	0.6
Loose pebbles	18.5	0.3	0	30	5.5	5.5	16.5	0.33	3.2
Lower dense pebbles	21	0.3	0	35	23	23	69	0.30	4.2
Medium dense	22	0.2	0	40	29	29	87	0.25	12
Dense pebbles	23	0.3	0	45	33	33	99	0.20	>20

Tab.3 - Structural parameters

Types	γ (kN·m ⁻³)	E (kPa)	ν	Sectional parameters
Segment	24	3.8×10 ⁷	0.2	D=6.4m, d=6.0m
Advanced tubal curtain	25	3.15×10 ⁷	0.3	Φ800 mm
Horizontal beam	25	3.15×10 ⁷	0.3	Φ800 mm
Anti-floating anchor	78	1.95×10 ⁸	0.3	Φ150 mm
Retaining pile	25	3.0×10 ⁷	0.2	Φ1200 mm
Temporary support	78	2.1×10 ⁸	0.3	Φ169 mm

Annotation: γ is the volume weight, ν is the poisson's ration, c is the cohesion, φ is the friction angle, E is te elasticity modulus, E_{50}^{ref} is the secant stiffness of triaxial test, E_{oed}^{ref} is the tangent stiffness of primary consolidation load experiments, E_{er}^{ref} is the unloading elasticity modulus.

Simulation of Construction Conditions

When the foundation pits are excavated, the foundation pit supporting structures are first applied, and then the soils are excavated. The excavation sequence is from the west side relief road of foundation pit to the east. The foundation pit is divided vertically into multi-layers. The depth of each excavation is 2 m. When the main foundation pit II and the east side relief road are excavated, the method of vertical stratification and horizontal segmentation is adopted to excavate the soil within 6 meters above the bottom of the pit. The test section of 6 m long foundation pit excavation above the tunnel is set up, as shown in Figure 8.

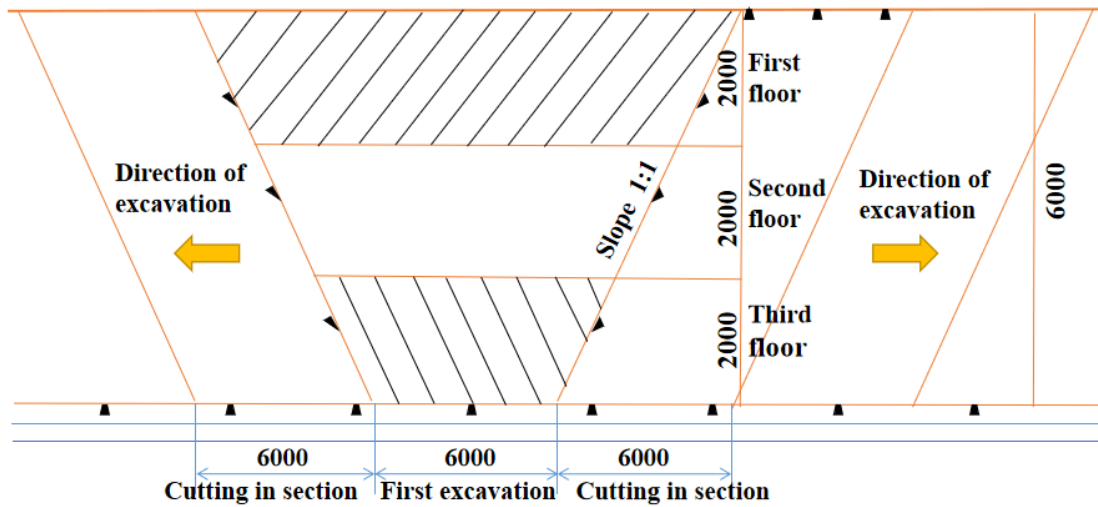
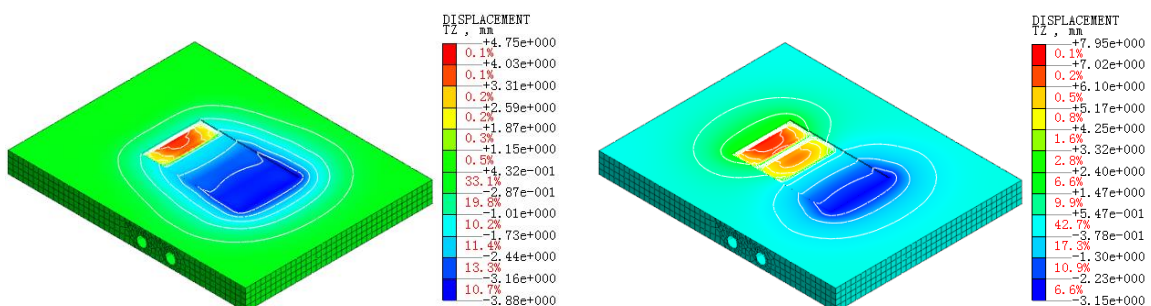


Fig.8 - Sketch of excavation test of foundation pit

RESULT ANALYSIS

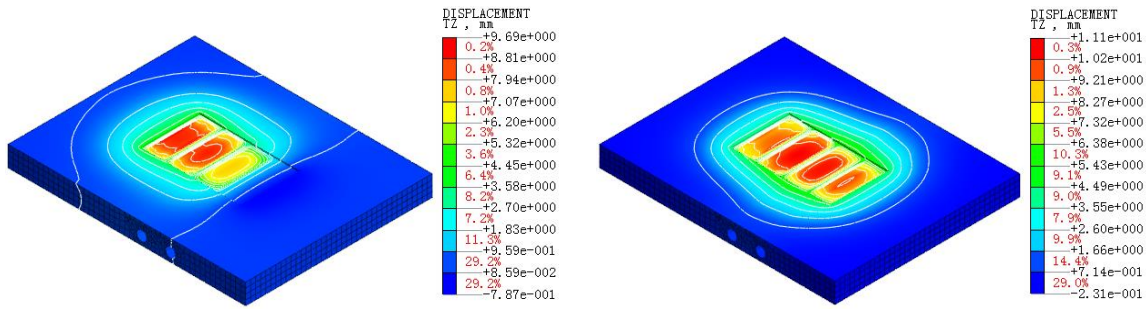
Deformation and Stress

Figure 9 shows the changing rule of the deformation of the bottom of foundation pit under different excavation stages. After the excavation of the west side relief road is completed, the maximum uplift deformation at the bottom of the pit is 4.75 mm, while the soil above the left side tunnel has a certain degree of sinking, with a maximum of about 3.9 mm (Figure 9a). After the excavation of the main foundation pit I is completed, the bottom uplift of the west side relief road foundation pit continues to increase to 7.95 mm, and the maximum uplift at the bottom of the main foundation pit I is 5.17 mm. At this time, the settlement of the soil above and around the left-line tunnel gradually becomes smaller. (Figure 9b). After the excavation of the main foundation pit II, the maximum bulge at the bottom of the pit is mainly located at the bottom of the main pit I, which is about 9.69 mm (Figure 9c). After the excavation of the municipal foundation pit is completed, the whole bottom of the pit is bulged, and the maximum bulge is 11.1 mm (Figure 9d).



(a) After the excavation of west side relief road

(b) After the excavation of main foundation pit I



(c) After the excavation of main foundation pit II (d) After the excavation of east side relief road

Fig.9 - Deformation of foundation pit bottom at different excavation stages

From the bottom bulge value of the foundation pit shown in Figure 10, it can be seen that the maximum bulge of the foundation pit occurs at the centre of the main foundation pit I, about 11.1 mm, and the ridge change of the main foundation pit II is 8-10 mm. The main foundation pits have a relatively large degree of uplift, while the foundation pits of east and west side relief road are relatively small. This is mainly because the main foundation pit has a larger excavation size and wide unloading range than the auxiliary road foundation pit, so the bulge deformation of the bottom of the pit is increased to some extent.

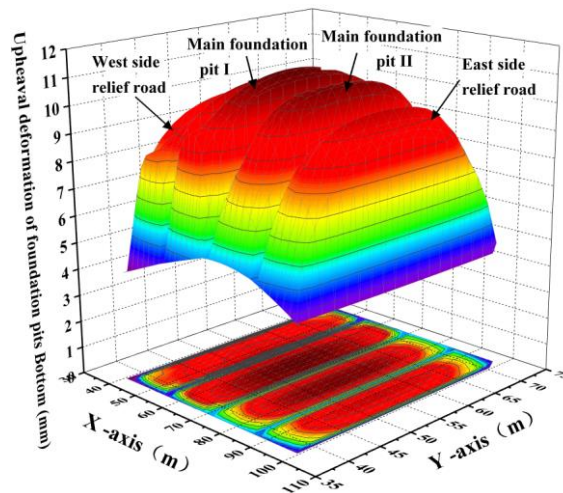


Fig.10 - Distribution of pit bottom upheaval after excavation of foundation pit

Figure 11 shows the vertical displacement of the left and right line tunnels under different working conditions. Since the west side relief road and the main foundation pit I are relatively far from the line 5 of subway, the vertical displacement of the tunnel is mainly settlement, and the maximum settlement is 3.8 mm. After the excavation of the foundation pit II above the right-hand subway tunnel is completed, the maximum uplift of the right-line tunnel is 6.37mm, while the deformation of the left-line tunnel is basically zero, and the tunnel undergoes upward uplift deformation after settlement. After the excavation of the foundation pits are completed, the maximum ridge of the right-line tunnel is 9.56mm, and the maximum ridge of the left line is 8.33mm, which occurs below the centre of the pit bottom and above the tunnel axis.

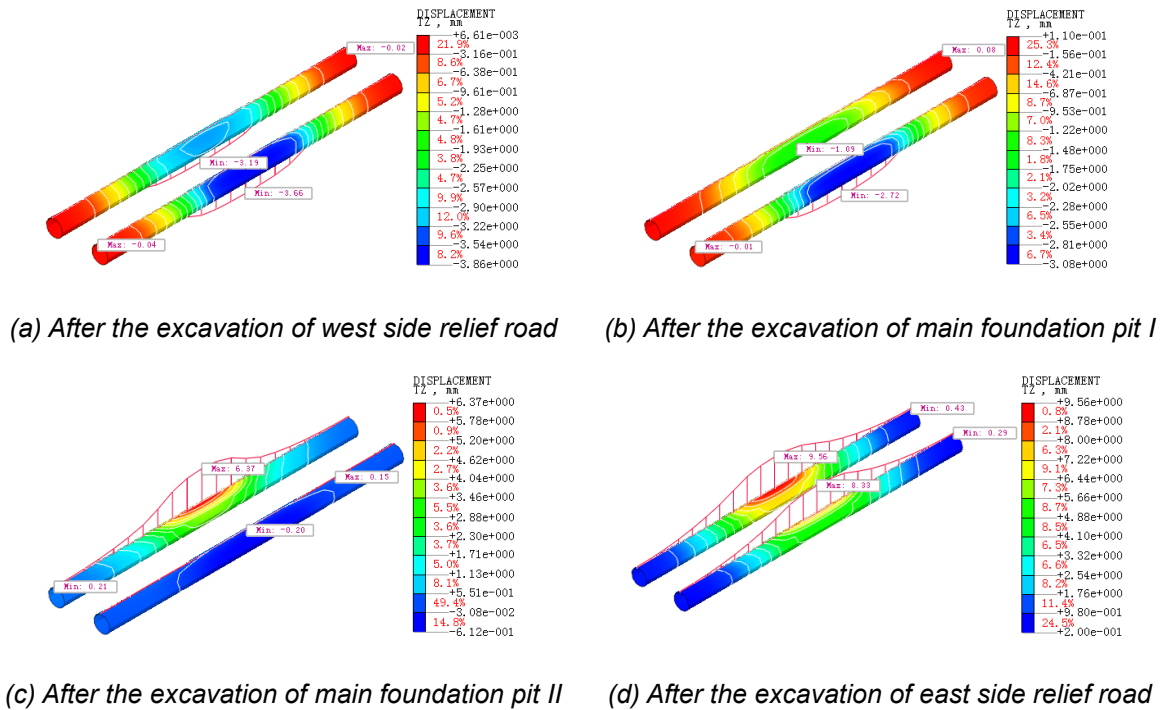


Fig.11 - Vertical displacement change of tunnels under different excavation conditions

It can be seen from the above analysis that the maximum settlement and uplift deformation of the tunnel in each working condition occur above the tunnel vault. In order to visually study the effect of soil unloading on the vertical deformation of the subway tunnel along the axis, a research point is selected every 2m along the longitudinal direction of the tunnel to extract the vertical deformation at the position of the tunnel vault, as shown in Figures 12. After the excavation of the west side relief road is completed, the left and right tunnels will undergo settlement deformation in the area below the foundation pit, and the main settlement is about 3-3.8 mm. As the foundation pit gradually excavated in the direction of the tunnel, the left and right tunnels began to bulge upward. When the excavation of the main foundation pit II is completed, the right-line tunnel in the area below the foundation pit exhibits a bulging deformation, and the maximum bulge amount is about 6 mm. However, the left-line tunnel deformation is almost zero, which means that the settlement and bulging of the tunnel cancel each other out. After the excavation of the foundation pit, the maximum ridge deformation of the right tunnel is about 9.56 mm, and the maximum ridge of the left line is about 8.33 mm, which is less than the proposed 10 mm deformation control standard.

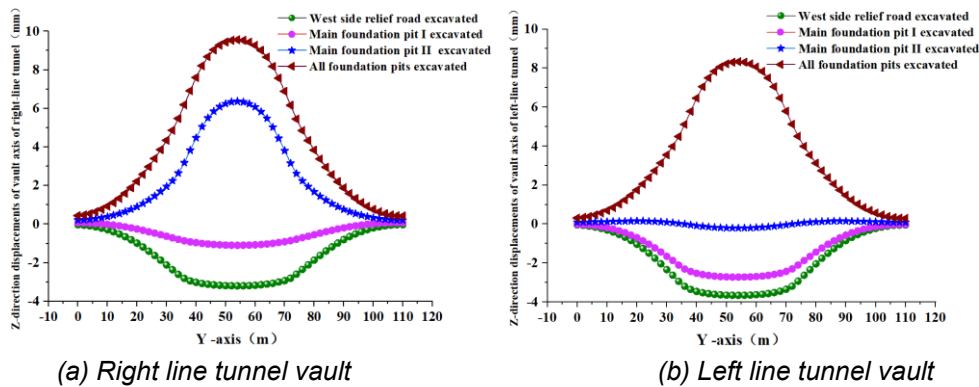


Fig.12 - Vertical displacement curve of tunnels vault under different excavation conditions

It can be seen from Figure 12 that the maximum deformation position of the left and right tunnels occurs at the middle of the tunnel ($Y=55m$), and also near the centre of the Y-direction of the municipal frame foundation pit. Therefore, the section is the most unfavourable section showing the safety of the tunnel structure when the soil is unloaded. The vertical displacement of the joint at the vault position of the section is extracted with the deformation value of the excavation step of the foundation pit as shown in Figure 13. It is noteworthy that when the construction of the main foundation pit II begins, the right tunnel begins to rise upward, the curvature of the tunnel uplift curve increases, and the deformation rate accelerates. At the same time, with the increase of the excavation depth of the foundation pit, the right tunnel has a larger increase rate and uplift value than the left tunnel, and the uplift deformation increases nonlinearly. When the east side relief road starts construction, the rate of change of the right-line tunnel uplift is relatively reduced, but the growth rate of the left-line tunnel is significantly increased. During the construction, the deformation of the subway tunnel should be monitored closely in real time, and effective and reasonable unloading methods should be adopted in time to ensure the safety and controllability of the subway structure.

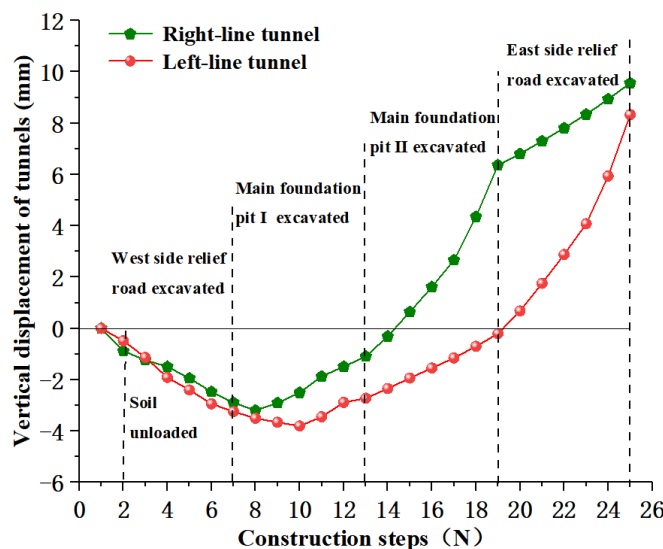
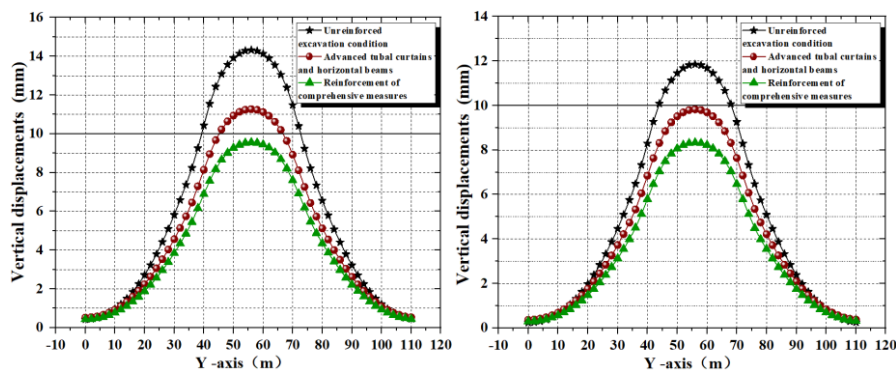


Fig.13 - Variation of vertical displacement of tunnels vault during unloading of soil

Reinforcement Effect

Reinforcement Advanced Tubal Curtains and Horizontal Beams

In order to further analyse the effect and degree of the active reinforcement measures of advanced tubal curtains and horizontal beams, the vertical displacement of left and right tunnel under three conditions is analysed by comparing the unreinforcement conditions and the reinforcement conditions of comprehensive measures. Figure 14 shows the variation of vertical displacement of left and right tunnel under different reinforcement conditions. The figure shows that the final vertical displacement of the left and right tunnels exceeds the stipulated 10 mm control standard under the unreinforced condition, which shows that the conventional unloading control measures cannot meet the control requirements of Metro deformation. After adopting advanced tubal curtains and horizontal beams reinforcement measures, the vertical uplift displacement of the tunnel decreases significantly, and the left tunnel uplift displacement decreases to about 10 mm, but the right tunnel uplift displacement still exceeds the limit, so the deformation of Metro Line 5 still does not meet the requirements.



(a) Vertical displacement of right tunnel

(b) Vertical Displacement of Left Tunnel

Fig. 14 - Vertical displacement of tunnels under different reinforcement measures

Reinforcement Anti-floating anchor cables

In order to obtain the treatment effect of anti-floating anchor cables reinforcement measures, the variation laws of vertical displacement of left and right tunnel under three conditions were compared and analysed in combining with the unreinforcement conditions and the reinforcement conditions of comprehensive measures. Figure 15 shows the variation of vertical displacement of left and right tunnel under different reinforcement conditions. The figure shows that the uplift displacement of the left tunnel is reduced to about 10.3 mm and that of the right tunnel is reduced to about 11.68 mm after adopting anti-floating anchor cables reinforcement measures, but all of them exceed the deformation limit, which indicates that anti-floating anchor cables reinforcement alone cannot meet the control requirements of Metro deformation.

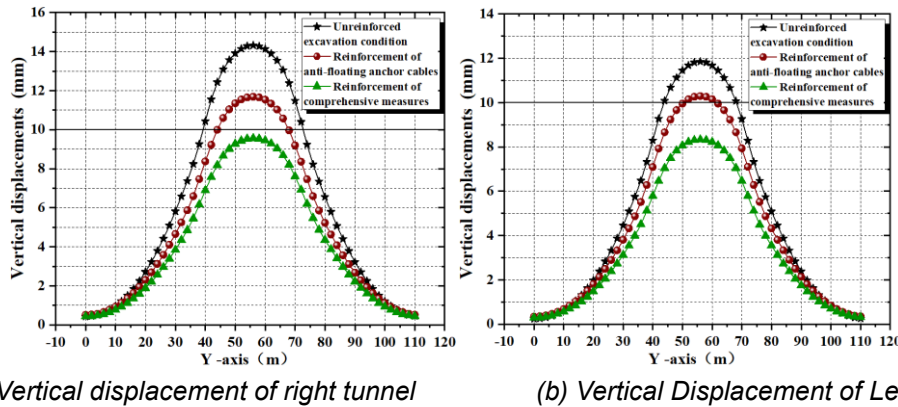


Fig.15 - Vertical displacement of tunnels under different reinforcement measures

From Table 4, it can be seen that the maximum longitudinal uplift of left and right tunnel is 11.85 mm and 14.32 mm under unreinforced condition after all excavation of foundation pit has been completed. The vertical displacement of the left and right tunnel is reduced to 9.28 mm and 11.27 mm, which reduces respectively by 17.1% and 21.3% after adopting advanced tubal curtains and horizontal beams reinforcement measures. The vertical displacement of the left and right tunnel is reduced to 10.29 mm and 11.68 mm, which reduces respectively by 13.1% and 18.4% after adopting anti-floating anchor cables reinforcement measures. After adopting comprehensive reinforcement measures, the vertical displacement decreases by 29.7% and 33.2% respectively, and the reinforcement effect is more obvious. Comprehensive reinforcement measures can meet the control requirements of Metro deformation, but the two measures cannot meet the control requirements of Metro deformation when used singly.

Tab.4 - Maximum vertical displacement of tunnels under three reinforcement measures

Tunnel displacement	Location of measured points	Unreinforced excavation condition	Reinforcement advanced tubal curtains and horizontal beams	Reinforcement anti-floating anchor cables	Reinforcement of comprehensive measures
Vertical displacement	Left line vault	11.85mm	9.82mm/17.1%	10.29mm/13.1%	8.33mm/29.7%
	Right line vault	14.32mm	11.27mm/21.3%	11.68mm/18.4%	9.56mm/33.2%

CONCLUSION

- (1) The comprehensive reinforcement measures such as advanced tubal curtains and horizontal beams, anti-floating anchor cables have obvious reinforcement effect. To a certain extent, the elastic modulus of the strata is improved, the rebound of the soil at the bottom of the pit is effectively reduced, and the excessive uplift of the tunnel structure is avoided.
- (2) After the excavation of the foundation pits are completed, the maximum uplifts of the left and right tunnels are 9.56 mm and 8.33 mm respectively, which are less than the control standard requirement of 10 mm, and have a certain safety reserve.
- (3) When the construction of the main foundation pit II begins, the right tunnel begins to uplift upwards, the curvature of the uplift curve increases, and the deformation rate accelerates. At the same time, with the increase of excavation depth of foundation pit, the increase rate and uplift value of the right tunnel are larger than that of the left tunnel, and the uplift deformations increase nonlinearly. When the construction of the east side relief road begins, the change rate of the right tunnel uplift decreases relatively, but the growth rate of the left tunnel increases significantly, and the horizontal displacements increase nonlinearly. Therefore, it is necessary to monitor the deformation of metro tunnel in real time and adopt effective and reasonable unloading methods in time, which can ensure the safety of metro structure.
- (4) Compared with the unreinforced condition, the vertical displacements of the left and right tunnels are reduced respectively by 13.1% and 18.4% after the anti-floating anchor cables reinforcement measures are adopted. The vertical displacements of the left and right tunnel are reduced respectively by 17.1% and 21.3% by adopting the advanced tubal curtains and horizontal beams reinforcement measures. But, the two measures cannot meet the control requirements of metro deformation when used alone.

REFERENCES

- [1] R. J. Finno, and L. S. Bryson, "Response of building adjacent to stiff excavation support system in soft clay," *Journal of performance of constructed facilities*, vol. 16, no. 1, pp. 10-20, 2002.
- [2] P. G. Hsieh, and C. Y. Ou, "Shape of ground surface settlement profiles caused by excavation," *Canadian geotechnical journal*, vol. 35, no. 6, pp. 1004-1017, 1998.
- [3] G. B. Liu, C. W. Ng, and Z. W. Wang, "Observed performance of a deep multistrutted excavation in Shanghai soft clays," *Journal of Geotechnical and Geoenvironmental Engineering*, vol. 131, no. 8, pp. 1004-1013, 2005.
- [4] M. G. Li, Z. J. Zhang, J. J. Chen et al., "Zoned and staged construction of an underground complex in Shanghai soft clay," *Tunnelling and Underground Space Technology*, vol. 67, pp. 187-200, 2017.
- [5] C. W. Ng, J. Shi, Y. Hong, "Three-dimensional centrifuge modelling of basement excavation effects on an existing tunnel in dry sand." *Canadian Geotechnical Journal*, vol. 50, no. 8, pp. 874-888, 2013.

- [6] H. Xu, H. W. Huang, and D.M. Zhang, "Centrifuge modelling of deep excavation over existing tunnels," *Proceedings of the Institution of Civil Engineers-Geotechnical Engineering*, vol. 167, no. 1, pp. 3-18, 2014.
- [7] C. W. Ng, H. S. Sun, G. H. Lei, J. W. Shi, and D. Mašín, "Ability of three different soil constitutive models to predict a tunnel's response to basement excavation," *Canadian Geotechnical Journal*, vol. 52, no. 11, pp. 1685-1698, 2015.
- [8] Y. Tan, X. Li, Z. Kang, J. Liu, and Y. Zhu, "Zoned excavation of an oversized pit close to an existing metro line in stiff clay: Case study," *Journal of Performance of Constructed Facilities*, vol. 29, no. 6, Article ID 04014158, 2014.
- [9] X. Xiao, J. J. Chen, M. G. Li, and J. H. Wang, "Field Monitoring of an Existing Cut-and-Cover Tunnel between Two Large-Scale Deep Excavations," *Journal of Aerospace Engineering*, vol. 31, no. 6, Article ID 04018082, 2018.
- [10] H. Liu, P. Li, and J. Liu, "Numerical investigation of underlying tunnel heave during a new tunnel construction," *Tunnelling and Underground Space Technology*, vol. 26, no. 2, pp. 276-283, 2011.
- [11] M. Doležalová, "Tunnel complex unloaded by a deep excavation," *Computers and Geotechnics*, vol. 28, pp. 469-493, 2001.
- [12] C. W. Ng, J. Shi, D. Mašín, H. Sun, and G. H. Lei, "Influence of sand density and retaining wall stiffness on three-dimensional responses of tunnel to basement excavation," *Canadian Geotechnical Journal*, vol. 52, no. 11, pp. 1811-1829, 2015.
- [13] G. Zheng, and S. W. Wei, "Numerical analyses of influence of overlying pit excavation on existing tunnels," *Journal of central south university of technology*, vol. 15, no. 2, pp. 69-75, 2008.
- [14] O. Kusakabe, T. Kimura, and N. Takagi, "Centrifuge model tests on the influence of axisymmetric excavation on buried pipes," *Proceedings of 3rd International Conference on Ground Movements and Structures*, London: Pentech Press, 1985.
- [15] Y. KOJIMA, and K. YASHIRO, "Deformation behaviour of tunnel lining due to ground surface loading and unloading above the tunnel," *Quarterly Report of RTRI*, vol. 46, no. 2, pp. 143-146, 2005.
- [16] J. S. Sharma, A. M. Hefny, J. Zhao, and C. W. Chan, "Effect of large excavation on deformation of adjacent MRT tunnels," *Tunnelling and Underground Space Technology*, vol. 16, no. 2, pp. 93-98, 2001.
- [17] A. V. Kivi, M. H. Sadaghiani, and M. M. Ahmadi, "Numerical modelling of ground settlement control of large span underground metro station in Tehran Metro using Central Beam Column (CBC) structure," *Tunnelling and Underground Space Technology*, vol. 28, pp. 1-9, 2012.
- [18] A. V. Kivi, M. H. Sadaghiani, and M. M. Ahmadi, "Analysis of interaction between tunnels in soft ground by 3D numerical modelling," *Bulletin of Engineering Geology and the Environment*, vol. 70, no. 3, pp. 439-448, 2011.
- [19] X. Xiao, M. G. Li, J. H. Wang, and J. J. Chen, "Numerical Evaluation of Control Measures for Tunnel Deformation Induced by an Oversized Deep Excavation," *Journal of Aerospace Engineering*, vol. 31, no. 6, Article ID 04018109, 2018.
- [20] Z. Zhang, M. Zhang, and Q. Zhao, "A simplified analysis for deformation behaviour of buried pipelines considering disturbance effects of underground excavation in soft clays," *Arabian Journal of Geosciences*, vol. 8, no. 10, pp. 7771-7785, 2015.

- [21] R. Liang, T. Xia, Y. Hong, and F. Yu, "Effects of above-crossing tunnelling on the existing shield tunnels," *Tunnelling and Underground Space Technology*, vol. 58, pp. 159-176, 2016.
- [22] J. F. Zhang, J. J. Chen, J. H. Wang, and Y. F. Zhu, "Prediction of tunnel displacement induced by adjacent excavation in soft soil," *Tunnelling and Underground Space Technology*, vol. 36, pp. 24-33, 2013.
- [23] G. Zheng, X. Yang, H. Zhou, Y. Du, J. Sun, and X. Yu, "A simplified prediction method for evaluating tunnel displacement induced by laterally adjacent excavations," *Computers and Geotechnics*, vol. 95, pp. 119-128, 2018.
- [24] J. Qiu, Y. Qin, Z. Feng, L. Wang and K. Wang, "Safety Risks and Protection Measures for the City Wall during the Construction and Operation of Xi'an Metro," *Journal of Performance of Constructed Facilities*, 2019, in press
- [25] Z. Wang, Y. Wang, and W. Cheng. "Investigation into Geohazards during Urbanization Process of Xi'an, China," *Natural Hazards*, vol. 92, no. 3, pp.1937-1953, 2018.
- [26] Z. J. Zhou, S. S. Zhu, X. Kong, J. T. Lei and T. Liu, "Optimization analysis of settlement parameters for post-grouting piles in loess area of Shaanxi, China," *Advances in Civil Engineering*, vol. 2019, Article ID 7085104, 11 pages, 2019.
- [27] C. T. Chang, C. W. Sun, S. W. Duann, and R. N. Hwang, "Response of a Taipei Rapid Transit System (TRTS) tunnel to adjacent excavation," *Tunnelling and Underground Space Technology*, vol. 16, no. 3, pp. 151-158, 2011.
- [28] Y. C. Zheng, K. Liu, Y. Fang, W. S. Zhang and J. Fang, "Rock burst Prediction Model Based on Entropy Weight Integrated with Grey Relational -BP Neural Network," *Advances in Civil Engineering*, vol. 2019, Article ID 3453614, 9 pages, 2019.
- [29] B. Zhao, D. Liu, and B. Jiang, "Soil Conditioning of Waterless Sand-Pebble Stratum in EPB Tunnel Construction," *Geotechnical and Geological Engineering*, vol. 36, no. 4, pp. 2495-2504, 2018.
- [30] X. Liu, Q. Fang, and D. Zhang, "Mechanical responses of existing tunnel due to new tunnelling below without clearance," *Tunnelling and Underground Space Technology*, vol. 80, pp. 44-52, 2018.
- [31] X. Huang, H. F. Schweiger, and H. Huang, "Influence of deep excavations on nearby existing tunnels," *International Journal of Geomechanics*, vol. 13, no. 2, pp. 170-180, 2011.

MODELING AND SIMULATION OF MECHANICAL PROPERTIES OF PULVERIZED COW BONE AND LATERITIC PAVING TILES

Peter O. Omoniyi, Jacob O. Aweda, Idehai O. Ohijeagbon, Ridwan A. Busari and Mustapha Ndagi

University of Ilorin, Faculty of Engineering and Technology, Department of Mechanical Engineering, Ilorin, Kwara State, Nigeria; omoniyi.po@unilorin.edu.ng; jacobaweda@gmail.com, idehaiohi@yahoo.com, busari.ridwan01@gmail.com, ndagimustapha@gmail.com

ABSTRACT

This study included the experimental production and investigation of the mechanical properties of paving tiles produced from a mixture of laterite, silica sand, pulverized cow bones, and cement. Empirical models of compressive and flexural strength were also developed and herein presented for the paving tiles. The maximum compressive strength of the paving tiles were obtained for 20, 15, and 10% cement content as 5.05, 5.05 and 3.08 MPa, while the maximum flexural strength for similar values of cement content were obtained as 1.83, 1.21 and 0.26 MPa respectively. The results indicate that there was no noticeable difference in the values of the compressive strength at 20 and 15% cement content, while a sharp reduction of the mechanical properties was experienced as the cement content reduces from 15 to 10%. Recommended composition for paving tiles with pulverized cow bones composite is cement, 15%; pulverized cow bones, 30%; laterite 35% and silica sand, 20% respectively. Sustainable production of paving tiles and a sustainable environment can, therefore, be enhanced by replacing granite constituent with waste cow bones, which can easily be replicated by the empirical models herein developed.

KEYWORDS

Empirical models, Compressive strength, Flexural strength, Pulverized cow bones, Laterite

INTRODUCTION

Global consciousness on the environment has been on the increase in recent years, which has engineered several existing environmental protection programs not only to focus on protecting the natural resources, but also to instigate the judicious use of waste materials, and curtail the level of environmental damage. It is of good benefit and importance for developing countries around the world to seek means to create a sustainable development in order to key into such protection programs. The increasing population of the world has propelled both private and public organizations to constantly embark on infrastructural development, a scenario that has encouraged the use of building accessories and products such as paving tiles. It is therefore imperative to constantly explore sustainable materials to develop some of the infrastructural products that would guarantee a sustainable environment [1].

Several applications are being developed to make use of discarded animal bones, in the field of biomedical engineering; animal bones have been used as reinforcement and binding agents for different composite applications such as polyesters, epoxies etc. [2-3]. The potentials of pulverized animal bones as pozzolanic material was also established by Falade *et al.* [4] and was

found to exhibit good pozzolan character. Therefore, recycled waste bones are considered as a composite material for the production of paving tiles in this study.

Paving tiles are usually of different shapes and sizes; they range from square, rectangle, star shape etc. The standard thicknesses are usually 60 mm with common dimensions of 60 x 30, 40 x 40, and 30 x 30 cm [5-6]. In Nigeria, the conventional materials used in the production of paving tiles are granite, silica sand, and cement as a binder. Making use of bones in the production of paving tiles will not only help clean the environment of the ugly pile of bones in abattoirs but would also provide a sustainable means of production, due to its availability. Furthermore, the breaking strength of 9.9 kg makes it a suitable substitute for granite particles in paving tiles productions [7]. Several works have been conducted on the use of readily available and affordable materials in the manufacturing of paving tiles. Ohijeagbon *et al.* [1] used laterite as a partial replacement of granite in the production of interlocking tiles due to the availability of laterite. Ajao and Ohijeagbon [8] successfully utilized corncobs, an agro-waste and charcoal to produce paving tiles, but the sustainability of corncobs waste presents a limitation due to the seasonal availability of agricultural wastes. Therefore this study aim at investing the impact of pulverized cow bones on the mechanical propertie of paving tiles and creating a model to predict the mechanical properties of produced paving tiles for future application.

METHODS

Laboratory Experiment

The raw materials used were laterite, silica sand, pulverized cow bones and cement. The particle sizes of materials used were 1000, 500 and 4750 μm respectively. Mass of materials required to cast a unit tile were weighed according to the proportion of aggregate mix presented in Table 1. The constituents were thoroughly mixed together before the addition of water and further mixing was done to obtain a homogeneous mixture. Each unit of tile was mixed independently to avoid rapid setting of the mixture. A mold size of 200 x 100 x 60 mm was filled to its maximum volume, rammed with a 2.5 kg rammer with 28 blows; the surface was leveled and trimmed. This was done in accordance with Agunwa [9] and Omoniyi *et al.* [10].

Used automobile engine oil was used to smear the inner surfaces of the mold preceding the filling up of the mold in order to avoid adhesion of the cast to the walls of the mold when unmolding. The paving tiles were unmolded after 24 hours and cured in water for twenty-one days (21) then sundried for another seven (7) days, making up a total curing duration of twenty-eight (28) days [9, 11-12].

Tab. 1 - Aggregate mix for experimental tiles.

Sample	Cement (% wt)	Pulverized Cow Bones (% wt)	Laterite (% wt)	Silica Sand (% wt)
A ₁	20	30	40	10
A ₂	20	20	25	35
A ₃	20	10	20	50
A ₄	20	5	20	55
B ₁	15	30	35	20
B ₂	15	20	35	30
B ₃	15	10	35	40
B ₄	15	5	30	50
C ₁	10	30	30	30
C ₂	10	20	45	25
C ₃	10	10	50	30
C ₄	10	5	40	45

Mechanical properties of lateritic tiles

Compressive strength

The test specimen was loaded into a universal testing machine. The load was slowly and carefully applied centrally on the tile specimens until the first sign of crack was observed and the load was then recorded. The compressive strength of each tile specimen was carried out in accordance with Equation (1) [13]:

$$\sigma = \frac{P_C}{A_C} \quad (1)$$

Where, P_C = maximum load on the specimen at failure, A_C = calculated cross-sectional area of the specimen and

σ = compressive strength of the test specimen.

Flexural strength

Universal Testing Machine was used in accordance with [8,14] to determine the flexural test. The specimen was supported horizontally on two vertical supports of known span and was loaded with known values of masses until failure occurred. The flexural strength for each tile specimen was then obtained using Equation (2):

$$R = \frac{3PL}{2bd^2} \quad (2)$$

Where, R = modulus of rupture, P = applied load at failure, L = length between the supports, b = width of the specimen and d = thickness of the specimen

Analysis of modeling of paving tiles

When a function with two or more independent variables (multivariate function) is given, multivariate approximation is necessary for interpolation, differentiation and integration [15]. Also, quadratic interpolation is possible, if three points are available for a set of data. A polynomial equation represented by Equation (3) is suitable to develop the models of mechanical properties of produced tiles [16-17]:

$$y = \alpha + \beta_1 X + \beta_2 X^2 + \beta_3 X^3 + \epsilon \quad (3)$$

The dependent variable y denote compressive strength and modulus of rupture and independent variable X , is represented by the percentage of pulverized cow bones, ϵ which is the error term.

Simple linear regression, which is a tool in predictive analysis, could be found suitable for modeling analysis as represented by Equation (4).

$$Y = ax + b + \epsilon \quad (4)$$

Where, Y is the response variable, a , b are constants, x is the independent variable and ϵ is the error term.

Equations (6) to (11) which were generated using the EXCEL spreadsheet were used in the determination of empirical model curves for compressive strength and flexural strength of lateritic paving tiles as shown in Figures 1 and 2.

Coefficient of Correlation

The coefficient of correlation as a measure of the relationship between two variables and was determined for each curve in Figures 1 and 2 by using Equation (5):

$$r = \frac{\sum (x - \bar{x})(y - \bar{y})}{\sqrt{\left\{ \sum (x - \bar{x})^2 \right\} \left\{ \sum (y - \bar{y})^2 \right\}}} \quad (5)$$

Where, \bar{x} and \bar{y} are the mean value of X and Y respectively.

RESULTS

Empirical Modeling of Compressive Strength

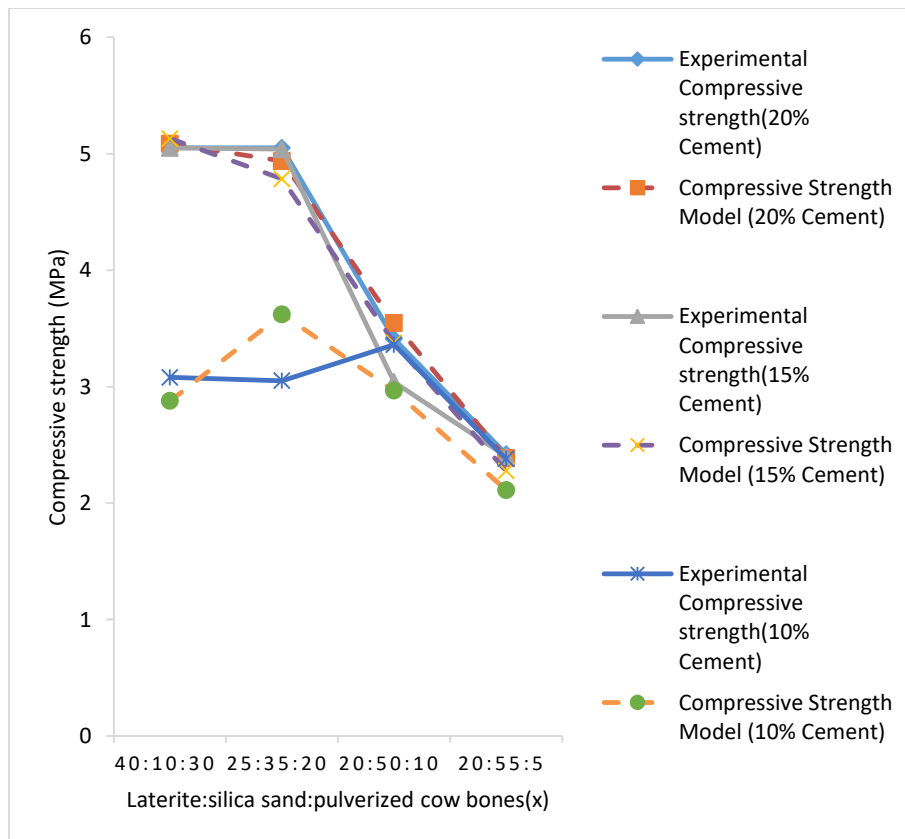


Fig. 1- Relationship between compressive strength and material composition

The compressive strength is shown in Figure 1 and Table 2 was found to decrease as the percentage of pulverized cow bones decreases in the composition of the paving tiles; this is due to the reinforcement the pulverized cow bones added to the strength of produced tiles. The reduction in compressive strength could also be attributed to the cement content, due to the fact that samples of paving tiles with 5-10% cement content had lower compressive strength. Samples with a laterite ratio of up to 25% and above exhibited an improved compressive strength due to the bonding properties of laterite. Equation (6) to (8), show the empirical model developed for determining the compressive strength of lateritic paving tiles at different cement composition of

20%, 15% and 10% respectively. The standard error E_{c1}, E_{c2}, E_{c3} and coefficient of correlation for each model show a good relation among the variables.

$$C_1 = -0.00621x^2 + 0.325407x + 0.913411 ; r = 0.9968 , E_{c1} = \pm 0.0338 \text{ MPa} \quad (6)$$

$$C_2 = -0.0053x^2 + 0.29963x + 0.909865 ; r = 0.9821 , E_{c2} = \pm 0.2010 \text{ MPa} \quad (7)$$

$$C_3 = -0.00699x^2 + 0.275405x + 0.910162 ; r = 0.7076 , E_{c3} = \pm 0.5944 \text{ MPa} \quad (8)$$

Empirical modeling of flexural strength

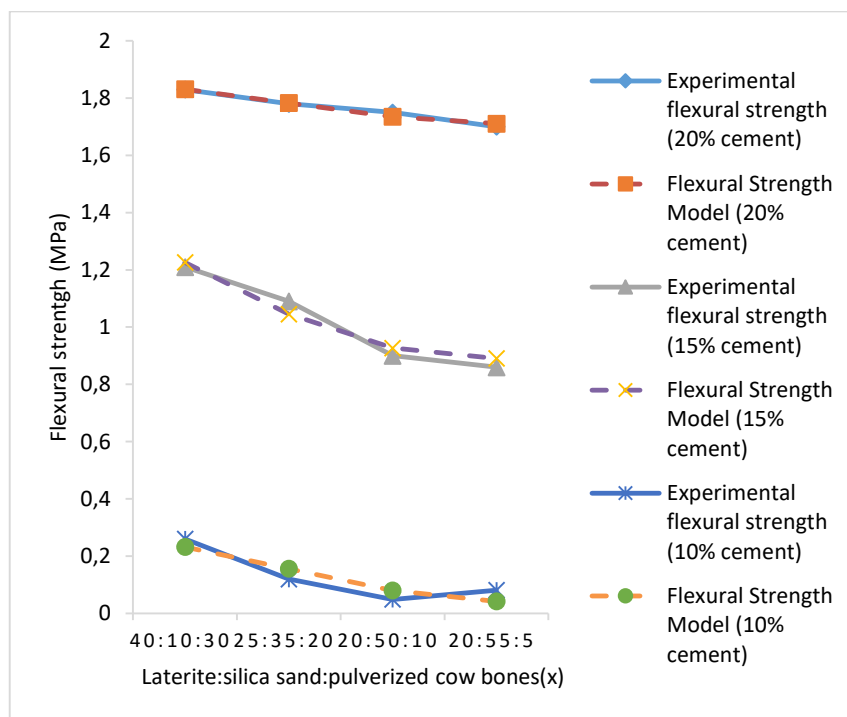


Fig. 2- Relationship between compressive strength and material composition among methods.

Figure 2 and Table 2 show the relationship between the flexural strength and composition of produced tiles at different cement compositions of 20, 15 and 10% respectively. Flexural strength was observed to decrease with an increase in silica sand addition, due to the grittiness of the material which reduces the bonding strength of the products. Conversely, flexural strength increases as the percentage composition of laterite and pulverized cow bones also increases. This was due to the adhesive properties of laterite and reinforcing properties of pulverized cow bones. Equations (9) and (11) represent the models of flexural strength and were observed to exhibit a linear relationship due to the close variation of the material composition at each mix.

$$F_1 = 0.004812x + 1.6868 ; r = 0.9798 ; E_{f1} = \pm 0.0003 \text{ MPa} \quad (9)$$

$$F_2 = 0.00031x^2 + 0.00257x + 0.87036 ; r = 0.9787 ; E_{f2} = \pm 0.0039 \text{ MPa} \quad (10)$$

$$F_3 = 0.007612x + 0.003809 ; r = 0.9078 ; E_{f3} = \pm 0.0046 \text{ MPa} \quad (11)$$

Tab. 2 - Experimental and estimated values of effect of pulverized cow bones on mechanical properties of tiles.

Sample	Cement (% wt)	Pulverized Cow Bones(% wt)	Laterite (% wt)	Silica Sand(% wt)	Mechanical Properties			
					Compressive strength (MPa)		Flexural Strength (MPa)	
					+	++	+	++
A ₁	20	30	40	10	5.05	5.09	1.83	1.83
A ₂	20	20	25	35	5.05	4.94	1.78	1.78
A ₃	20	10	20	50	3.41	3.55	1.75	1.73
A ₄	20	5	20	55	2.42	2.39	1.70	1.71
B ₁	15	30	35	20	5.05	5.13	1.21	1.23
B ₂	15	20	35	30	5.04	4.78	1.09	1.05
B ₃	15	10	35	40	3.04	3.38	0.90	0.93
B ₄	15	5	30	50	2.40	2.28	0.86	0.89
C ₁	10	30	30	30	3.08	2.88	0.26	0.23
C ₂	10	20	45	25	3.05	3.62	0.12	0.16
C ₃	10	10	50	30	3.36	2.96	0.05	0.08
C ₄	10	5	40	45	2.38	2.11	0.08	0.04

+Experimental tile specimens, ++Modeled tile specimens

CONCLUSION

Empirical models of the mechanical properties of paving tiles produced from aggregates of laterite, silica sand pulverized cow bones and cement, for cement addition of 20, 15 and 10% respectively were developed in this study and the models have been able to predict the trends of the mechanical properties of produced paving tiles. The maximum compressive and flexural strength of about 5.10 and 1.83 MPa were obtained at a composite composition of 30:10:40 of pulverized cow bones to silica sand to laterite. These were found to conform to the Nigerian Industrial Standard [18], which approves 2.5 MPa for load-bearing and 1.8 MPa for non-load bearing blocks. The higher the cement and pulverized cow bone content, the higher the compressive and flexural strength obtained. The use of pulverized cow bones as a constituent of paving tiles was found feasible and a viable means of reducing the environmental pollution. Also, replacing the more expensive granite constituent with waste cow bones would result in the cheaper production cost of paving tiles, creating a more sustainable environment. Developed empirical models from this study are useful for further investigation and product development of a similar nature.

ACKNOWLEDGEMENTS

The Department of Mechanical Engineering, University of Ilorin, is acknowledged for the use of the universal testing machine in its mechanics of machine laboratory.

REFERENCES

- [1] Ohijeagbon I.O., Olusegun H.D., Adekunle A.S., Adewoye O.S., Oladiji A.O., 2012. Impact of Suitable Replacement of Granite-Particles on Interlocking Tiles. *Journal of Engineering Science and Technology Reviews* vol. 5: 51-56.
- [2] Oladele O.I., 2013. Development of Bone Ash and Bone Particulate Reinforced Polyester Composites for Biomedical Application. *Leonardo Journal of Practices and Technology* vol. 22: 15-26.
- [3] Yadav P., Dhar, S., Vijaykumar K., 2013. Establish a Methodology for Predicting the Mechanical Properties of Composite Materials, *International Journal of Engineering Science and Innovative Technology*, 60-67.
- [4] Falade F., Ikponmwoosa E., Fapohunda C., 2012. Potential of Pulverized Bones as Pozzollanic Material. *International Journal of Scientific & Engineering Research* vol. 3.
- [5] Olusegun H.D., Adekunle A.S., Ogundele S., Ohijeagbon I.O., 2014. Analysis of Laterite- Granite Concrete Tiles Composite, *International Journal of Engineering*, 193-198.
- [6] Ohijeagbon I. O., Adekunle A. S., Omoniyi P. O., Adeboye B. B., Ajao K. S., 2019. Impact of Production Methods on Some Engineering Properties of Interlocking Tiles. *Adeleke University Journal of Engineering and Technology* vol. 2: 99-108.
- [7] Kim W.K., Donalson L.M., Herrera P., Woodward C.L., Kubena L.F., Nisbet D.J., Ricke S.C., 2004. Effects of Bone Preparation Methods (Fresh, Dry, Fat-Free Dry) on Bone Parameters and the Correlation Between Bone Breaking Strength and other Bone Parameters. *Poultry Science Association Report* vol. 83: 1663-1666.
- [8] Ajao K.S., Ohijeagbon I.O., 2016. Recycling of Ago-Waste to Produce Sustainable Paving Tiles, *International Conference Proceedings, Awka, Nigeria*.
- [9] Agunwa J.J., 2009. Study of Compressive Strengths of Laterite-Cement Mixes as Building Materials. *AU J. T technical Report* vol. 13: 114-120.
- [10] Omoniyi P.O., Ohijeagbon I. O., Aweda J. O., Abolusoro, O. P., Akinlabi E. T., 2020. Experimental Data on the Compressive and Flexural Strength of Lateritic Paving Tiles Compounded with Pulverize Cow Bone. *Data in Brief* vol. 33: 1-8.
- [11] Omoniyi P. O., Ohijeagbon I. O., Aweda J. O., Ibitoye S. E., 2018. Investigation of Brinell Hardness and Compressive Strength of Pulverized Cow Bones and Lateritic Paving Tiles. *Adeleke University Journal of Engineering and Technology* vol. 1: 59-69.
- [12] Aweda J. O., Omoniyi P. O., Ohijeagbon I. O., 2018. Suitability of Pulverized Cow Bones as a Paving Tile Constituent. *IOP Conference Series: Material Science and Engineering*, vol. 413.
- [13] EN-12390-3, Testing Hardened Concrete-Part 3: Compressive Strength of Test Specimen, 2001.
- [14] EN-12390-5, Testing Hardened Concrete, Flexural Strength of Test Specimens, 2001.
- [15] Olusegun H.D., Ohijeagbon I.O., Adekunle A.S., Oladosu O.A., Ogundele S. O., 2009. Modelling Characteristics of Lateritic and Granite Composite Tiles. *International Electronic Engineering Mathematical Society*. Vol. 7: 127-138.
- [16] Vandebogert K., 2017. Quadratic Interpolation [online] http://people.math.sc.edu/kellerlv/Quadratic_Interpolation.pdf.
- [17] Ohijeagbon I.O., 2008. The Estimation of Properties of Unfired Ceramic Products with Sawdust Additives, *African Reserch Review* vol. 2: 144-156.
- [18] NIS87, 2004. Standards for Sandcrete Blocks, Lagos: Nigerian Industrial Standard.

STUDY ON EARTHQUAKE DAMAGE MECHANISM OF AQUEDUCT STRUCTURE BASED ON DIFFERENT BOUNDARY

Xinyong Xu^{1,2}, Xuhui Liu¹, Cheng Zhang³, Xinyun Xu⁴, Jianwei Zhang^{1,2}

1. School of Water Conservancy, North China University of Water Resources and Electric Power, Zhengzhou 450046, China; xuxinyong@ncwu.edu.cn
2. Collaborative Innovation Center of Water Resources Efficient Utilization and Protection Engineering, Henan Province, Zhengzhou 450046, China
3. Changjiang River Scientific Research Institute of Changjiang Water Resources Commission, Wuhan 430000, China; 277523266@qq.com
4. China Three Gorges Pearl River Power Generation Co., Ltd., Guangzhou 510000, China; 854014625@qq.com

ABSTRACT

Numerically simulating an infinite domain foundation is an important method for solving structural dynamics problems. This paper introduces several artificial dynamic boundaries commonly used in the study of structural dynamics, and elaborates the theory and methods of the dynamic infinite element method boundary (IEMB) and viscous–spring artificial boundary (VSAB). The capacity of different boundary effects on seismic waves energy absorption is verified by establishing a layered half-space model. An irrigation aqueduct is taken as a research object. The IEMB, VSAB, and fixed boundary (FB) models are established and the Concrete Damaged Plasticity (CDP) constitutive is introduced, which is aimed at studying the dynamic failure mechanism and the rules of damage development to the aqueduct structure during the seismic duration. The results for the IEMB and VSAB show better energy absorption for the incident waves and a better simulation result for the damping effect of the far field foundation than that of the FB. Comparing the maximum displacement response rules of the three boundaries, it is seen that the maximum displacement response values of the VSAB and dynamic IEMB increased by 6%–48% and 9%–35%, respectively, over the FB. The calculation results of the VSAB are similar to that of the IEMB. The difference between the maximum acceleration response values is 2%–17% whereas the difference between the maximum displacement response values is 0.4%–19%. The IEMB studied in this paper provides a theoretical reference for large–scale building boundary treatment in structural dynamics calculations.

KEYWORDS

Irrigation aqueduct, Viscous–spring boundary, FEM–IEM interaction, Concrete damage plasticity, Seismic damage

INTRODUCTION

Aqueducts are a commonly used cross water transmission facility in water conservancy projects, and have the functions of irrigation, water delivery, and water supply. Numerous agricultural irrigation areas are located in earthquake–prone areas. Due to the high functional requirements for safe water transport, a study of the failure mechanism of the aqueduct structure under seismic loading can ensure the safe operation of aqueducts and the normal dispatching of water resources in irrigated areas.

To date, many achievements have been made in studying the mechanical properties of

aqueducts. Following the existing theory regarding small amplitude water sloshing, fluid–structure interaction between water and structure is usually considered in the previous dynamic analysis of water tanks [1–3]. The water tank and aqueduct are similar in structures, so some scholars considered the effect of fluid–structure interaction examined the dynamic failure mechanism of the aqueduct structures under earthquake ground motion [4–7]. Li, et al. [8] studied the seismic ground motion response to the long span of large–scale aqueduct structures by a simplified beam–water coupled system. Besides, some researchers have used different theoretical methods to study the seismic analysis of aqueduct structures under the influence of earthquakes [9, 10]. It can be seen from the above studies that numerical simulation is still a powerful tool to solve such problems in seismic engineering and aqueduct structural analysis. However, the propagation of seismic wave motion energy in the foundation and the reflection effects at the boundary conditions play a significant role in determining whether the dynamic calculations can achieve reasonable results.

The finite domain simulation of the seismic waves motion propagation used in traditional finite element calculations is prone to reflection on artificial boundaries and propagation of interference waves. Lysmer and Kuhlemeyer [11] first proposed a viscous boundary with a simple form but this was not suitable for the multidimensional situations of complex structures. Deeks and Randolph [12] considered soil–structure interaction (SSI) problems under dynamic action and proposed the earliest viscous–spring boundary based on the viscous boundary, and the numerical simulation example of transient radiation model problems was used to solve the transient SSI problems in the time domain. Gu, et al. [13] derived the viscous-spring artificial boundary (VSAB) equation based on the wave motion equation, demonstrated the high precision and adequate stability of a three–dimensional (3D) VSAB through a calculated example, and presented the concept of a consistent VSAB. Liao and Wong [14] presented and improved the transmitting boundary formula, and used multiple transmission methods to simulate the physical process of wave motion propagation. This method moderately improved the accuracy but the implementation process was more complicated. The infinite element method boundary (IEMB) is a numerical method based on the infinite element theory and developed to solve the infinite domain problem. In 1973, Ungless [15] first proposed the infinite element theory. Bettess [16] proposed mapping infinite elements for the first time based on the mapping between global coordinates and local coordinates, which is called Bettess elements. Zienkiewicz, et al. [17] based on the improvement of the work of Bettess elements, proposed the definition of mapping infinite elements and applied it to solve exterior wave problems. Yun, et al. [18] proposed and studied a new infinite element method to solve the two–dimensional (2D) and 3D pier-soil dynamic interaction in the frequency and time domains. The study results were verified by the applicability of dynamic IEMB, which has a better filtering effect on scattered waves than the VSAB [19]. Infinite element can be combined with finite element. The finite element method is used to simulate the near-field region, while the infinite element method is used to simulate the far-field region. The experience of many scholars in solving infinite domain problems shows that [20–23]: the coupling model of finite element and infinite element has extensive practicability in solving practical engineering problems, and that shows obvious advantages in simulating and approximate simulating infinite domain problems. In a word, it is often used to solve more complex unbounded problems together with the conventional finite element method, which is a supplement to the finite element method. Therefore, it has inherent coordination with the finite element method and has more advantages than other numerical methods such as viscous boundary method for solving unbounded domain problems. But, Dynamic IEMB has not been widely used in engineering as a method to solve 3D multidirectional mapping problems.

Based on the above factors, FB, VSAB and IEMB are used to simulate the infinite domain foundation to reflect the energy dispersion phenomenon of incident waves at different boundaries. The CDP constitutive [24–26] is introduced in this paper, which is aimed at studying the dynamic failure mechanism and the rules of damage development for concrete aqueduct structures subject to seismic ground motion.

DYNAMIC INFINITE ELEMENT BOUNDARY (IEMB) METHOD

IEMB principle

In the solution of dynamic problems, the model boundary may produce a boundary effect, in which the energy reflected on the computing domains and affects the calculation results. The IEMB of ABAQUS provides the first- and second-order infinite elements, the finite-infinite element method (FEM-IEM) interaction is used to simulate the infinite domain propagation of the far-field seismic waves motion. By defining an element with a decay function in the semi-infinite domain, the FEM-IEM interaction method is realized, which overcomes the defects of the finite element method.

The dynamic response to IEMB is considered based on a traveling plane wave with orthogonal boundaries. Therefore, it is assumed that the response adjacent to the boundary has a sufficiently small amplitude that deforms the medium in a linear elastic manner. Its equilibrium equation can be described as follows:

$$-\rho \ddot{u} - \frac{\partial}{\partial x} \cdot \sigma = 0 \quad (1)$$

where ρ is the mass density of the medium, $Kg \cdot m^{-3}$; \ddot{u} is the acceleration of the material particles, $m \cdot s^{-2}$; σ is the stress, Pa ; and x is the position. The material is assumed to be isotropic and linearly elastic; therefore, σ can be described by

$$\sigma = \lambda \Pi : \varepsilon + 2G\varepsilon \quad (2)$$

where λ and G are functions expressing lame constants and the shear modulus of the medium, respectively; $\lambda = E\nu / (1+\nu)(1-2\nu)$, $G = E / 2(1+\nu)$ (E is Young's modulus, ν is Poisson's ratio), and ε is the strain.

When the material response is introduced into the equations of equilibrium, and ε is assumed to be a small strain, ε can be computed by the following equation:

$$\varepsilon = \frac{1}{2} \left\{ \frac{\partial u}{\partial x} + \left[\frac{\partial u}{\partial x} \right]^T \right\} \quad (3)$$

Substituting Equations (2) and (3) into Equation (1), the governing equation of motion is obtained.

$$\rho u_i = G \frac{\partial^2 u_i}{\partial x_j \partial x_j} + (\lambda + G) \frac{\partial^2 u_j}{\partial x_i \partial x_j} \quad (4)$$

Assuming that the plane wave is along the X -axis, the equation has the following two forms of solution. Equation (5) describes the plane P -wave (longitudinal wave), and Equations (6) and (7) express the plane S -wave (shear wave).

$$u_x = f(x \pm c_p t), \quad u_y = u_z = 0 \quad (5)$$

$$u_y = f(x \pm c_s t), \quad u_x = u_z = 0 \quad (6)$$

$$u_z = f(x \pm c_s t), \quad u_x = u_y = 0 \quad (7)$$

where $c_p = \sqrt{\frac{\lambda + 2G}{\rho}}$ and $c_s = \sqrt{\frac{G}{\rho}}$, "-" indicates forward propagation along X , "+" indicates backward propagation along X .

To avoid the reflection of the P -wave and S -wave energy back to the finite domain medium of $X < L$, damping constants d_p and d_s are introduced to calculate distributed damping at the boundary junction of the finite domain and infinite domain ($X = L$). The damping stress can be

expressed as:

$$\sigma_{xx} = ma - d_p \dot{u}_x \quad (8)$$

$$\sigma_{xy} = -d_s \dot{u}_y \quad (9)$$

$$\sigma_{xz} = -d_s \dot{u}_z \quad (10)$$

in which σ_{xx} is the P -wave stress at the boundary junction of the finite domain and infinite domain. $\sigma_{xx} = (\lambda + 2G)(f_1' + f_2')$, the other stress component $\sigma_{ij} = 0$, and the velocity is $\dot{u}_x = -c_p(f_1' - f_2')$. Equation (11) can be obtained using the above equations.

$$(\lambda + 2G - d_p c_p) f_1' + (\lambda + 2G + d_p c_p) f_2' = 0 \quad (11)$$

To ensure that there is no reflected stress wave at the boundary position when the wave is incident in any form, it is necessary to ensure $f_2 = 0$ and $f_2' = 0$. The P -wave damping form can be deduced as follows:

$$d_p = \frac{\lambda + 2G}{c_p} = \rho c_p \quad (12)$$

As in the previous sections, the damping form of the S -wave can be determined as follows:

$$d_s = \rho c_s \quad (13)$$

It should be noted that the IEM method is the boundary treatment method for FEM-IEM interaction. By introducing these boundary damping values to avoid waves reflection effects at the location of a boundary, we can adequately simulate the propagation of wave motion in the infinite domain.

Viscous-spring artificial boundary (VSAB) method

Because the VSAB has been widely used in engineering, it is not derived in detail here. The specific derivation process can be found in [27]. Its implementation method in ABAQUS can be seen in Figure 1.

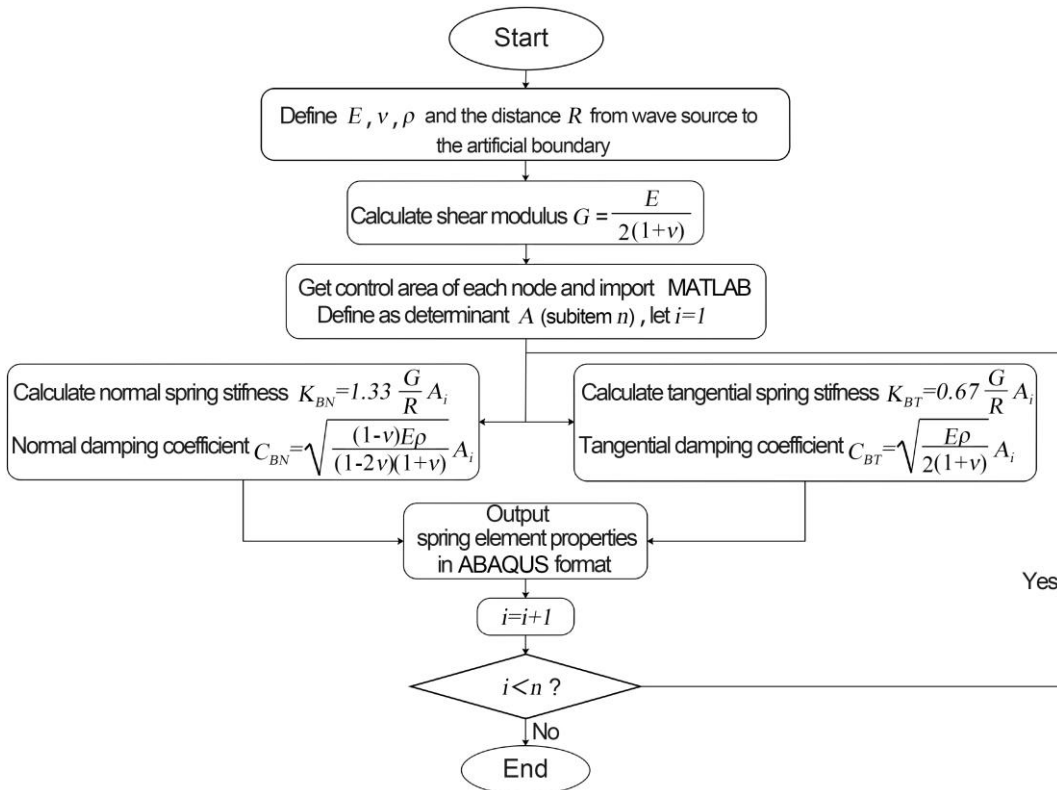
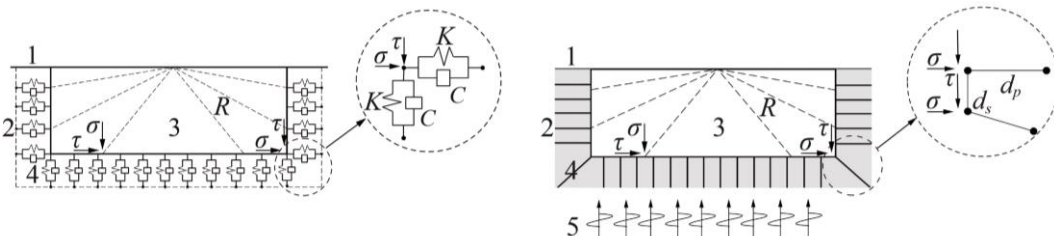


Fig. 1 – Flow chart of viscous–spring artificial boundary realization

Examples of numerical simulations

To verify the accuracy and reliability of the IEMB calculation method in the seismic responses of the aqueduct, the model of a 3D elastic homogeneous half–space was established by using the ABAQUS FEM code, considering the Lamb problem [28].

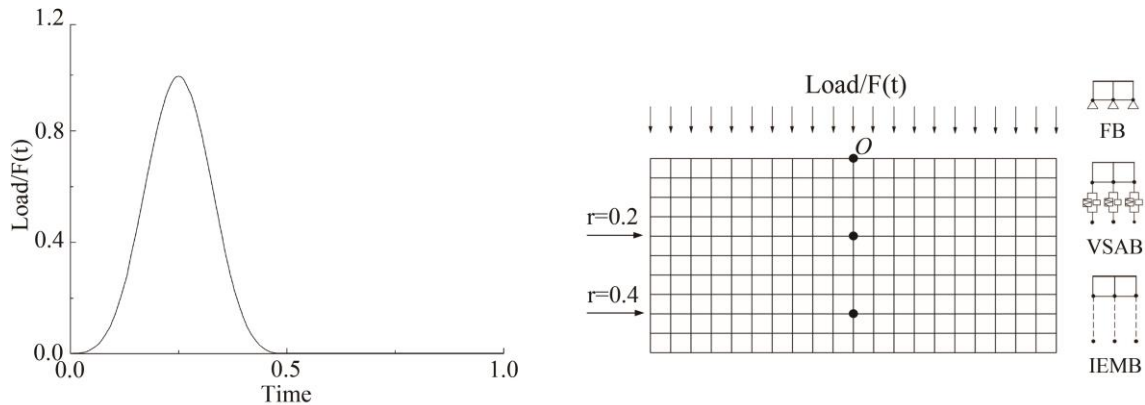
In this example, non-dimensional units are used. The range of the numerically computed object is taken as: $-0.5 \leq x, y \leq 0.5$, $-0.5 \leq z \leq 0$ with the finite element size taken as $\Delta x = \Delta y = \Delta z = 0.05$. Young's modulus of the medium $E = 40$, Poisson's ratio $\nu = 0.25$, and mass density $\rho = 1$. The duration $T = 5.0s$ and time interval $\Delta t = 0.001s$ are used for this example.



(a) Viscous-spring artificial boundary; (b) Infinite element method artificial boundary
Fig. 2 – Schematic diagrams of viscous–spring and infinite element method artificial boundary

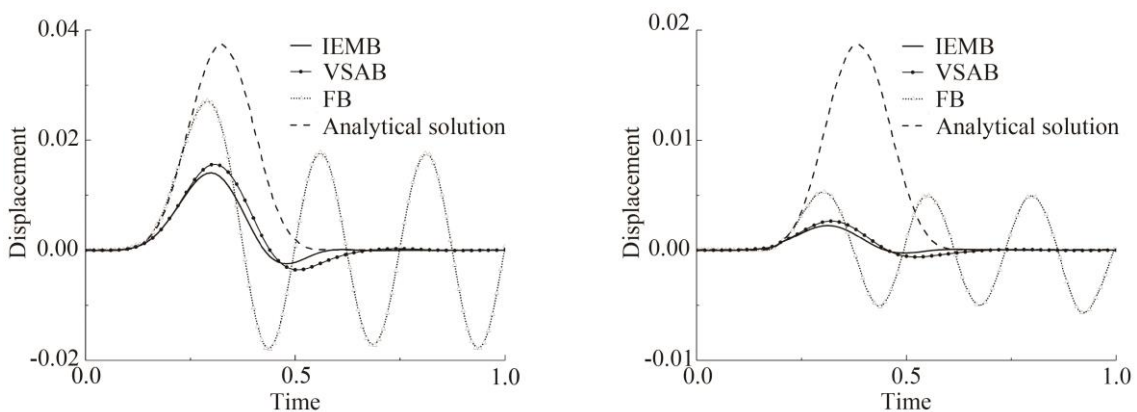
Note: *1. Free surface; 2. Infinite domain; 3. Near field; 4. Artificial boundary; 5. Seismic wave
 σ is the normal stress; τ is the shear stress; K is the spring stiffness; C is the damping coefficient; d_p is the normal damping; d_s is the tangential damping; R is the distance between the observation point on the free surface and the vertical load point.

Ignoring the dissipation effect of waves in the medium, the VSAB, IEMB and FB are respectively set at the boundary truncation position and compared with the analytical solution in this example. The VSAB and IEMB are shown in Figure 2. The time history of applying the load is shown in Figure 3(a), which acts on the free surface of the semi-infinite space as a concentrated vertical force. The observation points 0.2 and 0.4 away from the loading center point O are selected and analysed by calculating the relative displacement. The schematic diagram of the observation point is shown in Figure 3(b).



(a) Load time history; (b) Observation points of different boundary finite element model
 Fig. 3 – Finite element model and load time history curve

The relative displacement time histories in the vertical direction for each observation point under different boundary effects are shown in Figure 4. The analytical solution can be obtained by the integration of the fundamental solution for the load time histories. It can be seen from Figure 4 that the FB cannot cause nodes movement when the load is applied from the top of the model to the bottom. That is, the nodes at the bottom of the calculation model do not move in the FB condition, and the wave is reflected back to the elastic medium. Since there is no damping effect in the medium, the displacement curve oscillates back and forth in the medium elastic region, forming the displacement curve in Figure 4. When the VSAB is adopted, as shown in Figure 4, most of the energy is absorbed on the VSAB, while a small part is reflected back to the medium elastic area, and also absorbed in the following time period. However, when the IEMB is adopted, there is no energy reflection on the FEM–IEM interaction boundary. Results show that under the FB condition, the wave motion is almost entirely reflected. In contrast, the VSAB and IEMB show good energy absorption effect, and the wave propagation is almost completely dissipated on the boundary.



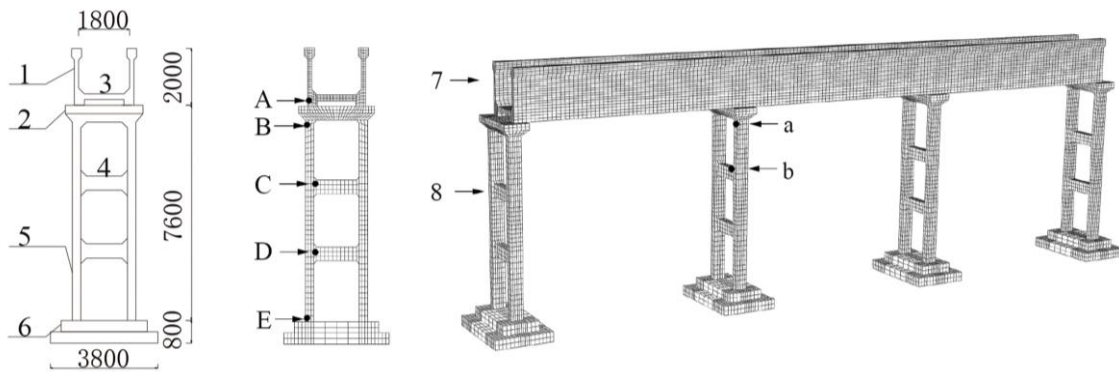
(a) $r=0.2$ (b) $r=0.4$
 Fig. 4 – Contrast diagram of the effect of each characteristic point on three boundary

SEISMIC GROUND MOTION FAILURE MECHANISM OF AQUEDUCT STRUCTURE BASED ON IEMB

The above analysis shows that the VSAB and IEMB have a good absorption effect on seismic waves compared with the FB, which can better simulate the procedure of wave motion propagation. However, it is not easy to evaluate how much influences this simulation has on the calculation of the actual project. The following is an example of a large-scale aqueduct actual project in a Chinese irrigation district, and the effects of the three boundaries are compared.

Example model and seismic wave selection

A three-span structure of the aqueduct is selected for this study. The overall structure includes the groove body, bent, bent column, and foundation, etc. The groove body is a rectangular structure with a single span length of 10 m. Figure 5 shows the bent which has an h-form frame structure, the aqueduct is 1.8 m wide and 2 m high, and the bent is 7.6 m high. C30 concrete is used to construct the groove body, and the CDP constitutive structure is introduced to simulate the dynamic damage development of concrete [24–26].



(a) Aqueduct structure diagram; (b) Finite Element Model of Aqueduct Structure
 Fig. 5 – Aqueduct Structure Diagram and Finite Element Model

Note: *1. Wing wall; 2. Pier cap; 3. Bottom plate; 4. Crossbeam; 5. Bent column; 6. Foundation platform; 7. Groove body; 8. Bent

A、B、C、D、E are feature points of damage; a、b are feature points of aqueduct structural seismic ground motion response.

The damage values range from 0 (no damage) to 1 (complete damage) to express the degree of damage to different materials. The various material parameters of the aqueduct structure are shown in Table 1.

Tab. 1 - Various material parameters of aqueduct structure

Material	Elastic modulus/(GPa)	Density /(Kg·m ⁻³)	Poisson ratio	Tensile strength/(MPa)	Compressive strength/(MPa)
Aqueduct(C30)	30	2500	0.167	1.3	14.3
Bent(C25)	28	2450	0.167	1.27	11.9
Foundation(C25)	28	2450	0.167	1.27	11.9
Ground	7	2100	0.3	–	–

The numerical model based on the IEMB is shown in Figure 6. In dynamic analysis, the amplitude attenuation of the response wave depends on the damping effect of the structure. However, it is challenging to determine the damping matrix of the structure. Since the structure of the natural modes, the mass matrix M is orthogonal to the stiffness matrix K , the damping matrix C of the structure is usually simplified as a linear combination of M and K .

$$C = \alpha M + \beta K \tag{14}$$

Rayleigh damping is used to analyse the equation. α and β can be expressed in terms of Equations (15) and (16).

$$\alpha = \frac{2\omega_i\omega_j(\xi_j\omega_i - \xi_i\omega_j)}{\omega_i^2 - \omega_j^2} \tag{15}$$

$$\beta = \frac{2(\xi_j\omega_j - \xi_i\omega_i)}{\omega_j^2 - \omega_i^2} \tag{16}$$

where ω_i and ω_j , respectively, take the first and second-order frequencies corresponding to the structure, and ξ_i resp. ξ_j take the damping ratio corresponding to the structure frequency.

The engineering foundation site classification is Class I, and the basic seismic intensity is VIII. The horizontal peak acceleration of rare ground motion is 0.331g, and the vertical peak acceleration is taken as two-thirds that of the horizontal direction. Following the principle of similar spectrum characteristics, the artificial wave TH3TG025 was selected as the seismic wave. The duration was set using 10% of the peak acceleration as the threshold [29]. The duration is calculated as 5 s, which meets the standard requirements of 5–10 times the basic period of the structure, time interval $\Delta t=0.02s$, and the acceleration time history of the seismic wave is shown in Figure 7.

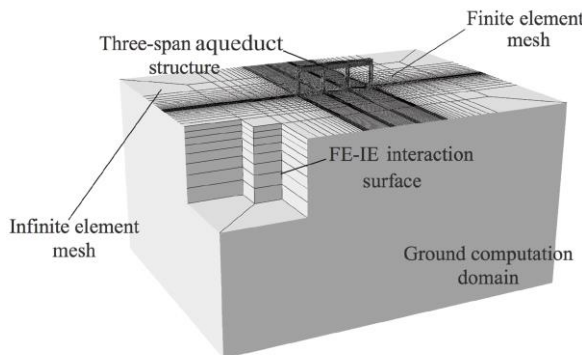


Fig. 6 – FE–IE interaction foundation model

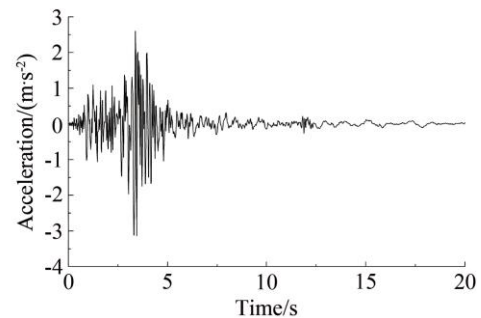
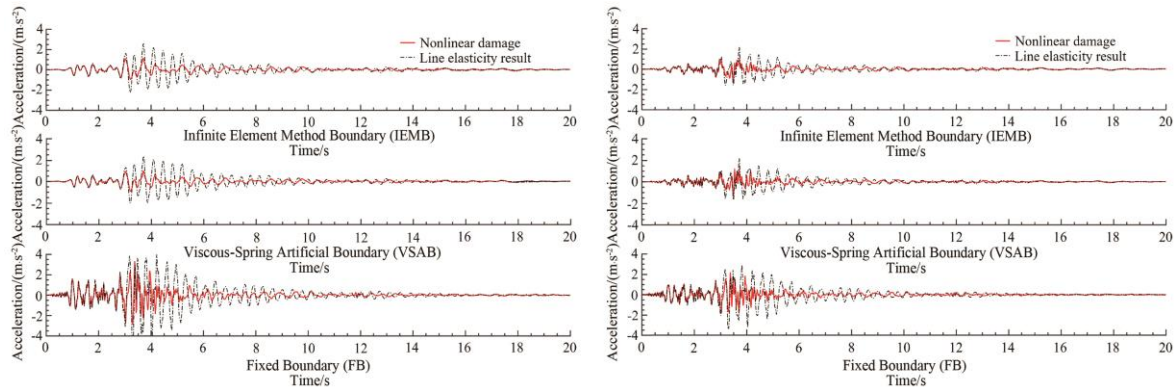


Fig. 7 – Time history records of seismic accelerations

Seismic ground motion response rules for the structure

Aqueduct structure acceleration response rules

The numerical calculation selects the top a of the bent and crossbeam end b as feature points for the seismic ground motion response analysis of the aqueduct. The results are presented in Figure 8.



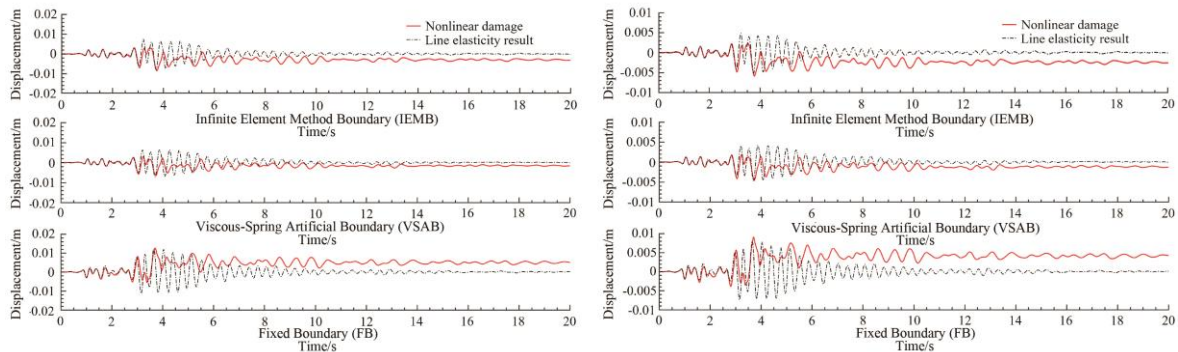
(a) Lateral flow acceleration at bent (point a); (b) Lateral flow acceleration at crossbeam (point b)
 Fig. 8 – Contrast diagram of each feature point's acceleration time histories

Note: *Feature point positions are shown in Figure 5(b).

As can be seen from the acceleration time histories of the aqueduct structure shown in Figure 8, the acceleration development trend of each feature point is basically the same under three different boundary conditions, and the maximum response occurs at a time of about 3 s, which is basically consistent with the occurrence time of the seismic peak acceleration. When considering plastic damage during strong earthquakes, the material will occur damage accumulation effect. The change rule of structural acceleration has a strong fluctuation, and the peak value is slightly lower than that in the undamaged state. With the increase in the height of the structure, the acceleration response tends to be amplified, and the displacement of the crossbeam at a lower position is less than that of the bent with a higher position. Finally, by comparing the calculation results of the IEMB and the VSAB, it is found that the difference between the two results is very small, ranging from 0.4% to 19%, but generally below 10%. The FB is 27%–77% larger than the IEMB and 38%–76% higher than the VSAB.

Aqueduct structure displacement response rules

The displacement change rule of each feature point of the aqueduct relative to the foundation is shown in Figure 9. During strong earthquakes, the displacement response of each feature point reaches its maximum value at times up to about 4 s, which is the same as the time when the seismic peak ground acceleration occurs. Before the duration of about 3 s, the earthquake excitation is small. During this time, the structure is in the elastic stage, so there was little difference in the response results whether to consider the damage. However, in the late period of the seismic duration, the structural displacement response has a certain displacement deviation from the foundation. The structure undergoes irreversible plastic damages during the earthquake. This is mainly due to the introduction of the CDP constitutive, which can describe the softening behaviour of a concrete structure after damage. The difference between the calculation results of the IEMB and the VSAB is between 2% and 17%. The difference is caused by the difference in the realization of IEMB and VSAB and the processing method of energy dissipation. The results show that the FB increases by 9%–35% compared with the IEMB, and increases by 6%–48% compared with the VSAB.

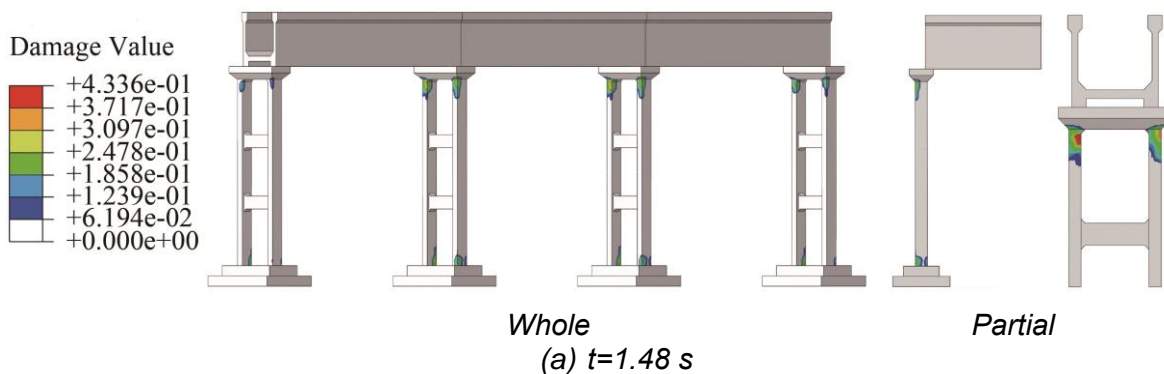


(a) Lateral flow displacement at bent (point a); (b) Lateral flow displacement at crossbeam (point b)
 Fig. 9 – Contrast diagram of each feature point’s displacement time histories

Note: *Feature point positions are shown in Figure 5(b).

Dynamic failure mechanism and the damage development rules of the aqueduct structures

Figure 10 reveals the dynamic damage development process of the aqueduct structure. During a strong earthquake, the damage to the bent column is relatively serious. Penetrating damage occurred at the top and bottom of the bent column and both ends of the crossbeam, but no damage occurred at the foundation cushion cap; due to the rigidity of the aqueduct structure, only slight damage was found only near the support of the bent. During the process of damage development, the structural damage to the aqueduct first appeared at the bottom of the bent column and the contact part of foundation at a time of 1.4 s, then the damage occurred at the top of bent in 1.48 s. From 1.48 s–2.82 s, the damage expanded from the bottom of the bent column to the upper part, and damage starts at the end of the lower crossbeam at 2.82 s, as shown in Figure 10(a) and Figure 10(b). Then, from 2.82 s–3.01 s, the damage to the lower crossbeam gradually spreads, and damage begins to appear at the upper crossbeam at a time of 3.01 s. A damage diagram is presented in Figures 10(b) and 10(c). During the seismic duration from 3.01 s–4.01 s, the damage is extended from the top and bottom of the bent to the crossbeam in the middle of the bent. The penetrating damage occurs at the top and bottom of the bent column and the crossbeam, respectively, as shown in Figure 10(d). Finally, in the last part of the seismic duration, the structural damage basically does not change because the seismic acceleration decreases.



(a) $t=1.48$ s
 Fig. 10 – Developing process of aqueduct’s damage under earthquake

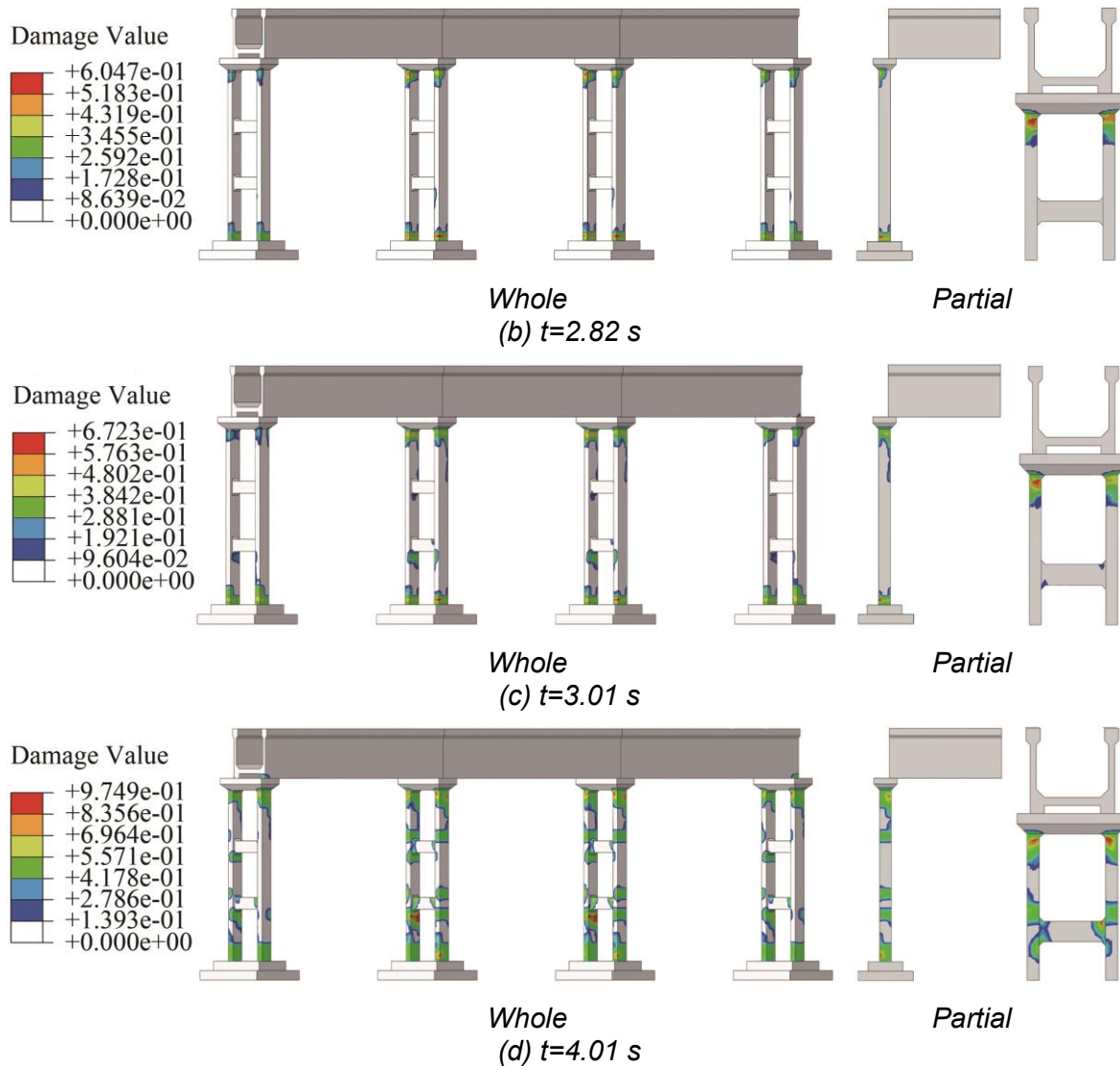


Fig. 10 – Developing process of aqueduct's damage under earthquake

The seismic action is closely related to the duration, During seismic wave motion, changes in the acceleration will also cause the structural stress state to change, which is a significant feature of dynamic load time history calculation. To order to explore the development process and rules of aqueduct structural damage during seismic wave motion, the feature points on one side of the structure are selected for analysis. The location of the feature points is shown in Figure 5(a), and the development and changes of damage value at each point are shown in Figure 11. The damage develops extremely rapidly during the course of the earthquake, and is complete in less than 4 s. After the top and bottom of the bent column are damaged, the damage extends to the middle of the bent column; therefore, the time at which damage occurs at the two crossbeams is the same, and soon reaches the complete damage. Compared with the time at which damage occurred at the bent and crossbeams, damage occurred at the bottom of the wing wall near the cushion cap at a relatively late time. After certain damage, the damage no longer changes.

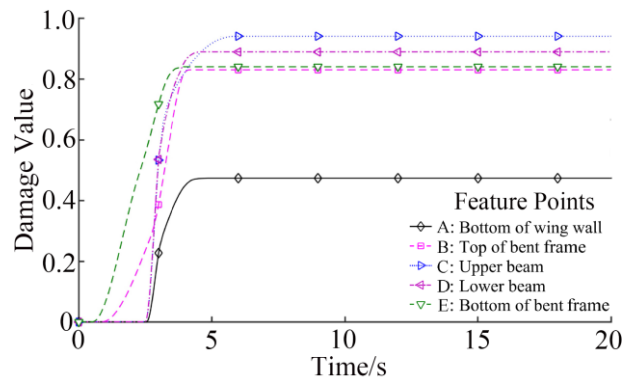


Fig. 11 - Feature point damage development process

Note: *Feature point positions are shown in Figure 5(a).

When the seismic ground motion acceleration reaches its peak value, the damage to the structure increases rapidly, indicating that the seismic peak ground motion acceleration has a significant impact on the damage of the structure. When comparing the development trend of damage at each position, it can be seen that the higher the position, the faster the damage development. At the bottom of the bent, the rate of damage development obviously lags behind that of other sections of the structure. A preliminary conclusion is that a higher the position causes a greater displacement and the faster the damage development. The above analysis reflects that the aqueduct structure is most likely to be seriously damaged at the junction of the pier cap and bent column during an earthquake, followed by the two ends of the crossbeam. Once the damage and cracking are serious, the whole aqueduct structure may collapse.

CONCLUSIONS

In this study, the IEMB, VSAB, FB methods and the CDP constitutive are adopted to study the mechanism and development rules of damage to large-scale irrigation aqueducts under the ground motion of an earthquake. The main conclusions are as follows:

(1) The effects of conventional FB, VSAB, and dynamic IEMB on the energy absorption and dissipation of impulse waves are compared. The FB cannot absorb the wave energy, and the displacement response will be enlarged by 6%–48% compared with the other two boundaries. Both the VSAB and the dynamic IEMB have a good energy absorption effect on the incident wave, with an error value between 2% and 17%. In the calculations for the towering cantilever structure model, the energy absorption of IEMB is slightly better than that of VSAB. Compared with VSAB, dynamic IEMB does not need a spring-damper mechanical system, and is simpler in form and more efficient in exact modelling.

(2) In aqueduct seismic ground motion response studies, it was found that with an increase in the height of the structure, the dynamic displacement response of aqueduct trends to enlarge. At the end of the seismic ground motion duration, large-scale damage occurred to the aqueduct support frame, resulting in a slight deviation from the structure displacement relative to the foundation.

(3) Through the analysis of the damage development rule, it discovers that the failure position of aqueduct structure is mainly focused on the intersection place of pier cap and bent column, and the intersection place of the bent column and the foundation of an aqueduct. It can be seen that the damage at the bottom of the pier cap appears a general down-slope tendency. These places are in weak areas of the aqueduct structure. Therefore, in the process of seismic design, relevant damping measures should be taken to control the damage development and prevent the overall aqueduct structure from being damaged or collapsed.

ACKNOWLEDGEMENTS

This study was supported by the National Key Research and Development Program of China (grant no 2018YFC0406901), and the National Natural Science Foundation of China (grant no 51979109), Henan Science and Technology Innovation Talent Program (grant no 174200510020), Henan Province University Science and Technology Innovation Team Support Plan (grant no 19IRTSTHN030). These supports are gratefully acknowledged and greatly appreciated.

REFERENCES

- [1] Housner G.W., 1963. The dynamic behavior of water tanks, *Bulletin of the seismological society of America*, vol. 53, no. 2. pp. 381-387.
- [2] Olson L.G., and Bathe K.-J., 1985. Analysis of fluid-structure interactions. A direct symmetric coupled formulation based on the fluid velocity potential, *Computers & Structures*, vol. 21, no. 1-2. pp. 21-32.
- [3] Omidinasab F., and Shakib H., 2012. Seismic response evaluation of the RC elevated water tank with fluid-structure interaction and earthquake ensemble, *KSCE Journal of Civil Engineering*, vol. 16, no. 3. pp. 366-376.
- [4] Ibrahim R.A., 2005, *Liquid sloshing dynamics: theory and applications* (Cambridge University Press).
- [5] Liu Y., Dang K., and Dong J., 2017. Finite element analysis of the aseismicity of a large aqueduct, *Soil Dynamics and Earthquake Engineering*, vol. 94. pp. 102-108.
- [6] Zhang H., Sun H., Liu L., and Dong M., 2013. Resonance mechanism of wind-induced isolated aqueduct–water coupling system, *Engineering structures*, vol. 57. pp. 73-86.
- [7] Ying L., Meng X., Zhou D., Xu X., Zhang J., and Li X., 2019. Sloshing of fluid in a baffled rectangular aqueduct considering soil-structure interaction, *Soil Dynamics and Earthquake Engineering*, vol. 122. pp. 132-147.
- [8] Li Y., Lou M., and Pan D., 2003. Evaluation of vertical seismic response for a large scale beam supported aqueduct, *Earthquake engineering & structural dynamics*, vol. 32, no. 1. pp. 1-14.
- [9] Zarghamee M.S., Rao R.S., Kan F.W., Keller T.O., Yako M.A., and Iglesia G.R., 1997. Seismic risk analysis of hultmann aqueduct, *Infrastructure Condition Assessment: Art, Science, and Practice*. pp. 346-355.
- [10] Chrysostomou C.Z., Stassis A., Demetriouder T., and Hamdaoui K., 2008. Application of shape memory alloy prestressing devices on an ancient aqueduct, *Smart Structures and Systems*, vol. 4, no. 2. pp. 261-278.
- [11] Lysmer J., and Kuhlemeyer R.L., 1969. Finite dynamic model for infinite media, *Journal of the Engineering Mechanics Division*, vol. 95, no. 4. pp. 859-878.
- [12] Deeks A.J., and Randolph M.F., 1994. Axisymmetric time-domain transmitting boundaries, *Journal of Engineering Mechanics*, vol. 120, no. 1. pp. 25-42.
- [13] Gu Y., Liu J.B., and Du Y., 2007. 3D consistent viscous-spring artificial boundary and viscous-spring boundary element, *Engineering Mechanics*, vol. 24, no. 12. pp. 31-37.(in Chinese)
- [14] Liao Z.P., and Wong H., 1984. A transmitting boundary for the numerical simulation of elastic wave propagation, *International Journal of Soil Dynamics and Earthquake Engineering*, vol. 3, no. 4. pp. 174-183.
- [15] Ungless R.F., 1973. Infinite finite element.
- [16] Bettess P., 1984. A new mapped infinite element for exterior wave problems, *Numerical methods in coupled systems*.
- [17] Zienkiewicz O., Bando K., Bettess P., Emson C., and Chiam T., 1985. Mapped infinite elements for exterior wave problems, *International Journal for Numerical Methods in Engineering*, vol. 21, no. 7. pp. 1229-1251.
- [18] Yun C.B., Kim D.K., and Kim J.M., 2000. Analytical frequency-dependent infinite elements for soil-structure interaction analysis in two-dimensional medium, *Engineering structures*, vol. 22, no. 3. pp. 258-271.
- [19] Qi Y., and Hisanori O., 2014. Study of ABAQUS dynamic infinite element artificial boundary, *Rock and Soil Mechanics*, vol. 35, no. 10. pp. 3007-3013.(in Chinese)
- [20] Zhang C.H., and Zhao C. B., 1987. Coupling method of finite and infinite elements for strip foundation wave problems, *Earthquake engineering & structural dynamics*, vol. 15, no. 7. pp. 839-851.
- [21] Godbole P.N., Viladkar M.N., and Noorzaei J., 1990. Nonlinear soil-structure interaction

- analysis using coupled finite-infinite elements, *Computers & Structures*, vol. 36, no. 6. pp. 1089-1096.
- [22] Viladkar M.N., Godbole P.N., and Noorzaei J., 1991. Soil-structure interaction in plane frames using coupled finite-infinite elements, *Computers & Structures*, vol. 39, no. 5. pp. 535-546.
- [23] Edip K., Garevski M., Butenweg C., Sesov V., Cvetanovska J., and Gjorgiev I., 2013. Numerical simulation of geotechnical problems by coupled finite and infinite elements, *Journal of Civil Engineering and Architecture*, vol. 7, no. 1. p. 68.
- [24] Xu X.Y., Ma Z.Y., and Zhang H., 2013. Simulation algorithm for spiral case structure in hydropower station, *Water Science and Engineering*, vol. 6, no. 2. pp. 230-240.
- [25] Lee J., and Fenves G.L., 1998. Plastic-damage model for cyclic loading of concrete structures, *Journal of Engineering Mechanics*, vol. 124, no. 8. pp. 892-900.
- [26] Oliver J., Oller S., and Oñate E., 1989. A plastic-damage model for concrete, *International Journal of solids and structures*, vol. 25, no. 3. pp. 299-326.
- [27] He J.T., Ma H.F., Zhang B.Y., and Chen H.Q., 2010. Method and realization of seismic motion input of viscous-spring boundary, *Shuili Xuebao (Journal of Hydraulic Engineering)*, vol. 41, no. 8. pp. 960-969.
- [28] Lamb H., 1903. On the Propagation of Tremors over the Surface of an Elastic Solid, *Proceedings of the royal society of London*, vol. 72. pp. 128-130.
- [29] Kanai K., 1983, *Engineering seismology* (University of Tokyo Press).

IMPACT OF ECO FRIENDLY BLAST FURNACE SLAG ON PRODUCTION OF BUILDING BLOCKS

Ashish Nim and Kundan Meshram

*Department of Civil Engineering, Oriental University Indore, Madhya Pradesh, India;
ashishn704@gmail.com, kundan.transpo@gmail.com*

ABSTRACT

Solid waste management is one of the prime concerns in the world due to ever increasing proportion of non-biodegradable industrial waste product. Blast Furnace Slag (BFS) is one of the largest by products of steel and iron industries which creates scarcity of land filling area due to ineffective reuse and recycle. The use of such substance to create building blocks not most effective makes it economical, however it also enables in decreasing disposal concern. Clay bricks are the oldest walling material of construction industries. Due to preferable mechanical properties bricks are considered as prime source of masonry units that is used as walling material. Conventional clay bricks required burning process known as kiln firing which emits huge amount of CO₂ into the atmosphere. World is facing same problem with the production of cement too. The major reasons behind pollution and environment depletion are due to unremitting decay in natural resources caused from deriving of raw materials such as sand, clay and dirt and also from huge amount of hazardous and non-hazardous wastes produced by the industries. Reuse of industrial waste such as BFS instead of naturally occurring raw material leads to contribute towards green environment. Present study intended toward use of steel and iron industry waste for manufacturing of building blocks to promote low cost housing along with mitigation of environmental violation. Based on the results, BFS may effectively replace with naturally occurring fine aggregates due to favourable physical properties. Durability aspects in terms of water absorption and compressive strength also found adequate as per the requirement of IS codes. An amount of partial to full replacement of BFS may allow as per required weathering conditions.

KEYWORDS

Industrial waste, walling material, Building blocks, Brick, Blast furnace slag

INTRODUCTION

Approximately 500 kg per tonne waste materials are generated from crude steel by steel plants. Out of these wastes, around 400 kg per tonne is only BFS [1]. India's crude steel production for 2018 was 106.5 Mt, up by 4.9% in 2017, meaning India has replaced Japan as the world's second largest steel producing country [1].

The most widely recognized walling material utilized in structure development is bricks. Bricks are the simplest and oldest building blocks used in construction. Annual production of bricks is currently 1391 billion units worldwide and the demand expected to be rising [3]. In India the annual demand is 200 billion bricks, producing around 250 billion bricks from 1, 50,000 kilns [2, 4]. The main ingredients used for bricks are derived from natural resources occupies more than 80% by volume. The traditional method consumes 350 million tonnes of fertile soil and 25 million tonnes of coal annually [2]. On the other hand manufacturing of cement along with its use also tends to increase the amount of CO₂. The huge consumption of

naturally occurring materials and energy eventually lead to exhaustion of environment.

In both developed and developing countries, the problem of waste management has already become an issue to be addressed immediately. This problem is compounded by the rapidly increasing amounts of industrial wastes of a complex nature and composition.

As per the review of previous research works, various variety of wastes have been utilized by the researchers in terms of developing building blocks. Table 1 shows a summary of research work done for production of building blocks/bricks from various industrial wastes. But the effective percentage of industrial waste utilization was quite inadequate due to unfavourable mechanical and chemical properties.

Tab.1 - Production of building blocks/bricks from various industrial wastes

S. No.	Waste material used	Outcomes	Reference No.
1	Paper mill sludge (PMS)	An optimum replacement of PMS at 10 % shows better results. With laterite soil the compressive strength at 850 ^o c temperature was found around 9 MPa increased up to 11MPa at temperature 900 ^o c.	[3]
2	Granite fines	Mardini blocks with granite fines show an increase of 120% in compressive strength as compare to conventional soil blocks. Also adobe blocks with granite fines show 135% more compressive strength as compare to conventional soil blocks.	[4]
3	Fly ash and quarry dust	Cement, fly ash, quarry dust taken 70%, 20%, 10% respectively, for manufacturing brick and it was observed that compressive strength of bricks was found 13.5 MPa relevant to normal bricks 14.0 MPa after 21 days curing.	[5]
4	Brick debris and quarry dust	Re bricks were found adequate in compressive strength 7.352 MPa at an optimum replacement of 20% as compare to fly ash brick 7-12 MPa and II nd class clay brick with strength more than 7 MPa.	[6]
5	Fly ash ,lime and gypsum	Fal-G Bricks with mix proportion of 60% fly ash, 15% lime, 15% gypsum and 10% sand shows better compressive strength 5.34 MPa as compare to clay bricks 3.98 MPa.	[7]
6	Rice husk (0 to 5%) by weight	Higher compressive strength obtained at 2% replacement of rice husk.	[8]

7	Waste marble powder 0% to 80% by weight	Found relative water absorption and mechanical properties up to 10% replacement.	[9]
---	---	--	-----

Keeping the views of previous research works, present study makes an effort to extricate the problem of managing steel industrial waste like BFS by its effective utilization to turn it into valuable building blocks as per required durability and mechanical properties ultimately leads to promote sustainable and low cost development and also to mitigate the depletion of natural resources.

MATERIALS AND METHOD

BFS was collected from the furnace workshop of Iron Industry located near Gadbad Puliya, AB Road, Indore, M.P., India. More than 20 steel and iron industries are working at present in Indore and also producing a huge amount of wastes every day. Characteristics of raw materials have been carried out considering procedure and requirements as described in IS Codes. In order to determine specific gravity, water absorption, silt content and unit weight of BFS and river sand, 1.18mm passing and 150µm retained particles were selected. The properties of BFS and river sand are showed in Table 2 and Table 3 respectively. Similarly, to determine properties of PPC cement the particle size were chosen it was finer than 90µm. Table 4 shows the properties of PPC cement.

Tab. 2 - Physical properties of BFS

Properties	Value	Procedure
Specific Gravity	3.2	As per IS 2386- Part- I and III:1963 [10,11]
Unit weight (kg/m ³)	1800	
Water Absorption	0.4%	
Silt Content	1%	

Tab. 3 - Physical properties of river sand

Properties	Value	Requirements as per IS 383:2016 [12] and IS 2386- Part- I and III:1963 [10,11]
Specific Gravity	2.6	2.5-3.0
Unit Weight (kg/m ³)	1560	-
Water Absorption	1.4%	Less than 2%
Silt content	3%	Less than 5%
Fineness Modulus	2.8	2.0-3.5

Tab. 4 - Physical properties of PPC cement

Properties	Value	Permissible values	Requirement
Unit Weight (kg/m ³)	1310	-	-
Standard Consistence	27%	25-35%	IS 4031- Part-IV and V:1988 [13,14]
Initial Setting Time	33 Minutes	Minimum 30 Minutes	
Final Setting Time	550 Minutes	Less than 600 Minutes	

BFS comprises the required properties that are useful to convert it into building materials. The physical property of BFS lies between required limits which show its adequacy.

EXPERIMENTAL PROGRAMME

Procedure for BFS based building block production

Crushed sample of BFS was replaced in different amount (10%, 20%, - - -, 100%) by volume of sand and a standard amount of 10% cement was added. The control building block specimens were also prepared (0% BFS) to set the benchmark for results. 40–45% of water was added to dry mix to convert it into the shape of building blocks. Brick hand moulds of size 19cmX9cmX9cm were used for casting building blocks. For initial removal of moisture brick specimens were air-dried at room temperature for 24 h and then placed into curing tank after stripping. The building block samples were designated as B represented the identity of BFS. Table 5 shows the composition of different mixes for preparing building blocks. Total 60 numbers of moulds were prepared to ensure the properties of building blocks.

Tab. 5 - Composition of different mixes

S. No.	Specimen	Proportion (by volume) C%-S%-SL%
1	B-0	10%-90%-00%
2	B-10	10%-80%-10%
3	B-20	10%-70%-20%
4	B-30	10%-60%-30%
5	B-40	10%-50%-40%
6	B-50	10%-40%-50%
7	B-60	10%-30%-60%
8	B-70	10%-20%-70%
9	B-80	10%-10%-80%
10	B-90	10%-00%-90%
C- Cement, S- Sand, SL- Slag		

Determination of properties of building blocks

Water absorption of prepared building blocks was determined as per the procedure described in IS-3495 (Part-III):1992 [15]. Compressive strength of building blocks was determined with digital compression testing machine (CTM 2000kN capacity) as per IS-3495 (Part-I):1992 [16]. Both tests were performed after 28 days curing. (Figure 1) shows BFS based building blocks after 28 days curing.



Fig.1- BFS based building blocks after 28 days curing

METHODOLOGY

The purpose of this research is to develop building blocks using BFS and to conduct experimental investigations demonstrating efficacy of the product. Method implying experimental work followed in this research is showed in (Figure 2).

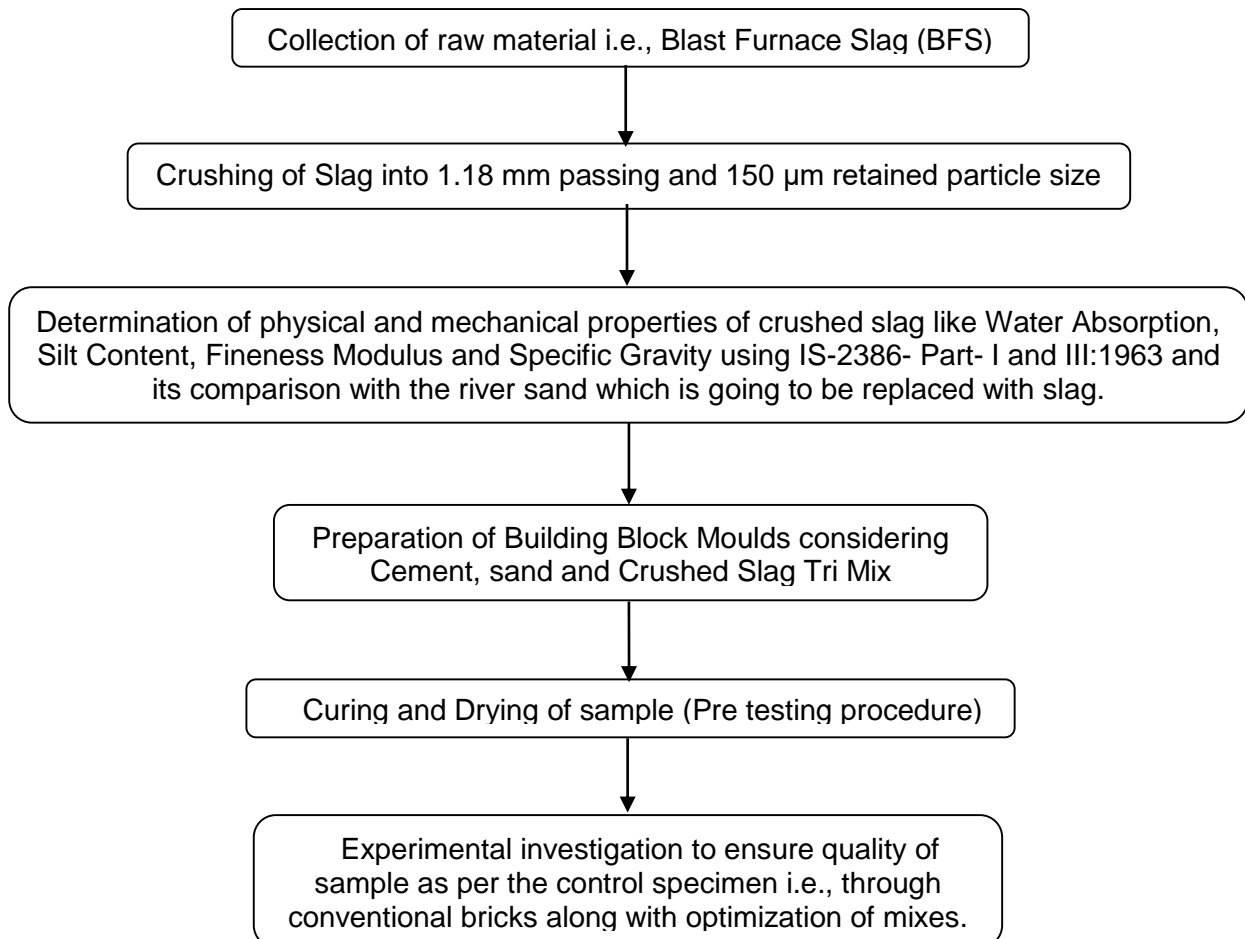


Fig. 2 -Methodology

RESULTS AND DISCUSSION

Determination of compressive strength

Compression test was carried out when building blocks acquired the necessary curing condition i.e., after 28 days curing and in wet condition. Table 6 shows the observations found during experimental investigation.

Tab. 6 - Compressive strength of building blocks

S.No.	Specimen	Average Compressive Strength (MPa)
1	B-0	7.25
2	B-10	5.85
3	B-20	6.40
4	B-30	6.65
5	B-40	7.10
6	B-50	5.45
7	B-60	5.25
8	B-70	4.90
9	B-80	5.60
10	B-90	4.50

Determination of water absorption

Water absorption test was carried out on completely dried samples. Initially blocks were dried using ventilated oven by maintaining temperature to 110°C. After drying, the blocks were immersed in clean water at a room temperature of 27 ± 2 °C for 24 hours. After 24 hours immersion the blocks were removed and wipe out using damp cloth. Table 7 shows the observation to demonstrate the results of water absorption of building blocks.

Tab. 7 - Water absorption of building blocks

Specimen	Dry weight W_1 gm	Weight (after 24 hours immersion into water) W_2 gm	Water absorption (%) $= (W_2 - W_1) / W_1 \times 100$
B-0	2390	2630	11.0
B-10	2450	2690	9.90
B-20	2515	2700	10.50
B-30	2580	2795	8.60
B-40	2600	2835	9.00
B-50	2645	2875	8.80
B-60	2685	2915	8.60
B-70	2700	2915	7.95
B-80	2735	2960	8.20
B-90	2760	2985	8.15

Characterization of Building Blocks

Experimental investigations for compressive strength and water absorption capacity were performed to insure the durability of BFS based building block samples as per IS code specifications. Building blocks found free from defects like bloating, cracks and efflorescence as examined on all types of samples from B0 to B10.

Water absorption is an important parameter to indicate open porosity. To ensure external weather resistance, the lower percentage of water absorption is always better. As per IS 12894-2002 [17], the average water absorption not more than 20 percent demonstrates a good quality of building block. (Figure 3) shows water absorption for BFS based building blocks. Maximum percentage of water absorption was found 11.0% proven the requirements as per IS code recommendations.

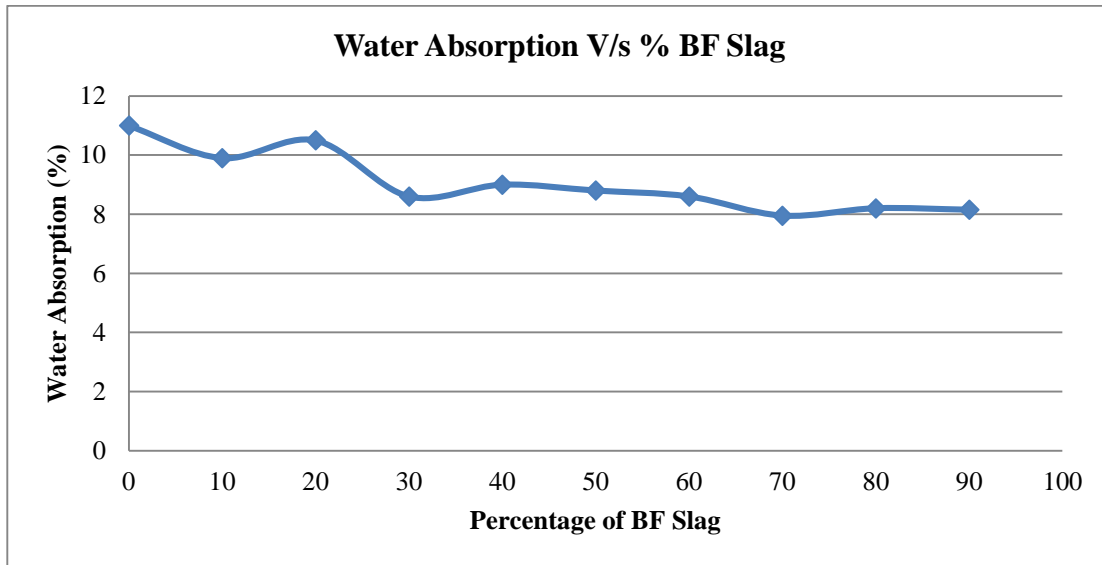


Fig.3 -Water absorption of BFS based building blocks

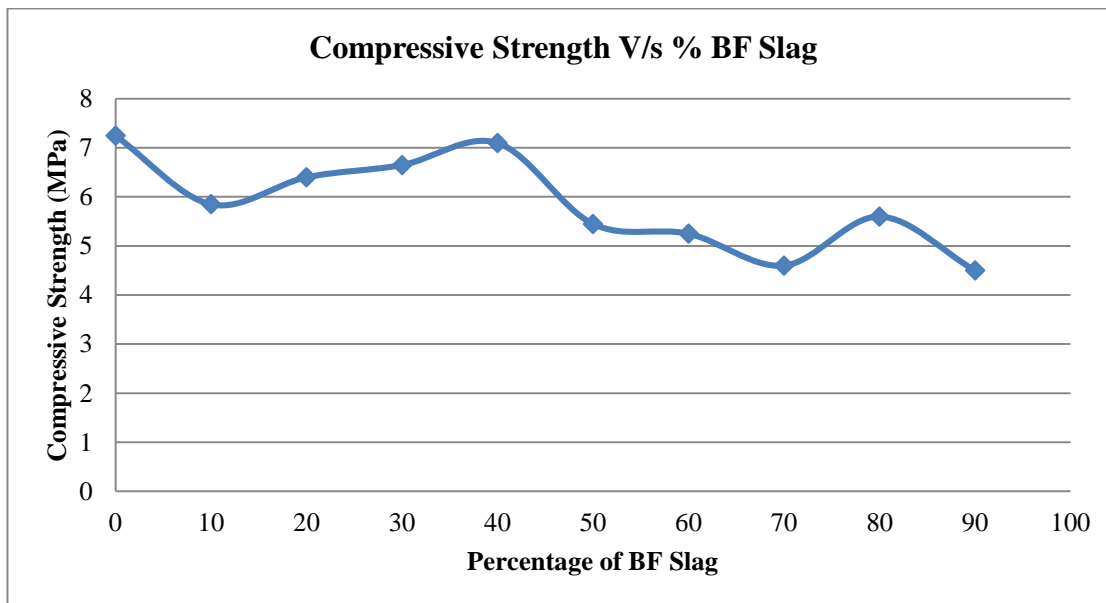


Fig.4- Compressive strength of BFS based building blocks

Compressive strength is the most critical index of building blocks and is shown in (Figure 4). Figure shows, as the percentage of BFS increase from 10% to 40%, compressive strength also increases. Replacements of BFS by more than 50% by volume exhibits decrement in the value of compressive strength. As per IS 1905-1987 [18], minimum compressive strength required by the building block after 28 days curing should not be less than 0.7 MPa for 1:8 mortar mix. Minimum compressive strength achieved by BFS based building blocks was found 4.50 MPa shows good quality requirements.

STATISTICAL MODELING

Development of regression model

A generalized correlation was developed considering experimental data carried out during research work in terms of water absorption, density and compressive strength. This developed correlation was as follows:

$$ACS = -0.03682(A) -0.02171(B) +0.004579(C)$$

Where,

ACS= Average Compressive Strength in MPa, (Dependent variable)

A= Slag (%),

B= Water Absorption (%) and

C= Density of building blocks in (kN/m³).

Correlation was developed considering 10 observations. The details of selected experimental data to develop correlation are showed in Table 8.

Tab. 8 - Details of selected experimental data to develop correlation

S.No.	Slag (%)	Water Absorption (%)	Density (Kg/m ³)	ACS (MPa)
1	0	11	1552	7.25
2	10	9.9	1590	5.85
3	20	10.5	1634	6.4
4	30	8.6	1675	6.65
5	40	9	1690	7.1
6	50	8.8	1715	5.45
7	60	8.6	1745	5.25
8	70	7.95	1754	4.9
9	80	8.2	1775	5.6
10	90	8.15	1795	4.5

The actual and predicted productivity has been carried out for developed regression model and their accuracy was determined through formulations as listed below. Equation (1) shows the formula for Mean Absolute Percentage Error (MAPE) whereas Average Accuracy Percentage (AA%) is presented as Equation (2) [20-21].

Accuracy of developed regression model

$$MAPE = (\sum |A-P|/A * 100)/n \tag{1}$$

$$AA\% = 100 - MAPE \tag{2}$$

The Coefficient of Determination (R²)

Tab. 9 - Statistical measures results

Measures	(R ²)	MAPE%	AA%	Observations
Results	0.992	7.70	92.30	10

Results enlisted in Table 9 show that the model is the best fitted on the basis of coefficient of correlation and regression. It is observed that the value of R², MAPE and AA% by MLR model demonstrates good agreement with the actual measurements.

CONCLUSIONS

The present study indicates feasibility of recycling BFS in the form of fine aggregate to create building blocks using it as a partial to full replacement. Based on the experimental results, following conclusions have been drawn:

- The physical properties of crushed BFS found permissible as desired by the naturally occurring fine aggregates and hence it may be a better alternative.
- To achieve higher weather resistance condition, maximum amount of BFS required to be replaced is 40% by volume. Beyond this limit BFS may replace fully with naturally occurring fine aggregates which may proof resistivity against moderate weather condition.
- Water absorption for BFS based building blocks found adequate to ensure durability and denser nature as required by the conventional bricks.
- Conventional bricks have to undergo kiln process and as result due to burning of fossil fuel in huge, environmental pollution take place. On the other hand, BFS based building blocks are free from kiln process and hence these blocks are pollution free and fuel saving as well.
- Reuse of wastes leads to reduce the scarcity in naturally occurring materials like sand, grit and clay.
- Raw material is derived from waste which may proof financial potential, therefore using BFS based building block overall cost of construction can be minimize.
- The use of environmental friendly walling materials made from industrial waste is still very limited, therefore it may provide a good scope of further research in context to reuse and recycle the wastes for producing cost effective and eco-friendly building materials.
- Awareness can be made to the society for reuse and recycle of waste and also to promote eco- friendly low cost building materials which have inferior acceptance till now.
- Ecological problem related to direct landfilling and incineration of wastes may lessen.

REFERENCES

- [1] Chokshi, Y., Sompura, N., and Dutta, S.K., 2018. Utilization of steel plants waste. *Material Sci & Eng*, vol. 2: 1144-1149.
- [2] Babu, S.V., and Krishnaiah, S., 2018. Manufacturing of eco-friendly brick: A Critical Review. *International Journal of Computational Engineering Research*, vol.8: 24-32.
- [3] Watile, R.K., Deshmukh, S.K., Durge, P.V., and Yawale, A.D., 2015. Utilization of rice husk for production of clay brick. *International Journal of Research in Advent Technology*, vol. 1: 119-203.
- [4] Lokeshwari, M., and Jagdish, K.S., 2016. Eco-friendly use of granite fines waste in building blocks. *Procedia Environmental Sciences*, vol. 35: 618-623.
- [5] Goel, G., and Kalamdhad, A.S., 2017. An investigation on use of paper mill sludge in brick manufacturing. *Construction and Building Materials*, vol.148: 334-343.
- [6] Venkatesh, G., Nandhakumar, K., Sadeeshkumar, R., Selvakumar, G., and Vaitheeswaran, M., 2017. Experimental investigation on cement brick with addition of quarry dust and fly ash. *International Journal for Technological Research in Engineering*, vol. 4: 1166-1168.
- [7] Ramkumar, S., and Rubini, S., 2017. An Experimental investigation of recycling of bricks. *Journal of Chemical and Pharmaceutical Sciences*, vol. 3: 119-121.
- [8] Watile, R.K., Deshmukh, S.K., Durge, P.V., and Yawale, A.D., 2015. Utilization of rice husk for production of clay brick. *International Journal of Research in Advent Technology*, vol. 1: 119-203.
- [9] Bilgis, N., Yeprem, H.A., Arslan, S., Bilgis, A., Gunay, E., and Marsogul, M., 2012. Use of waste marble powder in brick industry. *Construction and Building Materials*, vol. 29.
- [10] BIS:2386, 1963. Method of Test for Aggregate for Concrete, Part 1: Particle Size and Shape, in: (BIS) BoIS, (Ed.), New Delhi, India.

- [11] BIS:2386, 2016. Method of Test for Aggregate for Concrete, Part 3: Specific gravity, Density, Voids, Absorption and Bulking, in: (BIS) BoIS, (Ed.), New Delhi, India.
- [12] BIS:383, 2016. Course and Fine Aggregate for Concrete – Specification (3rd Revision), in: (BIS) BoIS, (Ed.), New Delhi, India.
- [13] BIS:4031, 1988. Methods of Physical Tests for Hydraulic Cement (1st Revision), Part 4: Determination of Consistency of Standard Cement Paste, in: (BIS) BoIS, (Ed.), New Delhi, India.
- [14] BIS:4031, 1998. Methods of Physical Tests for Hydraulic Cement (1st Revision), Part 5: Determination of Initial and Final Setting Times, in: (BIS) BoIS, (Ed.), New Delhi, India.
- [15] BIS:3495, 1992. Methods of Testing for Burnt Clay Building Bricks (3rd Revision), Part 3: Determination of Water Absorption, in: (BIS) BoIS, (Ed.), New Delhi, India.
- [16] BIS:3495, 1992. Methods of Testing for Burnt Clay Building Bricks (3rd Revision), Part 1: Determination of Compressive Strength, in: (BIS) BoIS, (Ed.), New Delhi, India.
- [17] BIS:12894, 2002. Code of Practice for Pulverized Fuel-Ash Lime Bricks (1st Revision), in: (BIS) BoIS, (Ed.), New Delhi, India.
- [18] BIS:1905, 1987. Code of Practice for Structural Use of Unreinforced Masonry (3rd Revision), in: (BIS) BoIS, (Ed.), New Delhi, India.
- [19] Sajjad, A., and Muhammad, K.K., 2017. Influence of glass powder and steel slag on properties of concrete: A review. *The Civil Engineering Journal*, Prague, vol.4: 386-393
- [20] Saleem, I., and Lena, H., 2019. Statistical studies of modis algorithm in estimating optical depth over the Czech Republic. *The Civil Engineering Journal*, Prague, vol.4: 523-531.
- [21] Neelima, S., and Sahimol, E., 2018. Equipment productivity forecasting model for multi-storey building construction through regression analysis. *IOSR Journal of Engineering* vol.8: 34-40.

TEMPERATURE MODELLING IN ASPHALTIC CONCRETE FACINGS, THE REFLECTIVE SURFACE EFFECT SIMULATION CASE STUDY: GHRIB DAM (AIN DEFLA, ALGERIA)

*Chebbah Lynda¹, Djemili Lakhdar², Chiblak Mohamed³,
Bouziane Mohammed Tawfik¹*

1. *University of Mohamed Khider, Department of Hydraulic BP 145 RP, Biskra 07000, Algeria; cheblyn@yahoo.fr, bouziane@inbox.com.*
2. *University of Badji Mokhtar, Department of Hydraulic B.P. 12, Annaba 23000, Algeria; lakhdardjemili@hotmail.com.*
3. *University of Damascus, Syria, Department of Hydraulic; alchiblak@mailblocks.com.*

ABSTRACT

The asphaltic concrete facing is one of the most widely used components for waterproofing rockfill dams. It is, particularly in the case of hydroelectric pumped storage facilities, often highly exposed to significant temperature fluctuations, which are caused by solar radiation, variation in the water level in the reservoir, frost in the winter season, as well as wind speed and direction, and precipitation. To better explain the heat transfer phenomenon, it is necessary to know the temperature variations in the different layers of the asphaltic concrete facing. This study describes the measurement of the temperature in the asphaltic concrete facing (raw and protected) of the Ghrif dam (Ain Defla, Algeria) and its evaluation using a numerical model of the heat flow using the Fluent software. First, a validation of the model by comparison with experimental measurements, in the case of a daily variation in ambient temperature, the comparison of the results of the calculation of the numerical model with the real measurements shows an excellent similarity. Then we simulate the application of thermal protection by adding a reflective paint to the facing surface. The results of this simulation show that the reflection of solar radiation by the reflective surface has the potential to cool the asphaltic concrete facing and reduce the temperatures significantly, the temperature peak as well as reduce it to 11.47 °C, this happens at noon when the heat is very high, which is significant for our asphaltic concrete facing, where the temperatures reach their maximum values (49°C) in the raw case (without protection).

KEYWORDS

Asphaltic concrete facing, Heat transfer, Ghrif dam, Reflective surface, Modelling, Fluent

INTRODUCTION

The waterproofing performance of asphalt has been known since ancient times. Even today, we can still see 3000-year-old asphalt based hydraulic structures, such as the Tiger dikes in Ashur, Mesopotamia, still in good condition [1].

Asphalt mixes are impermeable, durable, insensitive to water, resistant to most common chemical agents and microorganisms, have a high ability to solve many hydraulic problems, and the flexibility of asphalt waterproofing allows them to adapt to settling of their substrate without cracking or losing their properties [2,3].

The problem of waterproofing embankment dams arises whenever the calculation of superstructure infiltrations indicates unacceptable losses; these losses can either lead to the ruin of the structure by fox formation or, without affecting its safety, be disturbing for the operation of the dam [4, 5, 6].

Temperatures and atmospheric conditions have multiple impacts on hydraulic structures; these impacts are mainly related to changes in temperatures within the structure and its foundations. Air temperatures directly influence temperatures in the asphalt concrete facing, while atmospheric conditions (solar radiation, UV radiation, clouds, etc.) can exacerbate these phenomena [7].

MATERIAL AND METHODS

The originality of this study lies in the consideration of the cooling effect by adding a reflective surface. Using the Fluent software, we tried to model the transient thermal problem including solar radiation and natural convection on the surface of the asphalt concrete facing for a period of 17 hours. The work is organized in two parts:

The first consists in validating the numerical results by comparing them with the experimental values measured at the Ghrib dam asphaltic concrete facing.

The second, consists in protecting the asphaltic concrete facing by a reflective surface against the effects of solar radiation, this surface allows reflecting the radiations by its light colour in order to cool the asphaltic concrete facing.

The energy accumulation of the surface of the asphaltic concrete facing differs considerably from that of the natural soil due to the different properties of thermal radiation. The asphaltic concrete layers absorb large amounts of radiation during the day, which produces heating on the surface of the asphaltic concrete facing that is rapidly transmitted to the lower layers producing an increase in temperature inside them (Figure 1) [8].

Understanding and correctly determining the behaviour of energy accumulation helps in the process of making decisions about asphalt concrete facing construction technologies and studying the relative phenomenon of heat as a serious environmental problem [5,9].

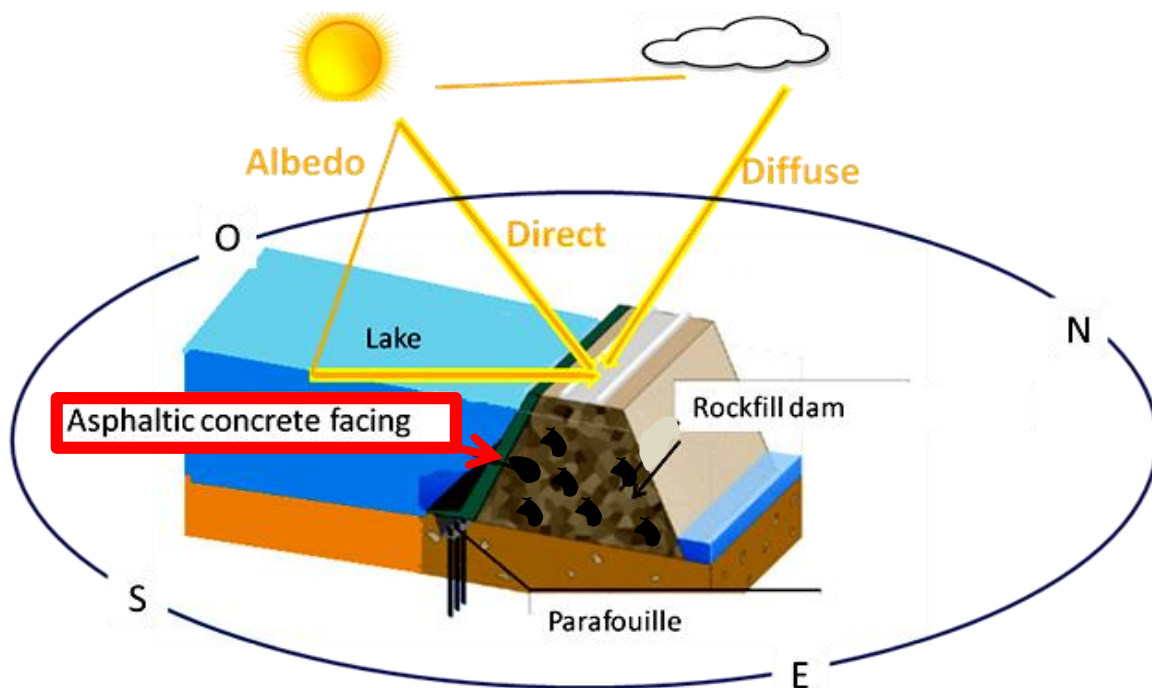


Fig. 1 - The solar components around the dam

Case study

The basic model on which the whole study will be based concerns the Ghrib dam, located in western Algeria in the commune of Oued Chorfa wilaya of Ain Defla (Figure 2a, 2b, 2c). It is located on the upper reaches of the Chelif River and is used for irrigation, drinking water supply and power generation.

The Ghrib dam was built in a poor support area. In order to avoid the risk of settling, a flexible dam capable of adapting to ground movements has been built. This structure is one of the first rockfill structures built with an upstream asphaltic concrete facing, it consists of a stowed rockfill dike, built between 1926 and 1938. Its capacity is 280 millionm³ [6,10].

On the dam we can distinguish two parts: the dam and the asphaltic concrete facing (Figure 3), on the asphaltic concrete facing thermocouples have been placed at three strategic locations, corresponding to the three parts of the experimental model (at 1cm, at 6 and at 10 cm counted from the surface of the surface), each zone includes 3 thermocouples spaced at irregular intervals.

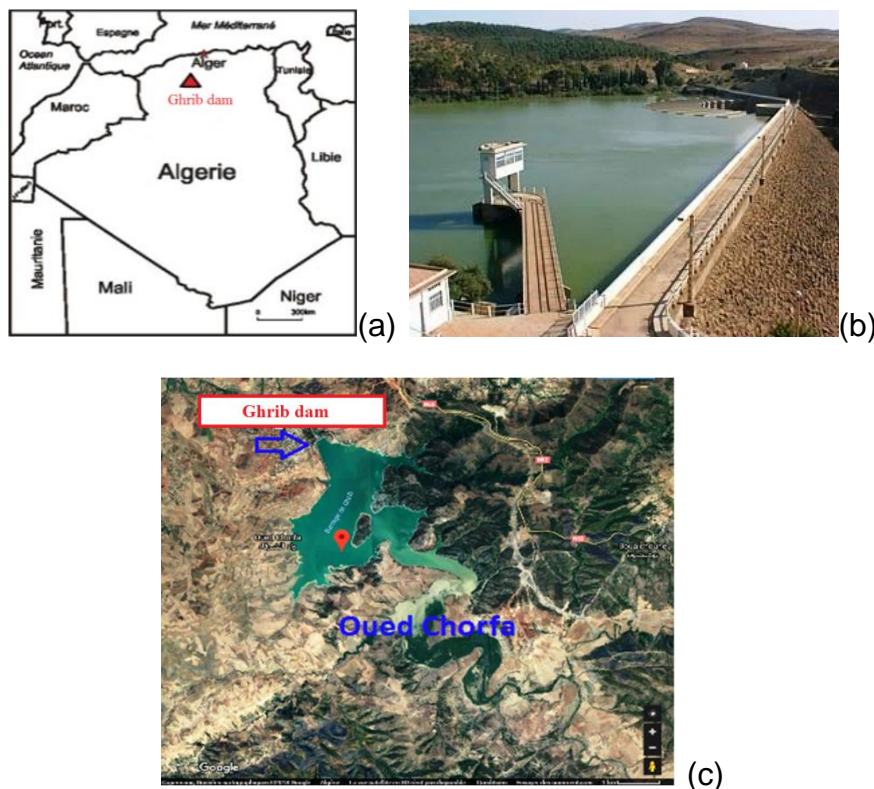


Fig.2 - Ghrib dam location (Ain Defla / Algeria): (a) Ghrib dam on Algeria map. (b) pic of Ghrib dam. (c) Ghrib dam water surface

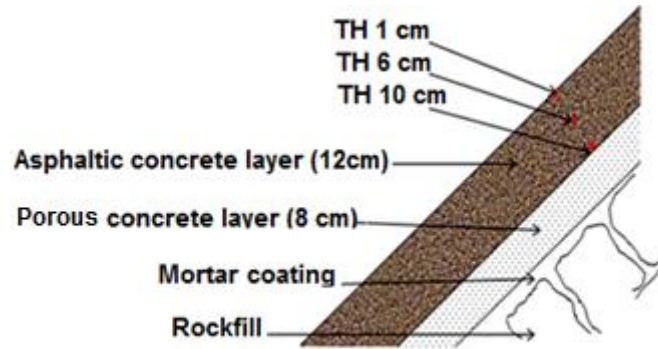


Fig.3 - Sketch of the asphaltic concrete facing of Ghrib, and the location of the sensors for temperature measurement (TH).

Configuration of the model and simulation

The simulated geometry is shown in Figure 4, where we observe the raw asphaltic concrete facing, which consists of two layers: a 12 cm thick asphalt concrete waterproof layer and an 8 cm thick porous concrete draining layer, resting on a rockfill dike (massive limestone).

Mesh geometry, where each layer represents a different material with different physical and thermal properties (Table 1). The structure represents a constant slope of 1/1. An unstructured mesh of quadrilateral and triangular type was used, 0.25 m in the rock slope and 0.01 m in the other layers. Temperatures are measured at the three digital thermocouples (TH) at initially defined positions of 1cm, 6cm and 10cm, with a time chronology of 60 seconds (time step); the maximum number of iterations has been set at 20.

Tab. 1 - Properties of the materials used [6]

Layers	Materials	Thermal conductivity (λ) (W m ⁻² °C ⁻²)	Weight density (ρ) (kg m ⁻³)	Specific heat (Cp) (W s kg ⁻² °C ⁻²)
1	Rockfill	2.8	2700	920
2	Asphaltic concrete	1.165	2230	930
3	Porous concrete	1.27	2310	942

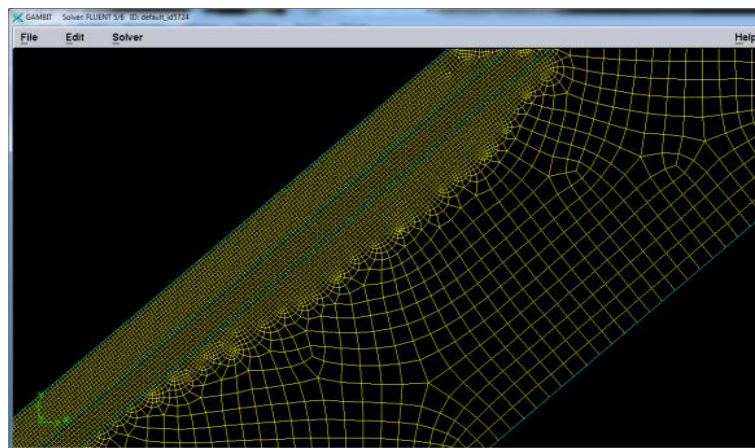


Fig.4 - Example of simulated geometry (raw asphaltic concrete facing)

Mathematical model

For the initial model, the various heat exchanges will be simplified. Thus, it is assumed that thermal transfer throughout the mask is dominated by conduction.

The temperature profile in the asphaltic concrete facing is therefore of the form $T(z,t)$. The heat propagation in the thermal diffusivity asphaltic concrete (a) (2), will be described by the heat equation (1) [10, 11,12]:

$$\frac{\partial T}{\partial t} = a \left(\frac{\partial^2 T}{\partial z^2} \right) \quad (1)$$

$$a = \frac{\lambda}{\rho C_p} \quad (2)$$

Where T is the temperature, λ is the thermal conductivity, C_p is the specific thermal capacity, ρ is the density of the material, z is the distance measured perpendicular to the facing towards the dam body and t is the time.

In the second case of simulation, the asphalt concrete facing is protected against the effects of solar radiation by a white reflective surface, taking into account the convective and radiative exchanges between this surface and the outside air (Figure 5), so in this step the heat transfer model changes from conduction alone to conduction, convection and radiation transfer (Figure 5), so equation 1 takes the following form [9,13]:

$$\frac{\partial T}{\partial t} = a \left(\frac{\partial^2 T}{\partial z^2} \right) - h(T_s - T_{ext}) - \varepsilon\sigma(T_s^4 - T_{melody}^4) - \alpha q_{sun} \quad (3)$$

Where:

h is the convective exchange coefficient of the air taken equal to $20 \text{ Wm}^{-2}\text{C}^{-1}$, T_s is the temperature at the surface of the asphalt concrete facing and T_{air} is the air temperature.

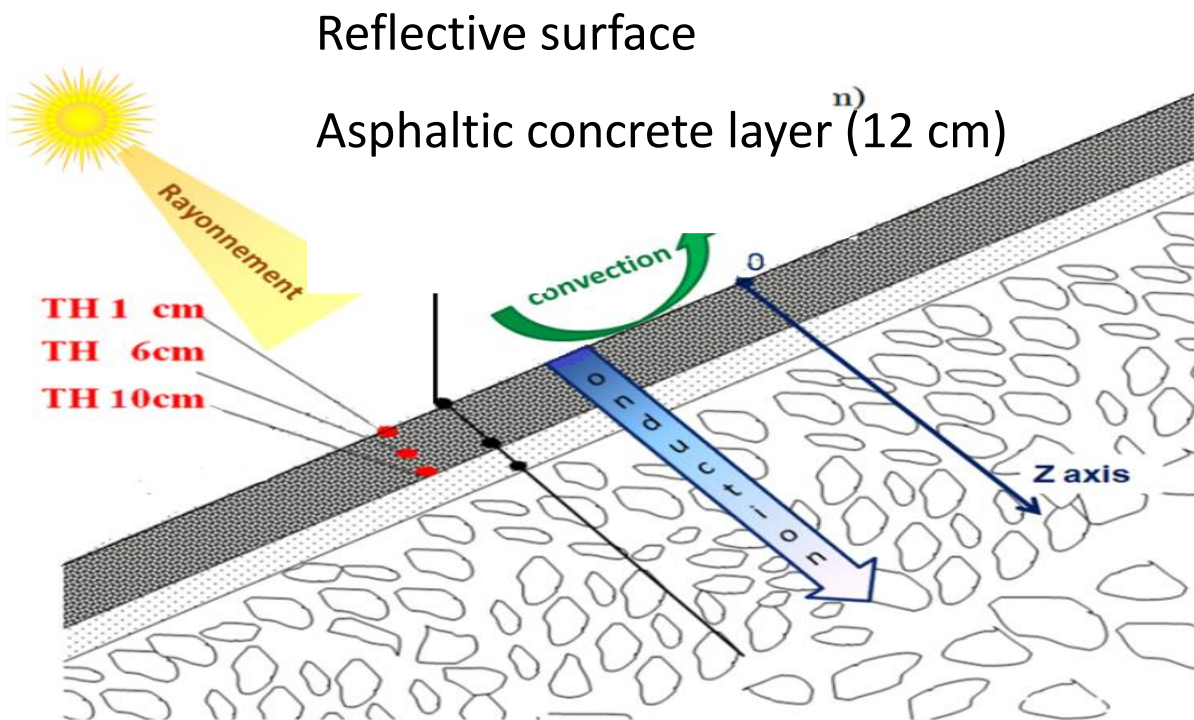


Fig.5 - Schematic section of the asphaltic concrete facing protected by reflective surface

Boundary and initial conditions

The purpose of the numerical model is to determine, from conditions at the limits imposed on its contour, the temperature profile inside the asphaltic concrete facing is simulated for the following two cases.

The first case is conduction only: a Dirichlet condition is introduced on the surface of the asphalt concrete facing is a temperature profile constructed from the experimental readings (Fr. Agence Nationale des Barrages et Transferts - ANBT) imposed on the surface of the Ghib asphaltic concrete facing (4).

$$T(z = 0, t) = T_{\text{experimental}}(t) \quad (4)$$

The second case requires the consideration of heat transfer by convection and radiation. In this case, the heat flux transmitted to the surface of the asphalt concrete facing towards the outside follows the following equation (5) [9].

$$q'' = h(T_s - T_{\text{air}}) + \varepsilon\sigma(T_s^4 - T_{\text{air}}^4) - \alpha q''_{\text{sun}} \quad (5)$$

Where: ε corresponds to emissivity and σ corresponds to the Stefan-Boltzmann constant ($\sigma=5.67 \cdot 10^{-8} \text{ Wm}^{-2}\text{C}^{-4}$) [INCROPERA and DE WITT 2002]. α corresponds to the absorbance of the asphaltic concrete facing surface to solar radiation, it is 0.95 [DJEMILI 2006; CHIBLAK 2005; CHATAIGNER 2008]. q''_{sun} represents the solar radiation flux reaching the surface in Wm^{-2} .

One of the difficulties of modelling comes from the fact that we do not know the precise value of the solar radiation flux as a function of time q''_{sun} . Indeed, the latter is influenced by the alternation of day and night, the inclination of the receiving surface, the presence of shadows, clouds, rain, etc. It can be calculated using the following formula (6):

$$q''_{\text{sun}}(t) = G_{\alpha}(t) + G_w(t) - A(t) \quad (6)$$

With:

$G_{\alpha}(t)$: Global radiation on a surface inclined as a function of time (Wm^{-2});

$G_w(t)$: Atmospheric radiation as a function of time (Wm^{-2});

$A(t)$: Reflected radiation as a function of time (Wm^{-2});

The solar radiation flux will be calculated for the day in question (clear sky), and the place in question by a sub-programme carried out under Matlab.

The temperature profile imposed on the surface asphaltic concrete facing take into account the air temperature, but also the effect of solar radiation. To do this, it will follow the following equation (7) [14, 9]:

$$T_{\text{air}}^*(t) = T_{\text{air}}(t) + \frac{\alpha}{U} q''_{\text{sun}}(t) \quad (7)$$

Where:

T_{air}^* : Modified air temperature taking into account solar radiation $^{\circ}\text{C}$;

U : corresponds to the thermal transfer coefficient between the outside and the interface, which takes into account the external convection coefficients and the equivalent thermal resistance on the interface equal to $20 \text{ Wm}^{-2}\text{C}$ [9].

For the boundary to the left of the models (in the dam body) and at a sufficiently high depth, the temperature of the structure is no longer influenced by the thermal input of the asphaltic concrete facing, this depth is, by hypothesis, equal to 1 m, located in the embankment dike, it is a Neumann condition representing a zero heat flux (8) [9,10 ,11,15].

$$\frac{\partial T(z=1,t)}{\partial z} = 0 \quad (8)$$

$$\text{The initial condition at the time } t=t_0: T(z, t_0) = T_0(z) \quad (9)$$

RESULT AND DISCUSSIONS

Validation of the model by experimental tests

On the graphical representations (Figure 5a, 5b and 5c), very close numerical and experimental values are observed with very significant correlation coefficients exceeding 0.97 for the three thermocouples. The relative difference of 0.19%, 0.35% and 0.48%, on average, respectively for TH 1cm, TH 6cm and TH 10cm. It should be noted that the maximum deviation for the thermocouple located at 1 cm is 2.07 °C and at 6 cm it is 2.76 °C, and at 10 cm it is 2.72 °C, these deviations are relatively small considering the dimensions and uncertainties involved; it can therefore be concluded that this model is validated.

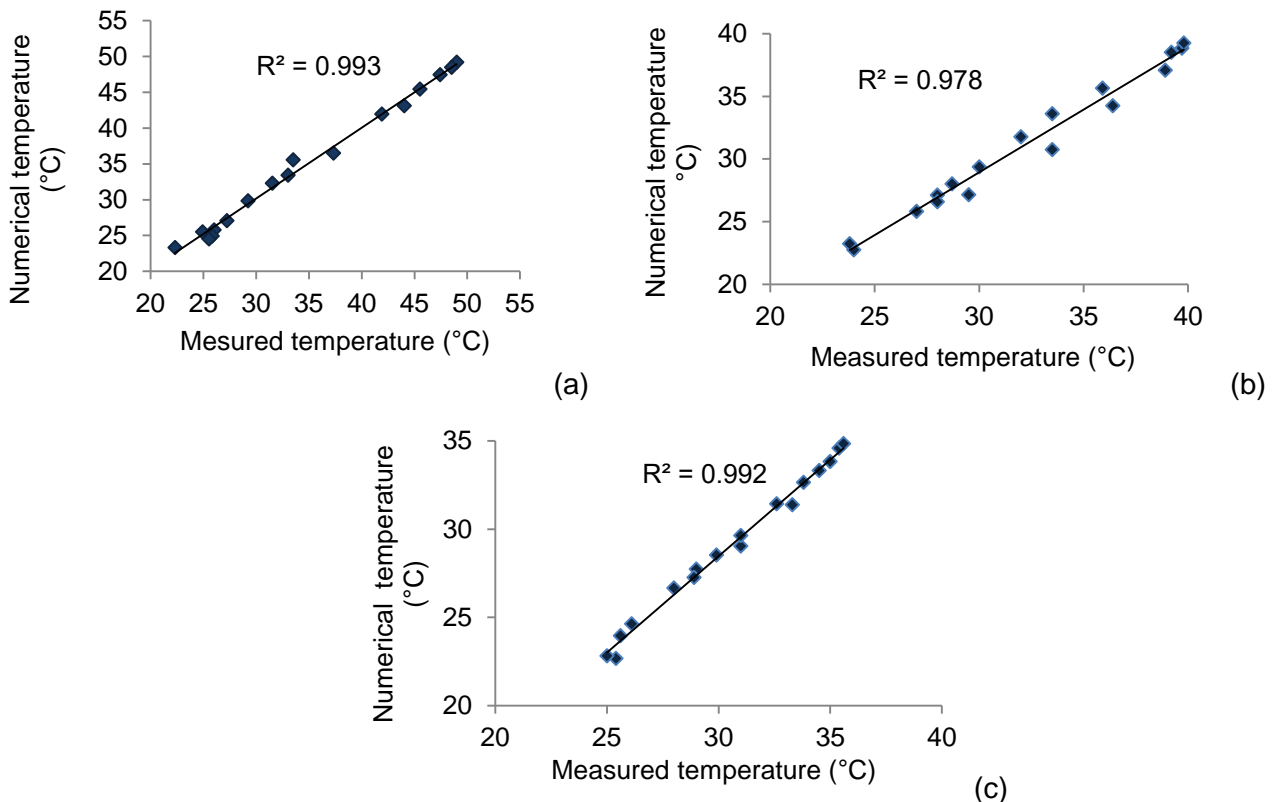


Fig. 5 - Correlation of experimental and numerical temperatures: (a) At TH 1 cm. (b) At TH 6 cm. (c) At TH 10 cm

Simulation of the raw asphaltic concrete facing (without protection)

Figures 6 and 7 illustrate the temperature evolution within the unprotected structure, at time 12.15 pm the temperature reaches a maximum value of 49.21 °C at the asphaltic concrete facing surface, then it decreases slowly and becomes stable beyond 0.80 m depth, knowing that the air temperature at this time is about 30.6 °C, we also observe that the minimum temperature recorded is from 23.04 °C at 6 am.

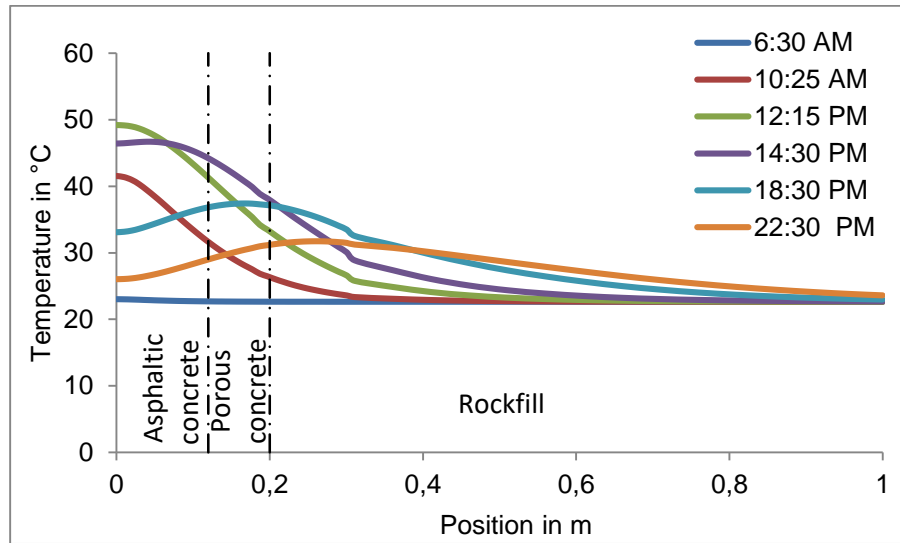


Fig. 6 - Temperature evolution within the raw asphaltic concrete facing

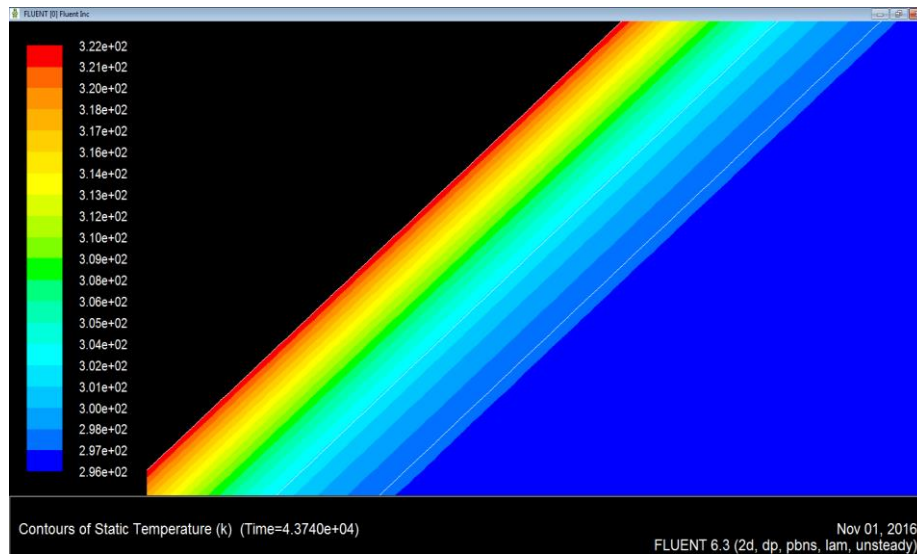


Fig. 7 - Simulation of the temperature variation within the asphaltic concrete facing at 12:15 pm

Simulation of the asphaltic concrete facing protected by a reflective surface

The following model attempts to cool the layers of the asphalt concrete with a reflective surface, where heat exchanges take place in conduction, free convection and also in radiation.

Temporal variation

The maximum simulated temperature at 1 cm from the protected asphaltic concrete facing surface is 37.53 °C at 12.15 pm, 31.42 at 14.3 pm for TH 6 cm, and at 10 cm it reaches its maximum value at 15.3 pm with 28.25 °C (Figure 8).

The minimum temperatures recorded at 6 am for the three thermocouples, respectively 19.84 °C to TH 1cm, 19.55 °C to TH 6cm and 19.5 to TH 10cm.

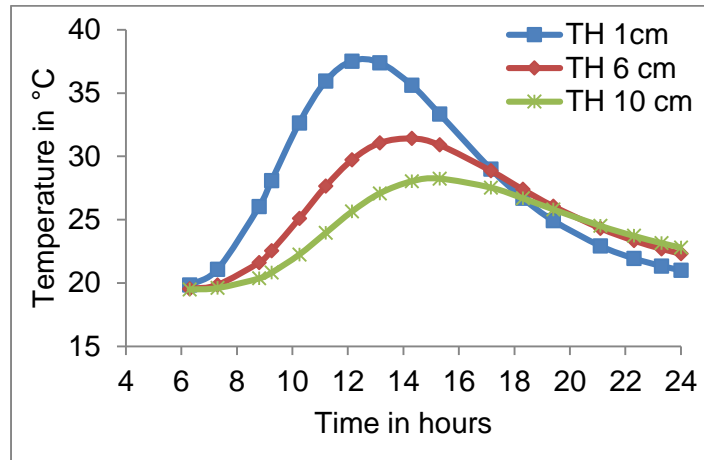


Fig. 8 - Temperature variation for the 3 thermocouples (TH), case of the protected asphaltic concrete facing

Spatial variation

The temperature at TH 1cm, reaches its maximum at 12.15 pm with a value of 38.47 °C and a minimum of 19.73 °C at 6.3 am (Figure 9 and 10).

It should be noted that the location of the maximum temperature varies with time:

- It is maximum at TH 1cm from 6.3 am to 12.15 pm, with a maximum value of 38.47°C at 12.15 pm;
- At 14.3 p.m., the maximum temperature at 4 cm is around 36.84 °C.
- At 6.3 pm, the maximum temperature increases to 17 cm, located in the porous concrete layer with a value of 30.15°C.
- At 22.3 pm, the maximum temperature is about 26.04 °C, at a depth of 26 cm, located at the body of the dam (rockfill);

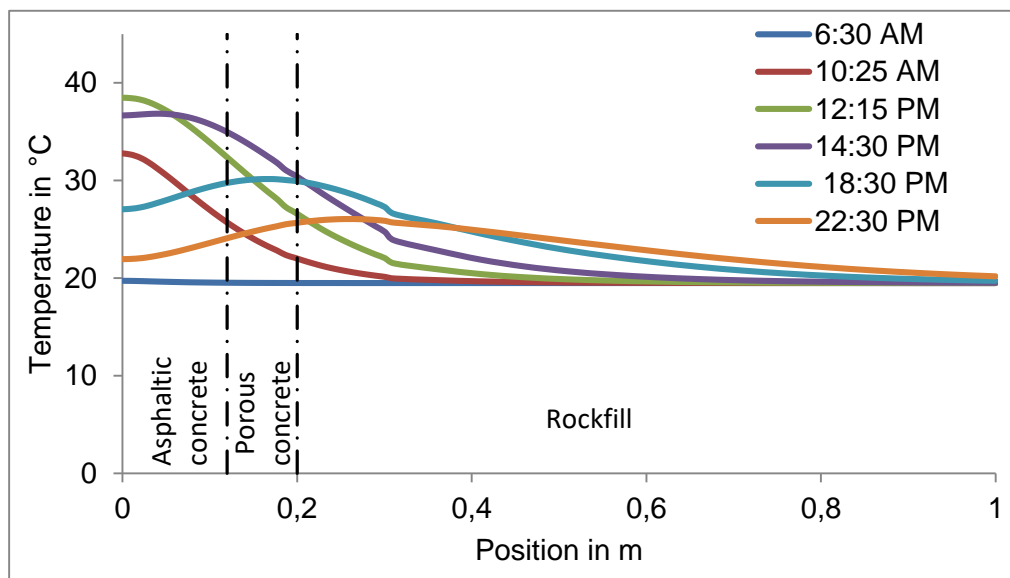


Fig. 9 - Temperature evolution within the protected asphaltic concrete facing

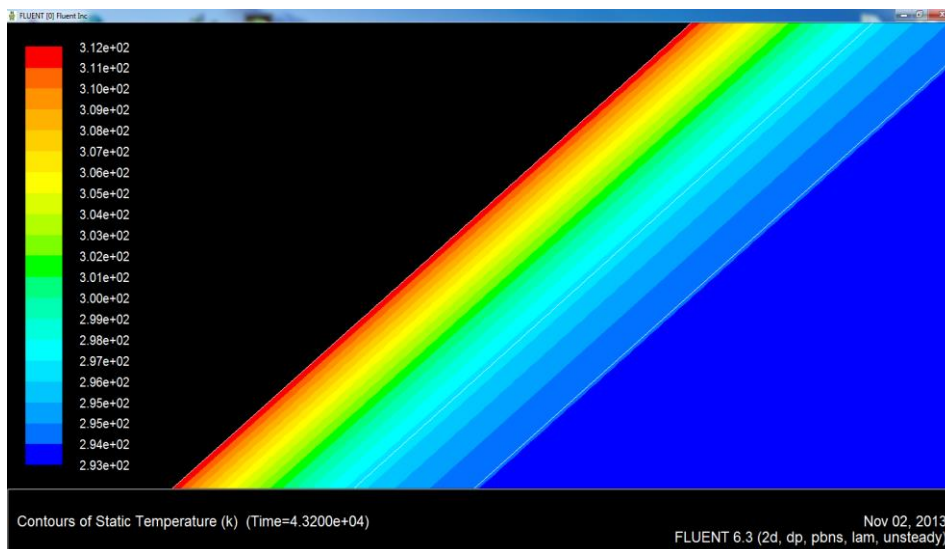


Fig. 10 - Simulation of the temperature variation within the protected asphaltic concrete facing at 12.15 pm

Effect of the reflective surface on asphaltic concrete facing temperatures

The analysis of the difference between the temperatures measured in the raw asphaltic concrete facing and the temperatures simulated on the asphaltic concrete facing protected by the reflective surface, at the level of the three thermocouples located at 1 cm, 6 cm and 10 cm, by the relationship:

Temperature difference = T measured (raw asphaltic concrete facing) - T simulated (protected asphaltic concrete facing).

The results are shown in the graph in Figure 11, where a cooling is observed that occupies the entire thickness of the asphalt concrete facing:

A maximum cooling time of 12.15 pm is recorded for the three thermocouples with 11.47°C for TH 1cm, 9.16°C for TH 6cm and 7.64°C for TRH 10cm.

The minimum cooling times are 6.3 am for the three thermocouples, 2.46 °C for TH 1 cm, 4.45 °C for TH 6 cm and 5.9 °C for TH 10 cm.

The presence of the reflective surface positively influences the heating of the asphaltic concrete facing or observes a significant cooling over the entire thickness of the asphaltic concrete facing and especially in the period of maximum temperature (period of high heat).

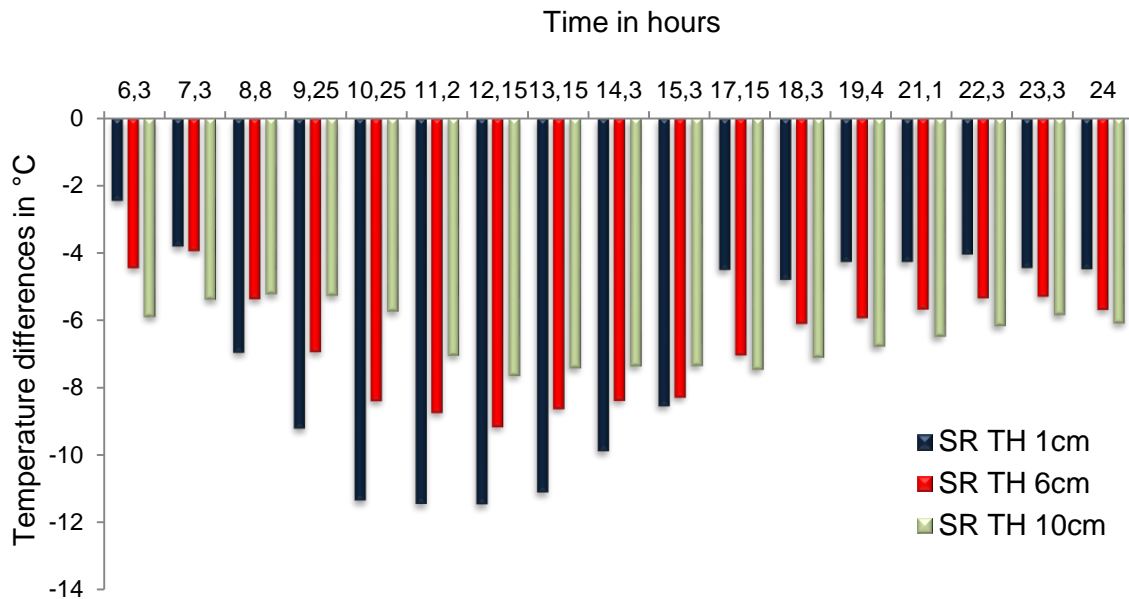


Fig. 11 - Difference between the temperatures measured in the raw asphaltic concrete facing and simulated on the protected asphaltic concrete facing of Ghrib dam (SR: reflective surface)

CONCLUSION

Fluent analysis has proven to be an interesting tool for simulating the transient temperature behaviour of the asphaltic concrete facing of Ghrib dam. The model simulates the temperature of asphaltic concrete facing at different levels in different layers and has been successfully validated by experimental data.

The use of a reflective surface on the asphalt concrete facing, aimed at reducing the absorbency of the asphaltic concrete facing, and thus lowering the temperatures at the surface and within the asphaltic concrete facing to avoid degradation of the asphalt concrete layers.

The protection of the asphalt concrete facing by the reflective surface provides cooling throughout the test period and occupies the entire thickness, with maximum values of 11.47°C, 9.16°C and 7.64°C for the three thermocouples respectively TH 1cm, TH 6cm and TH 10cm at 12.15 pm, i.e. during the period of high heat or when solar radiation reaches its maximum values.

Reflective surfaces are most effective when the surface is as clear as possible and when the surface covers the entire surface of the asphaltic concrete facing.

REFERENCES

- [1] Djemili L., Chiblak M., 2007. Study of the temperature distribution in the bituminous concrete facing used in fill dams in the region of west Algeria (Courier du savoir).Vol 8 . 576-579.
- [2] Djemili L. Et al.,2012. Comportement du masque d'étanchéité du barrage Ghrib (Algérie) en absence de la protection (Courier du savoir) . Vol 13. 21-25.
- [3] Fadel I., 2005. Asphalt mixture-designing basics in dams sealing - designing of impermeable asphalt shell used in AL-Sorani Dam, Tishreen university journal for studies and scientific research- engineering sciences series. Vol 27. 23-38.
- [4] Chebbah L. et al., 2016. Optimisation de la formule empirique la plus fiable pour la détermination de la température de la surface du masque en béton bitumineux. Cas du barrage Ghrib (Ain Defla, Algérie) SNEE 01 – Mila.

- [5] Chiblak M., Djemili L., 2011. Asphaltic concrete facing for rockfill dams in arid and semi-arid countries: A case study of Alsourani Dam, Syria, International Journal of the Physical Sciences. Vol 36. 8157 – 8163.
- [6] Djemili L., 2006. Critères de choix de projet des barrages en terre « étanchéité par le masque en béton bitumineux. PhD Thesis. Université de Batna pp. 91
- [7] Rychen R., 2013. Impact du changement climatique sur les infrastructures routières -Analyse de risque et mesures d'adaptation . PhD Thesis. EPFL, Lauzane, Switzerland pp. 389.
- [8] Perrot O., 2011. Cours de rayonnement .Département Génie Thermique et énergie I.U.T. de Saint-Omer Dunkerque pp. 101.
- [9] Chataigner Y., 2008. Modélisation du transfert thermique dans un remblai sur pergélisol élaborations de stratégies pour faire face aux changements climatiques. Thèse de maître es sciences (M.Se.). Université Laval Québec pp. 137.
- [10] Ghouielem.K. 2014. Impact du fluage et de température sur les organes de lutte contre les infiltrations dans les barrages. PhD Thesis. Université Mouloud Maameri Tizi ouzzou pp. 166.
- [11] Adam K. et al., 2016. Investigation on the temperature of the asphalt-concrete facing of embankment dams. International Journal of Pavement Research and Technology .Vol 9. 73–81.
- [12] Belghazi H., 2008. Modélisation analytique du transfert instationnaire de la chaleur dans un matériau bicouche en contact imparfait et soumis à une source de chaleur en mouvement .Thèse. Université de Limoges pp.171
- [13] Navaro J., et al., 2010. Modeling the cooling of asphalt mix from its output from a production plant to compaction on road construction sites
- [14] Incropera F P. Et al., 2006. Fundamentals of heat and mass transfer, 6th (Eds). John Wiley & Sons, Inc., USA.
- [15] Pilate O., 2007. Evolution de la température d'une couche d'enrobé bitumineux nouvellement posée . Centre de recherche routier , Bruxelles, Compte Rendu De Recherche, CR42/06, Belgium pp.88.

MATERIALS AND TECHNOLOGIES FOR THE STRENGTHENING OF HISTORIC MASONRY BY THE DEEP GROUT INJECTION AND SURFACE PENETRATION METHOD

Jiří Witzany¹, Radek Zigler¹, Klára Kroftová², Tomáš Čejka¹, Jan Kubát¹

1. CTU in Prague, Faculty of Civil Engineering, Department of Building Structures, Prague, Thákurova 7, Czech Republic; wizany@fsv.cvut.cz, zigler@fsv.cvut.cz, cejka@fsv.cvut.cz, jan.kubat.2@fsv.cvut.cz
2. CTU in Prague, Faculty of Civil Engineering, Department of Architecture, Prague, Thákurova 7, Czech Republic; klara.kroftova@seznam.cz

ABSTRACT

The grouting of historic masonry with degraded binders or masonry units, masonry with insufficient load-bearing capacity, masonry damaged by cracks, with a high void content and cavities and multi-leaf masonry is one of the rehabilitation methods of masonry frequently applied in practice, restoring its integrity and increasing its load-bearing capacity.

KEYWORDS

Masonry, Grouting, Cracks, Cavities, Brick, Stone, Experimental campaign

INTRODUCTION

The methodology for the design of the grout injection technique for masonry structures that would become the basis for the design and assessment of the grouting effectiveness in terms of the grouting agent, the grout injection method used and the grouted masonry properties have not been developed yet, and nor has the procedure for the selection of the technique, a suitable grouting mixture and the calculation procedure for the assessment of the effect on the pore system of the binder or masonry units (pore distribution, total porosity, pore type), verification of the masonry moisture content and chemism (pH, salt content and type).

The design of a grouting technique involves the specification of the purpose of grouting (grouting masonry as a whole, grouting of a binder or masonry units, reducing the void content, filling in cavities and voids, grouting cracks, strengthening surface and subsurface layers, etc.). A reliable grouting technique performed to the required extent requires the verification of the pore system, injectability and the penetration of the grouting mixture into the pore system for the selected grouting mixture and technology (optimum distance, diameter and depth of grouting boreholes, grout stability, setting and curing time, grout shrinkage, grout-masonry mutual reactivity). In this perspective, we must evaluate the total porosity, pore size and distribution and, on this basis, design the grouting mixture and the expected amount of applied grout penetrated into the grouting boreholes in relation to the total porosity. An integral part is the design of the grouting substance (based on hydraulic lime, silicates, resins, with a filler or without a filler, grout consistency), the injection technology and procedure (pressure, pressure less, single or multiphase grouting, overall grouting or in grouting strips, impregnation grouting).

The infusion and injection of substances with defined properties, usually in the liquid phase, into the pore structure is one of the methods of active modification of the physical and mechanical

characteristics of porous materials, such as strength, static and dynamic elastic modulus, hardness, resistance (mainly frost resistance), moisture absorption and others.

The building materials – natural and anthropogenic - used in the present-day civil engineering practice are characterised by a pore structure generally comprising the entire pore size spectrum, from nanopores to macropores. The effectiveness of grouting relies on numerous factors, particularly the transport of the injected substance through the pore structure. The transport is affected by the properties of the injected substance, the pore structure type of the injected material and, last but not least, by the application method of the injected substance. The issues related to the transport of injected substances in relation to the type of pores and the pore system (pore distribution, pore shape and surface, their mutual communication, etc.), in relation to the specific properties and composition of the injected substance and its irreversible changes during its transport through the pore system (viscosity, etc.), and the physical, chemical and mineralogical properties of porous materials and their stability in the stage of the injected mix application have not been satisfactorily solved so far.

The design and application procedures of grouting methods in building materials prevailing to-date resemble, in individual solved cases, a largely unreliable process based on insufficiently precise knowledge and empirical data (trial and error method). Due to the lack of expertise in this field, grout injection can be classified as a less reliable and, in many cases, insufficiently effective method.

The expected effect of grouting is achieved by both the required modification of the pore system and pore properties (total porosity, pore distribution, pore shape and interconnection, etc.) and the modification of the solid phase material characteristics by a chemical, or physical-chemical and mineralogical reaction of the grout and the solid material phase (binder component strengthening by a predictable crystallization of secondary minerals, stabilization of soluble substances).

Achieving the optimum conditions for the “injected substance - injected material” mutual interaction resulting in the required/modified properties and parameters of the injected material, requires a reliable transport of the injected substance into the pore structure in the contact area between individual components of the composite material (masonry, concrete etc.) and its optimum distribution within the pore structure. In this case, the desired change in the properties of the injected material is achieved by the “modification” of the pore system.

The effective reaction of the injected substance with the injected composite material (masonry units, aggregate, binder) solid phase requires the transport of the injected substance into the secondary system of individual solid phase components as well. In this case, the desired changes in the properties of the injected material are achieved not only by changing the pore system, but also by changing the properties of individual solid phase components.

GROUTING SUBSTANCES, MIXTURES AND GELS

The choice of the grouting substance relies, above all, on the masonry (masonry components) pore system, the mineralogical and chemical composition of masonry units and the binder, the void content, crack width and the extent of masonry disintegration and the degree of weathering, the type of masonry and the required effect of grout injection, in particular:

- improvement in binder properties (mechanical, chemical, etc.),
- improvement in properties of masonry units (mechanical, chemical, etc.),
- reduction of total porosity,
- reduction of the void content,
- filling in cracks and regaining integrity,
- filling in cavities,
- modification of chemical and physical characteristics (moisture absorption, resistance to aggressive substances).

The main properties of the **grouting mixture** include the rate of solidification and hardening (stability in the injection phase, thixotropy, consistency), particle size, viscosity, strength, physical and mechanical properties and durability. Experimental research has pointed out a significant effect of the compressive strength of the grouting mixture on an increase in the compressive strength of injected masonry.

Note: The pore size and distribution in individual components of the composite material - brick and stone masonry - is non-uniform and, as a result, the same applies to the penetration of the grouting mixture into the masonry pore structure after the grout injection. It is, above all, hydraulic lime-based grouts that are susceptible to premature setting, hardening thus reducing the pore permeability. In the case of an insufficient and non-uniform penetration of the grout into the masonry structure (pore system and voids), the masonry heterogeneity in terms of masonry strength and stiffness is increasing, which unfavourably affects the masonry failure mechanism (non-uniform distribution of normal stresses) reducing the ultimate compressive strength of masonry (Figure 1).

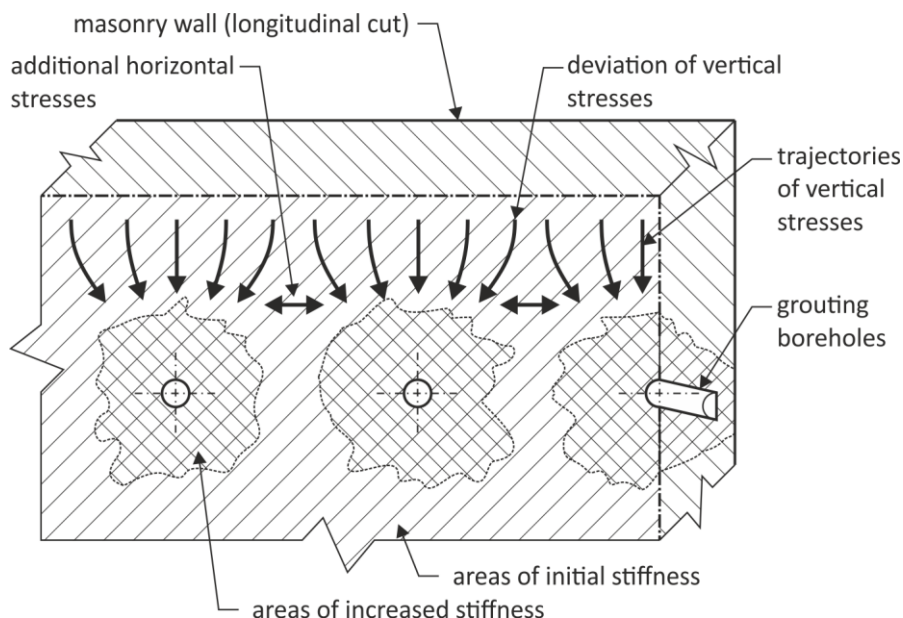


Fig. 1 - Increase of masonry stiffness due to the non-uniform penetration of the grout into the masonry structure

The design of a static grouting technique of masonry can be based on the WTA 4-3-98 guideline [1]. The principal properties of the grouting mixture include the rate of solidification and hardening, low viscosity, strength, stability in the injection phase, thixotropy, consistency, physical and mechanical properties, durability. The grouting mixtures can be divided into:

- **lime suspensions** which are characterized by good fluidity and filling ability without shrinkage after the addition of water, without the separation of excess water, high resistance to sulphates, but may have higher porosity,
- **lime-cement suspensions** are suitable for injecting masonry with a high void content and cavities, masonry damaged by a system of cracks (2 - 3 mm in width), disintegrated masonry and for grouting larger local cracks in historic brick or stone masonry,
- **cement suspensions** are less suitable due to their high viscosity and low stability – rapid sedimentation and premature clogging of cracks of smaller widths occurs during injection,

due to their relatively low tensile strength after hardening, low adhesion and greater shrinkage (failure of adhesion or the cement filling of cracks occurs), they are not suitable for application to heritage buildings,

- **acrylate mixtures** have low viscosity (approaching water viscosity), they can maintain permanent flexibility even under water, have high reversibility,
- **epoxy resins** achieve the required properties by the selection of suitable monomers, hardeners and the curing regime, accelerating additives, internal plasticizers, modifiers, fillers and extenders, they are among the most effective grouts for the remediation of damaged masonry and concrete structures,
- **polyester resins** have low viscosity and relatively simple curing reactions, their disadvantage is greater shrinkage (ca 5% by volume) and lower adhesion to some building materials,
- **polyurethane resins** have a high penetration capacity and are primarily used for reinforcing mortar in masonry joints to increase the load-bearing capacity of masonry.

The research project [2] addressed the development of consolidation agents based on lime nanoparticles not exceeding 1 µm in size, labelled CA-Mg, Ca4 and Ca4O, characterized by a high penetration capacity into the material structure [3-5].

Note: Grouting agents developed within the research project [2]:

Ca4 *The test portion of calcium methoxide was dispersed in isopropyl alcohol and distilled water was added. The mixture was left in a magnetic stirrer for 24 hours. The resulting suspension was produced by supplying the reaction mixture to a volume of 1 litre. The concentration of $\text{Ca}(\text{OH})_2$ is 5 g/l. Strengthening, sealing of concrete and brick, stone and mixed masonry, particle diameter of 220-360 nm*

Ca4O *The test portion of calcium oxide was dispersed in ethanol and distilled water was added. The mixture was left in a magnetic stirrer for 24 hours. The resulting suspension was produced by supplying the reaction mixture to a volume of 1 litre. The concentration of $\text{Ca}(\text{OH})_2$ is 5 g/l. Larger particles and lower viscosity than in Ca4. Strengthening, sealing of concrete and brick, stone and mixed masonry, particle diameter of 1330 – 1770 nm*

Ca-Mg *Test portions of calcium acetate $\text{Ca}(\text{OCOCH}_3)_2 \cdot \text{H}_2\text{O}$ and magnesium acetate $\text{Mg}(\text{OCOCH}_3)_2 \cdot 4\text{H}_2\text{O}$, which was dissolved in distilled water. Strengthening, sealing of concrete and brick, stone and mixed masonry, particle diameter of 35-835nm*

Compared to conventional lime macroparticles, lime nanoparticles finely dispersed in the nanosuspension have many times higher performance, high chemical performance, excellent plastic, consolidation and diffusion properties, low sintering temperature, cleaning abilities, etc. At the same time, lime nanoparticles are a material highly compatible with historical lime-based materials. The lime nanosuspension returns the missing binder to the masonry and plaster on the principle of carbonation, where the reaction with atmospheric CO_2 produces calcium carbonate CaCO_3 .

In addition to the stabilization, conservation and consolidation of degraded historic masonry, lime nanosuspensions also ensure a combination of deep consolidation of masonry by grouting and surface strengthening of preserved historically valuable, usually multi-layer plasters.

Historic masonry grouting aimed at improving its physical and mechanical characteristics can be performed with agents based on mineral substances, e.g. hydraulic lime with additives (brick dust, pozzolans, clays, etc.), which regulate the setting and hardening process, viscosity, etc., with agents based on lime and cement (e.g. trass lime and cement), or resin-based agents with suitable fillers (e.g. quartz sand with a maximum grain size of 1 mm).

In justified cases, a grouting mixture with a small amount of cement (5 to 10%), Roman cement, or with resin-based substances can also be applied. In exceptional cases where the

masonry reinforcement with a lime-based grout is insufficient, resin-based grouting agents may be used. Lime-based grouts fill up “free” spaces and minimally penetrate into the pore structure of masonry units and the binder.

Modified admixtures added to grouts based on hydraulic lime, such as pozzolan, lime, or clay and brick dust, are effective in modifying the rheological properties, volume changes and strength of the injected masonry. By adding pozzolan, lime and cement, the tensile and shear strength of masonry, the bonding of the original binder and the grout (new binder) can be affected. The grouting agents based on minerals and hydraulic lime are suitable for the masonry of historic and mainly heritage buildings.

Improved properties are achieved with suspensions of quick-setting cements with a larger proportion of solid gypsum-free clinker (suitable for the rehabilitation of historic buildings with a high moisture content).

Research into the effectiveness of cement suspensions for grouting masonry with poor load-bearing capacity has shown that the injected cementitious material fills in the cracks and cavities in the masonry, increases the contact between the masonry units and mortar and thus significantly improves its strength.

Silicate-based mixtures can be used to locally strengthen the material by modifying the properties of the masonry pore system. These mixtures, like resin-based mixtures, penetrate into the pore system to a depth of 50 to 60 mm from the grouting borehole. Grouting mixtures based on hydraulic lime with additives and silicate-based mixtures are applied for the strengthening of historic or heritage masonry.

The filling of cavities and cracks after grouting can be investigated with radar or ultrasonic devices.

Note: Mortars based on natural hydraulic lime, silica sand and crushed bricks can also be used for grouting [6]. Pozzolan, clay, brick dust admixtures and their combinations were also added to lime-based grouts to modify their strength development [7]. In justified cases, a grouting mixture with a small amount of cement (5 to 10%) can be applied.

*Experiments [8] were also conducted to verify the use of a grout with *Sporosarcina Pasteurii* bacteria, which modify the masonry pore system properties thus affecting the carbonation process, setting and hardening of lime in degraded masonry. The method was applied by low-pressure micro-grouting during the repair of soiled masonry achieving a compressive strength of microbial mortar of up to 55 MPa.*

GROUT INJECTION TECHNOLOGIES AND METHODS

Masonry grout injection can be performed as pressure or pressureless, single or multiphase, deep, surface or combined grouting.

Pressure grouting of masonry applies a pressure from 3 to 10 bar depending on the pore system, the tensile strength of injected materials and masonry, the type of grout and the purpose of grouting. Only such masonry (binder, masonry units) which has the necessary tensile strength to transfer the internal tensile stresses caused by pressure grouting can be injected under pressure. The used pressure is based on the requirement to achieve a reliable filling of the pores with the grout.

Pressureless grouting using hydrostatic pressure usually up to 3 bar requires good masonry permeability, low consistency and slow solidification of the grout.

The basic precondition for achieving the required effect of grouting in historic masonry is:

- evaluation of the masonry pore structure (pore distribution, pore size with the maximum proportion in total porosity), chemism (salt content and type, pH), masonry moisture content, masonry condition (disintegration, cavities, cracks, degree of weathering),

- grout design, its properties, composition or particle size allow a reliable filling of the pore structure, including cavities and cracks,
- verification of the grout penetration radius (distance from the grouting borehole),
- overall evaluation and design of the grout, grout injection technology and distance of boreholes.

The grouting aimed at improving mechanical or other properties of individual components of masonry is carried out by means of injection pipes, so-called packers, with a diameter of 20 to 30 mm, fitted into drilled holes sealed with gypsum or fast-setting mortar. The injection pipes (packers) can be made of plastic (working on the principle of a dowel and requiring a “stronger” material) or metal with a free-floating or fixed ball. Metal packers are anchored in the masonry by a ring seal in the lower part, which expands by screwing. For grouting degraded mortar, it is advisable to use metal packers with a free-floating ball.

The selected distance of boreholes is usually ca 0.2 m, max. 0.3 m (exceptionally, in justified cases, even larger) so that the pores, voids, cracks and cavities are properly filled. The grouting design includes the design of grouting packers and pumps, the distribution of packers, the distance, diameter and depth of the boreholes and the grouting technique. Only structures that are permeable can be injected - they have an open pore system composed of mutually interconnected pores - so that air can escape during grouting and the grout can penetrate into the masonry structure.

The depth of single-sided boreholes is 3/4 to 4/5 of the masonry thickness, in double-sided boreholes usually 1/3 to 2/3 of the wall thickness. The depth of the boreholes, the grouting procedure (singlephase, multiphase) and the grouting pressure must be determined with a view to the material and the masonry condition. The achieved compressive strength of grouted masonry depends on the amount and quality of the grout penetrated into the masonry.

With the use of individual boreholes, masonry grouting can be performed as overall grouting or grouting in strips, always proceeding from the lower section to the higher one. The density and distance of boreholes are specified as described above. Larger cracks (above 2 mm) must be cleaned, damaged parts removed, wedged and sealed before grouting.

The research project [2] addressed the design and laboratory verification of a special method – overall surface pressure grouting for the strengthening of mainly surface and subsurface masonry layers and a combined electrophysical method for high-volume grouting.

The method of strengthening materials by overall surface pressure grouting employs additional mechanical supply of substances based on Ca_2^+ , or based on silicates into the material structure and the activation of unreacted substances based on Ca_2^+ contained in the structure of injected materials to achieve an increase in strength, cohesion, or adhesion to the substrate. In overall surface pressure grouting, the injected solution is “pushed” into the pore system of (injectable) masonry so that the required gradual saturation of masonry pores occurs. The main advantage of this method is its high effectiveness and uniformity in terms of strengthening the plaster and increasing its adhesion to the substrate. With good injectability and an open pore system of masonry, this method may also enable a partial penetration of the grout into the subsurface layers of masonry, which usually show the highest degree of weathering and disintegration (deposition of leached salts). It is commonly assumed that masonry is weathered to a depth of ca 10 - 20 cm, and the remaining part of masonry is usually not affected by degradation processes.

The grouting agent must not contain particles that settle rapidly in surface layers (filling the pore system) and thus form a layer impermeable for further penetration of the grout. The surface and subsurface masonry layers of the grouted structure must not have a moisture content higher than 7% by weight (under ČSN P 730610 [9] – increased moisture content), and the total amount of salts must not exceed 1% by weight. There must be no surface crust on the surface of the

grouted structure that would prevent the grout penetration into the pore system of the structure, and the masonry surface must be free of major uneven spots, dirt and deposits. Overall surface pressure grouting is not suitable for reinforcing of masonry degraded by cracks or cavities.

During combined pressure and electrophysical grouting, the hydrostatically applied grouting substance penetrates into the structure through the action of an electrostatic field. Combined electrophysical grouting is based on the principle of active electroosmosis using the electrical potential to propagate the injected grout through a porous material with a pore distribution with radii in the range of $r \in (10^{-7}; 10^{-10})$ m, and pressureless or low pressure grouting uses hydrostatic pressure for the primary "impregnation" of the grouted structure with the grout.

Combined electrophysical grouting is based on the principle of a closed DC circuit composed of a low voltage source (≤ 30 V) and a connection between wall strip electrodes (cathodes – negative electrodes) located on opposite surfaces of masonry and anode (positive electrode) at the end of the injection tube inserted into a borehole reaching to the middle part of the masonry (Figure 2). The electric field that is created between the electrodes causes a directed accelerated movement of ions, e.g. Ca_2^+ present in the grouting mixture. The positive cations move towards the negative electrode (cathode), while the negative anions move towards the positive electrode (anode).

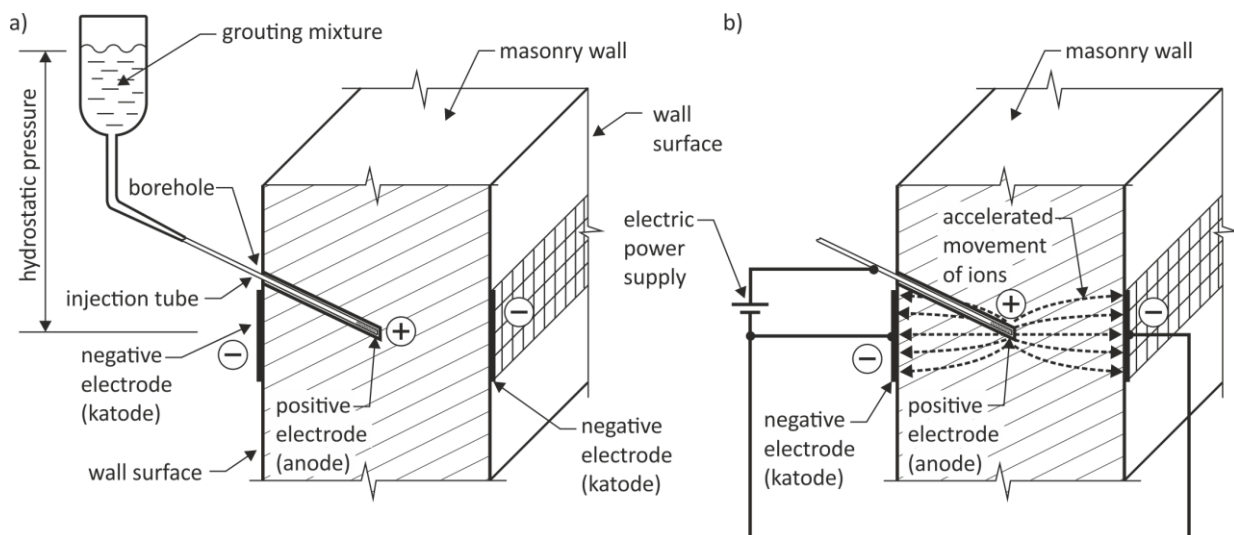


Fig. 2 - Combined electrophysical grouting of masonry structures; a) Grouting of masonry setup, b) Application of electrostatic field for propagation of grouting mixture through masonry

The depth and penetration rate of the grout into the structure varies depending on the pore system, the size and intensity of the electric field, the moisture content of the structure, the grout viscosity and the particle size in the grout. The uniformity of reinforcement depends on the electrodes used and the pore distribution. If strip electrodes are used, we may expect that the narrower the pore distribution range, the more uniformly the grout will be distributed across the cross-section of the structure. With an increasing proportion of pores with a radius greater than 10^{-4} m in the total porosity of the material, the effectiveness of combined electrophysical grouting decreases.

The combined electrophysical grouting method is not suitable for use in cases with too low pH ($\text{pH} > 6$), which often occurs in older historic buildings. To ensure its effectiveness in masonry with high salinity a voltage of up to 50 V is required compared to the commonly used voltage of 6 V. The effectiveness of combined electrophysical grouting also decreases with an increasing proportion of pores with a radius $r > 10^{-8}$ m, especially if $r > 10^{-4}$ m and larger. The proportion of

pores with a radius $r > 10^{-4}$ m and larger should not be greater than 10%, and the proportion of pores with a radius $r > 10^{-8}$ m should not exceed 30%. The combined electrophysical grouting method is not suitable for masonry with $\geq 1\%$ wt. salts and chloride contents $\geq 0.3\%$ by weight. The combined electrophysical grouting method is applicable to structures with a moisture content of 4% to 5% by weight so that there is enough space remaining in the pore system for the grouting substance propagation.

EXPERIMENTAL RESEARCH

The experimental research into the effect of grouting on the restoration of integrity and strength of historic brick and stone masonry degraded by cracks or by cavities located inside columns was conducted on experimental specimens with dimensions of 290 x 440 x 420 to 450 mm (brick masonry) and 500 x 600 x 720 to 750 mm (stone masonry). Five grouting agents were used in the research, of them 4 based on hydraulic lime mixtures and 1 resin-based mixture. The lime-based grouting agents were applied by low-pressure grouting using a screw grout pump (2 - 10 bar), and the resin-based grout was applied by pressureless grouting using hydrostatic pressure (ca 0.5 bar).

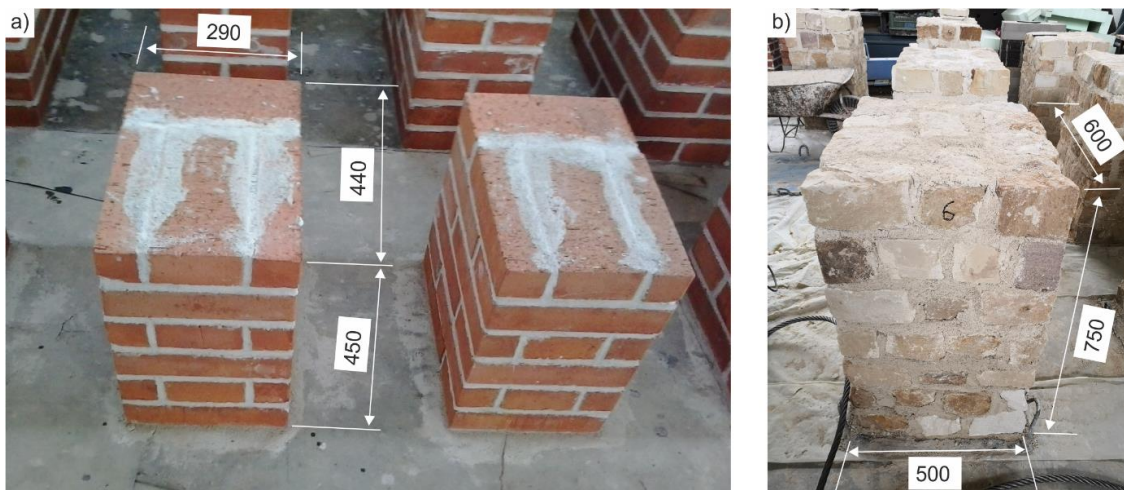


*Fig. 3 Experimental specimens with artificial crack and cavities;
a) Brick masonry, b) Stone masonry*

The total porosity of bricks ranged within 29.3 - 32.9% with a prevailing pore radius of 600-2000nm (42%), of sandy marlstone within 21.5 - 29% with a prevailing pore radius of 600-2000nm (25%), sandstone within 15.2 - 18.9% with a prevailing pore radius of 7500-30000nm (72%), trachyte within 6.8 - 11.8% with a prevailing pore radius of 150-600nm (35%), limestone within 1.2 - 2.1% with a prevailing pore radius of 10-25nm (25%) and mortars from 16.5 to 26.2% with a prevailing pore radius of 150-600nm (25%), (Figure 4).

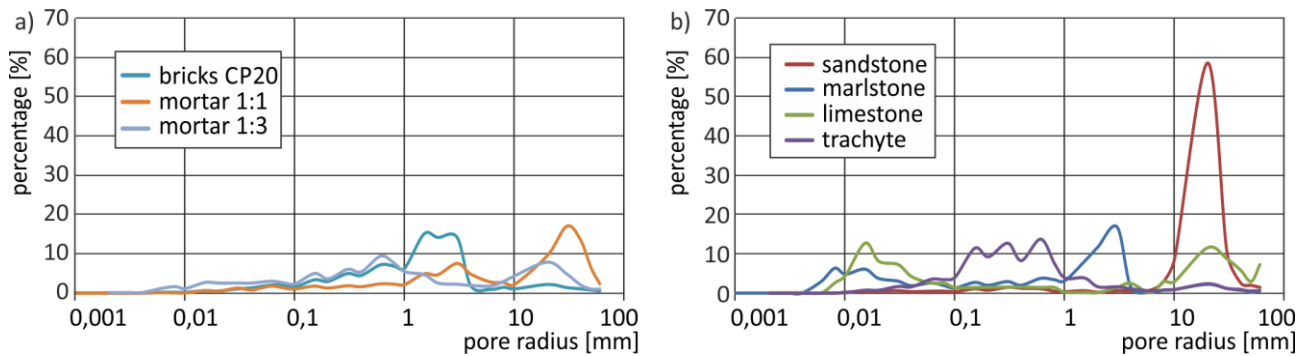


Fig. 4 - Distribution curves of pore representation in bricks and mortar (a) and stone masonry units (b)

The effectiveness of grouting in terms of the experimentally identified ultimate bearing capacity values of grouted brick and stone masonry columns with an artificial crack and an artificial cavity under concentric compression varies. In the case of columns with **an artificial cavity**, a demonstrable increase in the load-bearing capacity of the grouted column under concentric compression was manifested as a result of filling up the artificially created cavity with the grout. However, stone masonry columns showed greater variation in obtained results, due to their greater heterogeneity. In the case of grouted columns with **an artificial crack**, the grouting effectiveness in terms of increasing the load-bearing capacity of masonry under concentric compression was not manifested to the extent expected. In the case of masonry with an artificial crack, a partial increase in the load-bearing capacity of the masonry was achieved by grouting with the agent based on hydraulic lime nanoparticles, low viscosity resins and silicates. In the case of masonry with an artificial cavity, an increase in the load-bearing capacity of the masonry was achieved by grouting with all cases of the verified grouting agents. The basic precondition for achieving the required effectiveness of grouting is a perfect filling of the crack or cavity with the grout.

The relatively low effectiveness of grouting of masonry columns with an artificial crack, manifested during the dismantling of the columns after the test, is caused by insufficient filling of the cracks located in the vicinity of the grouting borehole due to premature grout settling or due to inadequate consistency of the grout:

- the ultimate bearing capacity of grouted brick masonry columns with **an artificial crack** under concentric compression (Figure 5a) ranges within 85 to 145 % of the ultimate bearing capacity mean value of reference columns under concentric compression (masonry columns with an unfilled artificial crack),
- the ultimate bearing capacity of grouted brick masonry columns with **an artificial cavity** under concentric compression (Figure 5b) ranges within 85 to 172 % of the ultimate bearing capacity mean value of reference columns under concentric compression (masonry columns with an unfilled artificial cavity),
- the ultimate bearing capacity of grouted stone masonry columns with **an artificial crack** under concentric compression (Figure 6b) ranges within 80 to 175 % of the ultimate bearing capacity mean value of reference columns under concentric compression (masonry columns with an unfilled artificial crack),
- the ultimate bearing capacity of grouted stone masonry columns with **an artificial cavity** under concentric compression (Figure 6a) ranges within 61 to 132 % of the ultimate bearing capacity mean value of reference columns under concentric compression (masonry columns with an unfilled artificial cavity).

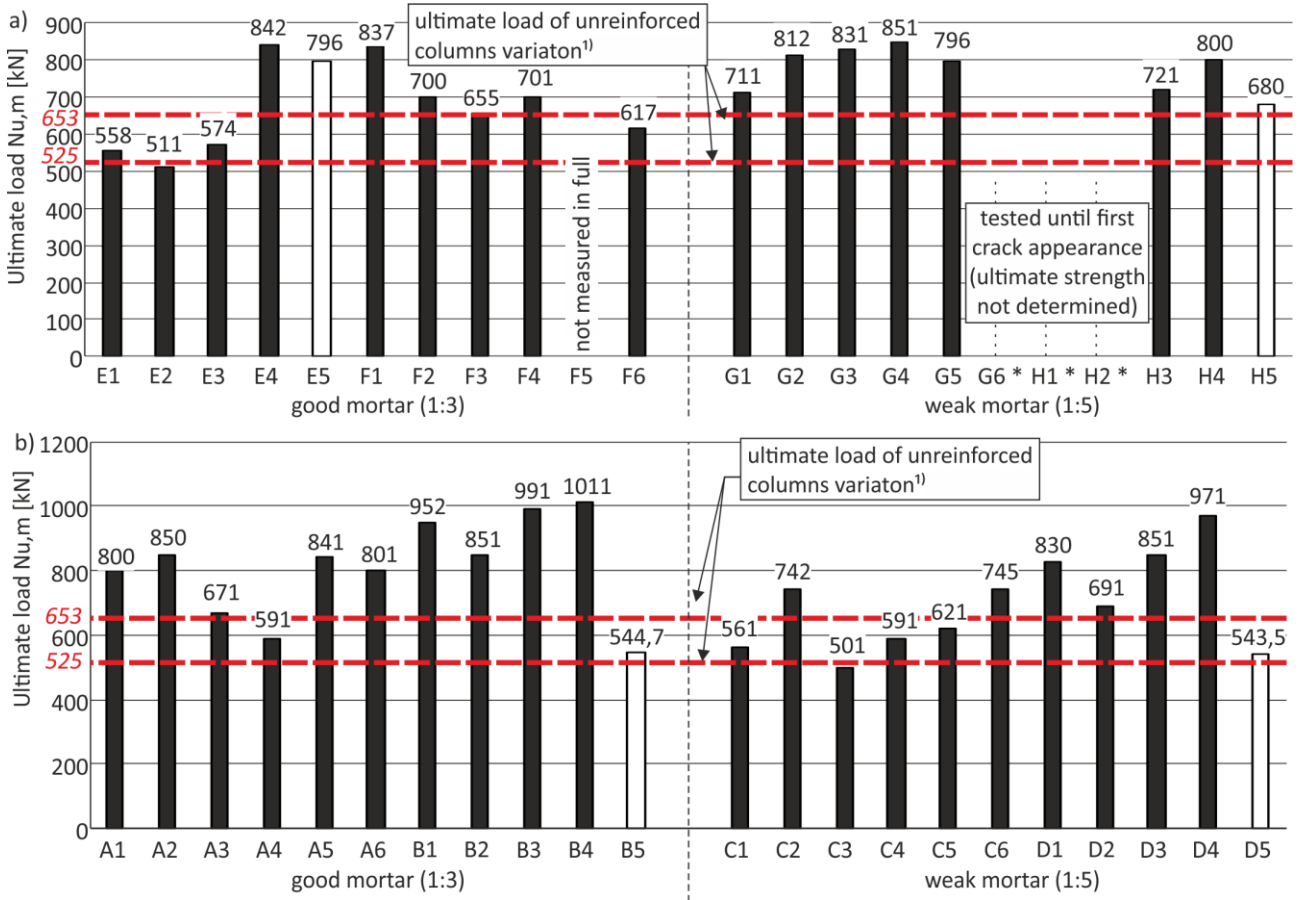


Fig. 5 - Comparison of experimentally determined ultimate strength in concentric compression of grouted brick columns with an artificial crack (a) and with an artificial cavity (b)

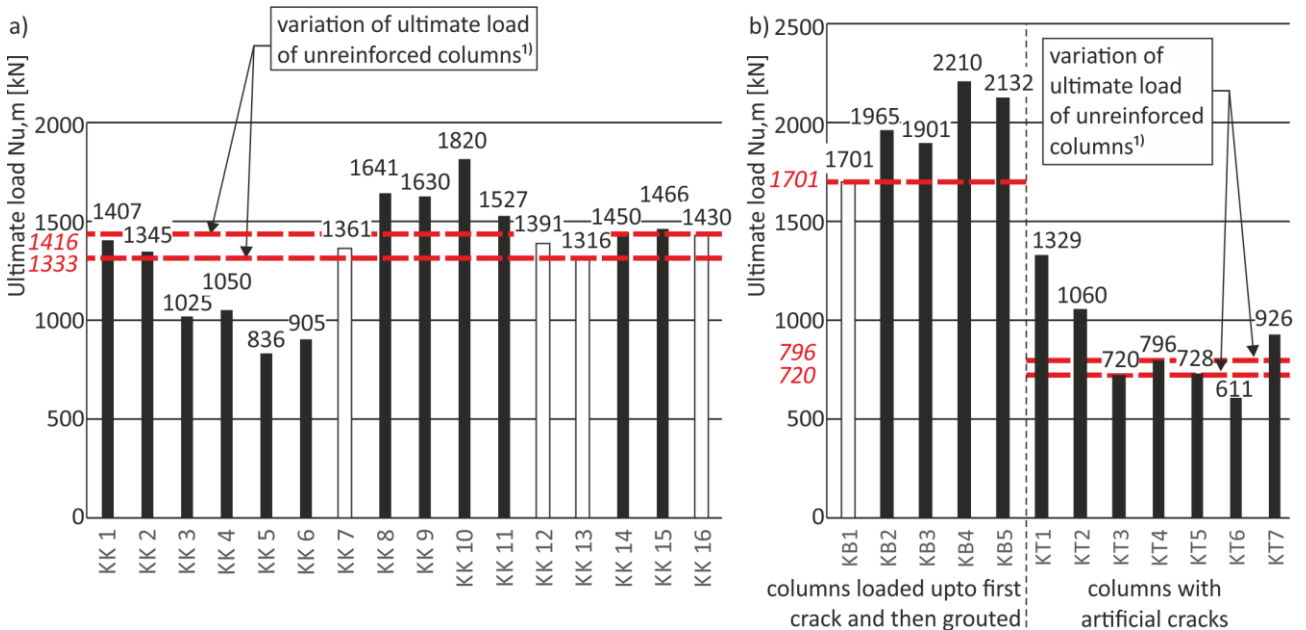


Fig. 5 - Comparison of experimentally determined ultimate strength in concentric compression of grouted stone columns with an artificial cavity (a) and with an artificial crack (b)

The experimental research has revealed a relatively significant effect of the mechanical properties of grouting agents (adhesion, compressive strength) on the effectiveness of grouting [10].

CONCLUSION

The experimental research [2] aimed at gaining new knowledge for the design of brick and stone masonry grouting techniques in terms of the stabilization and increase in the strength of masonry damaged by cracks, masonry with cavities and masonry with a high void content by applying grouting agents based on lime, resins and silicates has pointed out a considerable variability of the resulting grouting effectiveness. To achieve the required properties of grouted masonry the masonry must be diagnosed and the above grouting design procedure must be observed.

ACKNOWLEDGEMENTS

The article was written with support from the NAKI DG16P02M055 project “Development and Research into Materials, Procedures and Technologies for Restoration, Conservation and Strengthening of Historic Masonry Structures and Surfaces and Systems of Preventive Care of Historic and Heritage Buildings Threatened by Anthropogenic and Natural Risks”.

REFERENCES

- [1] WTA 4-3-98 Masonry repairs - stability and load capacity (WTA guideline). WTA, 2004
- [2] NAKI II DG16P02M055 research project (Ministry of Culture of Czech Republic) “Development and Research into Materials, Procedures and Technologies for Restoration, Conservation and Strengthening of Historic Masonry Structures and Surfaces and Systems of Preventive Care of Historic and Heritage Buildings Threatened by Anthropogenic and Natural Risks”, 2016-2020, lead researcher prof. Ing. Jiří Witzany, DrSc.
- [3] Škoda, D., Kuřitka, I., Kroftová, K., Kubát, J., 2019. Technology of preparation of barium and magnesium hydroxide nanodispersion and possibilities of their use in monument care. In: *Contemporary materials and technologies in civil engineering 2018*. Praha: Czech Technical University in Prague. Acta Polytechnica CTU Proceedings. vol. 21.
- [4] Kroftová, K., Kuřitka, I., Škoda, D., Šmidtová, M., Masař, M., 2017. *Synthesis of nanolime suspension and their potential use in cultural heritage preservation* In. EASEC 15 – The Fifteenth East Asia – Pacific Conference on Structural Engineering and Construction.
- [5] Kroftová, K., Kubát, J., Škoda, D., 2018. *Possibilities of Consolidation of Historical Materials with Selected Nanodispersions - Results of Experimental Research of the Strength Degree on Reference Formulas*, In. NaNs: Moderní materiály a technologie ve stavebnictví.
- [6] Maravelaki-Kalaitzaki, P., Bakolas, A., Karatasios, I., Kilikoglou, V., 2005. Hydraulic lime mortars for the restoration of historic masonry in Crete, *Cement and Concrete Research*, 35, pp. 1577-1586, DOI 10.1016/j.cemconres.2004.09.001
- [7] Papayianni, I., Pachtá, V., 2015. Experimental study on the performance of lime-based grouts used in consolidating historic masonries. *Materials and Structures*, 48, pp. 2111-2121, DOI 10.1617/s11527-014-0296-5
- [8] Yang, Z., Xiaohui Ch., 2013. A performance study of high-strength microbial mortar produced by low pressure grouting for the reinforcement of deteriorated masonry structures. *Construction and Building Materials*, 41, pp. 505-515. ISSN 09500618. DOI: 10.1016/j.conbuildmat.2012.12.055
- [9] ČSN P 730610 Waterproofing of buildings - The rehabilitation of damp masonry and additional protection of buildings against ground moisture and against atmospheric water - Basic provision, UNMZ, 2000

- [10] Witzany, J.; Zigler, R.; Kroftová, K.; Čejka, T.; Kubát, J.; Holický, M.; Karas, J., 2018. The Effect of Pore Distribution in Historic Masonry on the Grouting Method and Grouting Mix Selection, *The Civil Engineering Journal*, 3(10), 307-329. ISSN 1805-2576, DOI: 10.14311/CEJ.2018.03.0025